UNIVERSITY OF SOUTHAMPTON

FACULTY OF EARTH AND OCEAN SCIENCES

CONTROLS OF BRITTLE EXTENSION AT THE LARGE-SCALE AT MID-OCEAN RIDGES

by

GAVIN ANDREW HAUGHTON

Thesis for the degree of Doctor of Philosophy

September 2019

UNIVERSITY OF SOUTHAMPTON

ABSTRACT

FACULTY OF EARTH AND OCEAN SCIENCES

Marine Geology

Thesis for the degree of Doctor of Philosophy

CONTROLS OF BRITTLE EXTENSION AT THE LARGE SCALE AT MID-OCEAN RIDGES

Gavin Andrew Haughton

Seafloor morphology at Mid-Ocean Ridges is thought to be controlled by the interaction of tectonic and magmatic processes. In turn, these are thought to control the distribution of volcanic and brittle tectonic features on the seafloor over multiple scales; from the placement of individual faults measuring hundreds of metres, to shallow and deep bathymetric swales over tens of kilometres. It is unclear, however, whether there is a systematic relationship between these smaller and larger features, with varying melt supply, spreading rate, and spreading obliquity.

Here, to investigate this relationship systematically, I have developed an innovative method to robustly and objectively identify large scale variations in brittle tectonic extension, expressed on the seafloor as faults. This method allows comparison with a number of proxies for melt supply along-strike and orthogonally-away from spreading ridge segments. I objectively identify fault planes by cross-correlating dip, dip direction, and backscatter that might individually suggest their presence. The fault heave is measured to estimate extension over length and temporal scales comparable to those melt-related processes involved in forming second order ridge segments. Regions of high and low melt supply are identified and defined quantitatively from positive and negative anomalies in bathymetry. These indications are cross-validated by comparison to gravity anomalies and other bathymetric features diagnostic of high or low melt supply.

Following analysis of several mid-ocean ridge examples, spanning a range of spreading rates and ridge/spreading orientation, no consistent correlation between large scale extension and melt supply at scales of 1 km, 10 km, or 20 – 50 km was found. This null-result has three potential, contributing, explanations: First, environmental processes erode and mask faults, reducing their apparent heave which then deviates from the theoretical model. Second, fault extension occurs over a broader area surrounding the spreading axis while melt intrusion and delivery into the upper crust remains more focused on a narrow zone within the spreading axis. This would result in a spatial and temporal disconnect between the location and occurrence of brittle faulting and the location and timing of delivery of magma. Third, brittle extension and fault distribution may be locally controlled by dykes and lava domes, whose distribution may not scale-up to the larger magnitude of second order spreading centre features such as elevated and inflated segment centres and depressed and subsided segment ends.

Partial dataset available at https://doi.org/10.5258/SOTON/D1096, full dataset available as hard drives from Prof. Bramley Murton, National Oceanography Centre, Southampton, bramley.murton@soton.ac.uk

Table of Contents

Table of Tables

Table of Figures

Academic Thesis: Declaration of Authorship

I, Gavin A Haughton declare that this thesis and the work presented in it are my own and has been generated by me as the result of my own original research.

I confirm that:

1. This work was done wholly or mainly while in candidature for a research degree at this University;
2. Where any part of this thesis has previously been submitted for a degree or any other qualification at this University or any other institution, this has been clearly stated;
3. Where I have consulted the published work of others, this is always clearly attributed;
4. Where I have quoted from the work of others, the source is always given. With the exception of such quotations, this thesis is entirely my own work;
5. I have acknowledged all main sources of help;
6. Where the thesis is based on work done by myself jointly with others, I have made clear exactly what was done by others and what I have contributed myself;
7. None of this work has been published before

Signed: .....

Date: .....

Acknowledgements

I first and foremost could not have completed this research without the guidance of my PhD supervisors, Prof. Bramley J. Murton, Prof. Tim J. Henstock, and Dr. Tim Le Bas. I also thank Prof. Richard Hobbs for his guidance with the Costa Rica segment data sets.

I share my gratitude for the crew and researchers aboard the *RRS Charles Darwin* during cruise CD99 in 1996 for the original acquisition of the data. I would like to thank the British Oceanographic Data Centre for storing the bathymetry data used in this study, and OvationData/DPTS Limited for extracting and processing the raw data to produce workable multibeam bathymetry and backscatter.

I am grateful to the officers, crew, technicians, and science party on-board the *RRS James Cook* during cruise JC114. The OSCAR project is funded by NERC grant NE/I027010/1. Special thanks for *InterRidge* who provided a travel bursary that allowed Gavin Haughton to join JC114. The data is available from the British Oceanographic Data Centre. Bathymetry was processed in *CARIS*™ and analysed in *ArcGIS*™ with figures edited in *Adobe Photoshop™*. The seismic reflection profiles for Chapter 4 were processed using *Globe Claritas* by Dean Wilson.

Also, thanks to Rosalind Haskins for endless support and encouragement. The comradeship of sharing an office with Age Vellinnga and Jamie Hizzett was much appreciated

Chapter 1: Introduction

The Earth's surface is controlled by the large scale movement of lithospheric plates. These lithospheric plates consist of an upper layer called the crust, which has a distinct petrological composition from the mantle and undergoes brittle deformation. Beneath the crust is the remainder of the lithosphere, this is mechanically distinct from the mantle allowing for it to behave as a distinct moveable plate above the asthenosphere. The asthenosphere is the upper, ductile layer of the mantle whose high viscosity allows the lithosphere to remain mobile and distinct from the mantle.

Where these lithospheric plates move away from each other at divergent margins new crust is created. Divergent margins are mostly found within ocean basins where they form almost continuous mountain chains called Mid-Ocean Ridges (MORs). These MORs are where new oceanic crust is created at the location of plate separation, called the spreading axis. An understanding of the processes that produce the oceanic lithosphere along MORs will help us understand how the oceanic crust influences the seafloor's morphology. At MORs, morphology is largely determined by the interaction of two processes; tectonism and magmatism. Tectonism is the extensional strain on the crust occurring at the plate's boundary. Magmatism is how magma migrates through the lithosphere, solidifies and accretes to build new oceanic lithosphere at the spreading axis. This ratio of tectonism to magmatism is primarily influenced over tens to hundreds of kilometres by three largescale parameters; spreading rate, melt supply, and spreading direction.

The first three sections (1.1 – 1.3) of this Chapter explores each of these parameters and builds an understanding of how they influence surface morphology. These parameters influence morphology ranging from individual features, such as lava flows, to largescale surface structures, such as breaks along the MORs length producing segmentation. The fourth Section (1.4) of this Chapter is a detailed discussion of tectonism.

1.1 Spreading rate and its effect on morphology and structure

Spreading rate describes the speed at which tectonic plates migrate away from each other. This is the primary determiner of strain at MORs making it one of the major parameters controlling morphology. Spreading rate is influenced by several process acting upon the oceanic plate, the primary influence is slab pull where the older, cooler, denser oceanic lithosphere becomes a subducting slab into the mantle, beneath a less dense plate at a destructive margin. The larger and older the subducting slab is, and the greater the angle of subduction is, the greater tensile strain it will have on the rest of the plate, thus increasing spreading rate (Schellart, 2004). For example, an extremely rapid paleo-spreading rate of 140 mm yr^{-1} moved the Indian Plate into Eurasia is thought to have resulted from the combined pull of two parallel subduction zones (Jagoutz et al., 2015).

The second main influence is ridge push at divergent margins (Schellart, 2004). The strength of ridge push is determined by the height of the lithosphere close to the spreading axis above the rest of the plate that is at isostatic equilibrium, and the density of that uplifted lithosphere. The greater the uplifted lithosphere's height and density, and the less shear drag exerted from the asthenosphere, the more compressional force it exerts away from the spreading axis (Bott, 1991) which increases spreading rate.

There are also several minor influences on spreading rate acting upon specific plate boundaries. Most spreading ridges are passive, meaning the plates are separating due to slab-pull and ridge-push, irrespective of the mantle below, which partially melts to fill the space created. However, a potential third contributor to spreading rate can occur when a MOR is above actively flowing mantle. Where there is mantle anisotropy, indicating flow direction, which is aligned with paleo-plate direction, there can be an increase in plate velocity (Williams et al., 2016).

Another minor contributor to spreading rate is the degree of coupling of the plate to the asthenosphere. A well coupled plate and asthenosphere

can reduce spreading rates suggesting mantle drag can be either resistive or accelerative (Agnon & Eidelman, 1991). Additionally, transform boundaries are where two plates are moving past each other without creating or destroying crust, these provide resistive forces to spreading through lithospheric coupling (Forsyth & Uyeda, 1975). The relative strengths of these forces acting on oceanic plates will influence the spreading rate at the MOR and the amount of strain applied across the plate, this will influence the morphology created on-axis.

Spreading rate is commonly used to categorise MORs due to a non-linear correlation with crustal thickness (McKenzie & Bickle, 1988; Wang et al., 2015) and typical associated morphology. For example, it has been noted that an increase in seafloor ruggedness and axial valley depth occurs when spreading rate dropped from slow (30 mm yr^{-1} full rate) to ultra-slow (15 mm yr^{-1} full rate) in the South West Indian Ridge, without a change in crustal thickness (Sauter et al., 2011). MORs are generally categorised into slow, intermediate, and fast.

1.1.1 Slow MOR morphology

At slow spreading rates (<55 mm yr^{-1} full rate) the crust mostly cools on-axis (Chen & Morgan, 1990) making it more brittle. This results in high amounts of brittle deformation with seismicity reaching 8 km depth because lithospheric strength is inversely related to temperature (Toomey et al., 1988). This brittle deformation creates a rough topography, with the spreading axis being located within a 1 – 2 km deep axial valley (Figure 1.1A) with elevated rift flanks (Macdonald, 1982). It is typical for the ridge flanks to be asymmetrical (Murton & Rona, 2015; Sempéré et al., 1990).

Spreading axes do not continuously follow the plate boundaries trend, instead an axis is frequently broken into segments where it steps to the left or right, sinistral or dextral. At slow spreading ridges this segmentation length is around 400±200 km (Macdonald et al., 1991). These segments are separated by transform faults that are narrow, 2 – 20 km wide (Fox et al., 1969), and have depth anomalies below the average seafloor of 500 – 2000 m (Macdonald et al., 1991). These

transform zones are regions where segments from opposite plates are sliding past each other, resulting in shear stress, rather than tensile strain that occurs at the spreading axis.

The high amount of tectonic extension at slow spreading ridges creates long faults that have throws >200 m (Goff & Arbic, 2010; Macdonald, 1982). These large fault blocks create abyssal hills with high aspect rations in plan view, where heights range in the hundreds of meters and lengths parallel to the spreading axis are several kilometres (Goff & Arbic, 2010; Macdonald, 1982). Compared to faster spreading MORs, major volcanic eruption rates at slow MOR ridges are low, approximately once every 5,000 – 10,000 yrs, resulting in distinct, isolated areas of volcanism along the spreading axis (Macdonald, 1982). These can create distinct Axial Volcanic Ridges that are elongated along the trend of the spreading axis, symmetrical in profile and composed of hummocky lava flows (Figure 1.1A).

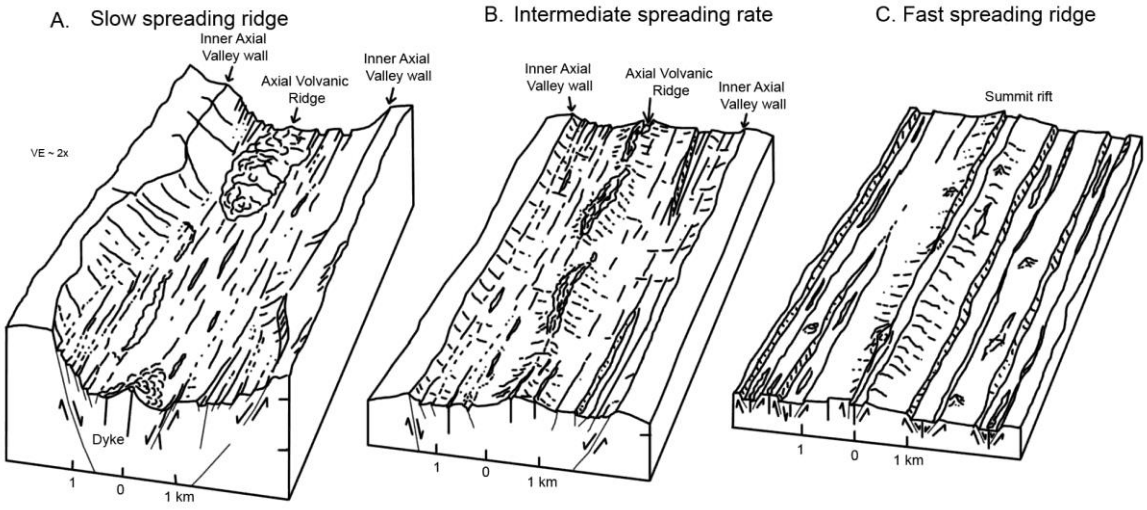

Figure 1.1*: Ridge morphology depending on spreading rate. Figure is taken from Macdonald, (1982). Mid-ocean ridge topography becomes more rugged with slower spreading rates.* ***A****: Slow spreading ridge with spreading axis at the bottom of a deep axial valley. Seafloor is very rugged and along-axis volcanism is sporadic.* ***B****: Intermediate spreading ridge with raised spreading axis in a shallow axial valley, along axis volcanism is almost continuous.* ***C****: Fast spreading ridge with raised spreading axis,*

smoother seafloor dominated by sheet flows and faults with low amounts of throw.

Two slow spreading ridges are analysed, firstly the Broken Spur segment of the Mid-Atlantic Ridge in Chapter 3 that has the typical morphology described. Later the Reykjanes Ridge in Chapter 5 that despite having a slow spreading rate, has a morphology more similar to a fast spreading ridge, due to influences I explain later.

1.1.2 Intermediate MOR morphology

At intermediate spreading ridges (55 - 80 mm yr^{-1} full rate) the rift valley is 50 – 200 m deep and resides within a broader axial high (Figure 1.1B). The topography is smoother than that seen at slow spreading ridges because of less faulting and more frequent volcanic eruptions. As indicated by faults having throws of >50 m and major volcanic eruptions occurring approximately once every 300 - 600 yrs (Macdonald, 1982).

In Chapter 4, I investigate the intermediate spreading Costa Rica spreading ridge. Morphologic features tend to be a mix of those described previously for slow spreading ridges and those described next at fast spreading ridges.

1.1.3 Fast MOR morphology

At fast spreading ridges (>80 mm yr^{-1} full rate) crust moves off-axis faster than the rate of cooling creating a shallower ductile layer that extends off-axis. This shallow ductile layer prevents the tectonic extensional strain causing as much brittle faulting at fast spreading ridges. This results in a smoother seafloor, shallower seismicity, and a triangular peak on-axis rather than an axial valley (Figure 1.1C) (Macdonald, 1982). The ridge flanks are typically shallow and symmetrical (Murton & Rona, 2015). At fast spreading ridges, segments separated by transform faults that are 600±300 km long and have depth anomalies of 300 – 600 m (Macdonald et al., 1991). At fast spreading ridges the boundaries between segments can also be propagating rifts, where the spreading axis of one

segment is retreating while the neighbouring axis is advancing, resulting in changes in segment length. Segments can also be separated by overlapping spreading centres, where the spreading axes of two segments overlap and are separated by a basin, eventually the axes may connect and one becomes extinct (Puthe & Gerya, 2014). The seafloor is smooth at fast spreading MORs because faults have low throws, mean of 41 m, and are spatially frequent, mean of 1.5 km (Carbotte & Macdonald, 1994), and major volcanic eruptions occur approximately once every 50 yrs (Macdonald, 1982).

Some of the described fast spreading ridge morphology is visible at the slow spreading Reykjanes Ridge in Chapter 5 because of its high melt supply as explained below.

1.2 Definition of melt supply and its relation to MOR morphology

There is a less clear relationship between morphology and magma supply than we have shown with spreading rate. Variance from the general morphology associated with spreading rate occurs where the MOR is associated with 'hot-spots', where the mantle below the spreading axis is hotter than average. Olivine crystals from lavas erupted at the Hawaii and Iceland hotspots indicated higher melting temperatures of 213 - 235°C and 162 - 184°C, respectively, above ambient mantle temperature below non-hotspot influenced MORs (Putirka, 2005). This causes the ridge to shallow and adopt a morphology more similar to a fast spreading MOR. Examples of MORs influenced by hot-spots in this way are; the Reykjanes Ridge close to Iceland, the Mid-Atlantic Ridge close to the Azores, and the Southeast Indian Ridge close to the Amsterdam–St. Paul hotspot (Escartin et al., 2001; Ma & Cochran, 1996; Searle et al., 1998). Conversely, where a MOR is associated with 'cold-spots' the mantle is at a lower temperature than average. Above cold-spots MOR morphology adopts slow-spreading characteristics. An example of this would be the Southeast Indian Ridge at the Australian-Antarctic discontinuity (Ma & Cochran, 1996).

As well as influencing entire MORs, magma supply also influences morphology within segments separated by transform faults, described as first-order segments. At the scale of first-order segments models have shown a correlation between fault heave and spacing with the proportion of magmatic intrusion and crustal thickness (Behn & Ito, 2008; Buck et al., 2005). Hence magma supply appears to provide another first order effect on MORs.

Melt supply is defined as what becomes accreted to the plate as the combined contribution of melt production in the upper mantle and the melt flux, the rate a parcel of melt can move through the crust. On average, at a global-scale, melt supply is thought to be fairly constant (Dick et al., 2003). This is reflected in the near-constant thickness of the magmatic portion of the ocean crust and the near consistency in mid-ocean ridge basalt compositions across a range of spreading rates from 15 to 150 mm yr^{-1} (McKenzie & Bickle, 1988; White et al., 1995).

The similarities in average melt supply between MORs is related to the common process of melt formation below MORs, this is the passive behaviour of mantle upwelling. Passive upwelling of the mantle occurs as a result of plate separation causing the asthenosphere, which is the highly viscous upper mantle, to upwell along the pressure gradient to fill the gap (Searle, 2013). In doing so its adiabat, representing the mantle's temperature and pressure, will cross the solidus, representing the pressure and temperature at which the rock melts, resulting in the production of melt (Figure 1.2). This process is called adiabatic melting and describes the production of melt due to a drop in pressure without a change in temperature. The amount of melt will be determined by how far the mantle adiabat diverts past the solidus without a reduction in temperature, causing decompression melting.

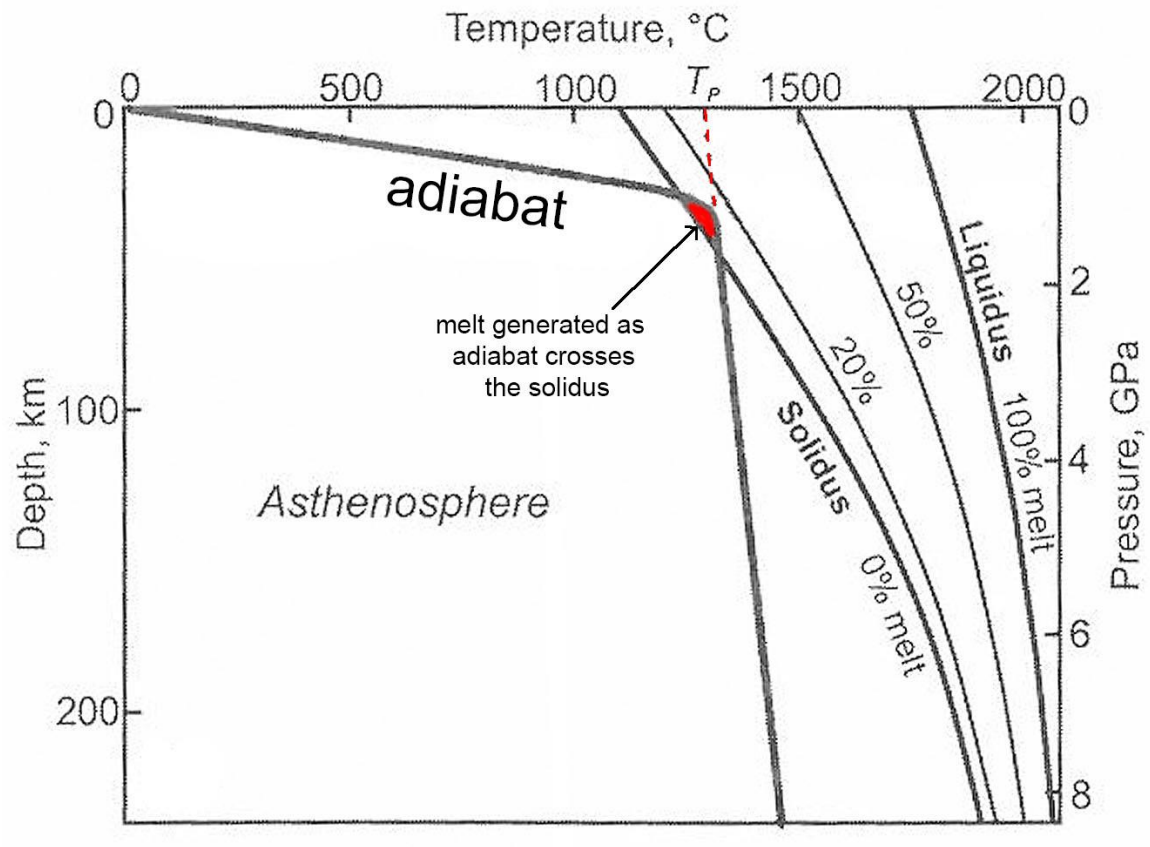

***Figure 1.2**: Mantle melting taken from Searle, (2013). Under MORs the mantle's adiabat crosses the solidus causing partial melting (highlighted red). The melt created after crossing the solidus follows the dashed line to the surface at MORs at the potential temperature, T_p, of 1280˚C.*

The region within the asthenosphere where the adiabat crosses the solidus is called the partial melt zone (red in Figure 1.2), this can be a 100 km wide region below the spreading axis (Morgan, 1987). Global major element variation indicates that low-pressure fractionation produced by adiabatic melting results in 8 - 20% melting (Klein & Langmuir, 1987). The integrated product of that melting forms the primary magmas leading to the construction of the oceanic crust (Klein & Langmuir, 1987; McKenzie & Bickle, 1988). The melt is focused within a few kilometres of the spreading axis by migrating perpendicular to the direction of strain. The strain within the viscously deforming asthenosphere produces anisotropy, where mineral alignment creates a fabric towards the direction of flow, and a porosity towards the bottom of the spreading axis that channels melt (Morgan, 1987).

Despite the global similarity in melt supply (Dick et al., 2003; McKenzie & Bickle, 1988; White et al., 1995), there is variation in melt supply along segments and between MORs. This variation is the result of factors that have affected the position of the mantle solidus and adiabat. Melt supply decreases where the mantle is colder, drier, and more refractory. The temperature gradient can also be disturbed by excessive heat loss by conductive cooling where warm lithosphere within a young segment is juxtaposed across a transform fault against colder lithosphere from older crust. Examples of this occur at the South-West Indian Ridge (Dean et al., 2009; Sleep & Warren, 2014) or at the intersection between MOR and major long-offset transform faults (Garfunkel, 1986; Langmuir & Bender, 1984).

The variations in melt supply are represented in geochemistry. Higher melt supply positively correlates with incompatible elements, these are elements that tend not to be incorporated in a crystal's lattice. High melt supply also positively correlates with Fe and Ca/Al, and negatively correlates with Na (Bown & White, 1994; Klein & Langmuir, 1987; Standish et al., 2008). Greater axial depths have higher Na suggesting their depth is related to lower melt supply (Klein & Langmuir, 1987). Major elements are elements composing >1% of a materials composition, differences in major

elements between MAR segments indicate melt columns in the partial melt zone can reach 60 - 90 km deep, depending on the initial mantle composition (Niu et al., 2001).

Large variabilities in melt supply influence crustal thickness and axial depth along MORs. For example, seismic refraction measurements of crustal thickness and rare-earth element inversions of MORs in the vicinity of hot-spots, tend to have a shallower axis and thicker crust, increasing from the average thickness of 7.1 – 8.3 km to 10.3 – 10.7 km, suggesting a higher melt supply (White et al., 1992). Along the Reykjanes Ridge near the Iceland hot-spot, an increase in mantle temperature of 50˚C above normal mantle potential temperature of ~1320˚C causes a gradual increase in crustal thickness to 10 – 11 km north of 57˚ N (Bown & White, 1994; White, 1997). Above this thicker crust, the Reykjanes Ridge axis is at a shallow depth of 1000 m (Searle et al., 1998), there is no discernible rift valley, and the faults are frequent but small in throw and length (Keeton et al., 1996; Murton & Parson, 1993; Parson et al., 1993).

Alternatively, where the mantle temperature is thought to be low, melt supply and crustal thicknesses are also low. For example, the Australian - Antarctic discordance has an average axial depth of 4000 m. This bathymetry anomaly resides over crust potentially as thin as 2 – 3 km. This crust resides over mantle with a very low velocity indicating it is colder than normal (Forsyth et al., 1987; Sempéré et al., 1991). It has also be observed that low melt supply at transform zones are associated with a thin mean crustal thickness of 3.9 km (Bown & White, 1994).

These variations in melt supply between MORs can determine the axial depth and crustal thickness. I have described the influence of melt supply at the first order scale of segments separated by transform faults. Melt supply also has finer scale, second and third order influences on morphology. These orders are hierarchical; nested in length and depth along the spreading axis, with the higher orders influencing morphology at shallower depths and shorter distances (Figure 1.3 and 1.4) (Carbotte et al., 2016; Macdonald et al., 1988). Although slight variations do occur at

individual spreading ridges, generally, the hierarchy apparent in bathymetry has been shown to be linked to the underlying magma supply system (Carbotte et al., 2016).

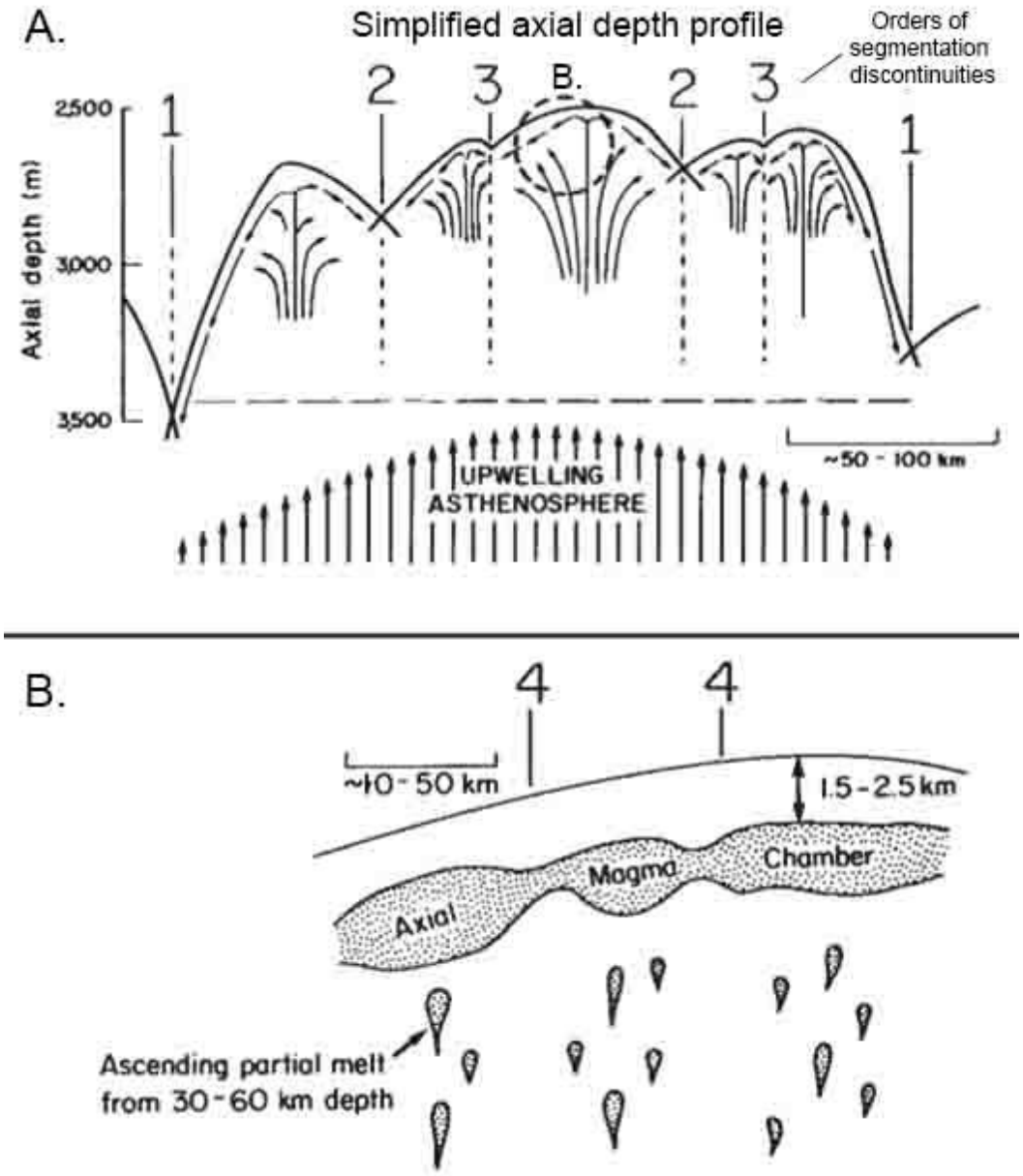

***Figure 1.3**: Image of orders of segmentation and their relationship to melt focusing from Macdonald et al., (1988). **A.** A simplified axial depth profile with along-axis discontinuities labels with numbers, numbers refer to the order of segmentation. The first order segment bound by transform faults labelled '1'. Second order segments bound by non-transform discontinuities labelled '2'. Third order discontinuities are bound by shallow depressions and have no off-axis trace, labelled '3'. Dashed circled region is extent of panel B. Asthenosphere upwelling creates the long*

wavelength melt supply signal for the segment. ***B****. Fourth order segmentation seen as distribution of volcanism along-axis. Each fourth order segment is fed by one active magma chamber.*

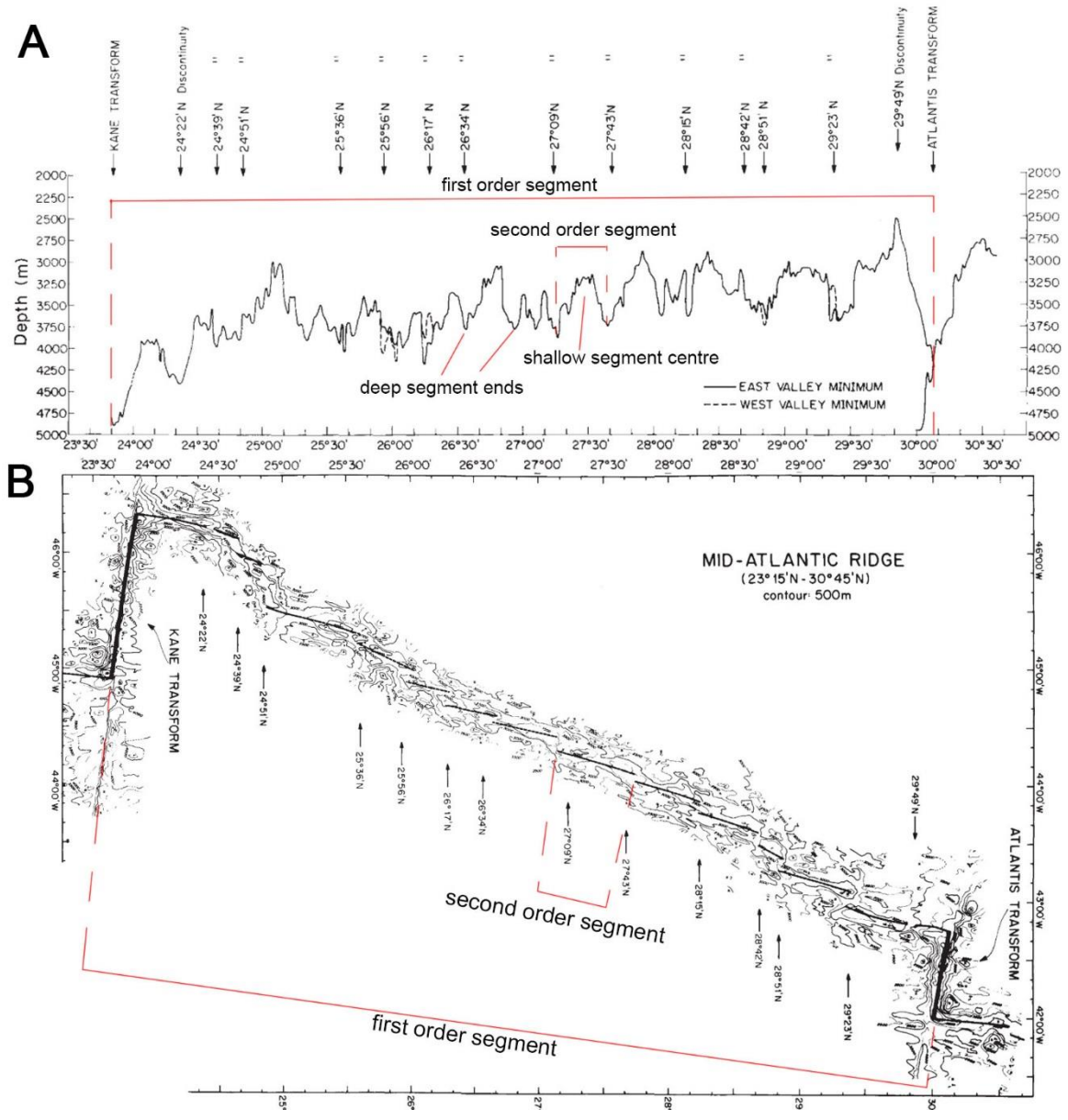

Figure 1.4*: Figure from Sempéré et al., (1990), edited and annotated to illustrate how the model of magmatic segmentation shown in Figure 1.3 explains the first order segmentation between the transform zones over hundreds of kilometres and the second order segmentation between the non-transform discontinuities over tens of kilometres.* ***A****: The along axis bathymetry of the Mid-Atlantic between the Kane and Atlantis transform zones. The bathymetric relief within the first order segment between the transform discontinuities is 800 – 1200 m. The bathymetric relief within second order segments between non-transform discontinuities is 600 m.* ***B****:*

Bathymetry contour map (500 m) of the Mid-Atlantic ridge between the Kane and Atlantis transform zones (Sempéré et al., 1990).

1.2.1 Examples of first order variations in melt supply

First order melt variation along MORs results from the spatial and temporal distribution of melt conduits that originate in the partial melt zone (Larson et al., 1985; Macdonald et al., 1988; Schouten et al., 1985).Carbotte et al., (2016) reviewed geophysical and geochemical observations from fast to slow spreading ridges where they found that tectonic first order segmentation, defined as being separated by transform zones, generally correlated with magmatic segmentation. However, this is not always a simple relation showed by geochemical reviews of the Kane fracture zone in the Mid-Atlantic Ridge and the Tamayo fracture zone in the East Pacific Rise by Langmuir & Bender (1984). Langmuir & Bender (1984)'s results showed that magmatic first order melt segments are indicated by geochemical discontinuities of higher levels of incompatible trace elements and higher levels of La/Sm, La/Yb, and FeO indicating low melt supply across the ridge discontinuities. At the Kane and Tamayo fracture zones, the first order segmentation of melt supply occurs at a smaller scale than tectonic segmentation that was inherited from continental break up (Figure 1.4). The discontinuities in geochemistry along the spreading axis has been interpreted to represent mantle heterogeneities (Langmuir & Bender, 1984).

1.2.2 Examples of second order melt supply processes

Within first order segments, as melt approaches the surface it concentrates into separate conduits at shallower depths to create second order segments consisting of spreading cells separated by non-transform discontinuities (Figure 1.3) (Carbotte et al., 2016). At slow spreading ridges, melt that flows along the base of the lithosphere may be focused into pools to create second order segments without the need for a connection to deeper, mantle conduits. A positive feedback between

pooling of mantle melt and lithospheric structure may then enhance the relation (Carbotte et al., 2016 and references within).

An analysis of all published geochemical, bathymetric, seismic, and gravity data of segmentation at different spreading rates (Carbotte et al., 2016; Schouten et al., 1985) concluded that, at all spreading rates, these spreading cells are segmented over 30 - 80 km. This controls the typical second order MOR morphology from deep segment ends to shallow segment centres (Figure 1.3A) (Sempéré et al., 1990). Along the MAR (25 - 27˚ N), the second order segments are spaced at 10 – 100 km intervals (Figure 1.4). At the centre of these segments bathymetry along-axis is shallow (Figure 1.4) and gravity anomalies are low. These are interpreted as the focusing of melt conduits causing variations in crustal thickness (Figure 1.5) (Sempéré et al., 1993). The shallow bathymetry of second order segments are offset by 15 – 30 km along non-transform discontinuities with deeper bathymetry, these discontinuities have off-axis traces that are not temporally fixed (Carbotte et al., 2016; Sempéré et al., 1993).

The impact of melt supply on the nature of accretion at MORs is also apparent in the gravity signature of oceanic crust by altering local-scale crustal thickness and composition. At high melt supplies the crust's gravity signature indicates magmatic accretion occurs in 2D, meaning that variation in melt supply only needs to be considered in two dimensions, depth below the axis, and distance away from the axis. At MORs with low melt supplies, accretion is 3D where variation occurs in a third dimension, along the axis (Figure 1.4) (Chen, 1992).

This is best represented in gravity anomalies (Lin et al., 1990) (Figure 1.5). Removing the topographic influence from measured free air gravity anomaly provides a Bouguer anomaly that reflect crustal density (Heiskanen & Moritz, 1967). Crust moving off-axis, cooling, increasing in density and crustal thickness can be modelled and removed from a Bouguer anomaly to calculate a Residual Mantle Bouguer Anomaly (RMBA). A negative deviation away from the model indicates the crust is thicker

and/or lower density, or a positive deviation indicates the crust is thinner and/or higher in density than predicted.

Where 3D accretion occurs melt is channelled to a centralised conduit, possibly by Rayleigh-Taylor instabilities (Schouten et al., 1985; Whitehead et al., 1984) producing a RMBA low 'bullseye' at the segment centre (Lin et al., 1990; Sempéré et al., 1993). These styles of accretion have associated axial morphology; first order magmatic segments with bullseye anomalies typically have long and narrow axial valleys, with a V-shaped profile. Whereas first order segments with no noticeable circular RMBA anomaly have a typical hour glass shaped axial valley, with a U-shaped profile (Sempéré et al., 1993). This 3D accretion can result in a bathymetric deepening of 0.3 – 0.8 km from the segment's mid-point to the segment's non-transform discontinuity (Figure 1.4) (Chen & Lin, 1999).

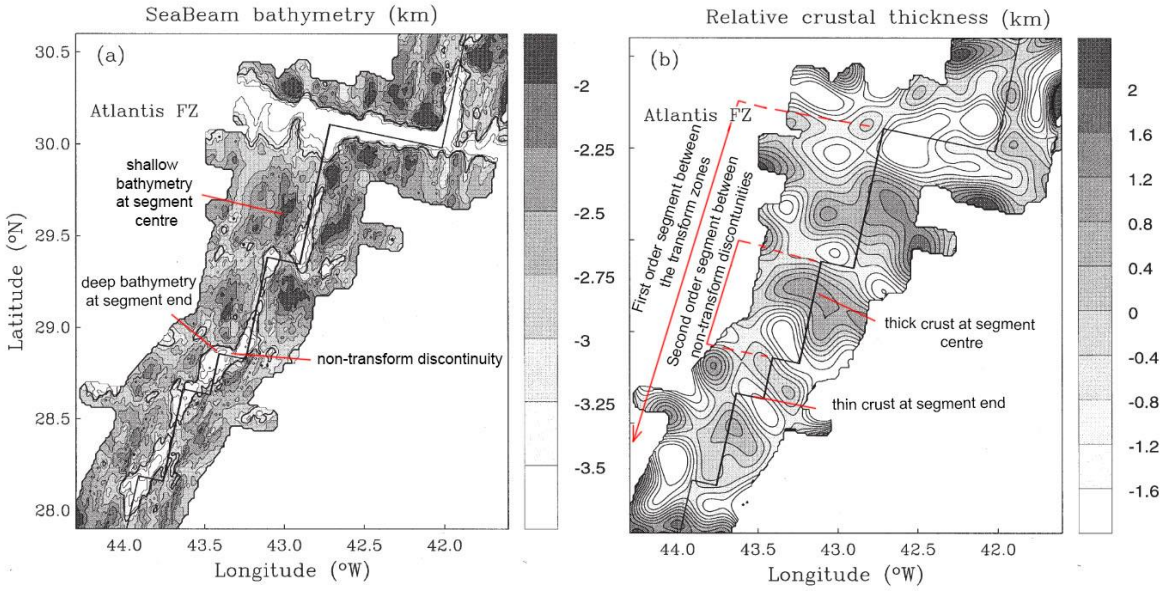

Figure 1.5*: Figure taken from Chen & Lin (1999) with some annotations added. Figure illustrates the magmatic segmentations influence on bathymetric depth, panel A, and crustal thickness, panel B.* ***A****: Sea Beam bathymetry map of the north MAR between 27.5° N and 30.7° N. The original Sea Beam bathymetric data from Sempéré et al., 1990 identifies the ridge axis contains six 20 – 80 km long spreading segments that are offset by the Atlantis transform (69 km) (Atlantis FZ) and four non-transform discontinuities (<30 km).* ***B****: Contour map of crustal thickness variations of the study area. It is derived by downward continuation of the*

residual gravity anomalies (Figure from Lin et al. 1990) from sea level to the 6 km depth of Moho from the seafloor.

Second-order segmentation is thought to result from a combination of instabilities within the melt column causing episodic convection, and compositional and thermal heterogeneities within the melt conduit (Macdonald et al., 1988; Schouten et al., 1985; Sempéré et al., 1990). For example, the focusing of melt supply may result from changes in the melt fraction and compositional changes in the underlying asthenosphere as indicated by changes in MOR basalt geochemistry from the northern Central Indian Ridge over 100s km and 10 - 100 kyr (Brandl et al., 2016; Kim et al., 2017). Modelling mantle heterogeneities also shows how these can influence mantle melt flow to MOR and affect the size, strength, and distribution of melt conduits which feed surface volcanism (Weatherley & Katz, 2016).

Elsewhere, transient and migrating fluctuations in mantle temperature and composition influence crustal structure, thickness and ridge morphology. White et al., (1995) studied V-shaped ridges bounding the Reykjanes Ridge, south of Iceland, and interpreted changes in mantle temperature of 30˚C occurring periodically every ~2 - 4 Myr. These pulses would migrate away from Iceland and increase crustal thickness by 2 km forming shallower regions. Plate spreading then divides the Reykjanes Ridge to form the V-shaped ridges (Jones et al., 2014; Murton et al., 2002; Parnell-Turner et al., 2014, 2017). The influence of the V-shaped ridges on tectonism will be investigated in Chapter 5.

1.2.3 Examples of third and fourth order melt supply processes and effects

Third and fourth order segments display no off-axial trends and are very short lived reflecting the localised melt supply of magma plumbing within the crust (Figure 1.3B) (Abelson & Agnon, 1997; Sempéré et al., 1993). High order features appear as en echelon jumps of elongated raised neo-volcanic regions that trace along the spreading axis. These volcanic ridges are separated by smoother seafloor or basins when two ridges

overlap (Sempéré et al., 1993). Discontinuities with offsets less than mantle melt column width (60 - 70 km) are likely fed from the same magma source (Blackman et al., 1993). Mapping of the neo-volcanic zone and measurements of crustal thickness show that, for most MOR, magmatic accretion occurs within the axis on crust less than 40 ka (Bown & White, 1994).

These orders of melt supply have influence on MOR morphology by creating nested bathymetric and gravity trends representing magma migrating towards the surface, the lowest order represents the deep processes within the mantle, while higher orders represent shallower processes within the lower crust (Carbotte et al., 2016; Sempéré et al., 1993). During my investigation I use trends in the bathymetry representing crust deeper or shallower than the mean bathymetry to identify the magmatic centres of second order segments as a proxy for high melt supply (Chapters 3 and 4). Melt supply that influences morphology at a higher resolution than the second order will operate within the upper crust and on the seafloor.

1.2.4 Melt supply and eruption processes' effects on morphology and structure

The brittle-ductile transition is an important geophysical boundary separating the upper and lower crusts. There is some contention about where the brittle-ductile transition occurs, the depth will vary along-axis and between MORs because the boundary is temperature dependant. Quartz begins to plastically deform at 300˚C and feldspar at 450˚C (Scholz, 1988), in glassy basalts this results in fully ductile behaviour above 700 - 800˚C, and above 550˚C for non-glassy basalts (Violay et al., 2012). Recovered rocks thought to have formed at the brittle-ductile transition are heavily mylonated indicating ductile flow (Scholz, 1988). Gabbro fluid inclusion analysis indicates the brittle-ductile transition occurs around 700˚C, possible at a minimum depth of 2 km (Kelley & Delaney, 1987). Earthquakes along the axial valleys of the MAR reach a depth of 5 – 8 km (Toomey et al., 1988), while at the East Pacific Rise they reach depths of 2

– 4 km (Riedesel et al., 1982) indicating potential depths for the brittle-ductile transition, below which, crust would be aseismic. Melt trapped within the lower crust accretes mostly as gabbro plutons (Chen, 1992), while melt that migrates above the brittle-ductile transition intrudes as blade like dykes (Behn et al., 2006; Buck & Poliakov, 1998). Therefore, the individual magmatic and tectonic features we identify on the seafloor likely have their origins within the upper crust. In this investigation I aim to identify if mapping collective features that must originate in the upper crust can reflect deeper processes like second order segmentation that originate within the asthenosphere.

The oceanic crust's structure is layered. Seismic refraction studies have divided the crust into several layers based on changes in velocity (Spudich & Orcutt, 1980). The deepest is the Mohorovicic discontinuity (Moho) which separates the mantle from the crust at a depth of 6 – 8 km. Layer 3 is the lower crust, and is made from a mix of mafic plutons and ultramafic rocks extending from 1.5 km depth to the Moho. Layer 3 is generally structured as interlayered gabbro and ultramafic rocks at the base, above which are layered gabbroic rocks, and at the top are isotropic gabbroic rocks. Above the plutonic rocks is Layer 2B, that consists of sheeted dykes. This layer is usually only found at faster spreading ridges. Layer 2A lies at the surface and consists of erupted lavas (Searle, 2013). For the purpose of my study I am mainly interested in magmatic features shown in Layer 2A because these can be identified from bathymetry, and faulting that can reach to the brittle-ductile transition.

If magma reaches the surface it can form hummocky Axial Volcanic Ridges (AVRs) (Figure 1.1) (Cann et al., 2015). AVRs are typical at slow-spreading ridges, where they are 200 - 400 m high, 3 - 4 km wide, and elongate perpendicular to the spreading direction. Volcanism along and between MORs will differ because melt supply, affected by temperature, will impact the eruption rate. Colman et al., (2012) studied the differences in eruption styles along the Galapagos Ridge when magma supply differs by 30%, based on liquidus temperature determined by MgO (2.7 – 8.4 wt. %

vs 6.2 – 9.1 wt. %). They found that lava from the region of low magma supply had a high phenocryst content (10 – 15 vol % plagioclase, 2 vol % olivine) suggesting melt spent more time crystallising in magma chambers. However, these lavas were often more magnesium-rich and have high levels of forsterite olivine phenocrysts, indicative of a high formation temperature between 1170 - 1210˚C. These phenocrysts were interpreted to indicate that lava in low magma supply regions pooled under hot conditions in deep-crustal or upper-mantle reservoirs. Once erupted, these lavas formed mainly pillow lavas (85%) with sheet and lobate flows comprising only 10%, indicating low magma eruption pressures. These findings suggest high temperature magmas have a low eruption rate.

In comparison, only micro-phenocrysts were found in lavas from regions with the high magma supply, indicating they cooled at lower temperatures (1080 - 1180˚C) and spent less time in the magma chamber compared to phenocrysts recovered from the low magma supply site. These lavas were dominated by fast eruption morphologies (sheet and lobate flows – 53%) with pillow lavas only comprising 47%. This was interpreted as shallow magma reservoirs erupting more frequently and more effusively than reservoirs at lower melt supply regions. The findings from Colman et al., (2012) identify one of the reasons why a higher magma supply creates a smoother seafloor at the MOR.

By examining high-resolution geochemical stratigraphic profiles using ocean drilling and trawled mid-ocean ridge basalts, Brandl et al (2016) determined that the melt extraction and migration occurs at over 100 – 1000 yrs. Suggesting that this is the longevity of third order magmatic pluming system without melt recharge.

As shown, melt supply has a significant influence at various orders on MOR morphology. During my investigation in subsequent Chapters, I aim to determine how tectonism is influenced by high melt supply close segment centres and low melt supply at the segment ends. Additionally, I map the distribution of magmatic features to determine where recent magmatism is focused along-axis. The volcanic feature maps are then

compared to measurements of tectonism to better understand their relation.

1.3 Definition of spreading obliquity and its relations to MOR crust morphology

The third influential parameter for MOR morphology is spreading obliquity. It has been found that fault length, orientation, and dyke length are shorter within oblique segments of the ultra-slow spreading South-West Indian ridge (SWIR) than the orthogonal segments (Montési et al., 2011).

Seafloor obliquity is defined as the difference from the MOR normal and the direction of plate separation (Fournier & Petit, 2007), with maximum strain direction occurring halfway between (Fournier & Petit, 2007). Abelson & Agnon (1997) categorised MORs as; 1) having a spreading axis that is oblique and concordant, e.g. the Reykjanes Ridge (Chapter 5); 2) spreading axis that is oblique and discordant, resulting in segmentation, e.g. sections of the Mid-Atlantic Ridge (Figure 1.4 and Chapter 3); 3) spreading axis that is orthogonal and discordant, e.g. the Costa Rica Ridge (Chapter 4). 72% of all MORs display spreading obliquity (Woodcock, 1986). Geometric models and observations indicate a negative correlation between ridge obliquity and spreading rate, and a positive correlation with melt supply (Tuckwell et al., 1999; Zhang & Gordon, 2016). Abelson & Agnon, (1997) supports this by observing that the Reykjanes Ridge has high magmatic overpressure because of its proximity to the Iceland hotspot, this overpowers remote tensile forces enabling ridge obliquity. Alternatively, at the East Pacific Rise high remote tensile forces from subduction zones overpower magmatic overpressure and increases segmentation.

Importantly, obliquity affects large scale tectonic morphology at the first and second order segment scale. For example, the Mohns Ridge (north of Iceland) and Reykjanes Ridge (south of Iceland) have 30˚ spreading obliquity creating ridge oblique en échelon horst and grabens

forming perpendicular to the stretching direction (Dauteuil & Brun, 1993; Murton & Parson, 1993).

Obliquity also influences melt distribution along axis. For example, at the Juan de Fuca Ridge seismic tomography indicated the mantle was obliquely diverging at 12˚ relative to the overlying plate motion. This correlated with multiple second-order discontinuities along the axis consisting of overlapping spreading centres (VanderBeek et al., 2016). Surprisingly they found that under the overlapping spreading centres the mantle's partial melt content was 1 - 5%, while it was <2% under the segment centre. This seemingly contradictory result was explained by obliquity reducing the permeability of the lithosphere causing melt to pool under the overlapping spreading centres at the segment ends. To reach the surface melt had to migrate along-axis until it reached the centre of the segment where fractures increased permeability (VanderBeek et al., 2016).

As shown, spreading obliquity has a significant influence on the segment-scale morphology. During our investigation we aim to determine how tectonism is affected by changes in spreading obliquity. Sections 1.1 – 1.3 have discussed the three principle parameters influencing MOR morphology, the next section builds an understanding of what is known about the controllers of MOR tectonism.

1.4 The causes of tectonism and its morphology

There are two main processes occurring at a MOR, magmatism has been discussed, and tectonism is the other. Extension at MOR results in faulting and dyke intrusion (Muirhead et al., 2015). When magma supply is low, stretching is accommodated by increased heave (horizontal displacement) along faults (Behn & Ito, 2008; Ito & Behn, 2008). MOR normal faults first initiate as discontinuous small fractures that rotate and coalesce to form more continuous faults. The fault dip starts at 60˚, then the hanging wall can rotate by as much as 30˚ with increased heave (Behn & Ito, 2008; Buck, 1988; Thatcher & Hill, 1995). Fault blocks therefore present an asymmetrical profile in bathymetry and in seismic reflection profiles; having a steeper lee slope that usually faces towards the spreading axis. Major axial wall faults nucleate 1 - 4 km off-axis (Escartin et al., 1999) within the zone of crustal fissuring (Macdonald, 1982) and complete most of their strain within 15 - 35 km off-axis (Buck et al., 2005; Escartin et al., 1999; Solomon et al., 1988; Wolfe et al., 1995) in the active fault zone (Macdonald, 1982).

A relationship between the length and strength of a phase of magmatic accretion on-axis and the height of abyssal hills has been modelled (Ito & Behn, 2008). The model indicates that a tectonic-magmatic cycle alternating between periods when all extension is accommodated magmatically, and periods when extension is accommodated tectonically can create the series of repeating abyssal hills seen at the centre of spreading segments (Figure 1.6) (Ito & Behn, 2008). This relation also applies when looking at magmatism along axis. Fault throw decreases towards the segment centre where the magmatism is higher (Howell et al, 2016). Thatcher & Hill, (1995) described profiles of fault scarps extending to tens of kilometres off-axis illustrating that a decrease in magmatic pressure on-axis decreases the horizontal stress which causes normal faults to fail. This results in an episodic increase in tectonism when magma reservoirs reduce in melt supply. They concluded that regions with narrow fault spacing result from periods of low axial magmatism (Figure 1.6). These studies model the hypothesised close relation between tectonism

and magmatism at the spreading axis. Subsequent chapters in my investigation will attempt to identify this modelled relation in mapped faults on the seafloor, where it should be possible to use large scale patterns in fault heave to identify larger scale changes in melt supply.

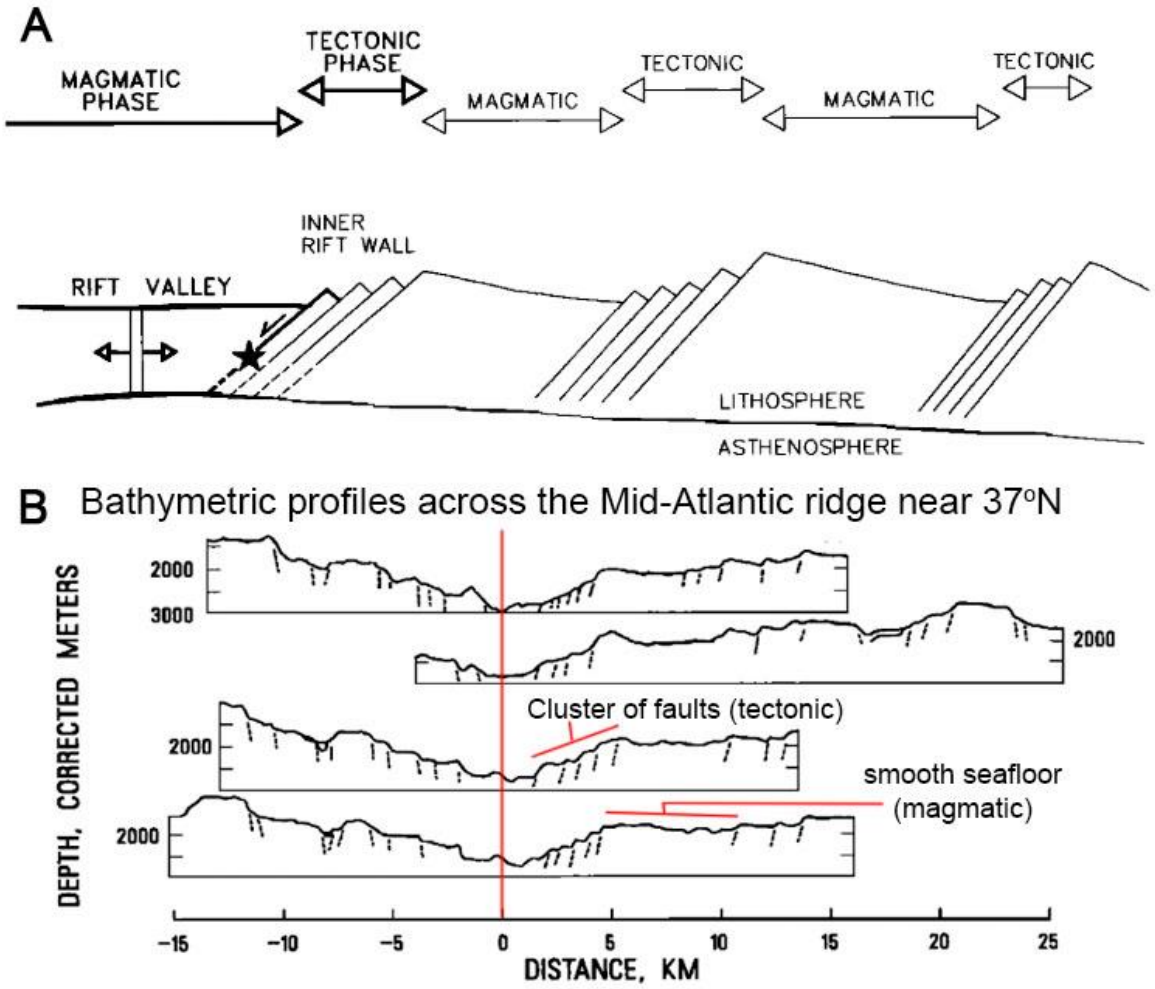

***Figure 1.6**: Figure from Thatcher & Hill, (1995) with annotation. **A**: Illustration of a model for tectonic-magmatic cycles. The crust is constantly extending at the Plate's spreading rate, but when there are periods of low melt supply the extension is taken up by normal faulting, creating seafloor with high relief, and when there is high melt supply the extension is accommodated by dyking, creating a smoother seafloor. **B**: Bathymetry profiles across the FAMOURS region of the Mid-Atlantic ridge near 37˚N spaced 2 – 5 km apart. Faults are dashed black lines. These profiles illustrate regions of clustered faults and rugged seafloor, which are explained by the model in panel A as periods of low melt supply.*

Furthermore, Shaw, (1992) found that faults have wider spacing and higher throws at segment ends, were Bouguer anomalies are high, indicating a thinner crust (i.e. where melt supply is lowest). Conversely, fault frequency is higher and throw is lower at the segment centre. Additionally, Escartin et al., (1999) measured fault heave from side-scan sonar at the 29°N segment of the Mid-Atlantic Ridge. They determined that, on average, tectonic strain was 10% along the MOR axis, with up to 50% spreading asymmetry occurring at the segment ends between the Inside Corner of the active transport zone and the spreading axis, and the opposite Outside Corner between the inactive transform zone and the spreading boundary. My investigation should be able to identify similar variations in fault heave along-axis.

Thermal modelling has also indicated plate thickness on-axis influences the axial valley width and height at slow-spreading ridges (Morgan et al, 1987). An 8 km thick brittle plate resulted in a 30 km wide axial valley, while a 10 km thick plate produced a 40 km wide axial valley. The model indicated that a change of the width of the axial valley by a few kilometres can produce kilometre scale relief. Therefore, we could predict that by measuring fault attributes along- and off-axis we could produce a proxy for brittle plate thickness.

Higher spreading rates results in hotter crust on-axis which has been shown to reduce the width of the seismogenic layer (Mark et al. 2018). A narrower seismogenic area reduces a fault's lifespan, explaining why extension at ultra-fast ridges are almost aseismic while slow spreading ridges have 60% of their extension as seismic. This results in fault nucleation increasing but extension along individual faults reducing (Mark et al. 2018). A brittle plate over a ductile fluid model indicated that the width of a zone of decoupling between the brittle oceanic crust and the plastically deforming mantle can influence axial valley morphology (Chen & Morgan, 1990). The zone of decoupling indicates distance from the spreading axis where stresses within the upper mantle exceed the strength of the brittle plate (Figure 1.7). Crust with a high temperature and thickness have a wide decoupling zone because oceanic crust becomes

more ductile than mantle at the same temperature. This model suggests that at slow-spreading ridges the decoupling zone is small, resulting in an axial valley created by the ductile flow of the mantle plastically deforming the crust. At fast spreading ridges the decoupling is larger allowing for the plate to deform separately to the mantle, resulting is brittle extension occurring on-axis and the axial flanks being supported by the buoyant mantle. Further off-axis the crust will cool enough that the layers will re-couple and create an off-axis zone of brittle deformation (Figure 1.7). The transition between these two states occurs around 70 mm yr^{-1} full spreading rate (Chen & Morgan, 1990; Macdonald, 1982). This model helps to explain the differences in tectonic surface morphology between slow and fast spreading ridges.

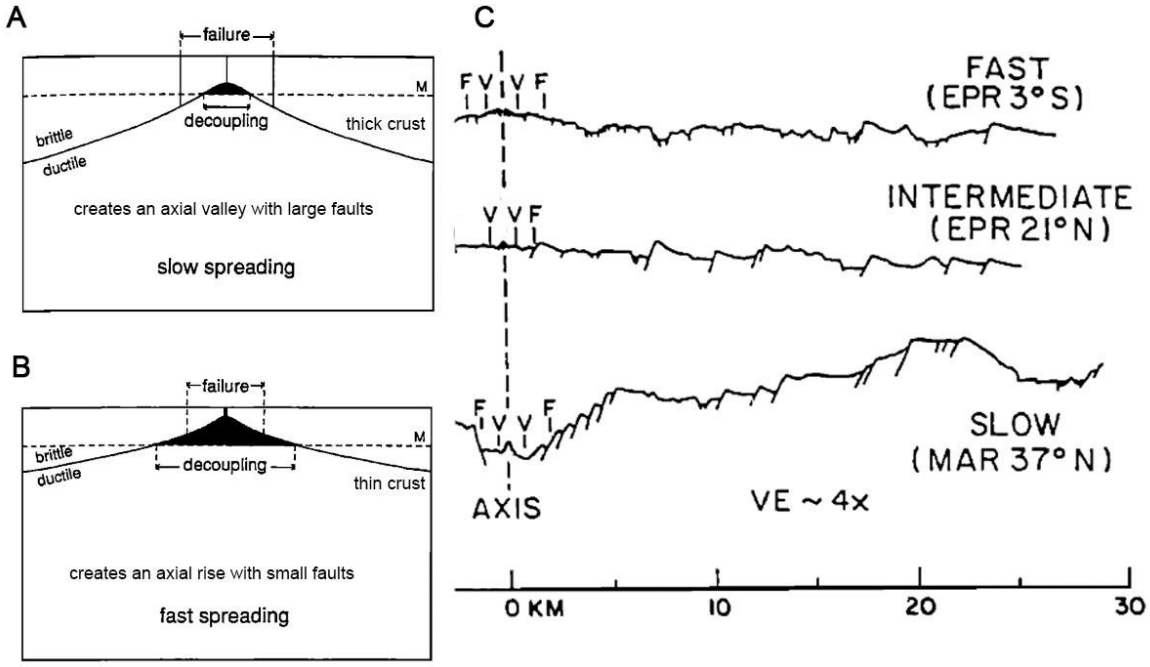

Figure 1.7*: Figure taken from Chen & Morgan, (1990) with annotation. Model of how coupling between brittle crust and ductile mantle influences the faulting occurring at the spreading axis.* ***A****: Where the spreading rate is slow, the crust will cool close to the axis, becoming thicker as the crust and upper mantle couple. Faulting within the zone of tectonic failure is not being isostatically supported by a ductile mantle, resulting in a deep axial valley and large faults.* ***B****: Where the spreading rate is fast, the crust remains thin and hot further off-axis, producing a large area of decoupled brittle crust over a ductile mantle. Here, faulting within the*

zone of tectonic failure can be supported by flow of the decoupled ductile mantle, allowing for an axial rise and small faults. ***C****: Bathymetric profiles across one half of fast, intermediate, and slow MORs, illustrating how the model in A and B could explain the axial morphology at different ridges.*

It was found that modelling dyke intrusion as episodic rather than continuous better reproduced the observed axial valley morphology (Liu & Buck, 2018). Dyking as short lived events reproduced the result of deeper axial valleys with more dyke intrusion in the lithosphere while shallower valleys had dykes reaching the surface (Liu & Buck, 2018). This suggests that the behaviour of individual dykes has an influence on morphology that is not accounted for when thinking of melt supply at the segment scale.

Tectonism can also help mobilise magma and result in eruptions, as demonstrated by seismic observations in Tan et al. (2016) of the fast spreading East Pacific Rise. Here, fracturing along the 35 km of the ridge axis due to the build-up of stress to a critical point resulted in magma lense movement, dyking, and surface eruptions across a 48 hr period (Tan et al., (2016).

Most of these studies have modelled the influence of melt supply on individual faults, however with the complex interaction of the three discussed parameters that influence MOR morphology (Sections 1.1 – 1.3), my study aims to determine if these results are repeatable in observational data.

1.5 Study areas

During this study I investigate three MORs that have at least one of the three MOR parameters (spreading rate, melt supply, and obliquity) different from each other, and where at least one parameter is in common. This allows the morphology between the MORs to be similar enough for comparison and differing enough so that the primary influential parameter on my results can be determined.

In Chapter 3, fault heave at the Mid-Atlantic Ridge's Broken Spur segment between 28°45'N – 29°15'N is analysed. This is a slow spreading, orthogonal, low melt supply MOR. At this segment I calculate large scale tectonic extension with a new method I have developed. The measured extension is then compared against two proxies for melt supply, the first is a well-established and published method using gravity anomalies, and the second is my own method using bathymetry anomalies. The Broken Spur segment has had fault tectonism previous studied, providing an opportunity to test my new method for calculating tectonic extension through comparison to published data.

In Chapter 4 I investigate one orthogonal and intermediate spreading segment of the Cocos-Nazca spreading system; the Costa Rica Ridge from 3°20'N; 84°11'W to 3°19'N; 83°15'W. At this segments I use my new method to calculate large scale tectonic extension and compare it to conventional methods. I then compare my measurement of bathymetry anomalies that are indicative of high or low melt supply.

In Chapter 5 the Reykjanes Ridge between Iceland and the Bight Transform zone at 57°N; 33°W is investigated. This MOR is oblique, slow spreading, and has a high melt supply because of the influence of the Iceland hotspot. I use my method to calculate tectonic extension along two seismic reflection profiles and compare it to a proxy for melt supply derived from gravity anomalies and bathymetry anomalies.

1.6 Objective seafloor mapping practices

The development of more powerful GIS and machine learning has enabled multiple methods for objectively categorising the seafloor. In this section I will outline some of these studies before developing my own method in Section 2.1 to identify faults.

Paulatto et al (2015) aimed to calculate extension along the MAR between 35˚40'N and 36˚40'N. To objectively identify faults they calculated a slope map to feed into an automated edge detection algorithm that identified maximum gradients. Weak gradients that connected to strong gradients identified lineations of sudden change in slope that were interpreted as faults. The faults identified using Paulatto et al (2015)'s method had, on average, higher backscatter than the surrounding seafloor (Eason et al., 2016). However, there were instances where this method selected hummocky volcanic terrain or failed to identify shallow faults (Eason et al, 2016).

Geomorphic analysis is increasingly being done using GIS tools to calculate terrain attributes, such as slope and slope direction. Lecours et al. (2017) compared the automated terrain attributes between multiple GIS programs to identify how differences in the algorithms calculate slightly different values for the same terrain attribute, with 79% of 230 attribute calculations producing unique values. This is important to bear in mind when comparing attributes between studies that may use different attribute calculations. My method avoids this by always using the same slope and slope direction tools within ArcGIS.

Faults were identified along the Chilean Ridge using slope and curvature maps of unfiltered bathymetry (Howell et al 2016). In their study, continuous linear high-slope features in plan view that have high curvature in profile were identified as faults. The addition of an attribute of high curvature was used to filter out volcanic ridges.

Juliani (2019) trained an artificial neural network to automatically identify faults from bathymetric profiles with a 92% accuracy. The

neural network uses slope and slope direction derived from the bathymetry to identify faults. An inherent uncertainty with using this method is how the training dataset was chosen. For example, if the training dataset was made from faults that were visually mapped using slope maps then it would include the same human biases.

These are some of the many methods being used to objectively identify mid-ocean ridge faulting. The main fault attributes used in all these methods are slope and slope direction, my method adds a third, acoustic backscatter.

1.7 Conclusion

A review of the literature indicates that seafloor morphology such as segmentation, distribution of volcanism, and faulting, is influenced by three parameters; spreading rate, melt supply, and spreading obliquity. In this introduction I have tried to separate out the effects of these three parameters, however in reality they influence each other so that no single morphological feature can be attributed to any one parameter. I have also discussed the formation of faulting at MORs and how tectonism is one of the processes influencing seafloor morphology, magmatism being the other. The research discussed in this introduction have led me to hypothesis that fault heave measured over a wide area should be related to changes in melt supply along axis or through time, and therefore tectonism could be used as a proxy for these larger scale parameters.

Most of these studies have analysed what each parameter's effect on the spreading axis is, through modelling and comparison to bathymetry profiles. However few have investigated their effects on collections of faults over an area comparable to orders of segmentation. Additionally, the models usually focus on altering one of these parameters to influences fault attributes, however at real MORs all three parameters vary and influence each other to create the complex MOR morphology. My investigation will focus on fault heave at the scale of second order segmentation. I will aim to identify faults using an objective and repeatable method then use fault heave to measure extension at scales comparable to

the second order segmentation of melt supply under MORs. By investigating multiple MORs, I aim to determine if it is possible to use tectonism to disentangle the influential parameters to match the results of the models, and to determine if these parameters have orders of influence on fault attributes.

1.8 Thesis Aims

- Objectively map faults at Mid-ocean ridges by statistically correlating multiple fault criteria to produce a fault probability map. This method is developed in Chapter 2 and thoroughly tested in Chapter 3. Developing a method to objectively identify faults will reduce subjective errors and increase confidence in my results. An objective method that is partly automated can be repeated in other study areas so results can be compared between mid-ocean ridges, this happens in Chapter 4.
- Calculate extension across and along Mid-ocean ridges using an automated and repeatable method. In Chapter 2 I develop a method for calculating extension. My method aims to make comparison of areas within and between mid-ocean ridges easier to comprehend. My method is tested against another measure of extension in Chapter 4.
- Measure a proxy for relative changes in melt supply at mid-ocean ridges.
- Using my measure of extension and relative changes in melt supply I should be able to determine their relationship. This will test the hypothesis that melt supply is directly related to extension as set out in section 1.4.
- Compare measurements of extension and melt supply across spreading ridges with varying spreading rates, spreading directions, and melt supplies. This will determine how much influence these other variables have on whether extension is related to melt supply.

Chapter 2: Methods

Mid-ocean ridges (MOR) control the morphology of the ocean crust, which is formed at the spreading axis of the plate boundary, and which eventually forms ~70% of the Earth's surface. The primary processes are magmatic and tectonic: either construction by magma intrusion and volcanism or destruction by tectonism. These processes vary over millions of years and at length-scales of tens of kilometres and are influenced at these scales by melt supply, spreading direction, and spreading rate (as discussed in Chapter 1). To measure tectonism, I must identify faults using an objective and repeatable method. Faults created at MORs and preserved in the off-axis crust can be identified using shipboard multibeam bathymetry, often gridded with a 50 m resolution (depending on depth and point density), and converted into 3D maps (Terrain models) of the seafloor. Where available, faults can be identified using side-scan sonar collected from a towed ocean bottom instrument collecting oblique measurements of seafloor acoustic reflectivity at a ~7 m resolution. When there is thick sediment cover, 2D seismic reflection profiles can be used to identify faults sub-surface. Fault heave then needs to be measured and used to calculate a proxy for large scale extension at scales similar to second order melt supply over tens of kilometres.

My measurement of extension can then be compared to proxies for magmatic activity. As discussed in Chapter 1, higher melt supply towards the centre of first and second order MOR segments produces a reduced gravitational signal and a shallower bathymetry compared to the segment ends. By identifying these regions of low gravitational anomalies and developing a method to quantitatively define regions of shallow and deep bathymetry I can define regions of relative low and high melt supply. The final stage of the investigation would be to compare my measurements of large scale tectonism to my proxies of melt supply to identify correlations.

Four primary data sets are used; In Chapter 3 the raw multibeam echo sounder data for the Mid-Atlantic Ridge segment at 29°N was acquired from the British Oceanographic Data Centre and processed to produce 50 m resolution bathymetry and acoustic backscatter. The side-scan sonar was acquired during cruise CD99 in 1996 (Searle, 1996) and was processed and used in Escartin et al., (1999). I have used the 7 m resolution side-scan sonar maps used in Escartin et al., (1999). In Chapter 4, I use bathymetry and acoustic backscatter to analyse the Costa Rica Ridge. This data was collected from the multibeam echo sounder during cruises JC112/113 and JC114 in 2015 as part of the University of Durham led 'Oceanographic and Seismic Characterisation of the heat dissipation and alteration by hydrothermal fluids at an Axial Ridge' (OSCAR) project (Hobbs & Perice, 2015). I processed the multibeam echo sounder to produce 50 m resolution bathymetry and acoustic backscatter. In Chapter 5, I use two seismic reflection profiles crossing the Reykjanes Ridge collected during cruise JC050 in 2011. The data sets will be described in more detail in the relevant chapters.

Bathymetry and acoustic backscatter data from JC050 (Chapter 3), JC112/113, and JC114 (Chapter 4) were processed using CARIS™, where stray beams and spikes were manually removed to avoid using a filter that would smooth the data. The insonification angle depends on whether the ship was travelling N – S or E – W relative to a seafloor feature. These angles were tested for their effect on horizontal and vertical resolution and it was determined that overlapping of all E – W and N – S track lines (i.e. $\geq$100% overlap) provided multiple beam angles to insonify seafloor features and produce the densest point cloud, with maximum spatial coverage. Coverage was improved and vertical fluctuations reduced by using the mean value of points in a process known as grid-binning where multiple soundings were averaged into one grid cell (e.g. of 50 x 50 m). A 50 m grid was chosen to achieve the highest spatial resolution without leaving gaps. Gridding resolution was tested at 25 m, which produced frequent data holes. Gridding at 100 m over-smoothed the data making meaningful analysis of steep fault scarps difficult, especially of the smaller faults with heave <200 m. The comparison between grid sizes can be seen

in Appendix A. The final 50 m resolution grids used a third order polynomial interpolation to fill any remaining small gaps in coverage. Finally, ArcGIS™ was used to analyse and interpret fault heaves to measure tectonic extension (Section 2.1.1).

2.1. Measuring tectonic extension over tens of kilometres

The analysis of tectonically-expressed extension focuses on normal fault's horizontal heave. In Escartin et al. (1999), high-resolution deep towed side-scan sonar was used to identify linear, high-acoustic backscattering reflectors that were interpreted as fault scarps. The apparent heave of these faults were used to calculate the percentage of measureable brittle tectonic extension (T%), which can be expressed as:

$$\frac{Total\ heave\ (m)}{total\ amount\ of\ crust\ accreted\ (m)} \times 100 = T\%$$

Escartin et al. (1999) used this method over several kilometres to each side of the spreading axis to calculate the T% of a spreading segment's Inside Corner, Outside Corner, and segment centre. For the purpose of my investigation, their method has been adapted and developed.

2.1.1 Identifying faults

My measurement of crustal extension uses an automated method to objectively identify faults in a repeatable and accurate way that can be used on multiple MORs, labelled the Fault Identification (FID) method (Figure 2.1).

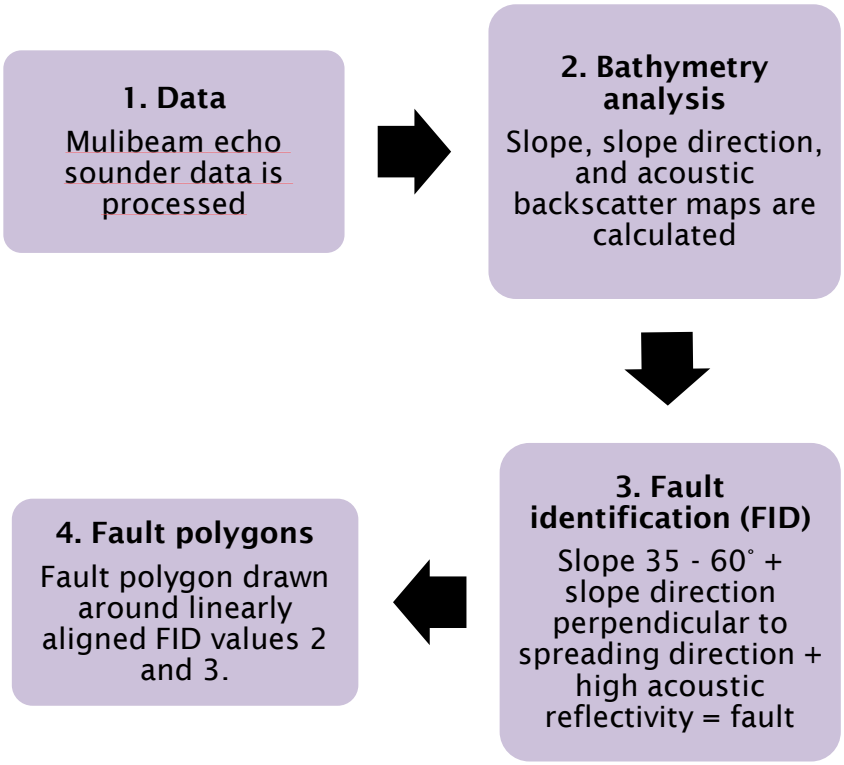

***Figure 2.1**: Flow chart of the Fault Identification (FID) method.*

In Figure 2.1, box 2, the seafloor attributes of slope angle, slope direction, and backscatter are calculated from bathymetry. Firstly, slope angle is calculated from a 3 x 3 cell matrix applied to the bathymetry model that calculates the maximum rate of change in cell values between neighbouring cells (i.e. change in depth) (Figure 2.2C). Secondly, slope direction is calculated from the downhill direction of the 3 x 3 cell matrix (Figure 2D). Finally, acoustic multibeam backscatter is extracted from the raw sonar data using the CARIS™ software. The backscatter data are in the form of snippets, with each cell of the grid treated as a side-scan sonar image in its own right, with backscatter amplitude values projected onto the seafloor. The result is a measurement of seafloor sonar albedo, with high backscatter indicating a hard subsurface typical of exposed rock, or steep incidence angle caused by the sonar grazing a slope at a high angle. Backscatter values are recorded in decibel steps. To objectively select high backscatter I divide the decibel range statistically into quintiles, with the highest quintile representing exposed rock (Figure 2.2B), and the lowest quintile representing thick, soft sediment. This process provides the three analytical data sets that are referred to in box 3, Figure 2.1.

Three criteria are selected from the three analytical data sets to identify spreading-induced extensional faults;

1. Steep slope angles.

Faults forming at spreading axis are expected to occur from simple shear as plates pull away from each other towards two opposite directions. Theoretical simple shear models indicate that normal faulting will initiate at 60˚. Seismic reflection profiles have identified faults initiating at dips between 60˚ – 80˚, then rotating 30˚ through extension (Minshull & Bull, 1997). Microseismic studies have identified fault planes slipping at angles between 35˚ – 55˚ (Toomey et al, 1985). A comparison of faults identified in bathymetry, in the continental environment, and earthquakes indicates normal faults initiate around 45˚ – 60˚ (Thatcher & Hill, 1995). Observations from manned submersibles have identified faults dipping from 30˚ – 90˚ (Karson et al, 1987).

The seafloor from Chapters 3 and 4 had 96% of their slope less than 30˚, the minimum slope angle described in the literature (Figure 2.2). The frequency of slopes between 30˚ – 90˚ followed an exponential decay, after 60˚ the relation between frequency and slope angle becomes less defined. This either reflects the low sample density for these extremely high values, only 0.002% of the pixels, or that these high slopes are the results of data artefacts (Figure 2.2). Values above 30˚ are geographically rare so should make a useful criteria for accurate identification of faults.

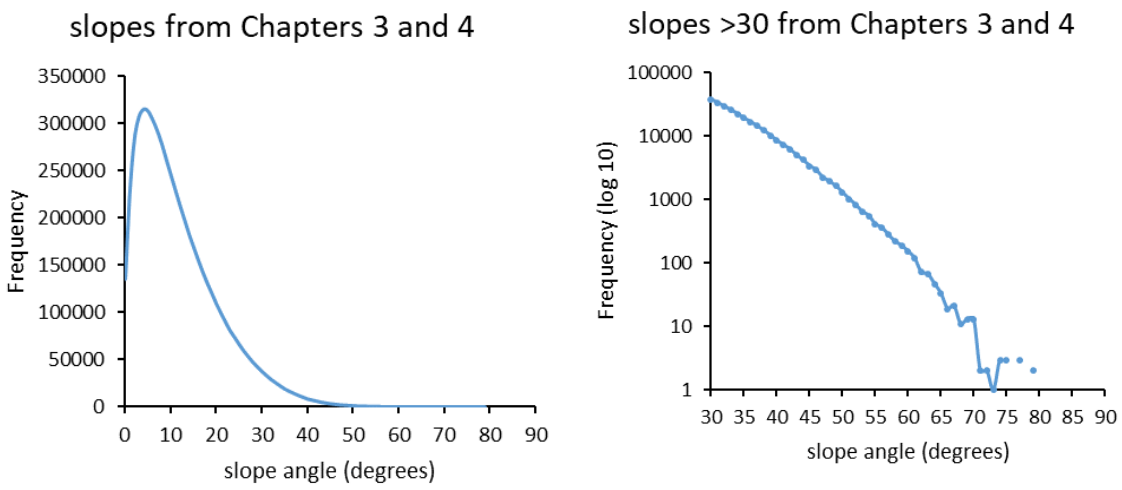

***Figure 2.2**: The distribution of seafloor slope angles for Chapters 3 and 4. Left: The majority of slope angles on the seafloor are below 30˚. Right: Slope angles higher than 30˚ follow an exponential decay and are very rare over 65˚.*

To test if the criteria of slopes >30˚ illustrate faults, example bathymetry profiles were taken at the Broken Spur segment stretching 44 km from 43˚11'W 29˚8'N – 43˚35'W 29˚7'N off-axis and at the Costa Rica segment stretching 101 km from 83˚41'W 3˚20'N – 83˚41'W 2˚25'N (Figure 2.3). In the bathymetry profiles, faults were identified as asymmetric ridges with their steep faces angled towards the spreading axis. These were compared to slope angle profiles. Along both profiles, 53 fault-like signals were visually identified (green arrows). Out of those, 45% corresponded with slopes >35˚, and 58% corresponded with slopes >30˚. Extending the slope threshold from 35˚ to 30˚ increases the amount of selected pixels along both profiles, however not all of these correspond with asymmetric

bathymetry profiles indicative of faults.

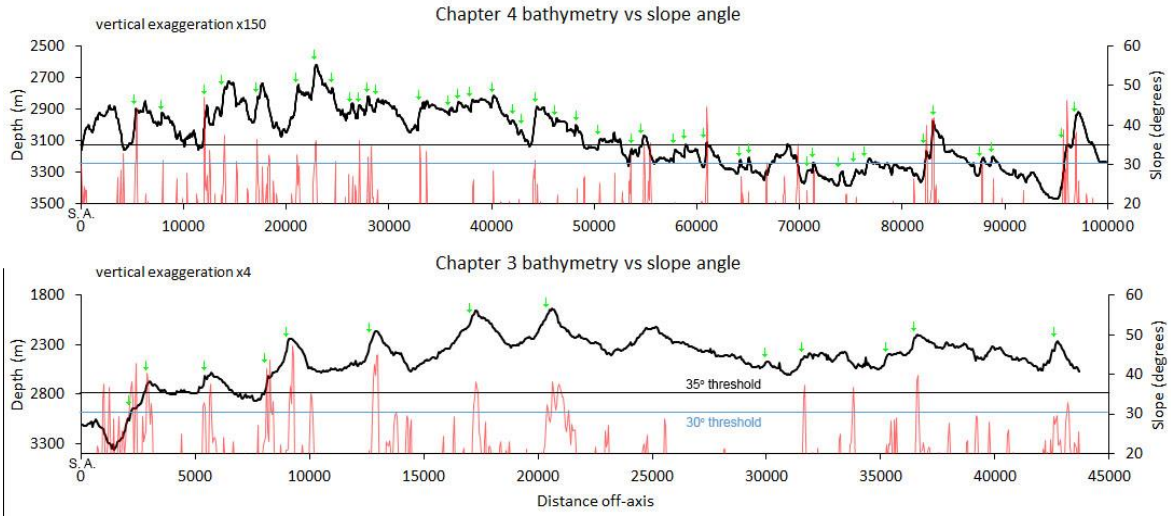

***Figure 2.3**: Bathymetry profiles (black) from the Broken Spur segment stretching 44 km from 43˚11'W 29˚8'N – 43˚35'W 29˚7'N off-axis (Top) and the Costa Rica segment stretching 101 km from 83˚41'W 3˚20'N – 83˚41'W 2˚25'N (Bottom). Horizontal black line marks a 35˚ slope threshold, horizontal light blue line marks a 30˚ slope threshold. Red Line is the slope angle along the profile. Green arrows indicate faults identified from the bathymetry profile as asymmetric ridges with their steep slopes facing towards the spreading axis.*

Regions of high angles (>30˚) do not always correspond to fault scarps in bathymetry. Some examples identified from Chapters 3 and 4 identified steep slopes associated with the sides of lavadomes and seamounds. Figure 2.4 suggests that decreasing the minimum slope angle criteria to 20˚ would select the edges of lava domes and the rugged seafloor, such as AVRs. A minmium slope angle of 30˚ still encompasses the edges of lavadomes and some rugged seafloor such as that which forms at AVRS. Increasing the minmum threshold to 35˚ halves the amount of pixels selected at the edges of lavadomes and selects almost no pixels from the rugged seafloor of the AVRs. However, slope angles above 35˚ still select the sides of large features such as seamounts.

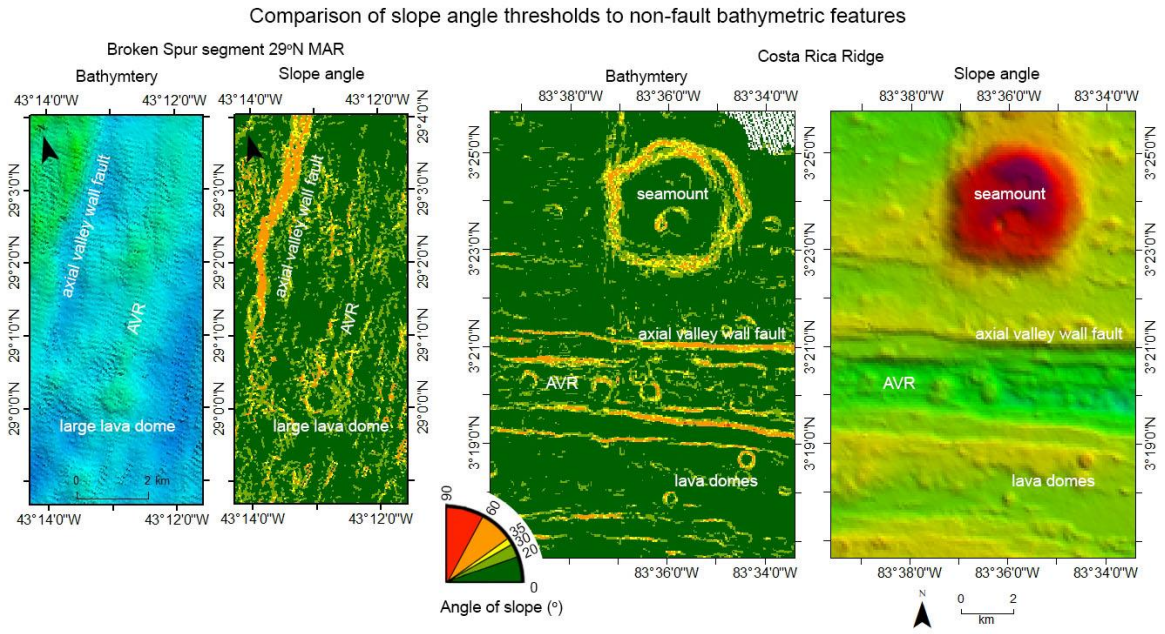

***Figure 2.4**: Maps of seafloor features with high slopes that do not correlate to faults. Left: Slope angles of 30˚ - 35˚ pick up the edge of lava domes and an axial volcanic ridge at the Broken Spur Segment. Right: Slope angles of 30˚ – 60˚ pick up the edges of lava domes and a seamount at the Costa Rica Ridge. This demonstrates that a higher slope angle threshold helps to reduce the influence of AVRs and lava domes on the FID map.*

The slope angles published in the literature and the analysis of my study site's slope statstistics resulted in me choosing a fault criteria between 35˚ – 60˚. A minimum value of 35˚ reduced the probability of selecting volcanic features. Slope angles over 60˚ may reflect artefacts in the data caused by sonar stray beams. 2. Slope dip towards or away from the spreading direction.

Extension in two directions away from the spreading axis should cause faults to fracture perpendicular to the spreading direction. Mid-Ocean Ridge earthquakes indicate that fault strike varies from this perpendicular by only 5˚ – 30˚ (Huang & Solomon, 1988). I expect this to create fault scarps the face towards the spreading axis.

A histogram of slope directions in Chapters 3 and 4 indicates that spreading direction creates a seafloor fabic where the majority of slopes are within a 90˚ range perpendicular to the spreading axis, too large a

range to be used to accurately identify fault surfaces (Figure 2.5). A 25˚ range incompases 17% of the seafloor for Chapter 3 and 23% of the seafloor for Chapter 4. A 45˚ range encompasses 30% Chapter 3 and 38% of Chapter 4's seafloor direction. A 65˚ range encompasses 42% of Chapter 3 and 51% of Chapter 4's seafloor data (Figure 2.5). A useful criterion needs to be accurate enough to identify meaningful seafloor features. A range of 65˚ identified half of the seafloor so is not accurate enough for meaningful interpretation.

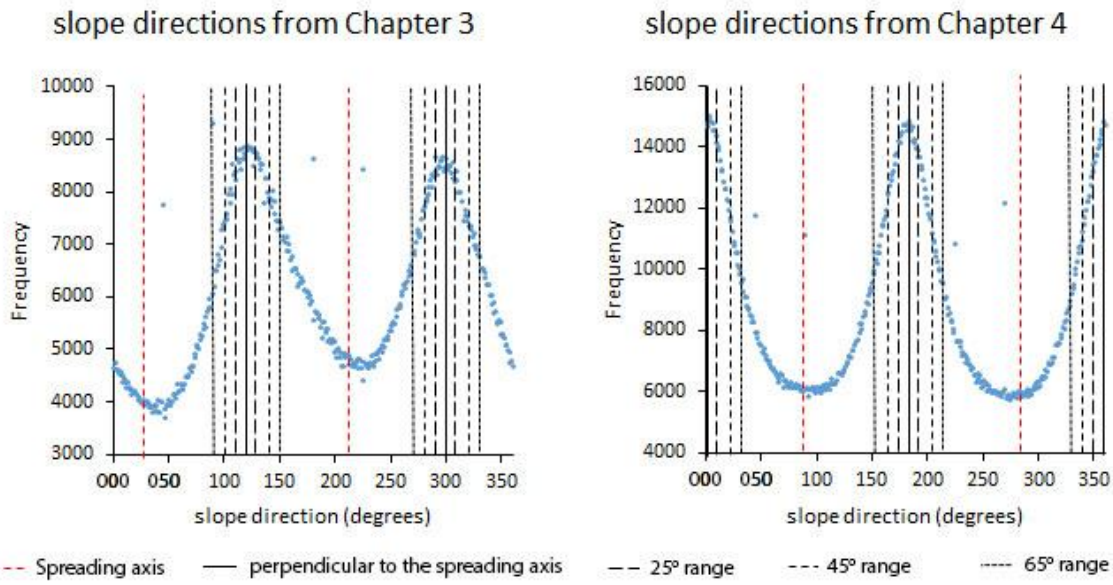

***Figure 2.5**: Histograms of slope direction (blue dots) from Chapters 4 (Left) and 4 (right). Dashed red lines are the strike of the spreading axis. Solid black line in perpendicular to the spreading axis. Around perpendicular there is a 25˚ range showing by large dashes, a 45˚ range shown by medium dashes, and a 65˚ range shown by small dashes.*

To determine whether a range of 45˚ or 25˚ perpendicular to the spreading direction is best for identifying faults I compare slope direction groups to the two example profiles taken from Chapters 3 and 4. Out of 53 faults identified from the bathymetry profile, 27 corresponed with a 25˚ range and 45 with a 45˚ range perpendicular to the spreading axis. This suggests that a broader range of 45˚ corresponded with potential fault scarps better than a narrow 25˚ range.

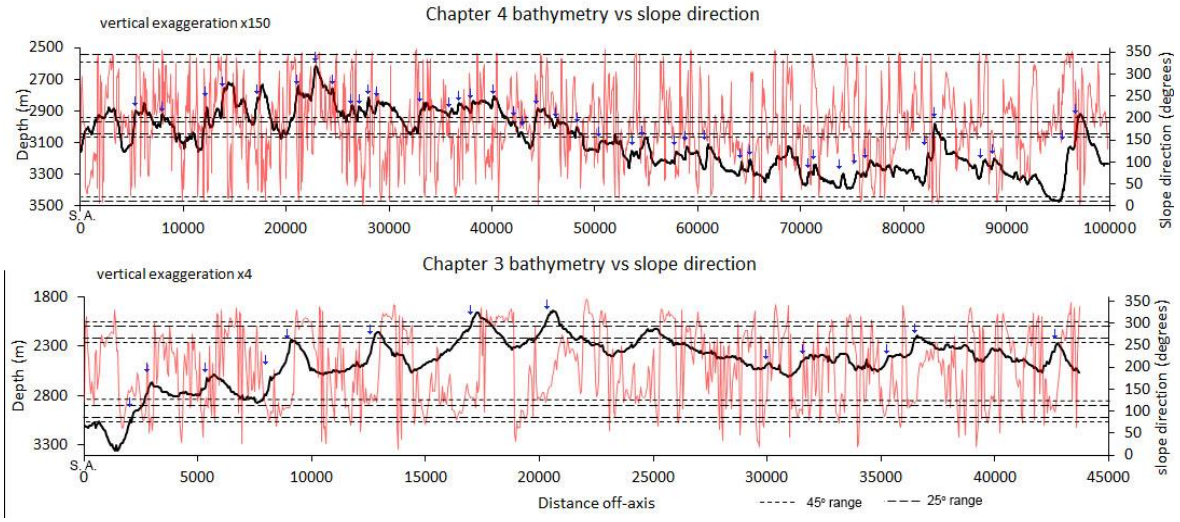

***Figure 2.6**: Bathymetry profiles taken from the Broken Spur (top) and Costa Rica ridges (bottom). Blue arrows indicate fault scarps identified from the bathymetry profile. Slope direction angles are in red with ranges perpendicular to the spreading axis in dashed lines. Large dashes are a 25˚ range and medium dashes are a 45˚ range.*

The tested ranges do not easily distinguish fault scarps from lava domes and AVRs. Narrowing the slope criteria from a range of 65˚ to 45˚ reduced the highlighted area of seamount in Chapter 4 (Figure 2.7). Reducing the slope direction range from 65˚ to 45˚ could help selected fewer rounded volcanic features. The axial valley wall fault in the Chapter 4 example indicates that narrowing the range to 45˚ does not affect the identification of linear faults. However, a narrower range does break up sinuous faults, shown by the axial valley wall fault in the Broken Spur example. A very narrow range of 25˚ breaks up both sinuous and mostly linear faults.

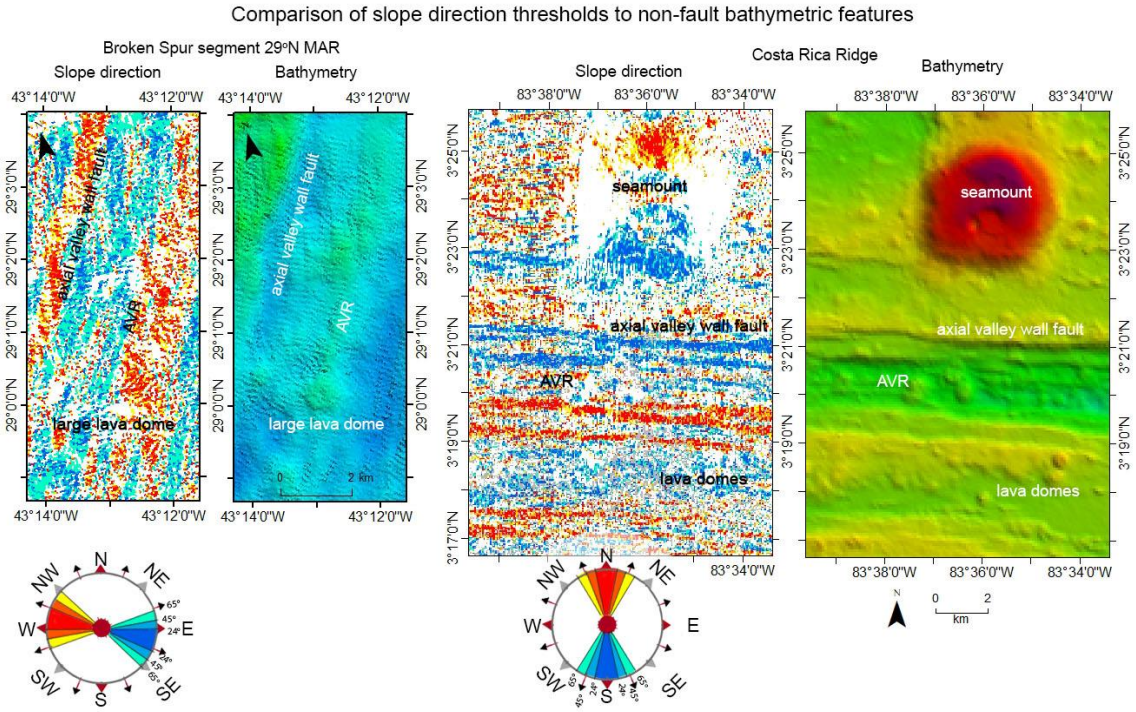

***Figure 2.7**: Maps illustrating what seafloor features highlighted with various ranges in slope direction with the Broken Spur on the left and the Costa Rica Ridge on the right. A 65˚ range in slope direction (yellow/cyan) highlights more rounded volcanic features while a 25˚ range (red/blue) breaks up sinuous and almost linear faults.*

Huang & Solomon (1988) and these sensitivity studies indicate that a slope direction range of 45˚ identfied fault scarps. Faults with orientations outside the 45˚ range are ignored as they are considered not primarily caused by the plate separation, and so contribute significantly less to the plate-separation induced extension.

3. High acoustic backscatter.

Multibeam backscatter strength is dependant on the transmission loss due to range, the absorption coefficent of water, the seabed conditions, and the insonification area. The range and absorption of water are easily corrected for when the data was collected. The resultant backscatter image is composed of variation due to the intrinsic backscatter strength of the seafloor and insonification area.

The insonification area is changed by the angle of incidence (Keenton & Searle, 1996). Backscatter is proportional to the square of the cosine of the incidence angle according to Lambert's Law (Keenton & Searle, 1996). The inflence of the incidence angle can be described as a slope perpendicular to the sonar beam which has a smaller insonifcation area and a stronger reflection, while a slope acute or sloping away from the sonar beam will reflect away from the receiver and insonify a larger footprint, producing a weaker reflection. Faults create a strong backscattering because of their exposed rock surface and, if they slope towards the sensor, their high incidence angles, making backscatter useful for identifying these features (Keenton & Searle, 1996). The relative reflectivity from faults is similar to the neovolcanic zone and is about 10 dB higher than average seafloor and 20 dB higher than sedimented basins according to density plots of backscatter intensity verse slope angle for variours seafloor morphologies by Eason et al, 2016.

To have a higher confidence that the backscatter is identifying changes in seafloor properties and not just incidence angle, my backscatter maps are created by combining the high values from east-west and north-south transects, and the overlapping port and starboard sides of the transducer. Ultimately, backscatter interpretation by itself can be difficult because of the role of incidence angle, that is why I combine it with other seafloor variables within my FID method.

If the seafloor had no faulting and sediment built up linearly with time, then it could be expected that a histogram of seafloor reflectivity from the spreading axis out would follow a negative correlation, with high reflectivity at the axis and no reflectivity at distance when sediment is thick enough to absorb most sonar. Actual histograms of multibeam backscatter do not produce a normal distribution, but are skewed towards the high reflectivity by a second peak (Figure 2.8). This second peak can be explained by faults exposing higher reflective surfaces far off-axis. To objectively identify which high backscatter signals indicate faults the histograms can be divided into quantiles, where each statistical grouping contains the same number of points. Selecting the upper most quartile,

quintile, or sextile influences what I define as high backscatter for my fault criteria.

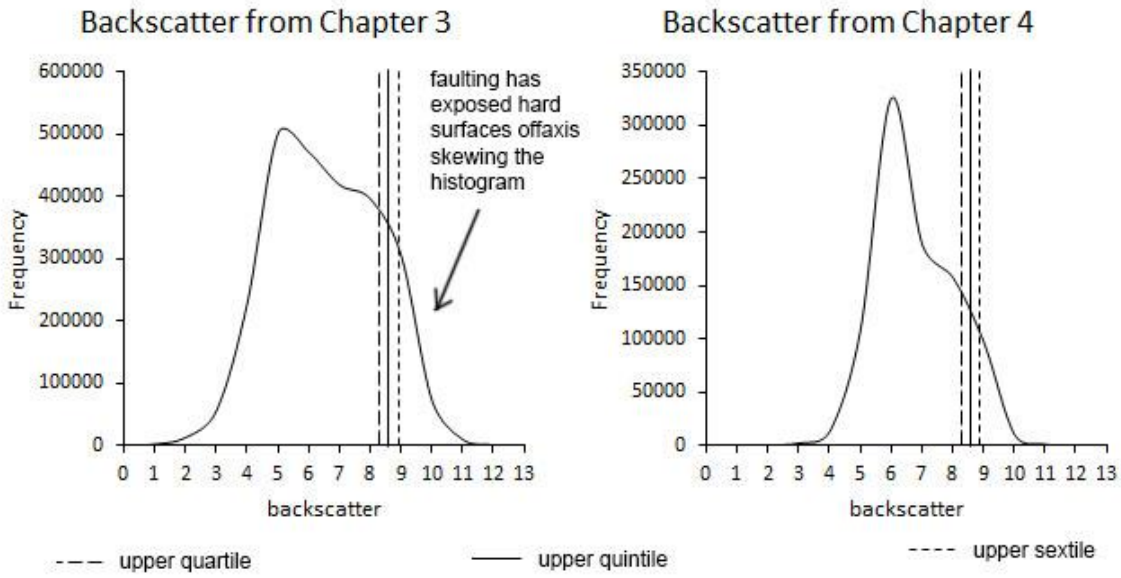

***Figure 2.8**: Histograms of multibeam backscatter across Chapters 3 (Left) and 4 (Right) datasets. The second peak between values 8 and 9 indicate that there are extra influences on backscatter than increased sedimentation away from the spreading axis, this is off-axis faulting exposing bedrock and providing regions of high incidence angles. Vertical lines are statistical grouped to define the lower limit of what constitutes 'high backscatter'. Long dashes are a quartile, solid line is a quintile, short dashes is a sextile.*

Identifying which statistical grouping to use requires a balance between ability to identify faults off axis and reducing the influence of low sediment cover close to the spreading. This region of low sediment cover and high reflectivity has the effect of 'eclipsing' faults by reducing the difference in acoustic signal between rocks exposed by faulting that those not sedimented on young crust. Using the upper quartile, this eclipsing region extends to almost 16 km off-axis for the Chapter 4 profile and 6 km for the Chapter 3 profiles. Using the upper quintile, this region extends to 7 km off-axis along the Chapter 4 profile, and 1.5 km off-axis along the Chapter 3 profile. Using the upper sextile, the region extends to 6 km off-axis for the Chapter 4 profile and 0.5 km for the Chapter 3 profile.

The eclipsing distance is then compared to the ability of each quantile to identify off-axis faults. Dividing the backscatter range into quartiles results in 22 out of 53 faults being identified (Figure 2.9). Quintiles resulted in 16 out of 53 faults identified. Sextiles resulted in 14 out of 53 faults being identified. Using quintiles to categorise high backscatter reduces the near spreading axis high reflectivity extent while still identifying faults along the example profiles.

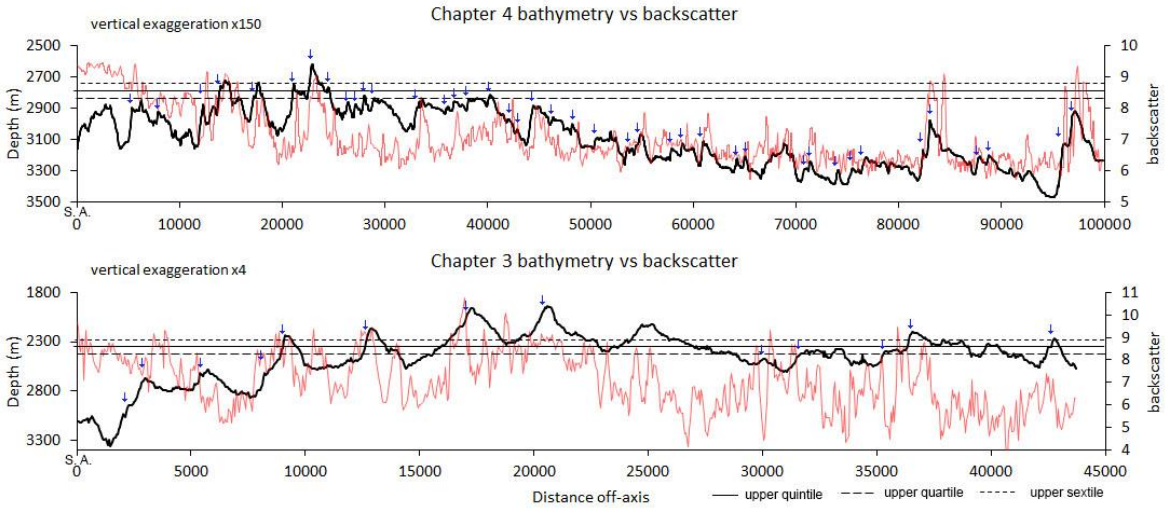

***Figure 2.9**: Bathymetry profiles (black line) taken from Chapter 4 (top) and Chapter 3 (bottom). Blue arrows are the where faults were identified using bathymetry profile. Red line is backscatter along the profiles. Long dashes in the lower threshold for the backscatter's upper quartile, solid line is upper quantile, short dashes is upper sextile.*

The FID map assigns a value of 1 to each criteria when fully met, allowing a maximum pixel value of 3. The FID value provides a measurement of confidence for the identification of pixels that could represent faults (e.g. pixels with a FID value of 3 have met all 3 criteria). A polygon is then hand drawn around linear clusters of FID values 2 – 3 (Box 4 Figure 2.1). The guiding of fault polygons using three fault parameters increases the accuracy of a fault pick and reduces subjective human error. The fault polygons are used to measure apparent heave ('apparent' is a term applied to the projection of the fault trace on to a horizontal surface, then the heave is calculated perpendicular to the fault strike). The identification of fault polygons are guided by a trained geologist, ensuring

that features such as seamounts, lava domes, and volcanic ridges are not highlighted, which may have been selected by an automated system.

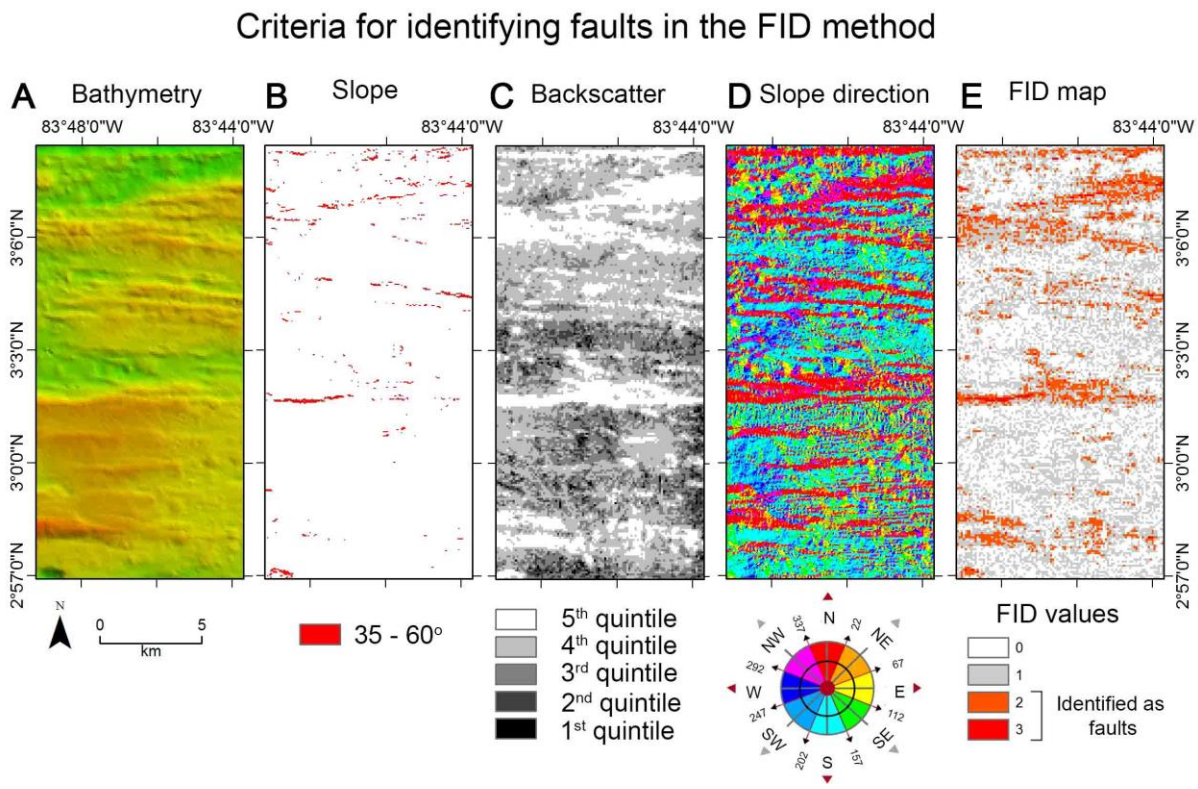

***Figure 2.10**: Identifying of faults using parameters selected from the attributes of bathymetry. **A**: bathymetry. **B**: Slope angles between 35 - 60˚. **C**: Backscatter in highest quintile. **D**: Slope direction towards and away from the spreading axis, north and south in this example. **E**: The FID map created by summing the maps that met the fault parameters. FID values 2 and 3 are used to guide fault polygons. This example is from the Costa Rica Ridge.*

The FID method was used in Chapter 3 and 4. Out of the 1167 faults identified at these two spreading segments, 35% of the fault polygons encompassed pixels with FID values 1, 53% with FID value 2, and 12% with FID value 3. The mean FID value of each fault was grouped into 0.5 bins and displayed in Figure 2.11, illustrating that the majority mean FID bin are values 1.5 – 2. The mean FID value for all faults identified in Chapters 3 and 4 was 1.6. All fault polygons contain FID values of 2 – 3, however, as these statistics show, when grouping lineations of pixel values 2 - 3 into a fault polygon there will be multiple pixels with values of 1 incorporated into the fault extent. These pixels with values of 1 have reduced the mean

FID value of faults to 1.6. The selection of faults from the FID map is further investigated in Chapters 3 and 4.

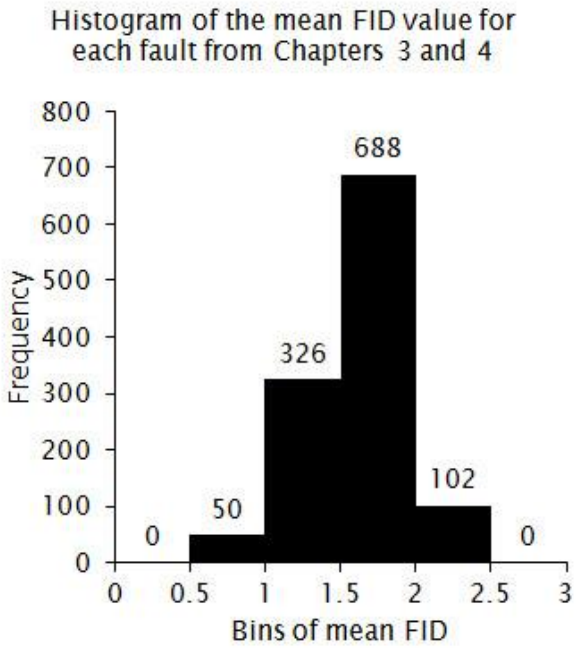

***Figure 2.11**: Histogram with bins of 0.5 illustrating the mean FID values within fault polygons from Chapters 3 and 4.*

After faults are identified, their apparent heave is measured. Apparent heave is the horizontal distance from the start (closest to the axis) of the fault expression to the end (furthest from the axis). For simplicity, future apparent heave is simply referred to as heave. The heave is used to measure extension over a large region.

There are some uncertainties inherent within the FID method, such as subjective error that can still occur during fault polygon drawing, as this is done by hand. However, this has been minimised by tightly following the FID values ≥2. Evidence of how tightly the FID values of 2 – 3 were followed is illustrated by the average FID values of fault polygons being in the 1.5 - 2 bin (Figure 2.11). Theoretical modelling by Escartin et al., (1999) illustrated the potential of fault foot-wall erosion and deposition on the hanging-wall to alter apparent heave by 40% of true heave. Another uncertainty comes from sediment thickness increasing off-axis, reducing slope, heave, and backscatter. Finally, there are uncertainties inherent in the multibeam data deriving from the beam width, location errors,

calibration, and sound velocity profiles. For the 12 kHz EM 120 multibeam system, used on the RRS James Cook during JC112/114, the pre-formed beam angle is 3˚ when the swath is at 140˚ (Kongsberg, 2005). At 3500 m water depth the beam footprint is 35m x 35m. All these uncertainties could influence the FID results and while I am unable to completely correct for them, an awareness of their potential influences allows for more accurate fault polygon drawing.

2.1.2 Percentage of measurable brittle tectonic extension (T%)

Cumulative heave is typically used to measure tectonic extension at spreading ridges to display plate asymmetry and the rate of off-axis extension (Escartin et al., 1999; Parnell-Turner et al., 2017). However, this method cannot be used to simultaneously identifying along and off-axis extension on a scale comparable to the large scale processes controlling MOR morphology, primarily, melt supply. I have developed a method that uses fault heave to calculate a 20 km derivative of cumulative heave to measure the percentage of visible brittle tectonic extension (T%) (Figure 2.12 and 2.13).

There are several reasons why T% is calculated over 20 km. Firstly, T% should reflect large scale regional extension, not individual seafloor features. The minimum window size was identified using a Fourier analysis of residual topographic anomaly (RTA) (Appendix B). My calculated Residual Topography Anomaly (RTA) calculates bathymetry deeper and shallower than the mean bathymetric depth, and is discussed further in Section 2.2. The Fourier analysis for crust from 0 – 7 Ma identified the smallest repeating large scale bathymetric feature has a 500 kyr wavelength (Appendix B), this likely represents abyssal hills. The MOR's spreading rate meant that the distance of these features provided a minimum window size of 2 km. Secondly, Section 2.1.4 tested the effect of window size on T% and concluded that 20 km was large enough to not measure individual features, but, not so large as to be unable to relate T% to crustal ages or second order segments. Thirdly, as discussed in Chapter 1, most active tectonic extension occurs within 2 - 35 km of the spreading

axis. To ensure that T% reflects seafloor morphology related to temporal changes in melt supply the T% window must cover a crustal area that was actively influenced by on-axis magmatism, giving a maximum size of 35 km. Finally, my investigation is primarily focused on identifying the morphological features of second order segmentation which represents the focuses of melt supply along MOR. Second order segments range in the tens of kilometres; therefore, a T% window of 20 km should measure related extension.

The first step of the T% method is how total heave is measured.. Each 20 km window is composed of parallel profiles. As MOR normal faults heave parallel to the spreading direction with very little rake (Thatcher & Hill, 1995), the profiles are orientated perpendicular to average fault strike. The spacing of the profiles is determined by the displacement-length scaling relationship which describes faults with lengths <1.5 km displace by <15 m (Dawers et a., 1993). However, because the bathymetry has a vertical resolution of $\leq$7 m, my analysis is unable to resolve faults <1 km in length. Due to this, profiles are spaced at 500 m to capture the smallest possible identifiable faults (Figure 2.13A). Additionally, having multiple profiles spaced at a high frequency along a fault's length allows multiple heave measurements per a fault, providing a representative measurement of extension. Finally, total heave is calculated along each profile then divided by the profile's length, and multiplied by 100 to calculate T% (Figure 2.13B). When a profile extends beyond the bathymetry it is clipped to the lateral extent of the bathymetry, ensuring T% is not artificially low. In Chapter 4, T% is compared to the traditional method of cumulative heave and a residual of the cumulative heave, to investigate if T% provides new insight into the distribution of extension.

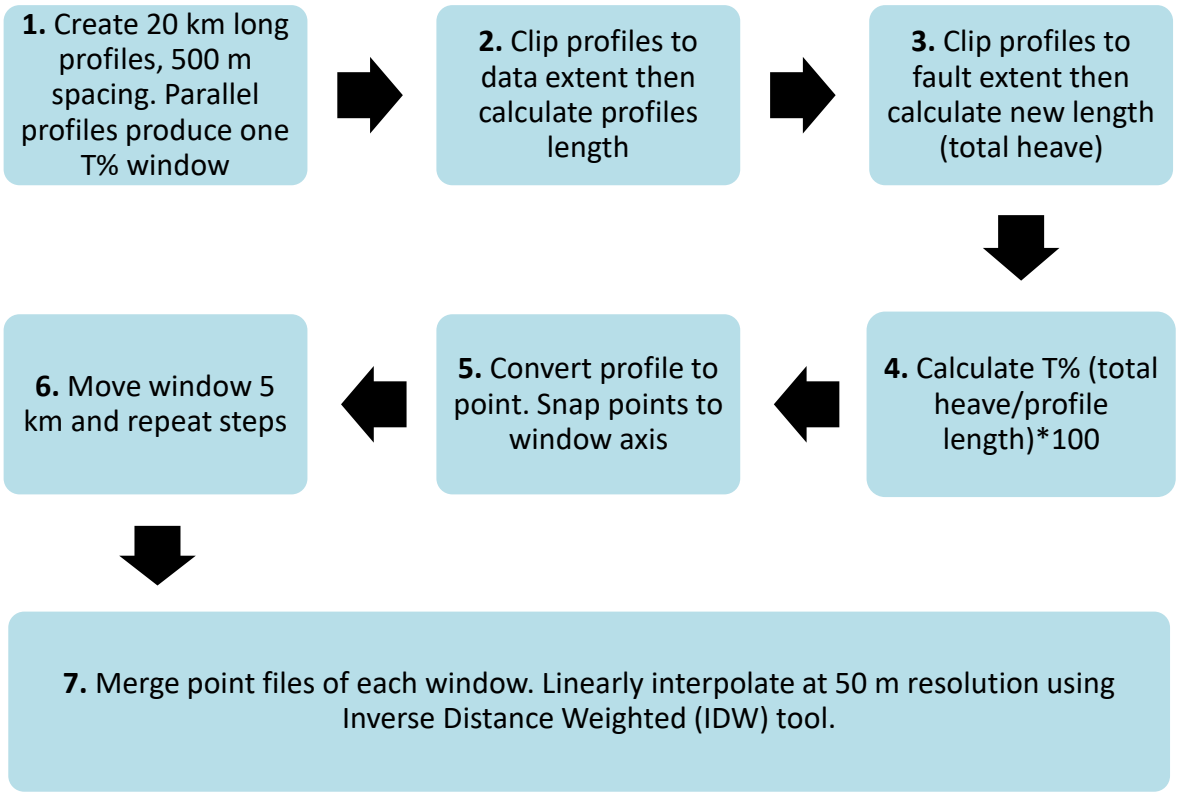

***Figure 2.12**: Flow chart illustrating the stages used to calculate T%. These steps are illustrated in Figure 2.13.*

The T% window is iteratively relocated away from the spreading axis at regular intervals, as shown in Figure 2.12, box 6 and Figure 2.13C. Each window overlaps with three adjacent windows with a spacing of 5 km, this provides ample overlap to prevent edge effects influencing the T% results. Finally, Figure 2.12 box 7 shows the last stage of the T% method. Here, T% values at the centre of each profile are processed with the ArcGIS™ tool 'Inverse Distance Weighted (IDW)' to join each T% point by a linear interpolation to produce an interpolated T% map, Figure 2.13E. In essence, T% essentially displays a derivative of cumulative heave averaged over a 20 km moving window.

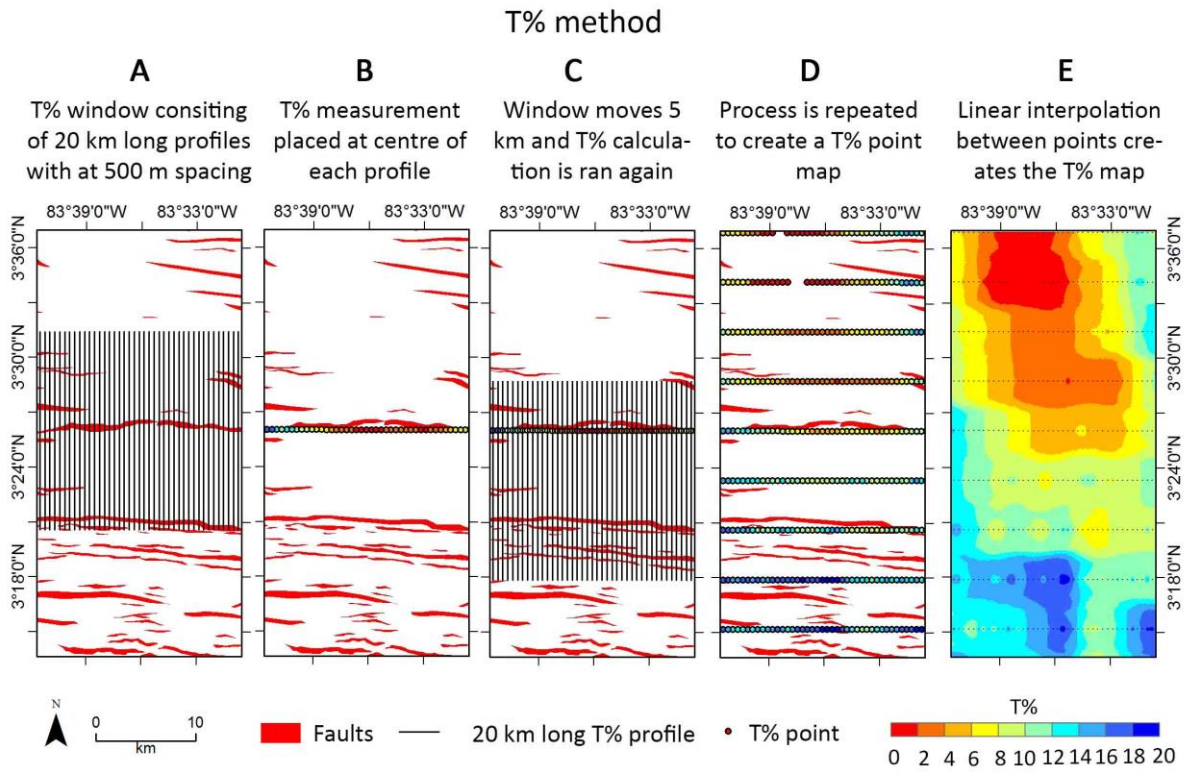

***Figure 2.13**: Stages to create a T% map: **A**: Create a T% window consisting of 20 km parallel profiles with a 500 m spacing (box 1 in Figure 2.12). **B**: Calculate T% along profiles using total heave/profile length*100 (boxes 4 and 5 in Figure 2.12). **C**: Move window 5 km (box 6 in Figure 2.12). **D**: Repeat process to calculate another row of T% points (box 6 in Figure 2.4). **E**: Use linear interpolation between points to create a T% map (box 7 in Figure 2.12). Small back dots are location of T% points.*

2.1.3 Uncertainties in calculating T%

As the FID and T% methods are innovative, I seek to establish confidence in their effectiveness by determining uncertainties resulting from the distance off-axis, i.e. the effect of sediment accumulation (Section 2.1.3.1), size of the T% window (Section 2.1.3.2), and resolution of the bathymetry (often depth and acquisition dependant) (Section 2.1.3.3).

2.1.3.1 The influence of sediment cover

The effect of increasing sediment thickness is tested for its influence on FID calculated fault heave. This is done by comparing fault heave from bathymetry models to faults heave measured along seismic aperture

profiles (SAP), which can image the basement through the sediment. Normal faults in the upper oceanic crust (Seismic Layer 2, having a geology of basalts and sheeted dykes) create asymmetric half-grabens in the basement horizon whose steep slope typically faces the spreading axis (Figure 2.14 panels 2a and 2b). Additionally, faults can be identified from profiles located >15 km off-axis, where sediments (Seismic Layer 1) is sufficiently thick that deformation by displacement along an underlying fault can be imaged. This syn-tectonic sediment dip changes up stratigraphy as accommodation space is provided, as shown in Figure 2.14 panels 1a and 1b. Fault heave is measured horizontally across Layer 2, between the top of the foot wall and bottom of the hanging wall. These criteria for fault identification along SAP are expanded and applied in Chapter 5.

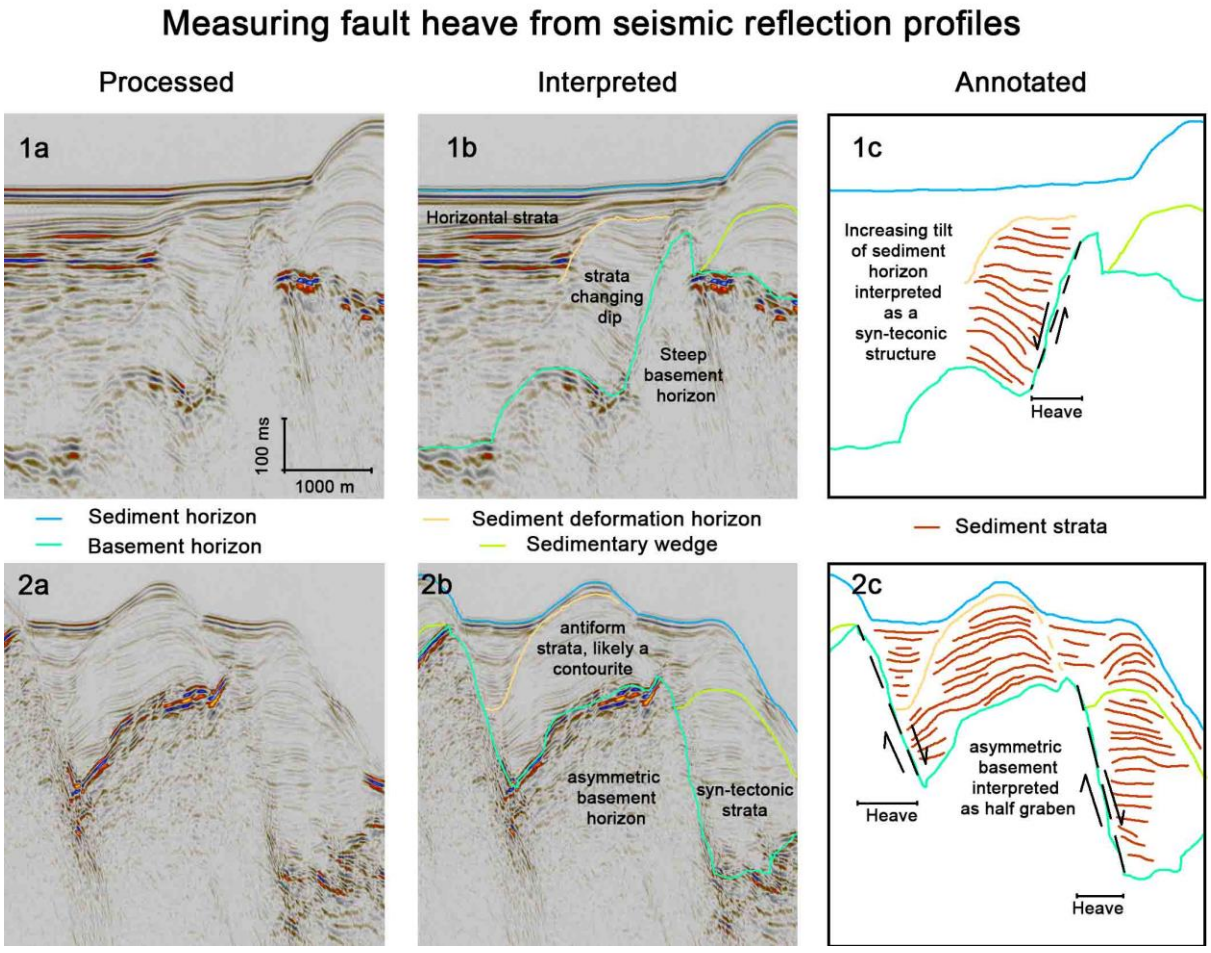

***Figure 2.14**: Signals interpreted as basement faults along seismic reflection profiles, this seismic profile is from Chapter 5. Light blue horizon is the water/sediment interface, turquoise horizon is the*

sediment/basement interface. Peach and light green horizons are sediment packets, possibly contourites. Faults are identified as the steep faces of asymmetric half-grabens.

Cumulative heave in Figure 2.15 was calculated along SAP_A (red) and the FID method (black), using data from Chapter 4. Cumulative heave from profile SAP_A starts 40 km off-axis where sediment thickness allows for fault identification. For comparison, cumulative heave from the FID map is started at the same off-axis distance shown in solid red (Figure 2.15).

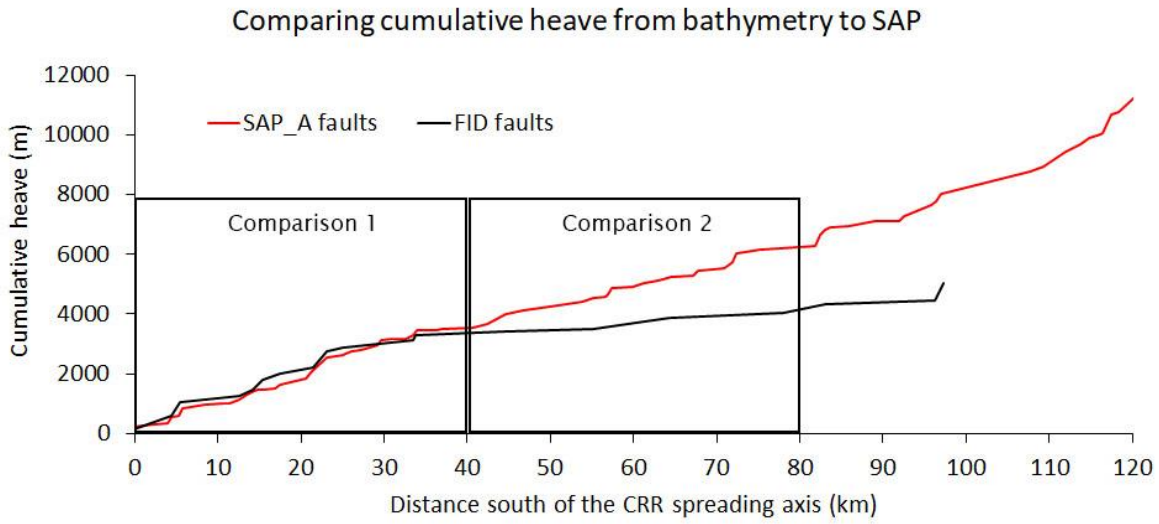

***Figure 2.15**: Cumulative heave along SAP_A (red) and using the FID method (black) south of the Costa Rica Ridge (CRR). Comparison sites 1 and 2 relate to Figures 2.16 and 2.17.*

By using 2 methods to measure heave, one that can account for sediment thickness and the other that cannot, it is possible to determine at what distance off axis the FID method ceases to be viable as a way to calculate T%. By 80 km off-axis (comparison site 1 Figure 2.15), there is a 7% cumulative heave difference between both methods (FID reached 3400 m and SAP_A reached 3550 m) indicating that FID is useful at this distance (Figure 2.15). In comparison, by 125 km off axis (comparison site 2 Figure 2.15), there is a 28% cumulative heave difference, with FID reaching a plateau around 4020 m while SAP_A continues to increase to 5550 m. The

point of divergence occurs between 40 – 50 km off-axis, suggesting after this point FID is not reliable at this intermediate spreading ridge.

The difference in cumulative heave can be further analysed by comparing the fault location and heave identified using the FID and SAP_A methods (Figure 2.16 & 2.17) along comparison sites 1 and 2 from Figure 2.15.

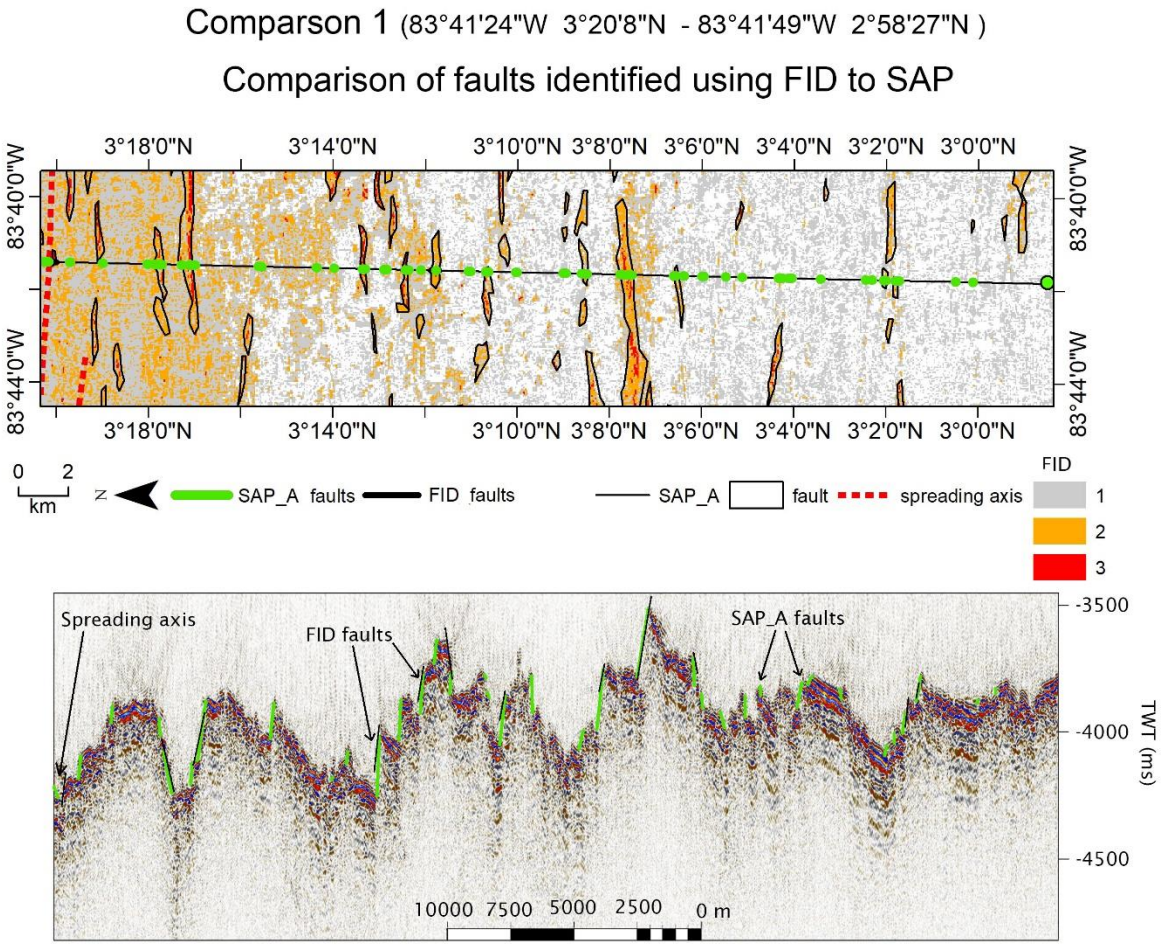

***Figure 2.16**: Comparison site 1 from Figure 2.15, 40 - 80 km off-axis. **Top panel:** FID map with faults outlined in black and green lines representing faults from SAP_A, below. **Bottom panel:** SAP_A with faults interpreted in green and FID faults as black. The shallowest strong reflector is the basement. There are no weaker reflectors above the basement indicating sediment is very thin.*

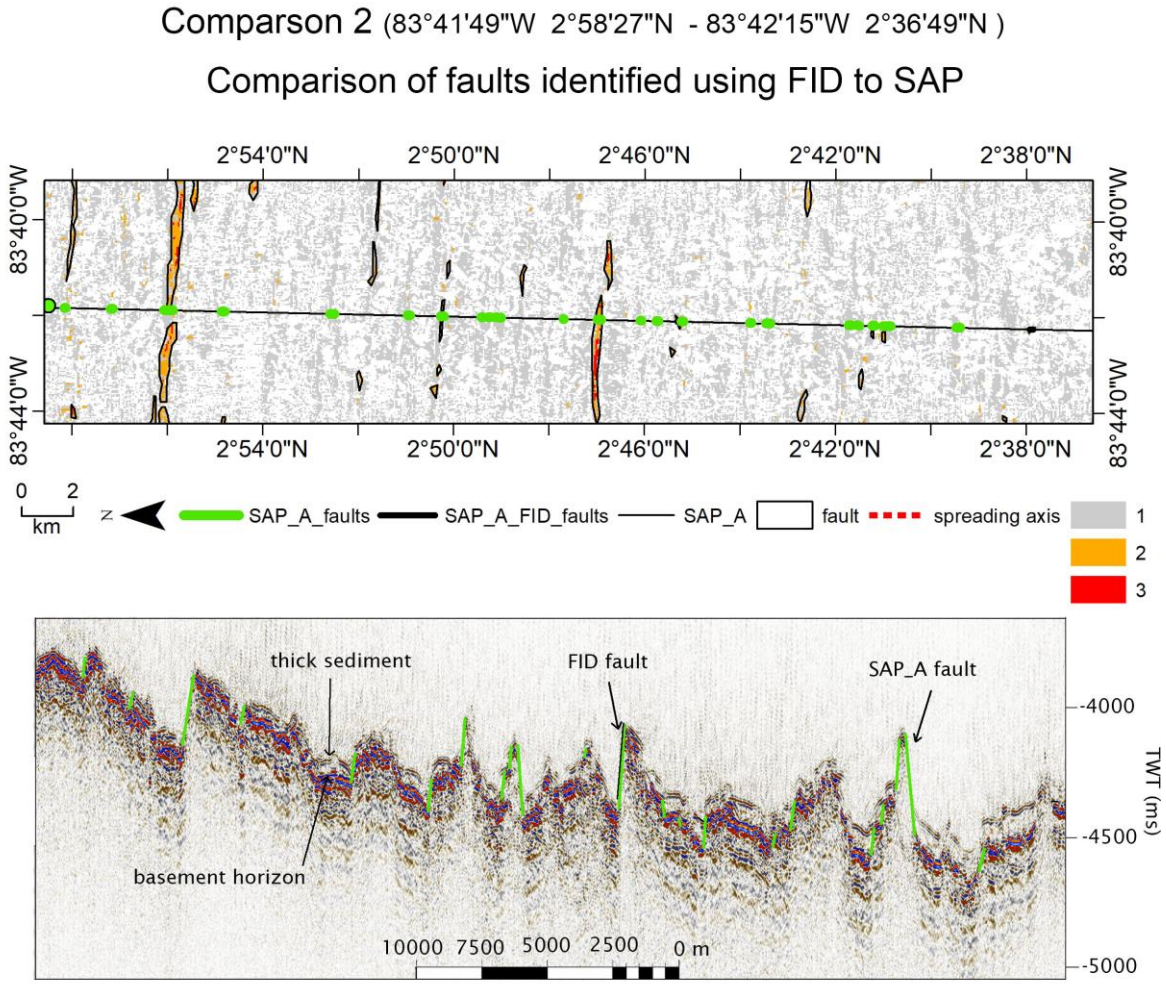

***Figure 2.17**: Comparison site 2 from Figure 2.15, 40 - 80 km off-axis. **Top panel:** FID map with faults outlines in black and green lines representing faults from SAP_A, below. **Bottom panel:** SAP_A with faults interpreted in green and FID faults as black. The shallowest strong reflector is the basement. There are no weaker reflectors above the basement indicating sediment is very thin.*

The divergence in measured cumulative heave between 40 – 50 km off-axis occurs where thick sediment ponds start to develop. In Figure 2.18, these sediment ponds start being visible in SAP_A when they reach a thickness of ~40 m. At this thickness all the faults with <60 m throw are not detectable by the FID method. The effect of sedimentation can be further analysed by comparing the methods at individual faults between 20

– 60 km off-axis. Within Figure 2.16, 4 faults were identified from the FID method and 16 faults from SAP_A between 20 – 40 km off-axis. All the FID faults have large heaves between 150 – 250 m while 95% of the SAP_A faults have heaves <150 m, with 50% having heaves <20 m.

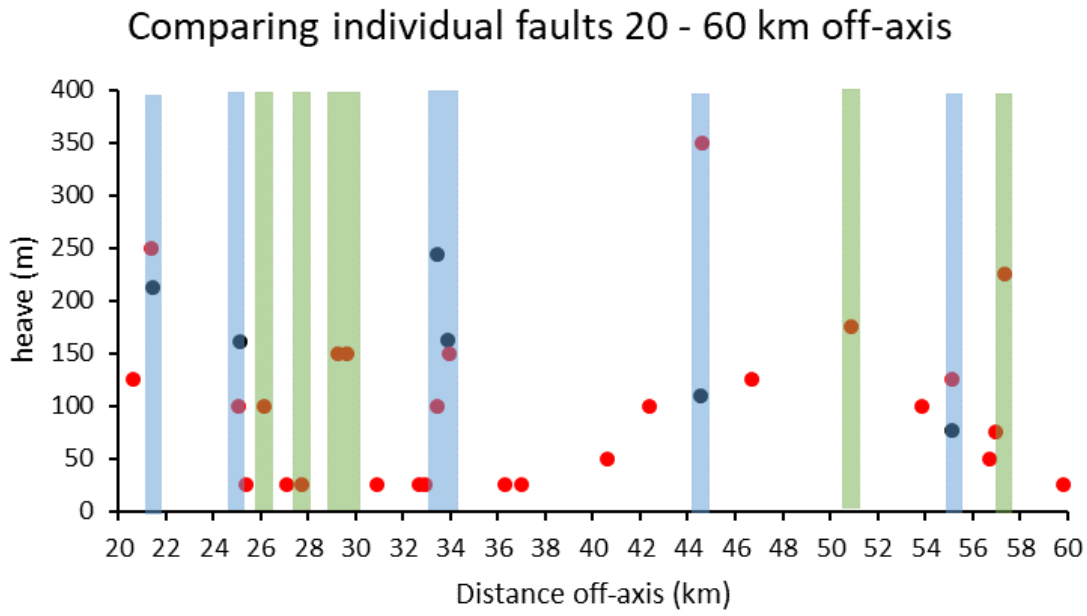

***Figure 2.18**: Differences in heave between individual faults from 20 – 60 km off-axis. Red dots are faults identified from SAP_A, black dots were identified using the FID method. Blue highlights are where faults were identified using both methods. Green highlights are 6 faults identified using SAP_A but not FID that are further investigated in figure 2.19.*

There were 6 faults (highlighted as blue in Figure 2.18) identified by both the FID method and seismic reflection profile. The heave of these 6 faults differed between methods by 9 – 70%, with 50% having higher heaves using the FID method. Greater than 40 km off-axis, heaves are higher using the SAP_A than FID, suggesting at this distance sediment is impacting apparent heave measurements from bathymetry.

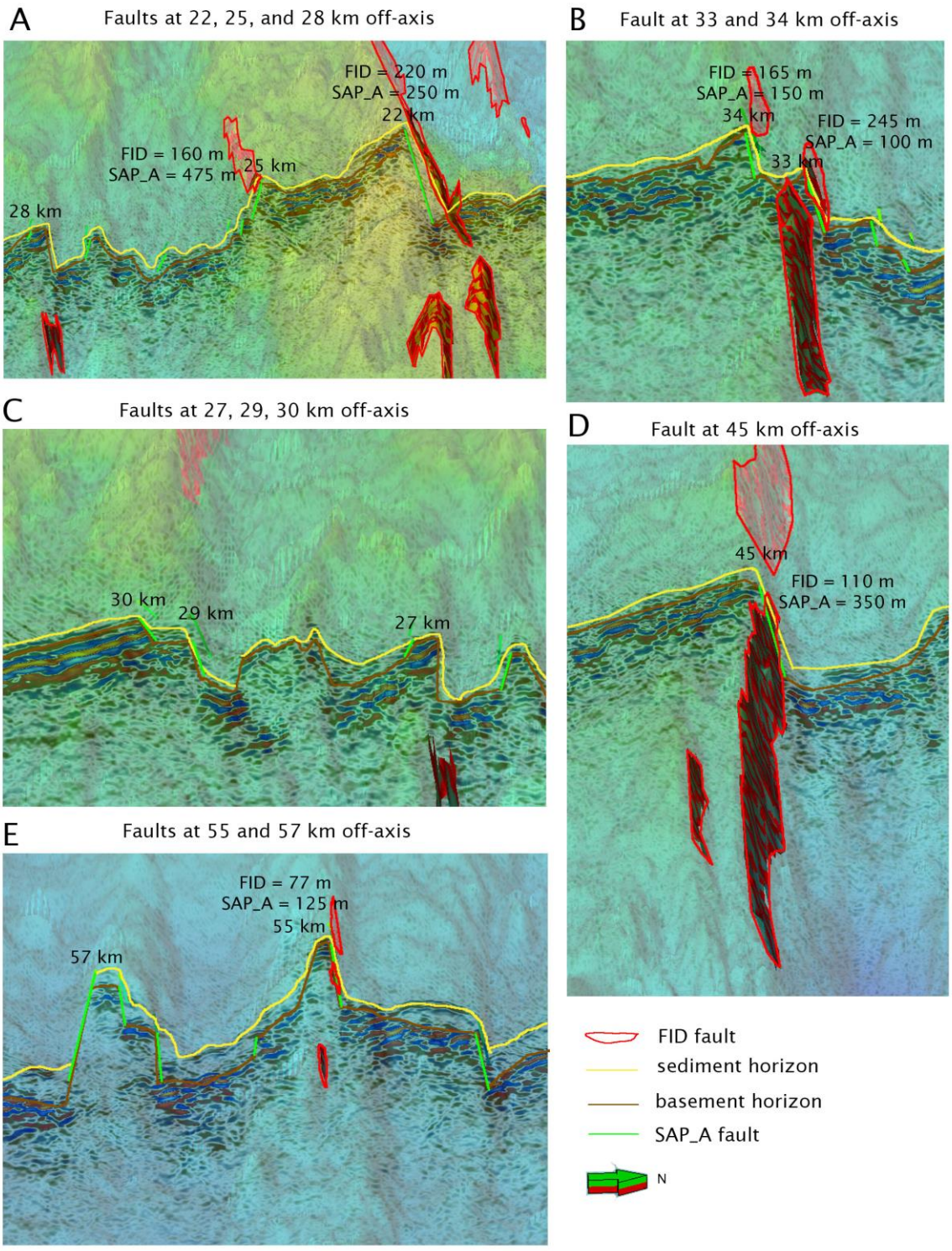

***Figure 2.19**: 3D perspective view of interpreted seismic reflection profile overlaid on bathymetry illustrating the 6 faults that had similar heaves highlighted in blue in figure 2.18 and 6 faults that where only identified using SAP_A highlighted in green from figure 2.18.*

Analysis of the 12 faults highlighted in figure 2.19 reveals more about why faults are and aren't identified by both methods. Regions where there

is a good match between both methods are the faults at 22 and 34 km off-axis. Both these faults face the spreading axis, have little sediment cover, form long continuous ridges and are made from a continuous fault, rather than collections of parallel faults.

Faults identified by both methods and produced heaves with differences >50% are located at 25, 33, 45, and 55 km off-axis (Figure 2.19). The faults at 33, 45, and 55 km are along steep continuous ridges where FID has identified them, however, at the point where the ridge crosses SAP_A the ridges angle is slightly shallower preventing the FID identifying it at this point. This irregular FID could have formed because the fault is slightly sinuous, preventing the slope direction criteria being met, or erosion and talus deposition has altered the slope preventing the slope angle criteria being met. The fault at 25 km is composed of parallel faults creating a stepped structure, these steps are then covered in sediment or talus that rounds out their topography preventing FID identifying them as faults.

Faults at 28, 27, 29, 30, and 57 km off-axis were all identified along SAP_A but not by FID (Figure 2.19). These faults occur at a much shallower angle than those identified using FID, they have small heaves and are generally completely covered by sediment. Near some of these faults, especially at 27 km off-axis, asymmetric breaks in the basement reflector have not been highlighted indicating the potential for human error when manually identifying fault scarps. The faults at 29 and 30 km off-axis were identified by FID to the west where the ridge is higher, however, the ridge is lower where it is crossed by SAP_A.

The divergence in cumulative heave between the datasets appears to occur because within 40 km off-axis the heave from the large faults identified by FID compensated for the smaller, shallower faults and stepped faults only identified along SAP_A. After 40 km off-axis the thicker sediment and basement erosion reduced apparent heave on faults and the scarps linear continuity. This eliminated the smaller and shorter faults from FID.

After 40 km off-axis, the reduction in FID faults results in T% reducing to <3% while T% along SAP_A remains >5% (Figure 2.20). The T% difference between the two methods increases to beyond 50% after 40 km, indicating this as a threshold for reliable T% calculation. Close to the spreading axis, T% measured from the seismic reflection profile is less than that using the FID. This could be because sediment is thinner close to the axis making it difficult to use sediment deformation to distinguish faults from volcanic features

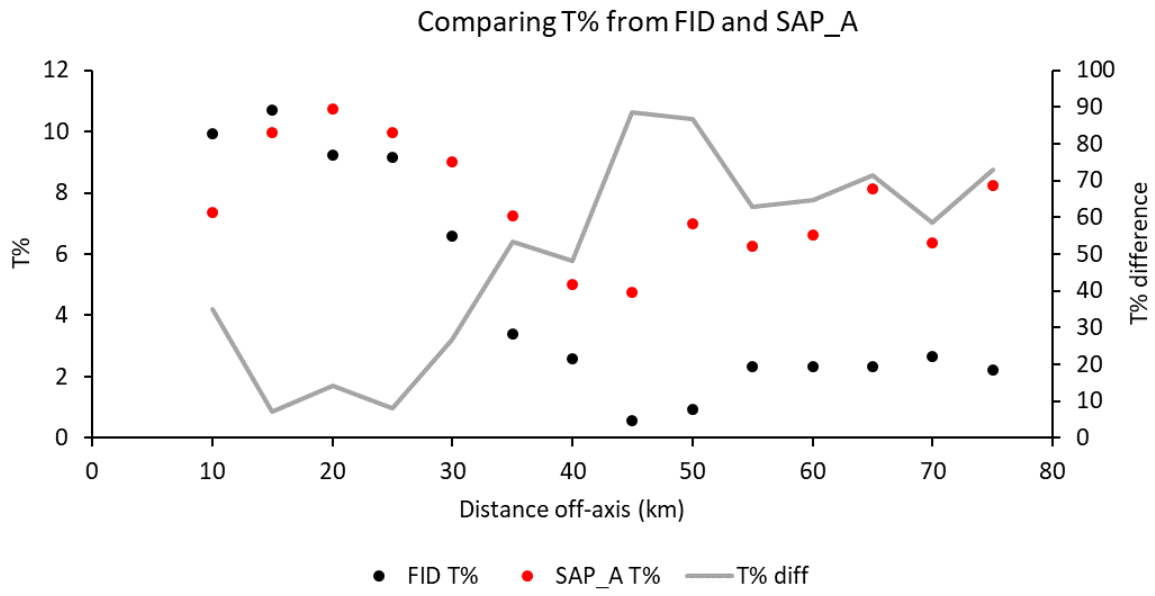

***Figure 2.20**: Calculation of T% at 5 km intervals using SAP_A (red) and FID (black). The difference in T% calculation is in grey, after 40 km off axis the difference is >50% indicating FID is not reliable after this distance.*

[GH1]

It is important to consider other uncertainties that could affect the results when relying solely on seismic reflection profiles. Firstly, faults may not be identified when close to the MOR axis because they are small and still growing, and thick syn-tectonic sediment packets have not yet been deposited. Secondly, fault scarp profiles can be affected by basement erosion and talus deposition. Thirdly, the effect of sediment loading on fault heave off-axis is uncertain. Finally, seismic reflection profiles have a <10 m vertical resolution while horizontal resolution can range from 10 - 100 m, affecting heave calculations. These uncertainties cannot be

corrected, and an awareness of their potential influences are considered when faults are digitised and interpreted.

2.1.3.2 Effect of window size on T%

The size of the moving window used to calculate T% can also influence the measured extension. As described in Section 2.1.2, T% windows are made of 20 km long profiles aligned parallel to each other, at a 500 m spacing. Figure 2.21 illustrates how a window length of 10 km and 30 km influences T% resolution.

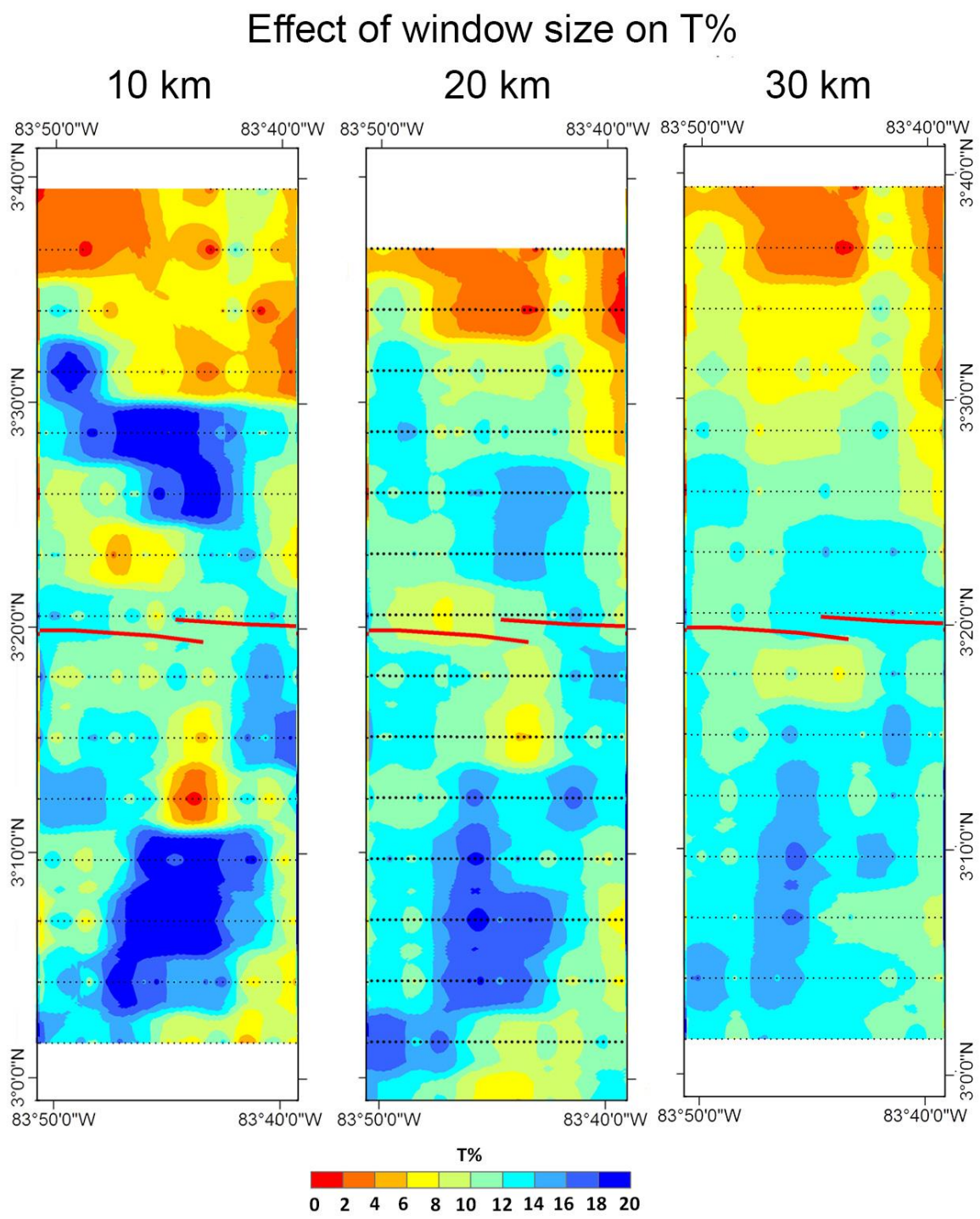

***Figure 2.21**: The influence of window length on T%. Red lines are the spreading axis and black dots are T% data points. Black dots are 500 m apart in the along-axis direction, and 5 km apart in the across-axis direction. Data are from Chapter 4.*

T% needs to be at a resolution comparable to large scale features, which are defined by low amplitude, long wavelength changes in bathymetry created by temporal and spatial changes in melt supply, e.g.

second order segments (Macdonald, 1982). A window 30 km long calculated T% in the N – S direction over too large an area to make meaningful correlations to smaller second order features. While a 10 km window length increases N – S precision, however, it was too short to calculate T% that was comparable in scale to second order segments. As discussed in Chapter 1, this is because tectonism in response to changes in melt supply (Ito & Behn, 2008; Morgan et al., 1987; Thatcher & Hill, 1995) can influence crust within 35 km of the spreading axis (Escartin et al., 1999; Toomey et al., 1988; Tucholke et al., 2008; Wolfe et al., 1995).

Additionally, Figure 2.21 reveals that the amplitude of T% signals reduces as window size increases, ranging from 0 - 28% with a 10 km window, and 0 - 20% with a 30 km window. Shorter windows are more sensitive to the influences of individual features with high amounts of heave, e.g. abyssal hills, and do not cover enough area to average the heave over. While larger windows will average the T% of individual features over a broader region resulting in a reduced T%. A 20 km window size is optimised for measuring T% over a distance that is comparable to the second order magmatic features discussed in Chapter 1, without over-estimating T% in response to individual seafloor features.

2.1.3.3 Effect of bathymetry resolution on apparent heave

The final test of my method is an exploration of how bathymetry resolution influences the number of faults identified, and hence the amount of heave calculated. Faults with <50 m heave and <7 m slip are below the detection limit of most deep-water multibeam bathymetry models. The effect this may have is calculated in Figure 2.22 by comparing 2 m resolution AUV bathymetry to 50 m resolution shipboard bathymetry from the Endeavour segment of the Juan de Fuca Ridge (cruise AT15-36 in 2008, Holden et al., 2008). The data sets were downloaded from the Marine Geoscience Data System operated by the Interdisciplinary Earth Data Alliance. The Endeavour segment's spreading rate is 57 mm yr^{-1} (VanderBeek et al., 2016) making it comparable to the Costa Rica Ridge in Chapter 4.

The 50 m resolution bathymetry had no acoustic backscatter available so the FID method was not employed, instead faults were identified from steep linear features parallel to the spreading axis in hill shaded bathymetry. The 2 m resolution bathymetry extends 15 km along the spreading axis and 1.8 km off axis, covering the axial valley wall faults.

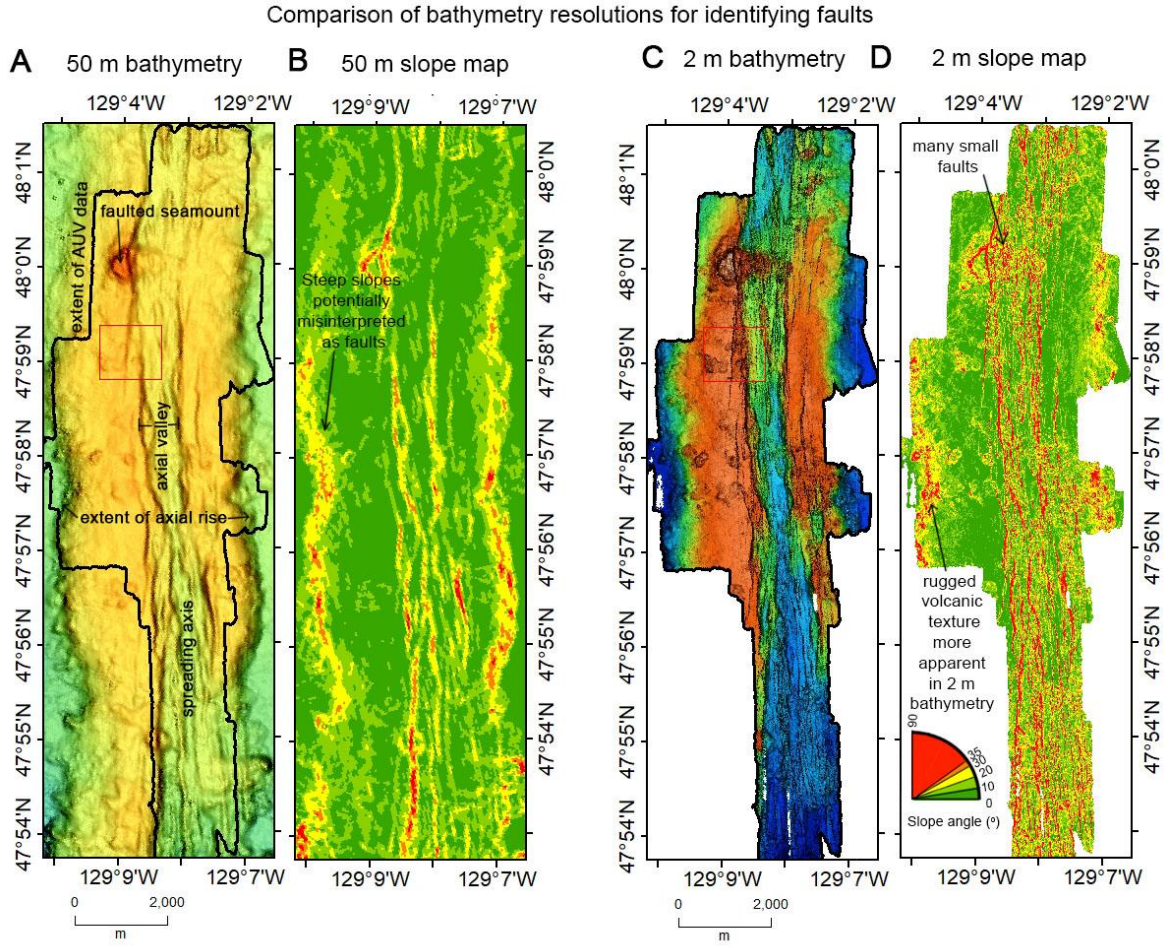

***Figure 2.22**: **A**: 50 m resolution bathymetry, red box is extent of figure 2.23, black outline is extent of 2 m resolution bathymetry. **B**: Slope map of 50 m resolution bathymetry that would be used in the FID method.. **C**: 2 m resolution bathymetry, red box is extent of figure 2.23. **D**: Slope map from 2 m resolution bathymetry that would be used for identifying faults in a FID method.*

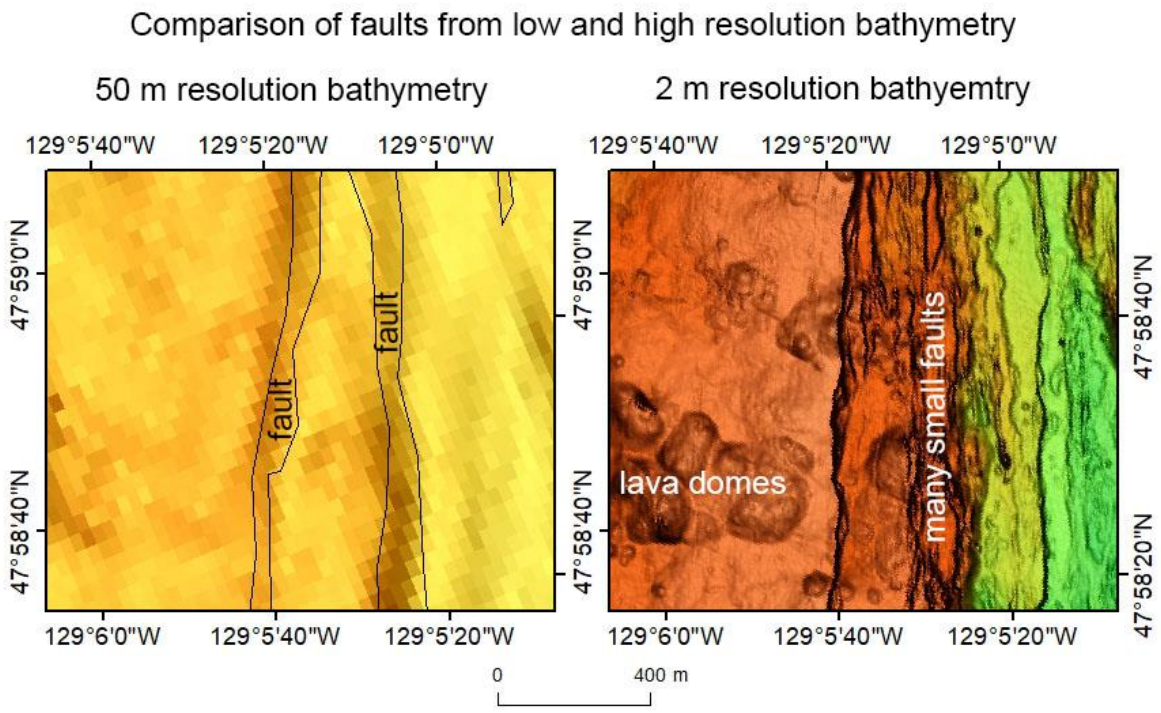

***Figure 2.23**: Zoomed view of axial valley faults from figure 2.22 showing the difference in visible fault structure from 50 m bathymetry (left) and 2 m bathymetry (right).*

Faults identified in the 50 m bathymetry (Figure 2.22A) are shown to be composed of many parallel small faults in the 2 m bathymetry (Figure 2.22C) resulting in a measure difference in apparent cumulative heave. This is illustrated further in figure 2.23, where what appears as two large axial valley wall faults with heaves of 50 – 75 m in the 50 m bathymetry are multiple parallel faults with heaves ranging from 5 – 30 m in the 2 m bathymetry. Differences also arise where a fault attribute is used to identify faults, such as the slope maps in Figure 2.22B and C. Steep slopes identified as faults from the 50 m bathymetry can occasionally be shown to be steep volcanic terrains visible from the 2 m bathymetry. This is particularly apparent at 1.2 km either side of the spreading axis at the flanks of the up-lifted axial high.

This assessment identified a fault area of 7,347,000 m^2 using the 50 m resolution bathymetry and a fault area of 3,000,000 m^2 using the 2 m resolution bathymetry. The 2 m bathymetry calculated 41% of the heave identified by the 50 m bathymetry. The significant difference in heave

identified at this fast spreading ridge may result from using slope to misidentify the flanks of the axial rise. Removing this misinterpretation 1.2 km either side of the spreading axis reduces the 50 m total heave to 4,663,000 m^2. Without the axial rise, 2 m bathymetry identified 64% of the heave identified by the ship bathymetry. None of my study areas are at fast spreading ridges with steep axial rises, so a difference of 36% between 50 m and 2 m bathymetry is a more likely estimate for the influence of bathymetry resolution on fault heave.

T% was calculated for comparison purposes. This example study site is much smaller than those in subsequent chapters meaning the T% windows had to be scaled down. Windows over the Juan de Fuca ridge are 1 km long, spaced at 100 m intervals, and stepped at a 200 m interval. The dimensions of these T% windows are not to be used to conclude relations between segment magmatism and tectonism, but are purely to compare how the difference in bathymetry resolution impact the apparent distribution and magnitude of tectonism.

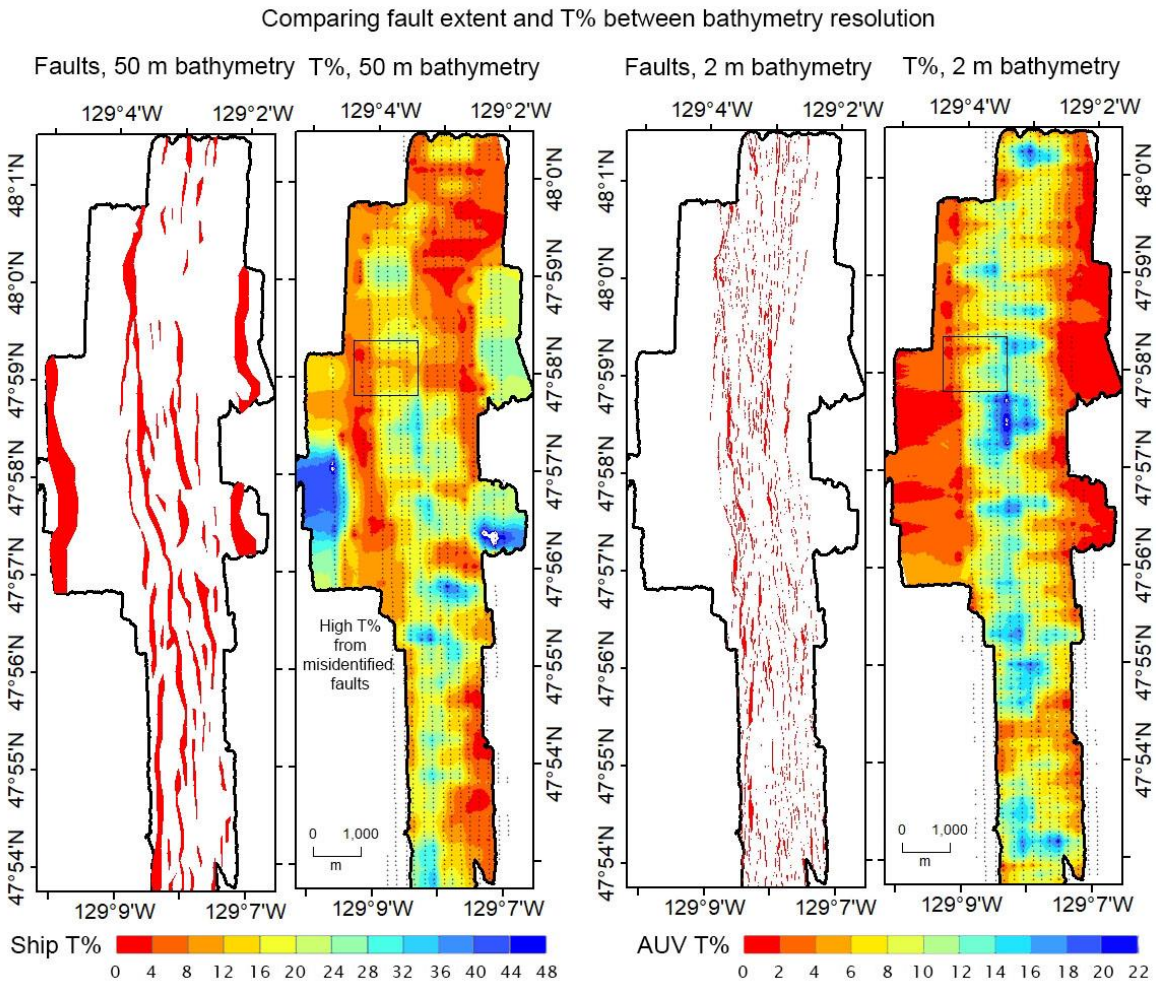

***Figure 2.24**: Example T% maps using faults identified from 50 m (left) and 2 m (right) bathymetry. Because of the small coverage the T% windows had to be scaled down, so cannot be used to compare with the other study areas. Here, T% windows over the Juan de Fuca ridge are 1 km long, spaced at 100 m intervals, and stepped at a 200 m interval. Black box is the extent of figure 2.23.*

The most apparent difference is that the 50 m bathymetry doubled the measured T%. The range in T% values within 1 km of the spreading axis is 45% for the 50 m bathymetry and 23% for the 2 m bathymetry. The smaller range in T% values suggests that identifying smaller faults with the 2 m bathymetry calculates a more even T% distribution along the spreading axis.

A measured difference in T% is apparent when comparing T% values within 1 km east and west of the spreading axis. The 50 m resolution calculated an average T% of 16.4% on the western axial valley wall and

13.8% on the eastern axial wall, indicating 16% asymmetry. The 2 m resolution produced an average T% for the western wall of 9.7% and 8.9% for the eastern wall indicating 9% asymmetry. This indicates that T% is more evenly spread across- and along-axis when identfying faults from high resolution bathymetry.

It could be expected that because the ship-board bathymetry is unable to identify faults <50 m it would result in a lower heave calculation. However, these results indicate that the lower resolution bathymetry measures broad slopes as one large fault when in reality it is many, small parallel faults. This study was on a fast spreading ridge, so it is possible that the over estimation will not be as severe for intermediate and slow ridges where smaller faults are able to nucleate and develop further into large faults. Despite the disparity between fault heave measured using two different bathymetry resolutions, it should be possible to determine relative changes in heave between ridges if a consistent fault measurement technique is used at data of the same resolution.

2.1.4 Further development of T% in subsequent Chapters

Further testing of my methods for measuring MOR tectonism occurs in Chapters 3 and 4 where I aim to predict how much heave is missed by assuming the relationship between fault heave and frequency follows an exponential decay. In Chapter 3, interpreted faults using my FID method are compared to the subjectively interpreted faults that used a single dataset in Escartin et al. (1999). I then calculate T% maps derived from different fault identification methods to determine if different methods produce different results when measuring tectonism at the large scale. In Chapter 4 my T% method is compared against cumulative heave and a residual of cumulative heave, these are the traditional methods for calculating extension at the large scale. From this comparison I aim to determine if different methods that are meant to be diagnostic of large scale extension are able to identify the same regions and relative magnitudes of extension at MORs.

2.2 Using Residual Topography Anomaly (RTA) as a proxy for melt supply

To explore a relation between measurements of tectonic extension and melt supply, I must develop a proxy for the melt supply. By using bathymetric data the proxy for melt can be derived from the same dataset used to calculate tectonic extension (T%), this ensures they are spatially comparable. Additionally, in most of the study sites bathymetry data has greater spatial coverage than gravity data, making it an appropriate dataset to utilise when investigating second order changes in melt supply.

Bathymetry is used to develop a proxy for melt supply by referring to two theoretical models for crustal isostasy. Firstly, I could use Pratt isostasy, which theorises that differences in topographic relief in isostatically stable crust, without structural support, are due to differences in density (Lowrie, 2007; Suppe, 1985). According to the Pratt model, a positive bathymetry anomaly could be created by low density crust which is either hot, or is composed of low amounts of Fe Mg, or has undergone extensive hydrothermally alteration suggesting the crust has a high permeability. Alternatively, Airy isostasy explains topographic differences as being due to differences in crustal thickness. In this model, regardless of crustal thickness, all crust is neutrally buoyant at the same level within a plastically deforming asthenosphere. Therefore, thicker crust produces shallower bathymetry than thinner crust (Lowrie, 2007; Suppe, 1985). This model fits well with the observation that along spreading axes, seafloor is systematically shallower at the centre of the segment than the segment ends (Kuo & Forsyth, 1988; Lin et al., 1990). This is consistent with thicker crust and models indicating focusing of mantle melt towards the segment centres (Whitehead et al., 1984).

To identify bathymetry anomalies, I need to be able to quantitatively define broad, shallow or deep bathometric regions relative to the crust's average depth. To calculate crustal density from the relative topography anomaly (RTA) I use the Pratt equation; $\rho_1 = \rho_c \frac{c}{h_1+c}$, where ρ_1 is the density of the elevated crust, ρ_c is the density of the crust (3 g cm^{-3}), c is

the thickness of the crust (6 km) and h_1 is the RTA (km). To calculate crustal thickness for the RTA I use the Airy equation; $b_1 = \frac{h_1 \rho_c}{\rho_m - \rho_c}$, where b_1 is the additional crustal thickness, and ρ_m is mantle density (3.3 g cm^{-3}) (Lowrie, 2007; Suppe, 1985). The decision of whether to choose the Pratt or Airy models to explain the bathymetry anomalies depends on whether the estimated crustal density or thickness is within a believable range for the MOR, and whether the estimated density or thickness aligned with local gravity anomalies.

These isostasy models were used by Wang et al., (2015) to explain large scale changes in bathymetry by subtracting a plate model from observed seafloor bathymetry to identify anomalous bathymetry. Positive anomalies were interpreted as representing low density Inside Corners or thicker crust formed at the spreading axis (Escartin & Lin, 1998). Despite crustal plates having some flexural resistance, the topographic changes described by the Pratt and Airy models are expected to be observable at the scale of second order segments (20 – 50 km).

2.2.1 Unloading sediment from the basement

The first stage of calculating RTA is to unload the basement of sediment. The sediment thickness increases as the crust moves off-axis, covering the basement and shallowing bathymetry. Additionally, sediment loading causes the basement to subside. This sediment layer must be removed and the basement un-subsided so that the RTA represents the basement depth. In this Chapter I will calculate an example to illustrate the basic principles, in the relevant chapters, RTA will be explained in greater detail using data relevant to the specific MOR.

Firstly, sediment thickness was measured using geophysical methods. In Chapter 3, sub-bottom profile data measured sediment depth to a crustal age of 3 Ma (Mitchell et al., 1998). In Chapter 4, the cruise JC114 produced three 270 km long synthetic aperture profiles (Hobbs & Perice, 2015). In Chapter 5, the cruise JC050 collected two seismic reflection profiles (White, 2011). The sediment and basement horizons for

the seismic reflection profiles in Chapters 4 and 5 were depth converted using a velocity of 1484 m s^{-1} for water and 1900 m s^{-1} for sediment (Jones, 2004). The collection and processing of these geophysical data sets are explained in more detail in their relevant chapters. The sediment thickness profiles were fitted with a linear fit, providing an average off-axis sediment thickness curve (Figure 2.25).

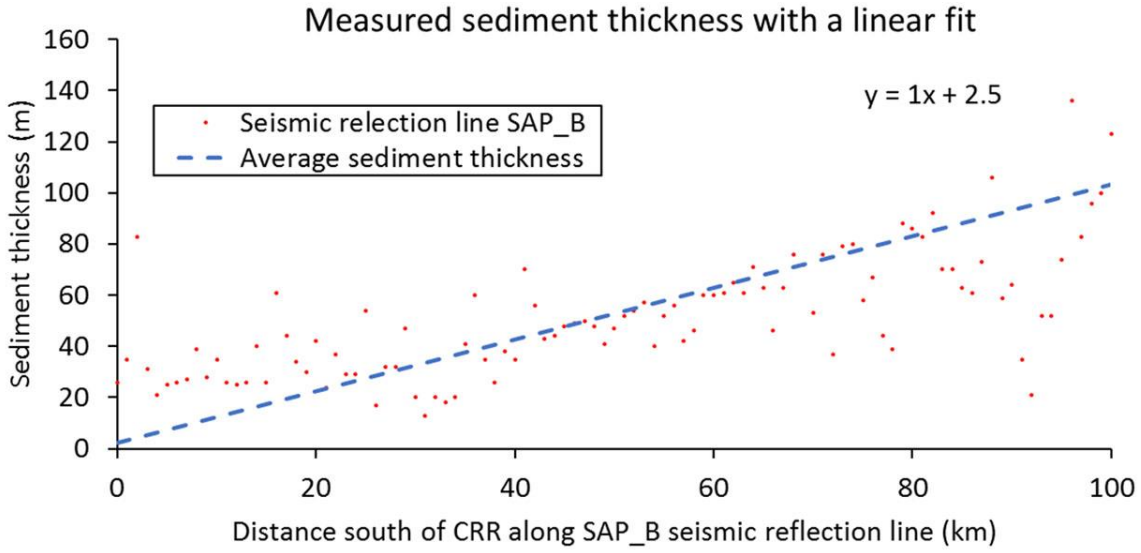

***Figure 2.25**: Measured sediment thickness every 500 m along the SAP_B seismic reflection profile (red dot). Dashed blue line is the average sediment thickness curve calculated by a linear fit.*

The sediment layer was then subtracted from bathymetry using the equation for the depth before sediment loading, t_b, (Le Douaran & Parsons, 1982): $t_b = t'_b - t_s \frac{(\rho_a - \rho_s)}{(\rho_a - \rho_w)}$. Where, t'_b = depth after sediment loading, t_s = sediment thickness, ρ_a = density of asthenosphere (3.2 g cm^{-3}), ρ_w = density of seawater (1.027 g cm^{-3}) and ρ_s = density of sediment (1.59 g cm^{-3}). Errors can occur due to variations in sediment composition or increasing density with depth. However, when sediment is less than 500 m thick the error is <10 m (Le Douaran & Parsons, 1982).

The calculated average sediment thickness curve smooths higher resolution basement topography, such as abyssal hills and lava domes. However, this will not impact the analysis of low relief trends over tens of kilometres in crustal morphology that may relate to orders of MOR segmentation, such as deep bathymetry related to non-transform

discontinuity (NTD) or shallow bathymetry related to a second order segment's magmatic centre. In addition, a precise measurement of sediment thickness is not required, because sediment thickness has a minor effect on the final RTA map. For example, at 50 km off-axis sediment is predicted to be ~60 m, however, once sediment is removed and the crust is isostatically adjusted, the bathymetry only shallows by 20 m.

2.2.2 Calculating average crustal depth with age

Once sediment is removed, the next stage is to calculate the average crustal depth with age that does not represent any local bathymetry anomalies. This is then used to quantify how far bathymetry positively or negatively deviates from the Plate's average depth. When there is enough off-axis bathymetric coverage, this average crustal depth can represent the influence of off-axis subsidence due to plate cooling. In Chapter 4, this was done by calculating the average basement depth along 35 km long profiles aligned parallel to the spreading axis. These profiles were spaced at 1 km internals going off-axis to produce a plot of average sediment unloaded basement topography.

The profiles are then correlated to crustal age, for this example, using data from Chapter 4. A linear interpolation was used between the magnetic isochron from Hey, (1977) to produce an age map. A linear fit of the average sediment unloaded basement topography measured at 1 km intervals off-axis against the square root of age described the average crustal depth with age (Figure 2.26). From Chapter 4 the average crustal depth with age was calculated as 231 $t^{1/2}$ when t ≤4 Myrs (Figure 2.26).

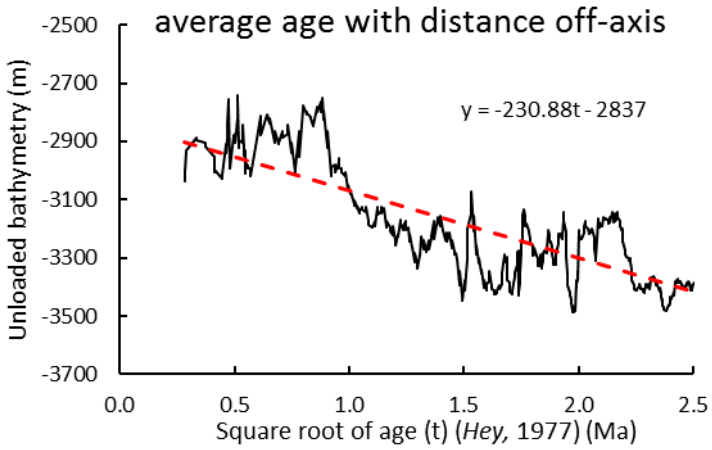

***Figure 2.26**: The average unloaded bathymetry measured at 1 km intervals off-axis is plotted against the square root of age. A linear fit to the plot describes the average crustal depth with age ignoring local bathymetry anomalies. Subtracting this linear fit from the unloaded bathymetry calculates RTA, positive and negative deviations away from the predicted depth for the age of the crust.*

The linear fit describing the average crustal depth with age ignoring local bathymetry anomalies (Figure 2.26) is then subtracted from the sediment unloaded basement bathymetry to provide the residual topographic anomaly (RTA) map. Described here is the general method of calculating RTA, each Chapter will describe in detail how this general method is slightly adapted to utilise each Chapter's regional data sets and age maps.

2.3 Determining melt supply from gravity anomalies

To determine whether the Pratt or Airy isostasy models should be used to interpret the RTA, I also use gravity anomalies to determine the magnitude of crustal changes that are believed to relate to melt supply. Changes in crustal thickness, composition, or temperature will influence the crust's density and gravitational attraction. A weaker gravity anomaly relates to thicker, low density crust, which was created from a high melt supply. A strong gravity anomaly relates to high density crust that may contain more Fe and Mg. A strong attraction could also result from ultra-mafic rocks exerting a greater surface attraction when the crust has been thinned by low melt supply. Alternatively, a hot lithosphere or large regions of serpentinisation will reduce crustal density and produce a weak gravity anomaly. The gravity anomaly used depends on the availability of published gravitational anomaly data.

The simplest to calculate gravity anomaly is the Free Air Gravity Anomaly (FAA). A FAA is calculated by correcting for the Earth's spin and oblate spheroidal shape. Corrections are also made for height above sea level. The FAA tends to closely correlate with bathymetry, further processing to remove the influence of water depth calculates Bouguer anomalies (BA) using: $BA = FAA + (2\pi G(\rho c - \rho w) \times h)$. Where ρw = density of water (1.027 g cm^{-3}), ρc = density of crust (determined by Nettleton's method), h = depth of water column (m), $G = 6.673 \times 10^{-8}$ (Office of GEOINT Sciences, 2008). The density of the seafloor can be estimated using Nettleton's method, this tests a series of densities from 3 – 2 g cm^{-3} and uses the density which creates a BA with the minimal correlation to bathymetry. Changes in crustal density are considered significant if the BA deviate from a mean by a minimum of ±20 mGal (Tassara et al., 2005). BA also contain a terrain correction to correct for the gravitational attraction of nearby 3D surface features.

Further processing of BA can calculate the mantle Bouguer anomaly by correcting for the effects of the water/sediment and crust/mantle interacting which are assumed to be parallel. This correction assumes a

constant plate thickness and density. This results in the mantle Bouguer anomaly identifying regions of the crust less dense or thinner than the assumed crustal thickness and density. The mantle Bouguer anomaly can then be corrected for the hot, less dense, mantle under the ridge axis to calculate the residual mantle Bouguer anomaly (RMBA). Density variations in the mantle are usually small indicating that variations in the RMBA arise from changes in crustal thickness (Searle, 2013).

In Chapter 3, I use a RMBA map published in Lin et al., (1990). In Chapter 4, there was no published Bouguer anomaly map for me to compare RTA against. Therefore, in Chapter 4 I cannot validate the RTA representing crustal density or crustal thickness anomalies against gravity. In Chapter 5 there was no RMBA available that followed the two seismic reflection profiles. However, in Chapter 5 gravity anomalies are used to identify V-shaped ridges that are hypothesised to represent periods of high melt supply. I used satellite FAA from Bonvalot et al., (2012) WGM2012 earth gravity anomaly map, that has a ~3.7 km^2 resolution, to detected laterally extensive ridges of 45 - 70 mGal (Hey et al., 2010; Jones et al., 2002; Martines & Hey, 2017: Parnell-Turner., 2014; White et al., 1995). Each chapter describes more specifically how gravity anomalies were processed and used for each MOR.

2.4 Conclusion

In conclusion, MOR morphology is determined by the interaction of magmatic and tectonic process. To measure these processes I have developed methods to identify faults, measure tectonism, and locate bathymetry anomalies related to melt supply.

To measure faults I have developed a reproducible and objective method using sonar data to analyse the seafloor attributes of slope angle, slope direction, and high acoustic backscatter. I then cross-correlate fault parameters from these three attributes to produces a fault identification map (FID map) that helps reduce subjective errors by guiding the drawing of fault polygons.

To measure extension, I use the fault heave to calculate the percentage of measurable brittle extension (T%) over a 20 km moving window. T% measures the tectonic extension at a scale comparable to second order magmatic processes, as described in Chapter 1.

Melt supply changes that create regional anomalies of shallow and deep bathymetry will be quantitatively identified using a Residual Topographic Anomaly (RTA). RTA is calculated by firstly unloading the bathymetry of sediment. The unloaded bathymetry is then subtracted from a linear regression that describes the average crustal depth off-axis ignoring regional bathometric highs and lows. RTA quantifies the deviations in bathymetry from the average plate depth that can be explained using the Pratt or Airy isostasy equations. To determine which isostasy equation should be used, the RTA is compared to gravity anomalies when available. When gravity anomalies are not available, RTA can be used to locate the relic bathymetry differences that result from second order melt segmentation; e.g. a deep segment discontinuity or a shallow segment centre.

Chapter 3: Broken Spur segment 29°N MAR

3.1 Introduction

This Chapter aims to test the hypothesis that melt supply, which controls crustal thickness at first order segments, has an influence on the proportion of tectonic extension expressed as brittle faulting at the seafloor. To investigate this, I have focused on the Broken Spur segment, between 28°45' N – 29°15' N, on the slow (full rate 24 – 28 mm yr^{-1}) and orthogonal spreading Mid-Atlantic Ridge. This chapter compares the percentage of measurable brittle extension at the seafloor (T%), derived from fault heave measured using the Fault Identification (FID) method, with the Residual Topographic Anomaly (RTA) and Residual Mantle Bouguer Anomaly (RMBA) that are considered a proxy for crustal thickness. All these methods are described in Chapter 2. In the first instance, the reliability and precision of the FID method is assessed though comparison to a similar study producing a fault heave map, made by Escartin et al., (1999).

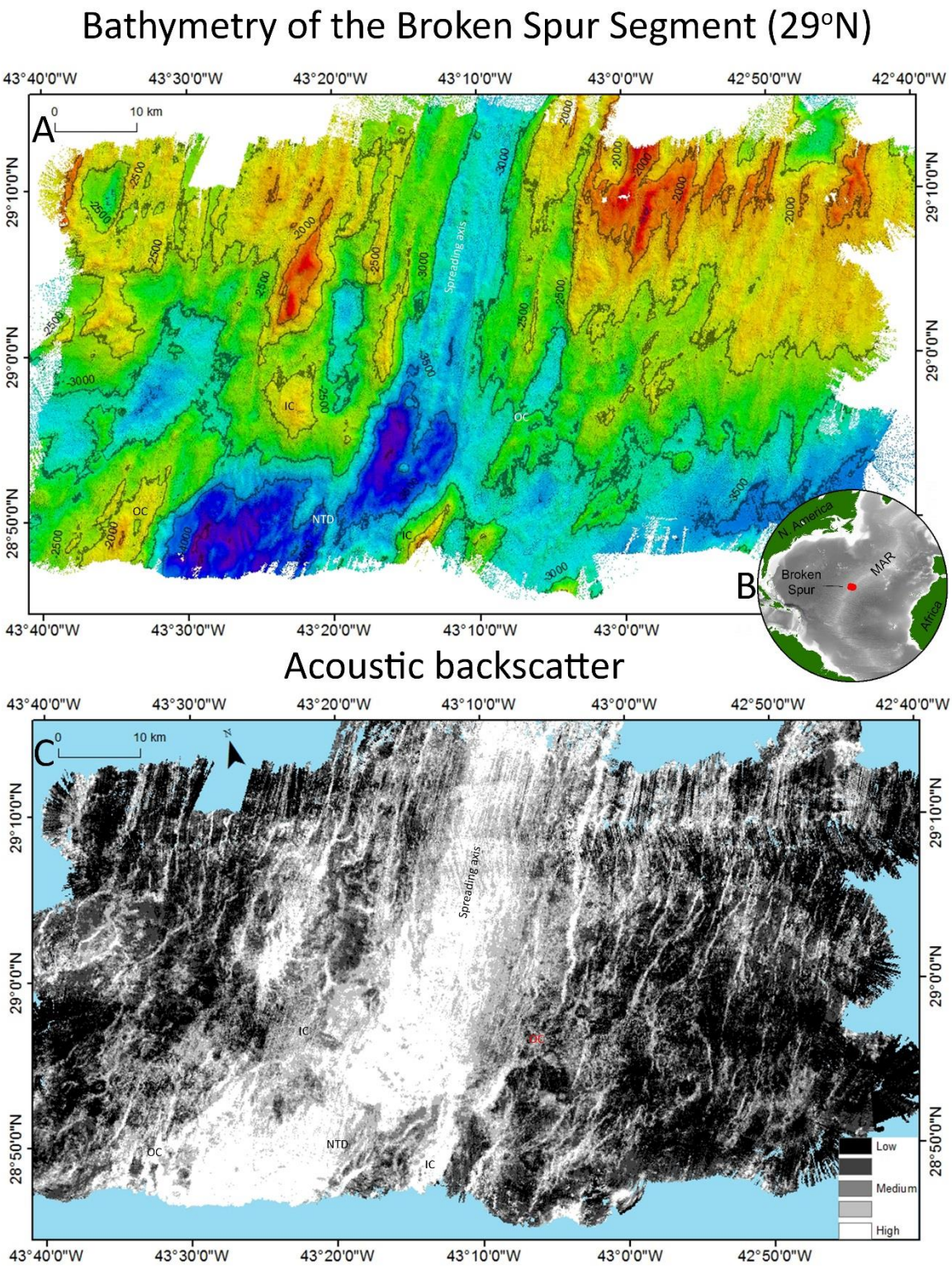

***Figure 3.1**: **A**: 50 m grid of bathymetry from ship board multibeam echosounder with 500 m contours. **B**: (inset) Location of the Broken Spur segment along the MAR (red dot). **C**: Multibeam backscatter intensity (bright is high), statistically grouped into quantiles. The high backscatter area in the centre of the segment indicates the youngest seafloor. NTD = non-transform discontinuity, OC = Outside Corner, IC = Inside Corner.*

The Broken Spur segment has been well studied. Previous work identified the segment as being 62 km long and bound by second order non-transform discontinuities (NTDs) at 28°51' N and 29°23' N (Sempéré et al., 1993). This indicates the Broken Spur segment is a second order feature, and is typical of the Mid-Atlantic Ridge and slow spreading ridges in general. In bathymetric profiles drawn perpendicular to the spreading ridge axis, the segment appears asymmetric with a shallower and steeper eastern axial valley wall (Sempéré et al., 1993) (Figure 3.1A). The segment has a narrow and deep rift valley producing a V-shaped cross-sectional profile and an hour-glass shape in plan-view. The axial valley's mid-point (29°04' N) narrows to a width of 5 km and shoals to a depth of 3200 m (Sempéré et al., 1993). This large scale morphology, and the association of the segment centre with a circular negative mantle Bouguer anomaly (i.e. lower density), resulted in Sempéré et al., (1993) suggesting that the Broken Spur segment is characterised by melt supply from the mantle focused towards the segment centre.

Other studies focused on the segment's tectonic activity. Wolfe et al., (1995) measured micro-seismicity and identified two foci of tectonic activity, one at the segment's southern end and the other at the segment centre. Inversion of travel times for seismic velocity structure revealed thin crust at the southern end of the segment, at its Inside Corner, consistent with the residual mantle Bouguer anomalies (RMBA) (Lin et al., 1990). At the segment's southern end, the micro-earthquakes' hypocentres indicate slip along steep, high-angle (~45°) fault planes that are oriented ~20° counter-clockwise from the trend of the axial valley. This indicates an element of shear induced rotation of the stress tensors towards the south of the segment, consistent with sinistral slip at the NTD. The second hypocentre focus, at the segment centre, is thought to originate from volcanic and hydrothermal processes within a thick magmatic crust.

Smith et al., (1995) mapped the segment using side-scan sonar and identified a symmetrical ridge of hummocky lava flows within the axial valley that forms an axial volcanic ridge (AVR) and, elsewhere, a seamount

density of 110 per 10^3 km^2. In general, the AVR is a few kilometres wide, 150 m high, trends 013° ±5°, and includes scattered hummocky seamounts along its length, the tallest being 350 m (Sempéré et al., 1993; Smith et al., 1995). Outside of the AVR, the seamounts have smoother tops and lower aspect ratios (i.e. height/width) indicative of higher effusion rates.

Rommevaux et al., (1994) compared bathymetry depth to gravity anomalies in the south of the Broken Spur segment (28° N – 29° N). They used gravity to determine the positions of spreading centres, Inside Corner, and Outside Corner. The Inside Corner and Outside Corner were described in Chapter 1. As a summary, an Inside Corner is a broad shallow region between two active plate boundaries at Mid-Ocean Ridges. One plate margin is a transform zone or NTD at a segment's end and the other is the spreading axis where crust is being created. An Outside Corner is positioned opposite to an Inside Corner; between the spreading axis and the inactive transform zone or NTD. An Outside Corner is not as shallow or tectonised as an Inside Corner (Tucholke & Lin, 1994). Rommevaux et al., (1994) results found that the spreading centre had low RMBA (-40 – -10 mGal), and RMBA was higher (-15 – 0 mGal) at the Inside Corner than the Outside Corner, indicating the Inside Corner has thinner crust. Rommevaux et al., (1994) also found that the axis was asymmetric with thinner crust on the N. American plate.

Tectonic extension at the Broken Spur segment was previously studied by Escartin et al., (1999) using 6 m resolution side-scan sonar (Figure 3.2A and B), in which strong linear reflectors were interpreted as faults, and 100 m resolution swath bathymetry. They identified three measures of tectonic extension: the average heave along profiles oriented perpendicular to the ridge axis; the slopes of cumulative heave profiles; and the cumulative fault heave divided by the profiles' length. Escartin et al., (1999)'s profiles measure heave and its derivatives from the spreading axis outwards. In addition, Escartin et al., (1999) also measured fault spacing using the distance between the centre of each fault and, secondly, the length of each profile divided by the number of faults along the profile.

Escartin et al., (1999) aimed to determine whether the crustal thickness changes between the segment's ends (primarily the Inside Corner and Outside Corner) and the Segment Centre were reflected in changes in the heave and spacing of faults. Segment Centres are typically broad shallow regions, located near the geographical centre of the segment, with an abundance of volcanic features and a thick mafic crust which forms above focused magmatism. Escartin et al., (1999) concluded that the side of the axial valley on the N. American Plate expressed 50% more tectonic extension than that on the Eurasian Plate. That tectonic extension, as expressed on the axial valley wall faults, is relatively constant along axis and asymmetric across axis, with the N. American Plate having 15% extension whereas the Eurasian Plate has only 7% extension. In general, averaged over the entire area, they found that 10% of the seafloor was generated through brittle tectonic extension and 90% by volcanic or magmatic accretion.

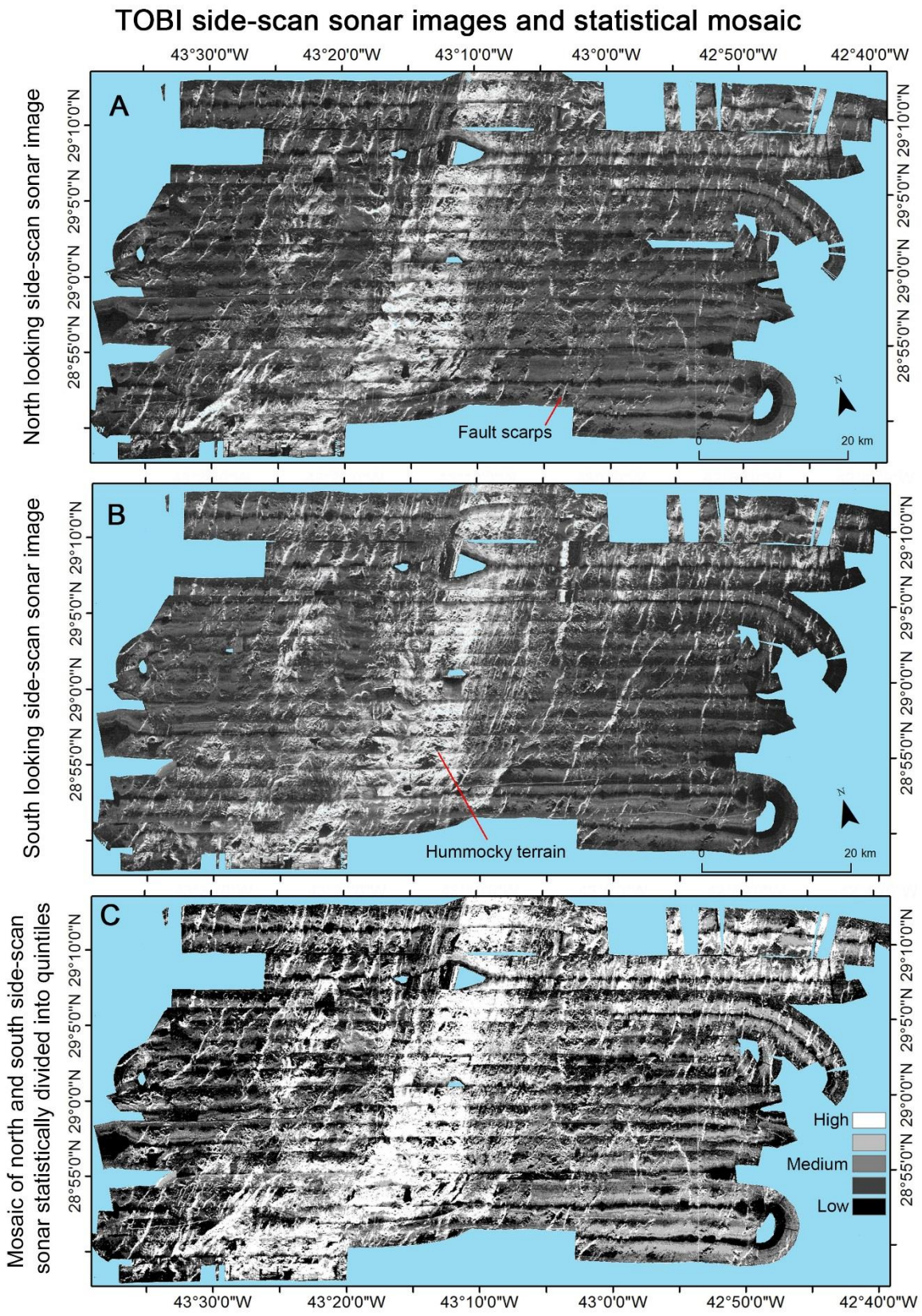

***Figure 3.2**: 30 kHz, TOBI Side-scan sonar GeoTIFFs, low intensity is presented as black (from Escartin et al., 1999): **A**: North facing side-scan sonar image. Linear features with high values were interpreted as fault scarps (Escartin et al., 1999; Searle et al., 1998; Smith et al., 1995). **B**:*

South facing side-scan sonar image. Hummocky terrain was interpreted as pillow lava domes along the spreading axis (Searle et al., 1998). ***C****: mosaicked north and south looking side-scan sonar using highest value within each grid cell so that all strong reflectors that are potential faults were incorporated into the final mosaic side-scan sonar map. Values are statistically grouped into quintiles. Upper most quintile is selected as a fault.*

A study by Paulatto et al. (2015) investigated the variation in faulting and magmatic input along four second order segments separated by non-transform discontinuities between 35°40'N and 36°40'N. These segments, from north to south, are AMAR, AMAR Minor N, AMAR Minor S, and S. AMAR (the Broken Spur segment). Being so proximal to my study area and having a similar geological setting, their findings should be similar to what I expect to find. In their study, faults were identified using an automatic edge detecting algorithm as discussed in Chapter 1.6. Paulatto et al., (2015) found that faults at the centre of the segments were small and closely spaced. Towards the inside corners faults are less steep with larger throws and larger spacing. They found there is a discrepancy of a few degrees between fault orientation and the azimuth of the spreading axis suggesting that shear is not entirely taken up at the NTDs resulting in some oblique spreading. This discrepancy is larger towards the segment ends and could affect the slope direction criteria of the FID if obliquity causes faults to face greater than 22.5° either side of perpendicular to the spreading axis.

Paulattos et al., (2015) measured extensions in the same way as Escartin et al., (1999) did, cumulative fault heave divided by profile length (16 km). They calculated extension as 20% to 30% for the S. AMAR and AMAR segments, 40% for the AMAR Minor S and AMAR Minor N segments. The non-transform discontinuity near the Rainbow vents recorded extension between 60% – 70%. They found asymmetric extension between the plates, with inside corners reaching almost 100% extension near the Rainbow Oceanic Core Complex. They generally found a strong correlation between high RMBA and high tectonic extension, suggesting that along axis morphology was linked to along axis melt supply. However, this is not always the case as the S. AMAR NTD has a high RMBA indicating thinner crust but no change in seabed morphology or their measure of extension.

My analysis of brittle extension and magmatism at the Broken Spur segment comprises several components: (i) using my FID method to measure faults (ii) compare the fault map to the published, manual, interpretation of seafloor faulting by Escartin et al., (1999) to test the effectiveness of the automatic FID technique. (iii) Calculate the Residual Topography Anomaly (RTA) and compared it with the published Residual Mantle Bouguer Anomaly (RMBA) map to confirm if RTA is a useful indicator for crustal thickness as determined by RMBA. (iv) Measure tectonic extension to compare with the estimates of crustal thickness provided by RTA and RMBA to test for coherency in the signal from melt focusing, melt supply, and brittle stretching of the crust.

3.2 Results

3.2.1 Overview of bathymetry and side-scan sonar data sets.

Bathymetry data was collected using a SIMRAD EM12 multibeam echo-sounder (Searle, 1996). The multibeam soundings were processed in CARIS™ by removing spikes and stray beams manually; no filters were applied. The cleaned data was gridded at 50 m into a bathymetry map (Figure 3.1A) and a multibeam backscatter map (Figure 3.1B).

The 30 kHz side-scan sonar attached to a Towed Ocean Bottom Instrument (TOBI) was towed along east – west lines, 2 km apart and up to 35 km off-axis (Searle, 1996). The side-scan sonar had a scan width of 6 km and operated 400 – 600 m from the seafloor. It consisted of two parallel 30 kHz transducers, each mounted on either side of the TOBI vehicle, with a downward inclination of 20° from horizontal generating a north and south looking image separated by a nadir. The 2 km spacing and parallel orientation of the survey lines ensured the study area was fully covered by each of the port and starboard transducers of the side-scan sonar, with only minor gaps and nadir. The result are both north (Figure 3.2A) and south (Figure 3.2B) looking side-scan sonar images. The original processed GeoTIFF files of the side-scan sonar images were used and

georeferenced to topographic features identifiable in both side-scan sonar images and the bathymetry. The north and south looking side-scan sonar maps were mosaicked, preserving the highest value within each grid cell. The mosaicking ensured that potential faults could be identified from the north and south looking data within one map. The resulting image was then statically grouped into quintiles (Figure 3.2C) so that high backscatter was statistically defined and not subjectively defined, as in Escartin et al., (1999).

3.2.2 Bathymetric features

The multibeam bathymetry data for the area reveal broad differences that are used to subdivide the area into domains considered to have geological significance (Figure 3.3). The study area has broad shallow bathymetric features that typically extended over >25 km^2 and are elongated along the strike of the spreading axis (Figure 3.3 red outlines). These shallow regions reside at a mean depth of 2230 m and extend from 1890 – 2630 m depth and predominantly occur in the north, centred along latitude 29°8' N. Another large domain type identified from the bathymetry are basins (Figure 3.3 blue outlines), defined as enclosed deeps, ranging from 3150 – 3605 m, and which cover a broad region, typically >25 km^2. The basin regions have a mean depth of 3410 m and morphologically have a flat base. These deep features are concentrated in the south, along 28°51' N.

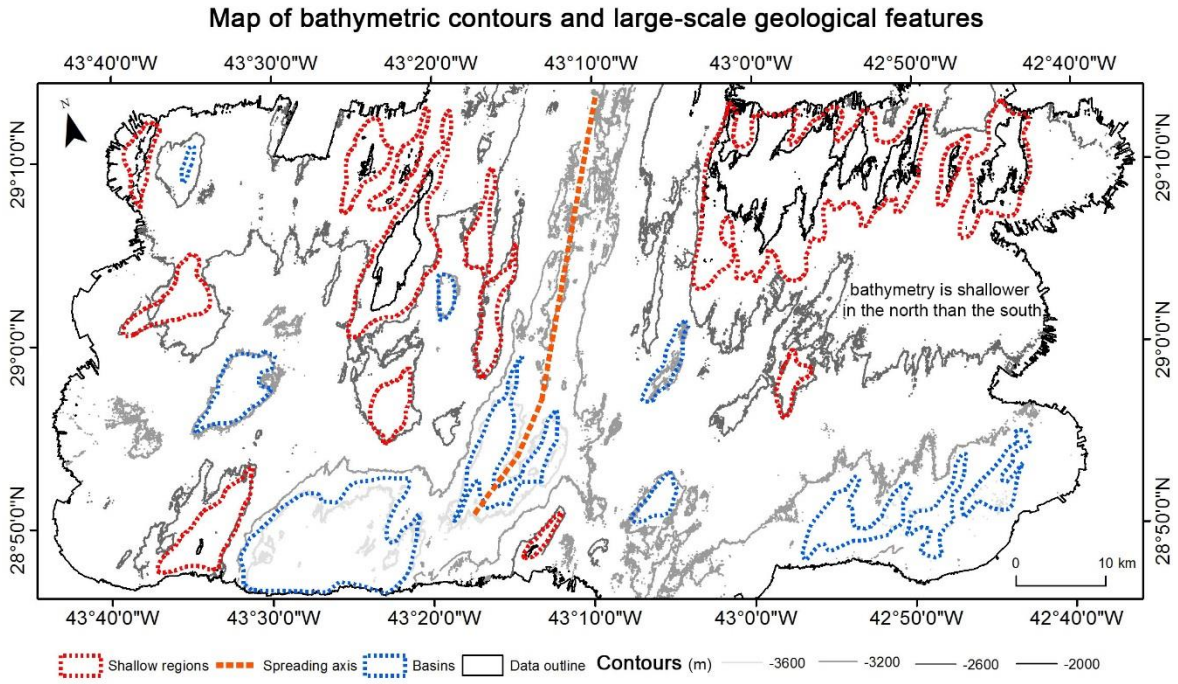

***Figure 3.3**: Geological map identifying the broad bathymetric domains at the Broken Spur segment. These include shallow regions (red), basin regions (blue), and the spreading axis (orange).*

The single largest volcanic feature identified is the Axial Volcanic Ridge (AVR), defined from bathymetry, not side-scan sonar. This is formed from a series of symmetrical bathymetric ridges in the centre of the axial valley and together define the AVR. The AVR is 43 km long, between 29˚14' N - 28˚53' N (Figure 3.4 profile D), has an orientation of 031˚, a width ranging between 1480 – 3660 m, and height between 225 - 320 m. The AVR is located along the bottom of a 1000 – 600 m deep axial valley, flanked by inward facing axial valley wall faults (Figure 3.4 profiles A - C). The AVR itself has a hummocky morphology (Figure 3.4 profile D), indicative of multiple eruptive features formed from fresh lava flows centred along the spreading axis producing pillow lava mounds (Smith et al., 1995).

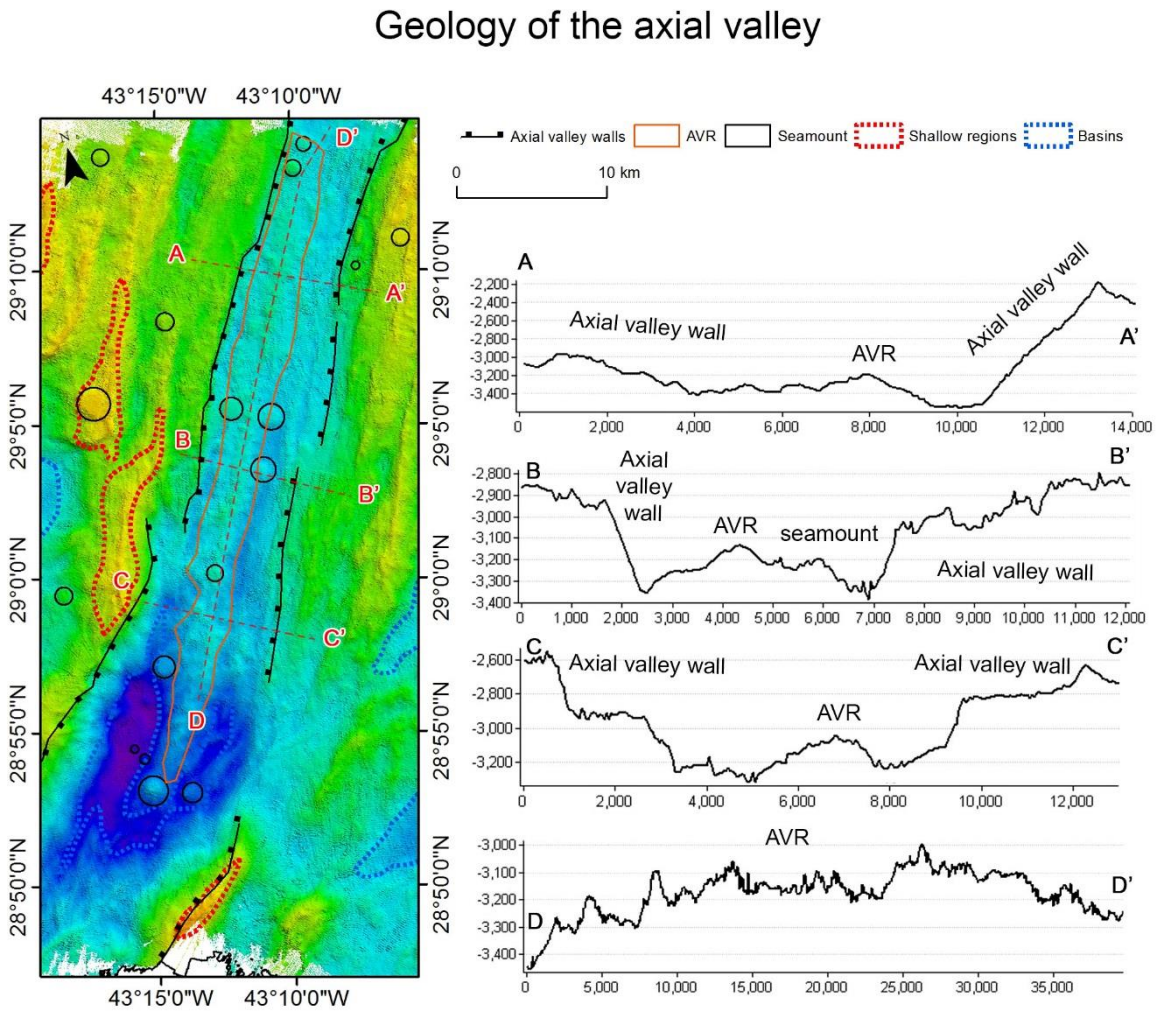

***Figure 3.4**: Geological map of the axial valley, AVR, and spreading axis. Profiles A – C illustrate the morphology of the deep axial valley with the AVR at its centre. Profile D illustrates the rugged morphology of the AVR following the spreading axis.*

The axial valley wall faults (Figure 3.4 and 3.9) located north of 29˚ N, are orientated ~028˚. With increasing distance south of 29˚ N, their orientations rotate clockwise and gradually become more northeast – southwest, reaching a mean of ~061˚ at 28˚50' N. The spreading axis is located in the axial valley and coincides with the AVR and most recent volcanics as shown by the acoustic high backscatter and side-scan sonar intensities (Figure 3.6). The spreading axis at the AVR trends 031˚ and, like the axial valley faults, rotates clockwise further south to 046˚ approaching the NTD where no AVR is visible.

The next largest volcanic features identified are seamounts, identified as circular features greater than 400 m in diameter, with a mean diameter of 1180 m (range: 480 - 2390 m) and mean height of 240 m (range: 115 - 420 m). The identified seamounts coincide with those described in Sempéré et al., (1993) and Smith et al., (1995).

3.2.3 Fault identification

Seafloor normal faults were identified using the FID method described in Chapter 2. Within this Chapter, the FID method cross-correlates four criteria for the parameters; slope direction perpendicular to the strike of the spreading axis (078.5° – 121.5° and 258.5° – 303.5°, Figure 3.5A); slope angle between 35 - 60° (Thatcher & Hill, 1995) (Figure 3.5B); side-scan sonar intensity in the upper most quintile (Figure 3.6A); and multibeam backscatter in the upper most quintile (Figure 3.6B).

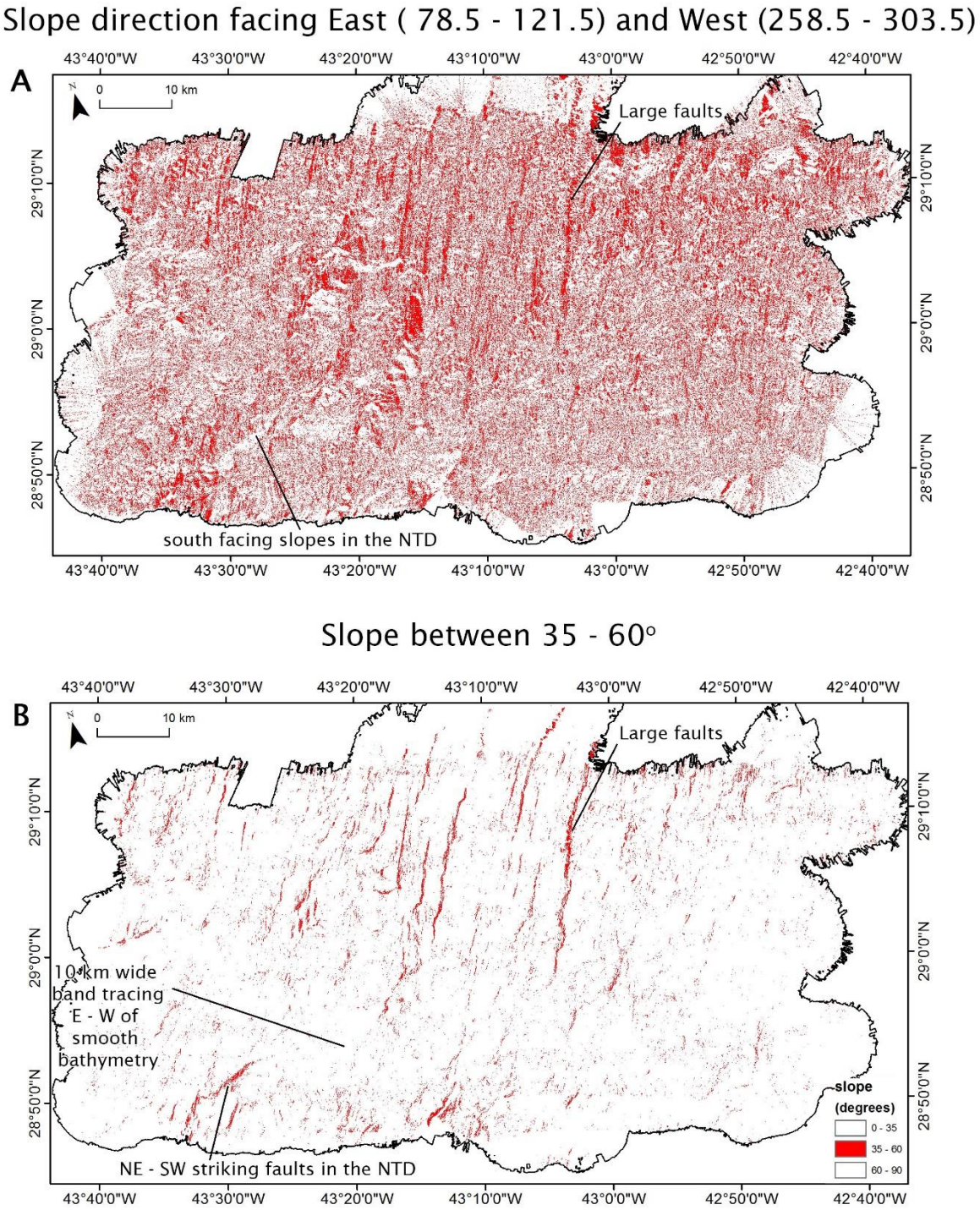

***Figure 3.5**: Maps of parameters used for the FID map. **A**: slope direction map where all slopes facing perpendicular to the trend of the spreading axis are given a value of 1. **B**: slope angles that are between 35 - 60˚ meet the criteria of a fault and are given a value of 1.*

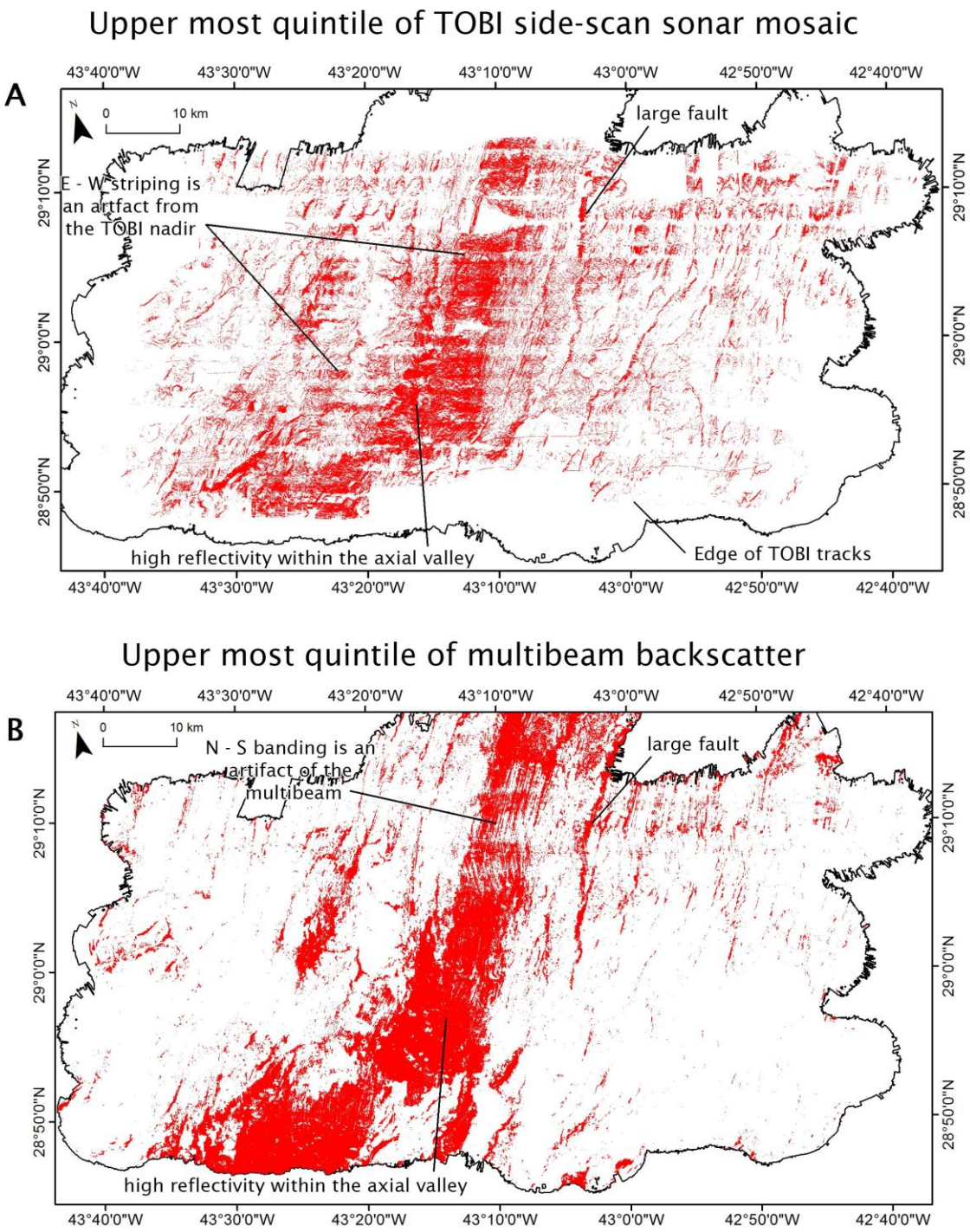

[GH2]

Figure 3.6: *Maps of parameters used for the FID map.* ***A****: Mosaic of north and south looking side-scan sonar where acoustic reflections in the upper most quintile are given a value of 0.5.* ***B****: Multibeam backscatter map where acoustic reflections in the upper most quintile are given a value of 0.5.*

The parameter for slope direction (Figure 3.5A) was met by 28% of the bathymetry. This produced a speckled signal over the study area resulting from the ruggedness of the seafloor. This parameter highlighted continuous fault scarps facing towards the spreading axis, mostly north of 29°00' N. South of 29°00' N, fewer slopes meet the parameter, most noticeably around 28°52' N between 43°31' W and 43°20' W. This region of fewer east - west facing slopes occurs in line with the non-transform discontinuity (NTD).

The parameter for slope angle (Figure 3.5B) was met in only 3% of the area. The slope parameter map highlights long, north – south trending, faults at the axial valley walls and within ~15 km either side of the spreading axis. Along 28°50' N, coincident with the NTD, there are multiple steep slopes identified orientated NE - SW. There is also an east – west oriented, ~10 km wide band extending along 28°55' N where the slope parameter is not met.

The side-scan sonar parameter for faulting was met by 20% (Figure 3.6A) of the study area. Almost all the seafloor within 6 km of the spreading axis has reflectivity within the upper most quintile making it difficult to distinguish faults. This is similar to the 7-8 km off-axis plateauing of reflecting noted by Eason et al, (2016) when using multibeam backscatter to identify faults along the MAR between 35°45'N - 36°35'N.

Although the combined north and south looking side-scan images are effectively nadir free, some high reflectivity artefacts and signals from within the NTD remain that skewed the fault identification. In places, high intensity side-scan sonar intensities from further off-axis also met the fault identification parameter, highlighting numerus north – south trending lineations that are identified as faults.

The parameter for multibeam backscatter was met by 16% of the seafloor (Figure 3.6B). Similar to the side-scan sonar, almost all the seafloor within 6 km of the spreading axis met the fault criteria. The NTD also had reflectivity mostly in the upper most quintile. Backscatter values

meeting the fault criteria became scarce beyond 20 km off-axis, particularly south of latitude 29°00' N. Backscatter values within the fault parameter identified multiple north – south trending linear features in the shallow ridge flank regions and within the Inside Corner, the largest being 20 km long and ~1.3 km wide. There is also a region of high backscatter identified around longitude 43°25' W and latitude 29°00' N – 29°09' N.

Side-scan sonar and multibeam backscatter identify similar seafloor attributes to provide similar results. To combine these four fault criteria into an FID map that is not biased towards acoustic reflectivity, three combinations of criteria were tested (Figure 3.7). The map that had the largest coverage and was most able to produce FID values that related to faults (values 2 – 3) was selected.

Firstly, side-scan sonar, slope, and slope direction were given a value of 1 each and summed into a FID map (Figure 3.7A), making them equally weighted. This reduced the study area extent to that of the TOBI tracks and produced a 5 km band either side of the spreading axis of values 2. A broad region of value 2 is unhelpful for precisely identifying faults. This 10 km wide value 2 band was created by summing slope direction and side-scan sonar.

Secondly, multibeam backscatter, slope, and slope direction were equally weighted and summed (Figure 3.7B). This FID map has a larger extent than the previous one by including all the bathymetry data coverage. This map also produces a band of value 2 extending 5 km either side of the spreading axis. This value 2 band was created by the summing of backscatter with slope direction. The backscatter produced few FID values to identify faults past 20 km off-axis on either Plate.

Finally, backscatter and side-scan sonar were equally weighted by applying their fault criteria with a value of 0.5. These were combined with slope and slope direction (each with a value up to 1) to create an FID map with combined side-scan sonar and backscatter able to reach a maximum FID value of 1 (Figure 3.7C). This final FID map had full coverage of the bathymetry data's extent. High FID values were found within 5 km of the

spreading axis and the method also identified more faults off-axis than the method that only used backscatter alone. However, it was not as effective off-axis as the FID using only the side-scan sonar intensity and ignoring the multibeam acoustic backscatter.

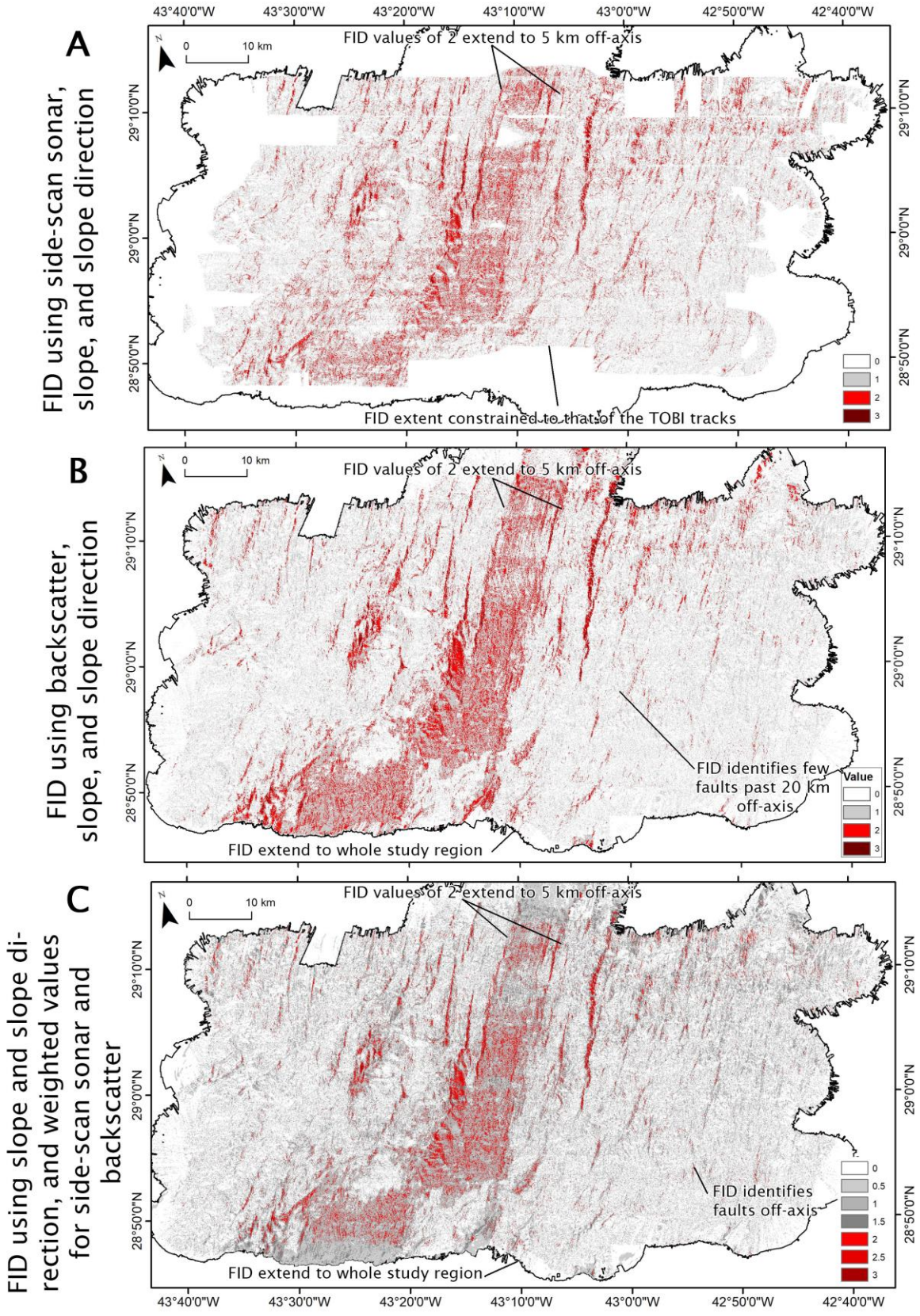

[GH3]

***Figure 3.7**: Testing combinations of backscatter and side-scan sonar for the FID map. **A**: FID map using side-scan sonar, slope, and slope direction, each parameter is given a value of 1. **B**: FID map using multibeam*

*backscatter, slope, and slope direction, each parameter is given a value of 1. **C**: The FID map using a combination of side-scan sonar and backscatter, each with a value of 0.5, with slope and slope direction, each with a value of 1. Map C was used for identifying faults.*

The FID map that weighted equally for backscatter and side-scan sonar (Figure 3.7C) was used to identify faults using the method described in Section 2.1.1. This map did not identify high FID values as far off-axis as the map only using side-scan sonar (Figure 3.7A), however this was compensated for with larger coverage. The FID method identified a high abundance of faults within 20 km of the spreading axis, beyond which the frequency of fault picks reduces. The largest faults are located close the axial valley. Faults are more numerus north of latitude 29°00' N, coincident with the shallower regions. There are also clusters of faults identified around 29°02' N; 43°25'W (Figure 3.17), and 28°50' N; 43°30' W (Figure 3.11).

The high FID values within the axial valley results from high intensity backscattering of side-scan sonar and multibeam sonar off the AVR and its hummocky morphology within the axial valley (Figure 3.6), providing a value of 1 (Figure 3.4 profile D). Additionally, the AVR's erratic slope directions interfere with the slope direction parameter of the FID map (Figure 3.5A), providing a value of 1. The combination of these two parameters results in the axial valley being populated with frequent and often isolated FID values of 2, making fault identification difficult.

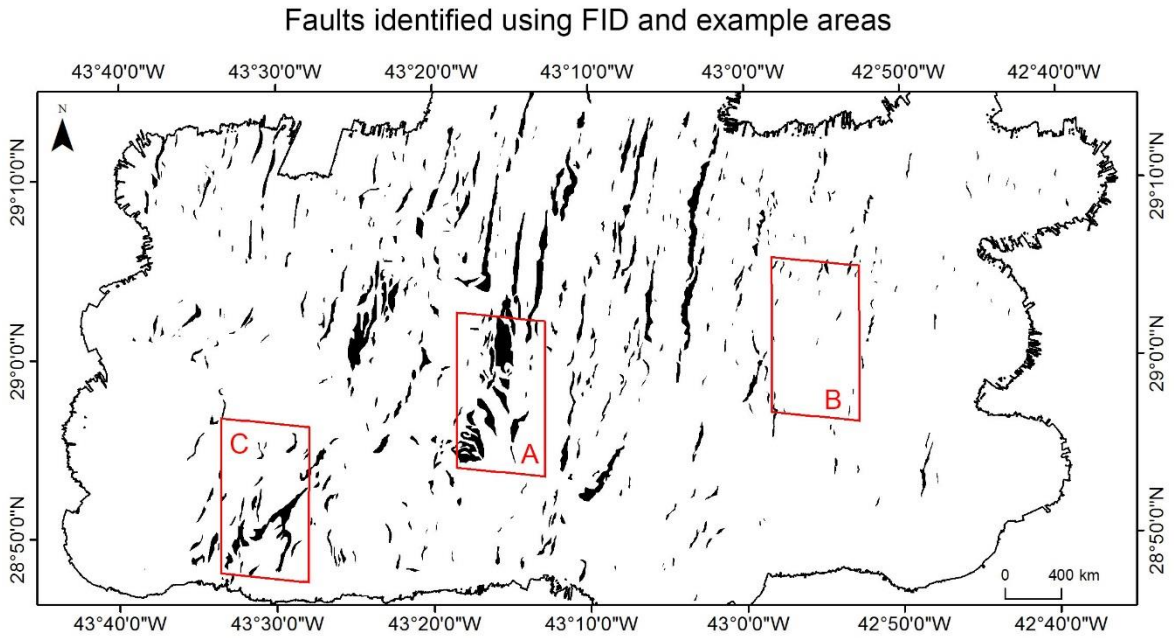

***Figure 3.8**: Fault map using the FID map with equally weighted backscatter and side-scan sonar (Figure 3.7C). Fault extents were manually drawn around FID values ≥2. Study sites A, B, and C illustrate how the FID map was influenced in various locations and how this effected fault identification. Box A spans the axial valley wall fault and includes the spreading axis. Box B is >20 km off-axis, where few faults were identified. Box C is located at the NTD where east – west shear influences fault strikes.*

Extracting the area of each fault polygon's (Figure 3.8) FID parameters (Figure 3.5 and 3.6) identifies what percentage of each attribute was incorporated into the faults (Table 3.1). This helps identify which parameters mostly contributed to fault identification.

Slope direction contributes least to the fault polygons with only 9% (Table 3.1) being incorporated into the final faults. This is because slope direction towards and away from the axis accounts for 28% of the seafloor (Figure 3.5A). Multibeam backscatter contributes 17% and side-scan sonar contributes 13% to the final fault maps. This lower percentage is likely because most of the acoustically reflective seafloor is within the spreading axis where few faults could be seen (Figure 3.6). Slope angle contributes 38% towards the fault polygons, making it the most sensitive parameter.

	Area of fault parameters (km^2)	Area of Faults (km^2)	%
slope direction	1712	151	9
multibeam backscatter	1011	168	17
slope angle	182	69	38
side-scan sonar	1287	173	13

Table 3.1*: The percentage area that each fault parameter contributed to the final identified faults using the FID method.*

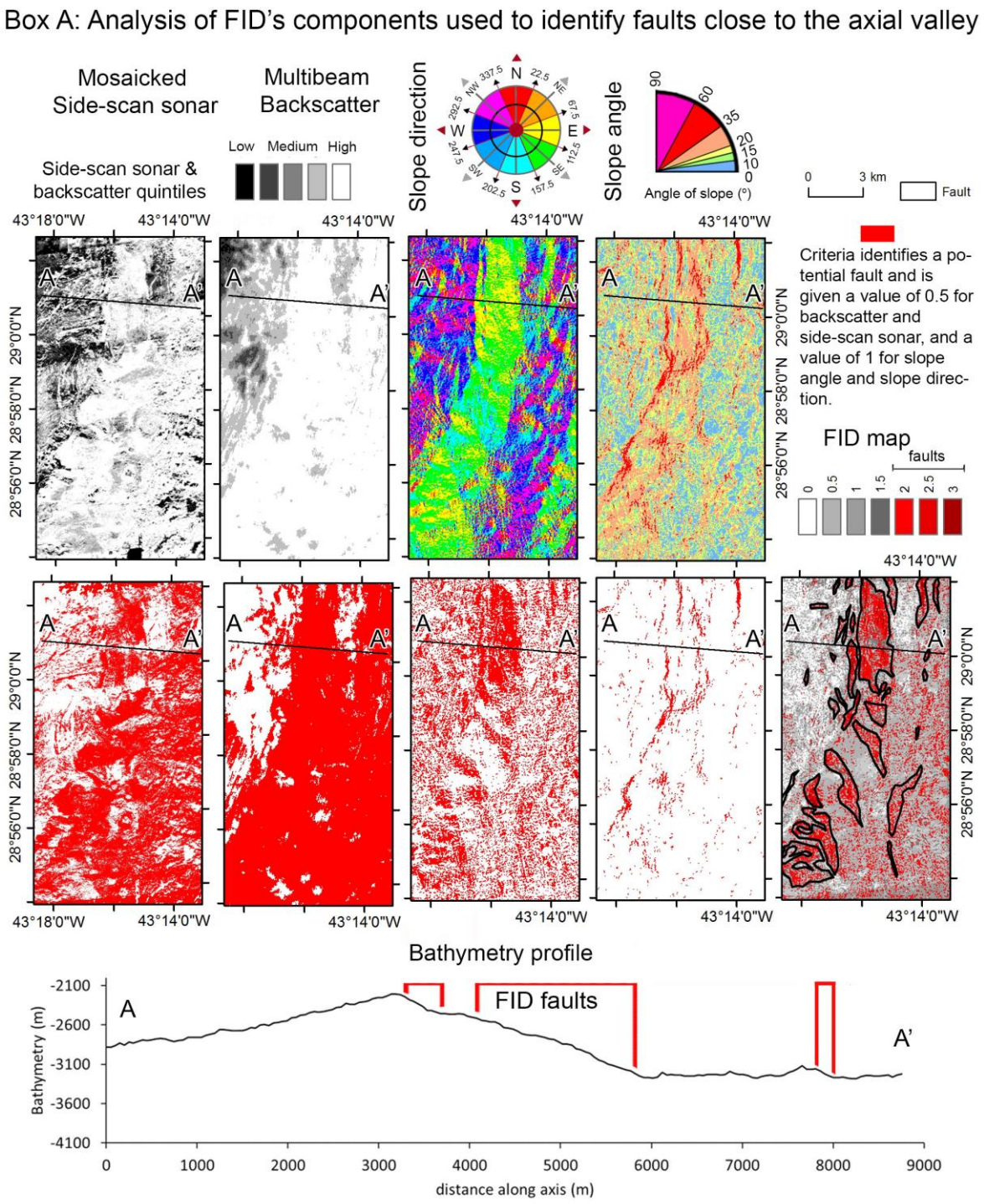

[GH4]

***Figure 3.9**: Study of FID criteria that influence fault extent close to the spreading axis (box A Figure 3.8). Top row are the seafloor attributes used to identify faults and bottom row are where the parameter to indicate a fault was met. The bathymetry profile, A – A', illustrates how well the FID has done to identify fault scarps visible in bathymetry.*

Close to the spreading axis, FID struggles to identify faults because of high intensity acoustic backscatter and side-scan sonar reflectivity dominate the parameter (Figure 3.9). However, it is also likely that faults in the area occupied by the neovolcanic terrain and AVR are poorly developed and often masked by volcanic flows. The FID identifies the axial valley wall faults as steep slopes, especially when the slope direction is facing towards the spreading axis. However, when the slope direction is outside the 45° sector aligned with the direction perpendicular to the spreading axis, the FID does not identify a fault (slope direction panel in Figure 3.9). This results in some large axial valley wall faults being broken-up by the FID and interpreted as several parallel faults (FID panel in Figure 3.9). Despite this, the FID map has reliably identified the top and bottom of the axial valley wall fault (bathymetry profile A – A' in Figure 3.9). The change in the fault's direction occurs with proximity to the NTD.

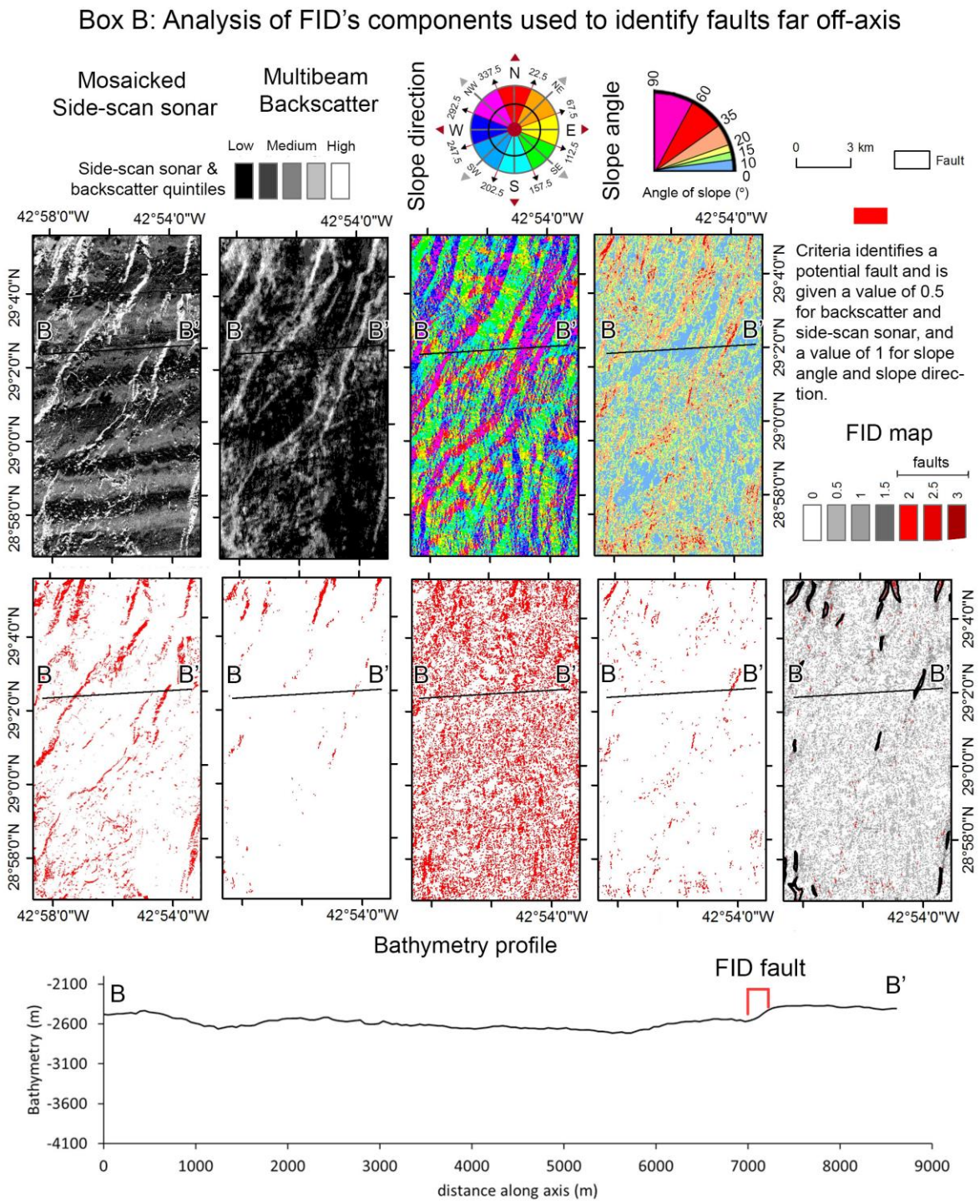

[GH5]

***Figure 3.10**: Study of FID criteria that influence fault extent far from the spreading axis (box B Figure 3.8). Top row are the seafloor attributes used to identify faults and the bottom row are where the parameters to indicate a fault was met. The bathymetry profile, B – B', illustrates how well the FID has done to identify fault scarps visible in bathymetry.*

Far from the spreading axis (>20 km) fewer faults were identified. The FID did not identify many potential faults because of reduced multibeam backscatter intensity and little change in slope (Figure 3.10). Thicker sediment off-axis could create an acoustically absorbent surface and bury fault scarps. Multiple linear reflectors that are potential fault scarps were identified in the side-scan sonar, but because these scarps had relief <120 m over a distance of >300 m they did not create significantly steep linear features to meet the slope or slope direction criteria (reference the side-scan sonar, bathymetry profile, slope, and slope direction panels in Figure 3.10).

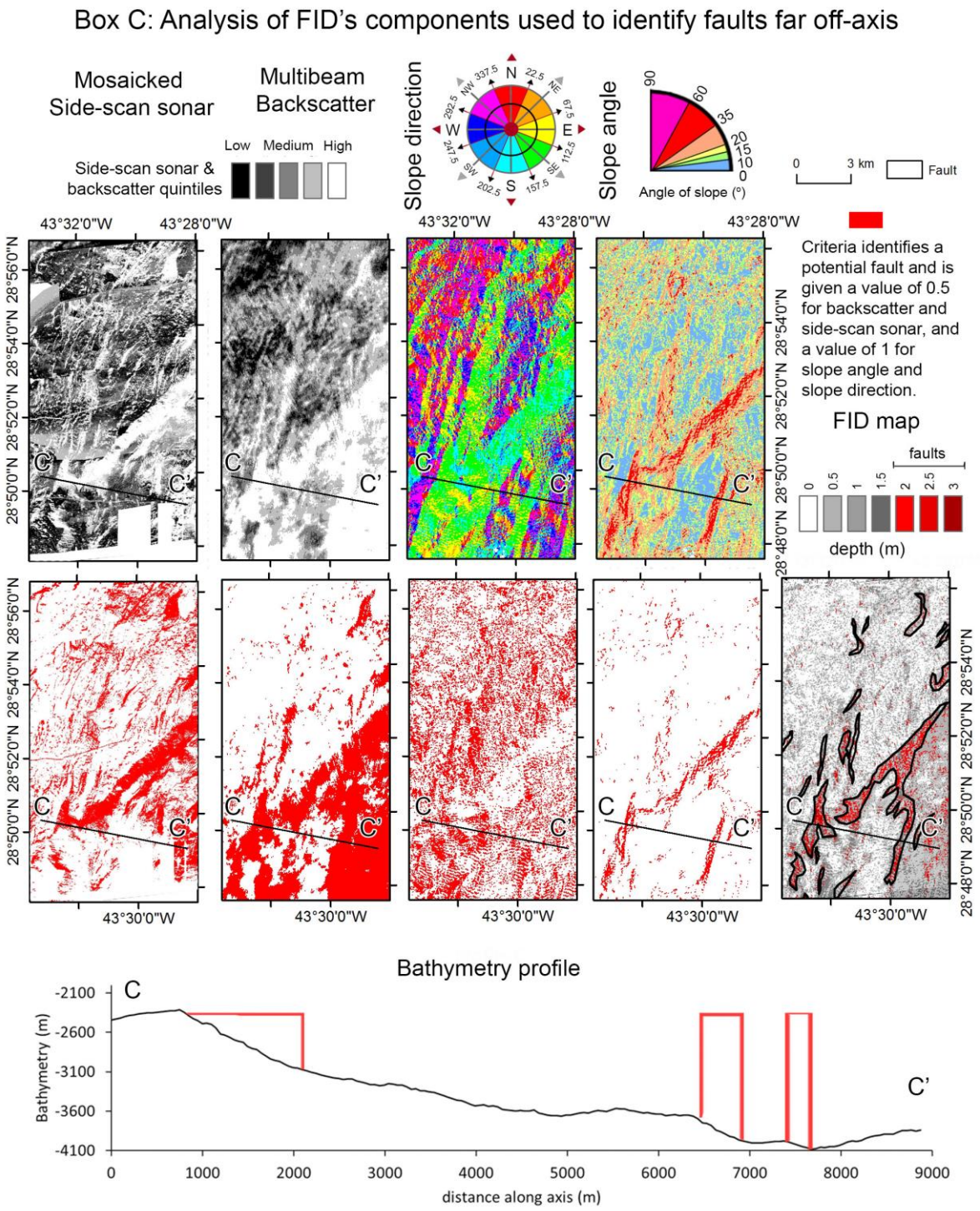

[GH6]

Figure 3.11: *Study of FID parameters that influence fault extent near the NTD (box C Figure 3.8). Top row are the seafloor attributes used to identify faults and bottom row are where the parameters to indicate a fault was met. The bathymetry profile, C – C', illustrates how well the FID has done to identify fault scarps visible in bathymetry.*

Within the NTD, sinistral shear causes fault strikes to rotate clockwise and become more northeast – southwest oriented. This prevents them meeting the criteria for slope direction and reduces the FID value (slope direction panel in Figure 3.11). High backscatter and side-scan sonar reflectivity within the NTD meets the parameters for faults, making individual fault scarps difficult to identify (backscatter and side-scan sonar panels in Figure 3.11). However, the criteria for slope angle is met, allowing for the FID map to identify faults within the NTD and off-axis of the NTD, even though the slope direction parameter was not as reliable. When these FID identified faults are compared to a bathymetry profile they have reliably identified what appears to be steep fault scarps (FID map panel and bathymetry profile C – C' in Figure 3.11).

3.2.4 Measured fault attributes

Fault heave is a measure of horizontal displacement. To measure the variation in fault heave across the study area, heave was measured at 500 m intervals along a fault's strike. This ensures representative measurements of heave from a fault's widest and narrowest points. However, this also results in higher fault frequency (Figure 3.12A) than the actual number of faults identified; which were 473. At the Broken Spur segment heave varies from 50 - 2700 m and is mostly between 100 – 200 m (Figure 3.12A).

As noted in Chapter 2, when studying the effect of bathymetry resolution on fault identification, most faults are smaller than the 50 m grid resolution of the data. This explains why the fault heave frequency rapidly declines for faults with <100 m heave (Figure 3.12A). To estimate how much heave was missed, I calculated an exponential curve for the heave between 100 – 1000 m. The integral of the measured heave between 0 – 1000 m was 501,550 m (Figure 3.12B). While, the integral of the exponential curve was 567,710 m. Suggesting that faults with heaves less than <100 m should provide an extra 61,160 m of heave across all the profiles used to calculate fault heave. This estimates that I am missing 11% of total heave due to the bathymetry's resolution. I calculated how this

may influence T% by calculating 120 E – W profiles spaced at 500 m intervals that extend across the study area. These profiles trace along those used in the T% windows (Figure 3.14). The total length of these profiles was 10,858 km. 4.6% of the profiles' length showed heave, as compared to a predicted 5.2% heave. This suggests that being restricted to a 50 m resolution reduced identified heave by 0.6%. T% is calculated slightly differently, however the principle is similar suggesting that the bathymetry's resolution is potentially reducing T% by 0.6%. Assuming that this unaccounted for heave is evenly spread across the study area, the T% distribution will underestimate brittle extension by 11.5% of the total.

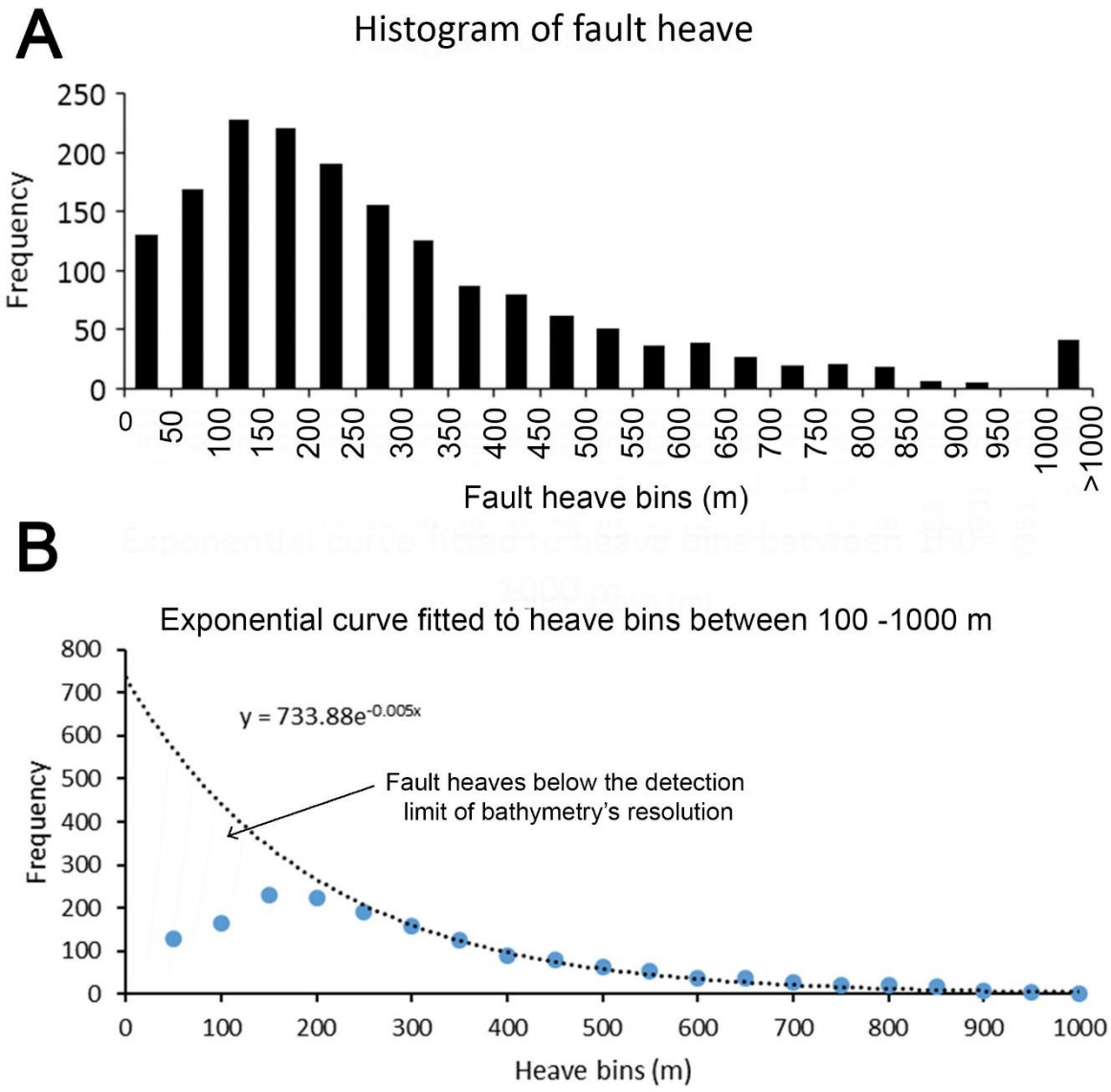

***Figure 3.12**: **A**: Histogram of fault heave in 50 m bins. **B**: exponential curve calculated from fault heaves between 100 – 1000 m to estimate how much heave was missed because of the detectability limit.*

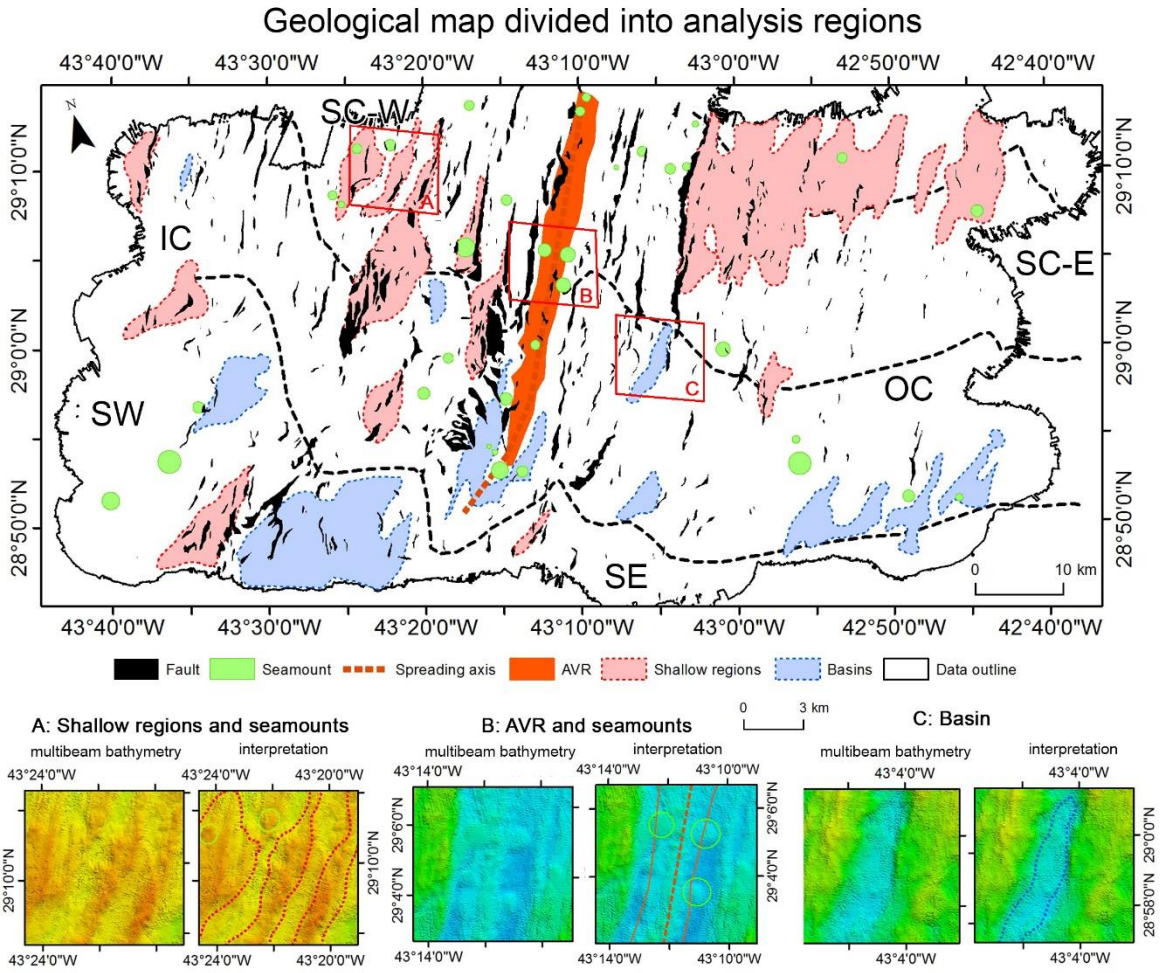

***Figure 3.13**: Geological interpretation of bathymetry (Figure 3.1). Shallow regions and Basins (Figure 3.3) divide the segment along 29˚ N into north and south. The spreading axis and AVR (Figure 3.4) divides the segment into the Eurasian (east) and N. American (west) Plates. Faults were identified using FID values 2 - 3 (Figure 3.7C). The segment is divided into regions for analysis (Escartin et al., 1999); used are the SC-W = spreading centre west, SC-E = spreading centre east, IC = Inside Corner, OC = Outside Corner. I added analysis regions SW = southwest, and SE = southeast.*

The geological features described so far were compiled into a geological map (Figure 3.13) and used to divide the Broken Spur segment into six study regions, with four of them the same as those used by Escartin et al., (1999). The two most north regions are the off-axis relics of the spreading centre on the N. American Plate, the spreading centre west region (SC-W in Figure 3.13), and on the Eurasian Plate, the spreading

centre east region (SC-E in Figure 3.13). These regions are north of 29° N, where bathymetry is generally shallow (Figure 3.13 box A) and aligns with the shallowest point of the AVR (Figure 3.13 box B). The regions of the spreading centre west and spreading centre east are interpreted as the focus of magmatism at the centre of the segment. Two other study regions encompass the Inside Corner and its off-axis trace on the N. American Plate, the inside corner region (IC in Figure 3.13), and the Outside Corner and its off-axis trace on the Eurasian Plate, the outside corner region (OC in Figure 3.13). These study regions are south of 29° N, typically have basins (Figure 3.13 box C) and border the off-axis trace of the relic NTD. The last two study regions are located south of 28°50' N, where the spreading axis is located ~18 km to the west. This indicates the southwest region (SW in Figure 3.13) and southeast region (SE in Figure 3.13) that covers the northern most edge of the next Mid-Atlantic Ridge segment. These six analysis regions based on regional geology will be used to compare mean T%, RTA, and RMBA across the segment to explore the relation between these three diagnostics to the geology.

3.2.5 Measuring tectonic extension

The fault map (Figure 3.8) was used to calculate T% as described in Chapter 2. T% was calculated by the total heave divided by a 20 km long profile orientated towards 112° (perpendicular to the spreading axis orientation). These 20 km long profiles were aligned parallel to others spaced at 500 m intervals to create a window (Figure 3.14). The windows stepped at 5 km intervals in an off-axis direction, 21 windows were used in total. The profiles are cropped to the data extent before T% is calculated. The T% measurement was placed as a point at the centre of each profile. These points where linearly interpolated between to create the T% map (Figure 3.15).

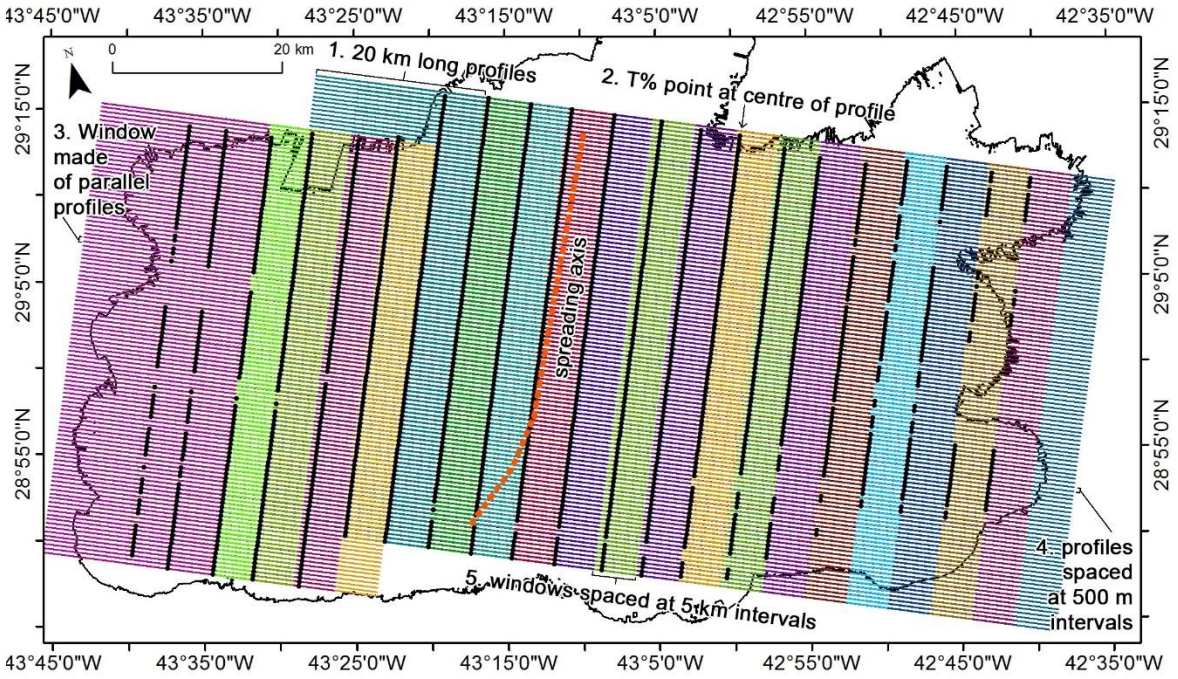

***Figure 3.14**: The profiles and windows used to calculate the T% map. Profiles are orientated perpendicular to the spreading axis, profiles are 20 km long and spaced parallel at 500 m intervals N - S to create a window. Profiles are clipped to the data extent (black outline) before T% is calculated. Each window steps at 5 km intervals E - W. A point is placed at the centre of each profile with the T% measurement.*

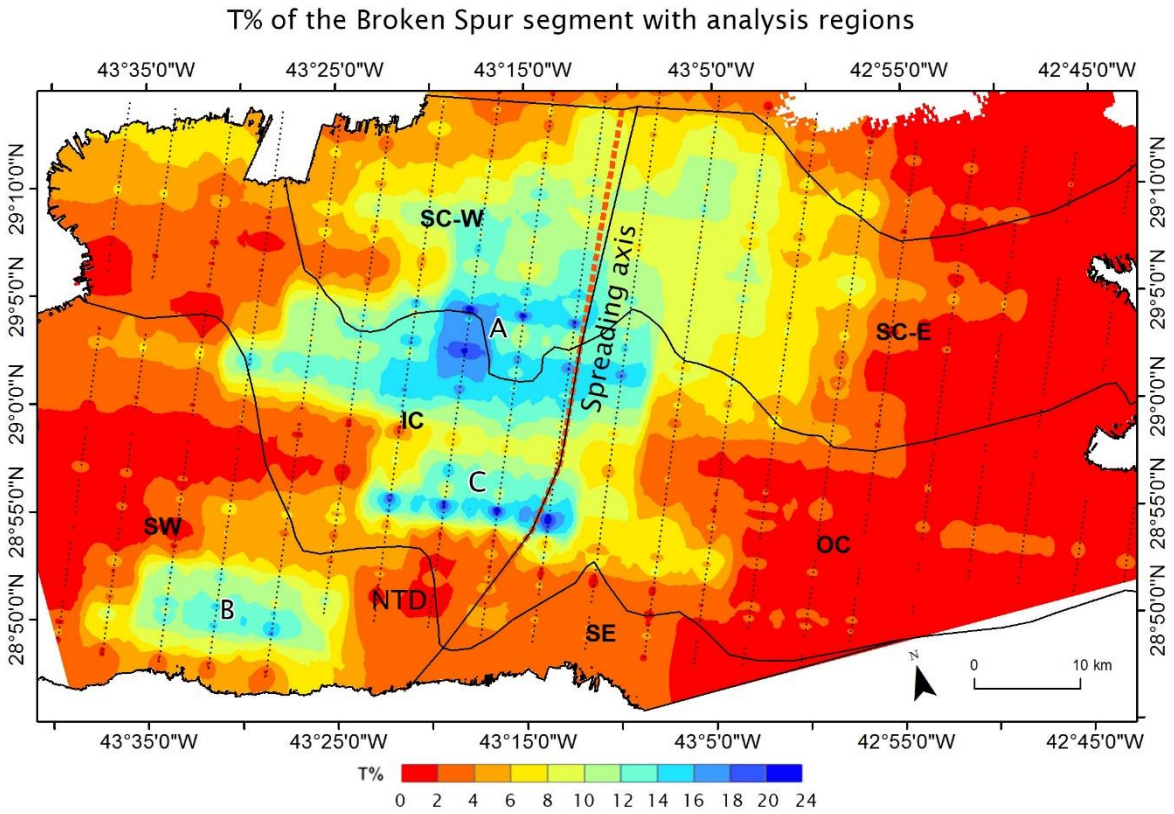

***Figure 3.15**: T% map calculated using the T% profiles (Figure 3.14) with the FID faults (Figure 3.8). Black dots are T% measurements joined by linear interpolation (Figure 3.14). Labels A, B, and C indicate three areas of high T% >10% and studies in Figures 3.21, 3.22, and 3.23.*

Region	mean T%	min T%	max T%
SC-W	8.8	1.9	23.6
SC-E	4.8	0.0	14.8
IC	7.3	0.3	22.9
OC	3.5	0.1	22.2
SW	4.4	0.1	18.9
SE	2.7	0.4	10.0

***Table 3.2**: The mean, minimum, and maximum T% within each of the study regions in Figure 3.15.*

At the segment scale, there is asymmetry in the magnitude and distribution of T% over the N. American Plate (western) compared to the Eurasian Plate (eastern) (Figure 3.15). Within 18 km of the axis in the spreading centre west region and inside corner region, the mean T% is 10±1.2%. While, within 18 km of the axis in the spreading centre west and

outside corner regions, the mean T% is 8±0.9%. After 18 km off-axis, T% reduces, reaching ~4% on the N. American Plate around 32 km off-axis, and on the Eurasian Plate reaching 0% around 32 km off-axis.

As discussed in Chapter 2, sediment thickness increases off-axis making faults harder to identify. This is illustrated by the reduction of backscatter and slope parameter values, used to indicate faults in the FID map, with greater distance off-axis (Figures 3.5 and 3.6). Looking at the segment as a whole, the high T%, >10%, occurs between 43°07' W – 43°22' W and 28°54' N - 29°09' N (areas A and C in Figure 3.15). There in another region of high T% within the southwest region (area B in Figure 3.15).

Patches of high T% (>10%) create three distinct areas. The largest area covers 569 km^2 centred at 43°16' W; 29°3' N ('A' in Figure 3.15). Here, mean T% is at 13±1.4% and reaches a maximum of 24±2.5%. The area is predominantly along the border between the spreading centre west region and the inside corner region, and also encroaches into the spreading centre east region and outside corner region. The second largest area covers 127 km^2 and is centred at 43°31' W; 28°50' N ('B' in Figure 3.15). Here, mean T% is 11±1.2% with a maximum of 19±2%. This area is elongated in an E – W direction and resides within the southwest region. The final high T% area covers 113 km^2 and is centred at 43°17' W; 28°55' N ('C' in Figure 3.15). Here mean T% is 13±1.5% with a maximum of 23±2.5%. This area is elongated in an E – W direction and is mostly located within the inside corner region, and on the boarder of the outside corner region.

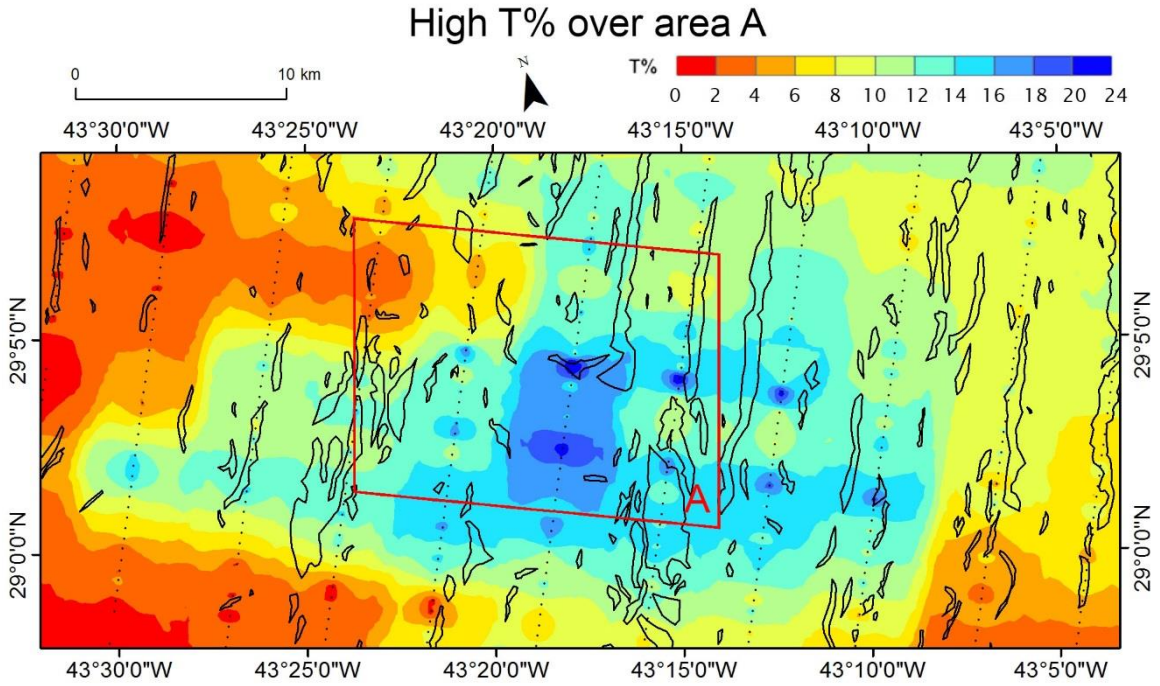

***Figure 3.16**: High T% area A (Figure 3.15) in the spreading centre west and inside corner regions. Faults outlines in black. Red box A is of an oceanic core complex (Figure 3.17). Dots are T% measurements at the centre of 20 km long profiles.*

In the interpretation, T% cannot be attributed to any specific features within a location of less than 10 km east or west of a T% point, marking the centre of a 20 km long T% profile. Therefore, the highest T% will occur within 10 km of high densities of faults. T% is a diagnostic for identifying broad regions of crustal extension over areas >20 km in an E – W direction.

The centre of the high T% area A (Figure 3.16) is located within 10 km of the axial valley wall faults at 43˚15' W, and a cluster of faults at 43˚25' W, indicating these two clusters of features are responsible for the high T%. A study of the axial valley wall faults indicates they typically have high heave and throw (Figure 3.4). The cluster of faults at 43˚25' W is only found at this location (Figure 3.8). It occurs on a shallow region and to the south of a domed bathymetric feature (Figure 3.17A).

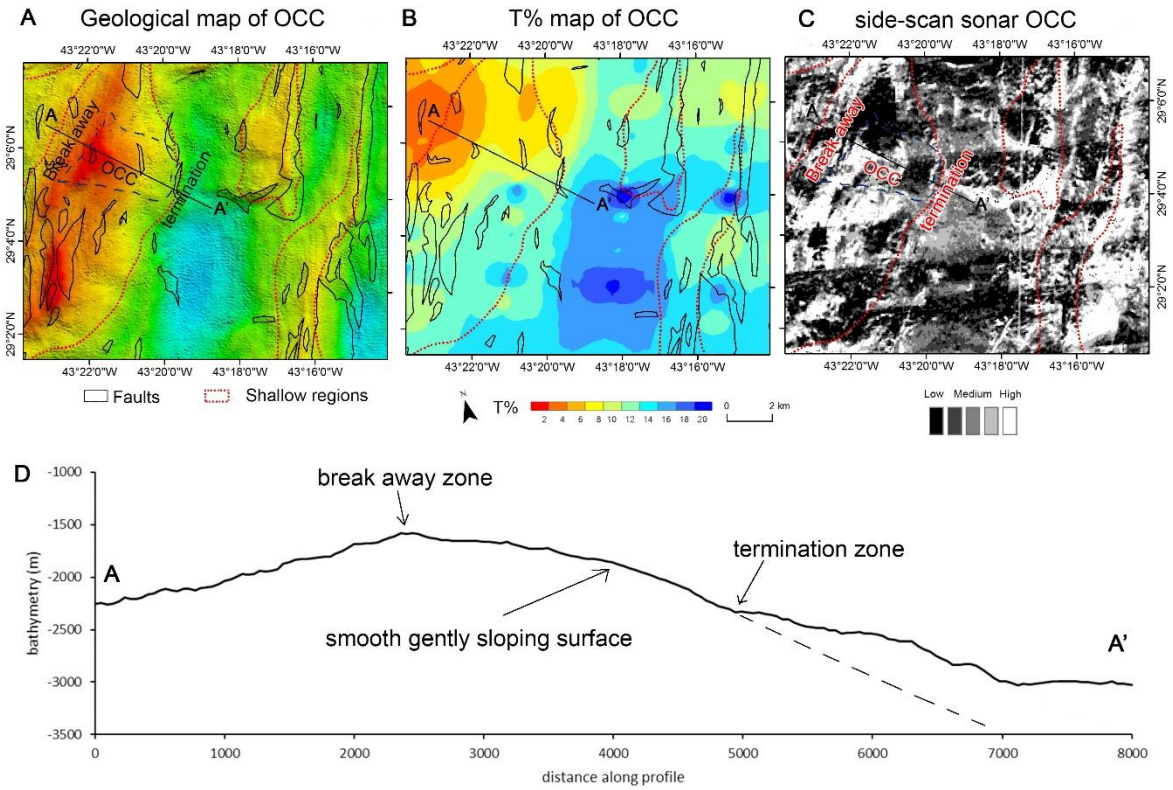

***Figure 3.17**: OCC study (box A in Figure 3.16). **A**: shaded relief of bathymetry with OCC highlighted and geological interpretation. **B**: T% with geological interpretation. **C**: Side-scan sonar with oceanic core complex outline and shallow regions. **D**: Bathymetry profile A - A' across the oceanic core complex interpreted with potential break away zone and termination zone of the detachment fault.*

The cluster of faults contributing to area A's high T% is south of a shallow feature at 29°4'7" N that extends over 295 km^2, is 2 - 3 km wide, and 2.5 km long (profile A - A' Figure 3.17). The feature's eastern face is smooth, and shallowly dips towards the spreading axis, while the top and western face has three ridges interpreted as fault blocks. The shallow region's morphology is similar to that described in Smith et al., (2006, 2008) for off-axis extinct oceanic core complexes along the MAR.

Oceanic core complexes can form as continuous features, with swales and faulted blocks riding on one detachment fault for up to 100 km, or discontinuous where each detachment creates one swale (Smith et al., 2008). The shape of this oceanic core complex (Figure 3.17) suggests it is discontinuous. Oceanic core complexes are typically 15 - 30 km in width and length, meaning that if this feature is an oceanic core complex, it is a

very small one. Oceanic core complexes typically rise several thousand metres high above the surrounding seafloor, the one here rises 1000 m. The breakaway, where the fault initiated, is rotated 15˚ - 20˚, indicative of flexural rotation of the footwall (Smith et al., 2006, 2008). An elongated oval basin 10 - 20 km long forms off-axis of the breakaway at 43˚24' W; 29˚4' N from the same flexural rotation (Cann et al., 2015). The breakaway marks where the detachment fault first initiated and forms a continuous ridge at the highest point of the oceanic core complex, furthest from the spreading axis (Figure 3.17). The termination zone marks where the footwall's fault face emerges from beneath the hanging wall to the seafloor. The distance from the breakaway to the termination zone measures the detachment fault's heave as ~2.5 km.

The detachment fault's shallow dipping surface (Figure 3.17D) and low acoustic reflectivity (Figure 3.17C) has not been identified as a fault, and so has not contributed to the T% calculation (Figure 3.17B). If the detachment fault's ~2.5 km of heave had been correctly identified, it would have potentially provided an additional 12.5% of T%, raising the region within 10 km of the oceanic core complex to 22±2.5%. This oceanic core complex formed within the spreading centre west region, however oceanic core complexes are commonly found at inside corner regions (Dick et al., 1981; Karson & Dick, 1983).

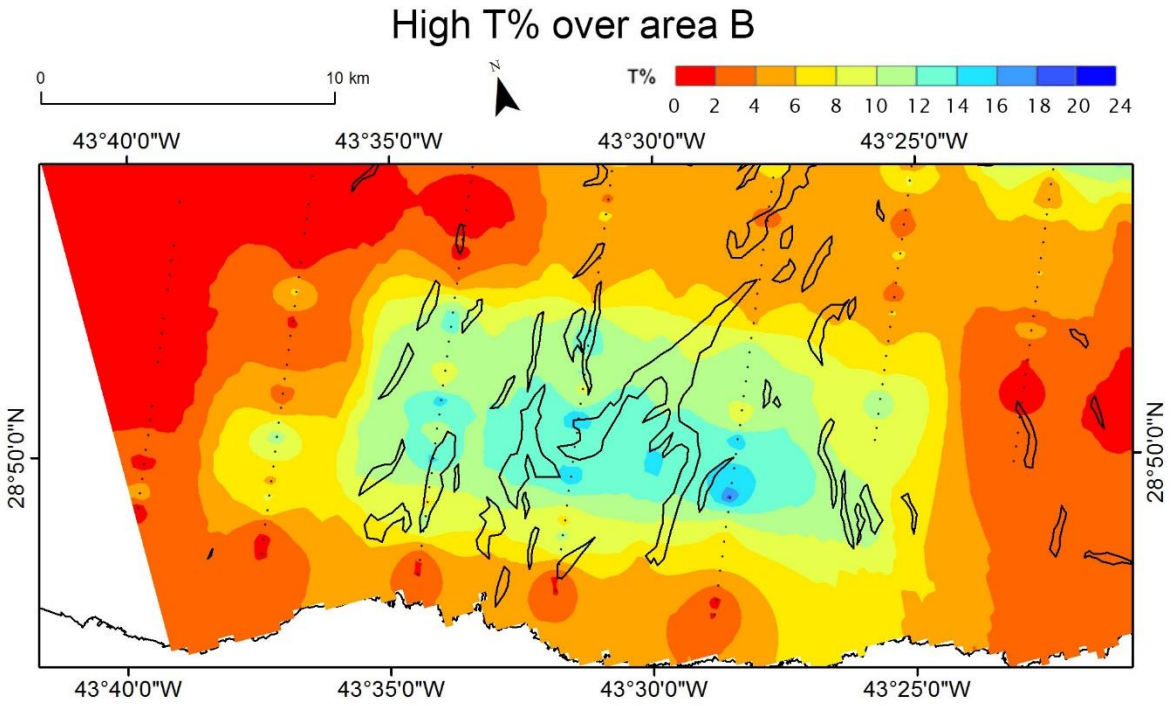

***Figure 3.18**: High T% area B (Figure 3.15) located in the southwest region (Figure 3.13).*

The second largest T% region by area is located in the southwest region (Figure 3.18). The high T% in this area results from large faults measuring 1.2 – 10 km in length and striking 024˚ - 060˚, the largest of which is 10 km long, bifurcates, and strikes 039˚. This high T% resides over a region of shallow bathymetry at a depth of 2600 m that abuts against a deep basin at a depth of 4000 m. This area is south of the NTD, placing it in the expected location of an Outside Corner.

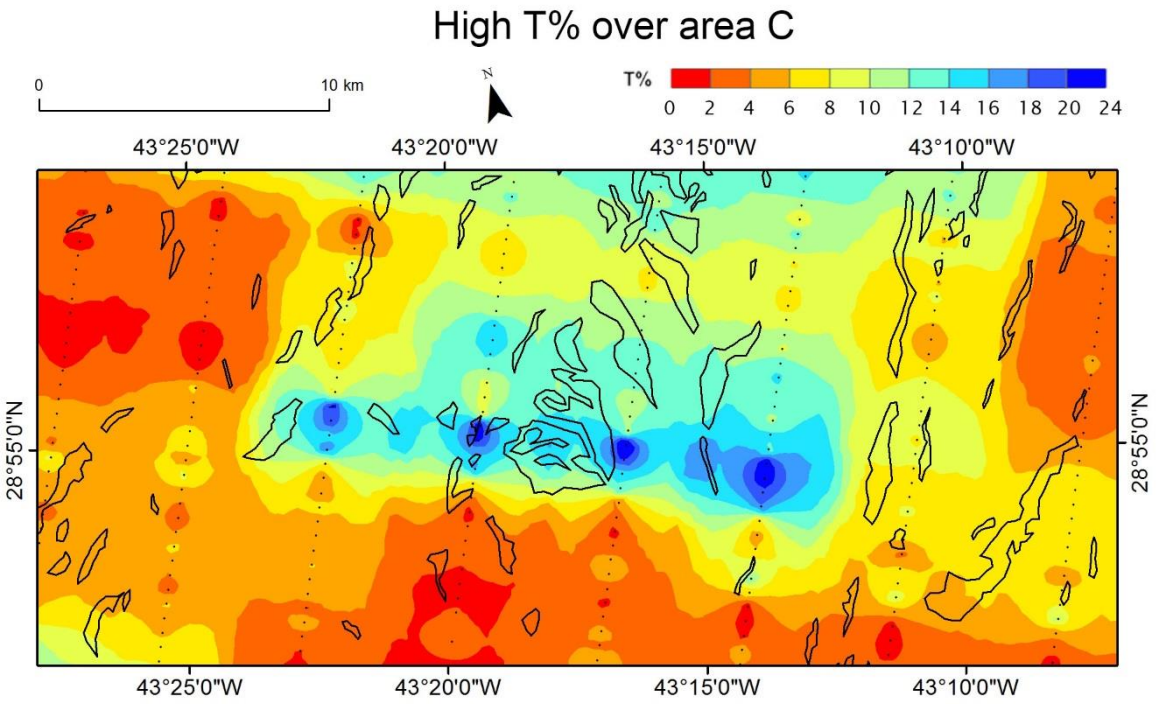

***Figure 3.19**: T% high in area C (Figure 3.15) located in the inside corner region (Figure 3.13).*

The third largest area of high T% is area C (Figure 3.19) located in the inside corner region (Figure 3.13). The high T% occurs within 10 km of a large axial valley wall fault that has been segmented by the FID method (Figure 3.9). This segmentation likely reduced T% along the fault's strike, artificially separating area C from area A (Figure 3.15). The location of area C north of the NTD, places it in the location of the Inside Corner, a location that is expected to have high levels of tectonism. Due to their tectonic situation, Inside Corners typically have thinner crust (Tucholke & Lin, 1994).

3.2.6 Comparing the FID's fault map to Escartin's fault map

The T%'s reliability is fundamentally reliant on the ability of the FID method to identify faults. By comparing the faults identified using the FID method to those identified by Escartin et al., (1999)'s method, I can determine how fault maps differ despite both trying to identify the same seafloor features over the same area. Exploring the differences in our fault maps will highlight potential positives and negatives of my FID method for

finding faults compared to their method. However, it is not possible to definitively determine which method is best because remote sensing requires ground truthing for validation.

Escartin et al. (1999) used side-scan sonar (Figure 3.2A and B) to identify faults in the Brocken Spur segment. They use a subjective, non-statistical approach to identify strong linear reflectors that they interpreted as faults (Figure 3.2B). They measured heave as the fault polygons' width.

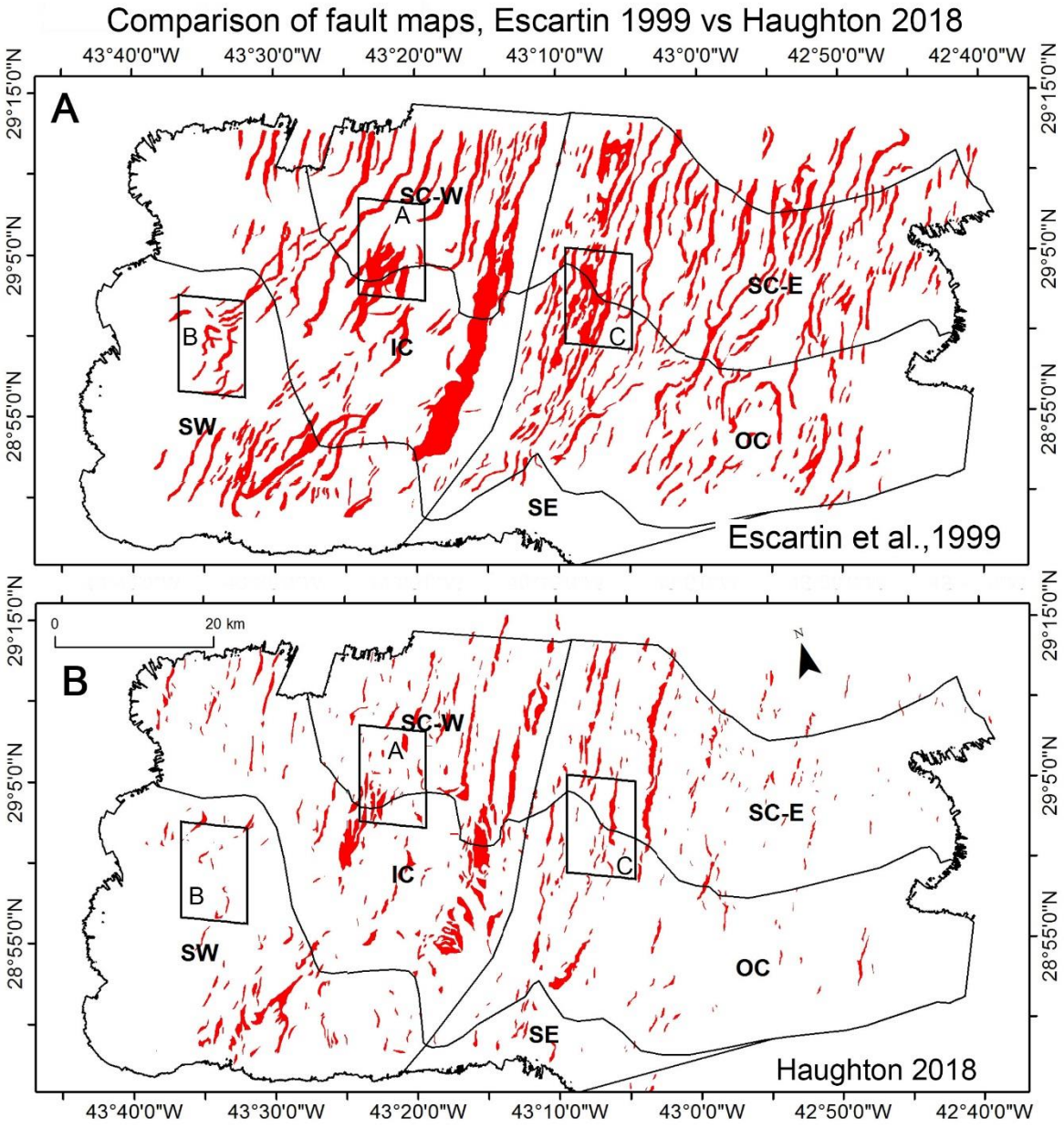

***Figure 3.20**: Comparison of fault maps, faults are in red. **A**: Escartin et al., (1999) used strong acoustic reflectors from side-scan sonar. **B**: fault polygons identified using the FID method (Figure 3.8).*

Table 3.3 summaries key fault properties over the segment according to the different subsets. My FID faults (Figure 3.20B) overlap 30% of Escartin et al., (1999)'s faults extent (Figure 3.20A).

	Fault polygon comparison				
	mean length (m)	**max (m)**	**min (m)**	**average strike (°)**	**total area (km^2)**
Haughton	1920	16,220	190	041	290
Escartin *et al.*	4040	36,550	590	043	780

***Table 3.3**: Comparison table of total fault attributes from Figure 3.20.*

To determine if Escartin's fault polygons are highlighting faults, their overlap with seafloor parameters commonly associated with faults such as steep slopes and sloping towards or away from the spreading axis was measured. This calculation is done by measuring the area of each FID parameter within Escartin's faults as a percentage of the total area of the FID parameter.

The highest contributor to Escartin's faults were 29% of slopes between 35 - 60° (Table 3.4). The next most common fault parameter within Escartin's faults were 28% of upper quintile side-scan sonar and 22% of upper quintile multibeam backscatter (Table 3.4). This is a higher percentage than the FID faults (17% of backscatter and 13% of side-scan sonar) (Table 3.1) which is to be expected because side-scan sonar was their only fault parameter. The reason Escartin et al. used less than a third of high side-scan sonar reflectivity could be due to them not using a statistical method to quantitatively define what they meant by high acoustic reflectivity values. Instead, their subjectively defined high reflectivity circled as faults included side-scan sonar values in the second and third highest quintiles. Additionally, the reason their faults cover less than a third of upper quintile side-scan sonar intensities could also be due to Escartin ignoring the high reflectivity of the axial valley. The percentage of faults overlapping with side-scan sonar and multibeam backscatter is similar to that for slope angle, suggesting these two attributes are related.

Escartin's faults overlapped 17% of slopes facing towards or away from the spreading axis (Table 3.4). This is higher than the 9% overlap of the FID faults (Table 3.1).

	Area of fault parameters (km^2)	Area of Faults (km^2)	%
slope direction	1712	288	17
multibeam backscatter	1011	218	22
slope	182	53	29
side-scan sonar	1287	356	28

***Table 3.4**: The percentage of fault parameters that were overlapped by Escartin's faults.*

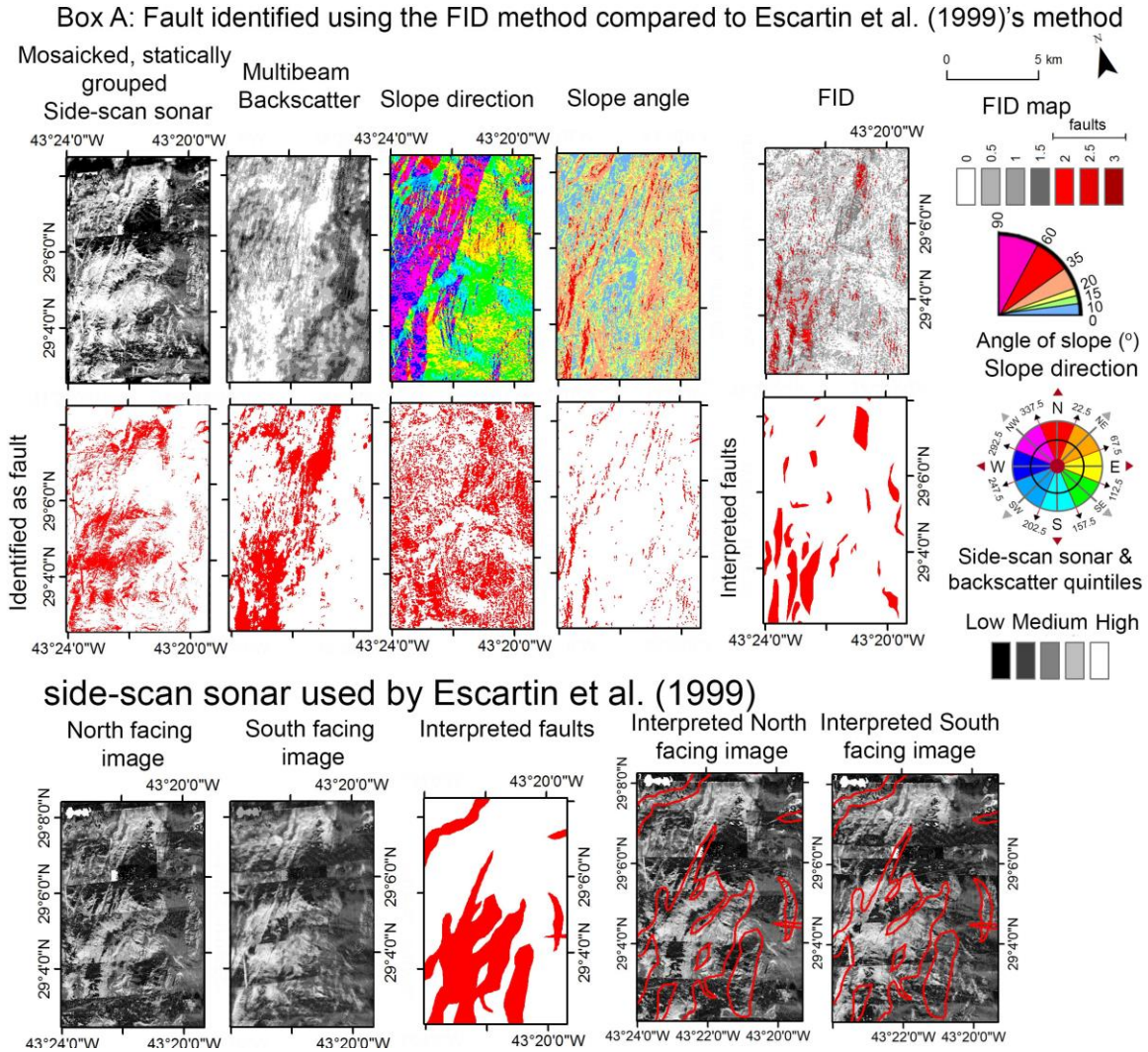

[GH7]

***Figure 3.21**: How fault identification differs within Box A of Figure 3.20. Top two rows of panels are the parameters used in the FID method to*

identify faults. Bottom five panels are the north and south looking side-scan sonar images without any statistical grouping applied with Escartin et al's (1999) fault interpretation overlaid.

Closer investigation of individual faults identified using the two methods indicates why the fault maps differ, and how this difference alters the measured fault geometry. High acoustic reflectivity could represent slumping, this could explain why the FID faults south of the oceanic core complex (Box A in Figure 3.21) identified primarily using a combination of slope and high reflectivity resulted in a smaller polygon. Both Escartin's and the FID's fault polygons failed to identify the oceanic core complex.

A comparison of the upper quantile of side-scan sonar and multibeam backscatter used by the FID method to the fault polygons draw by Escartin should be similar, however they are different (Figure 3.21). The difference results from Escartin using two side-scan sonar images without any statistical grouping of the values to identify faults. The difference is visible where Escartin has not interpreted a bright backscatter region at 43°21' W; 29°8' N (Bottom panels of Figure 3.21). In this region, there are multiple linear bright reflectors <350 m wide and <2 km long that are visible in the TOBI images. However, these small linear traces were not identified suggesting there is more subjectivity in their fault interpretation than simply highlighting strong reflectors.

Another key difference is that the fault polygons drawn using the FID map are tightly bound to the extent of FID values 2 - 3, while Escartin's polygons are not tightly bound to the edges of strong reflectors, some even incorporate low reflectivity regions (e.g. compare FID panels and faults to Escartin's side-scan sonar with fault overlay panels in Figure 3.21).

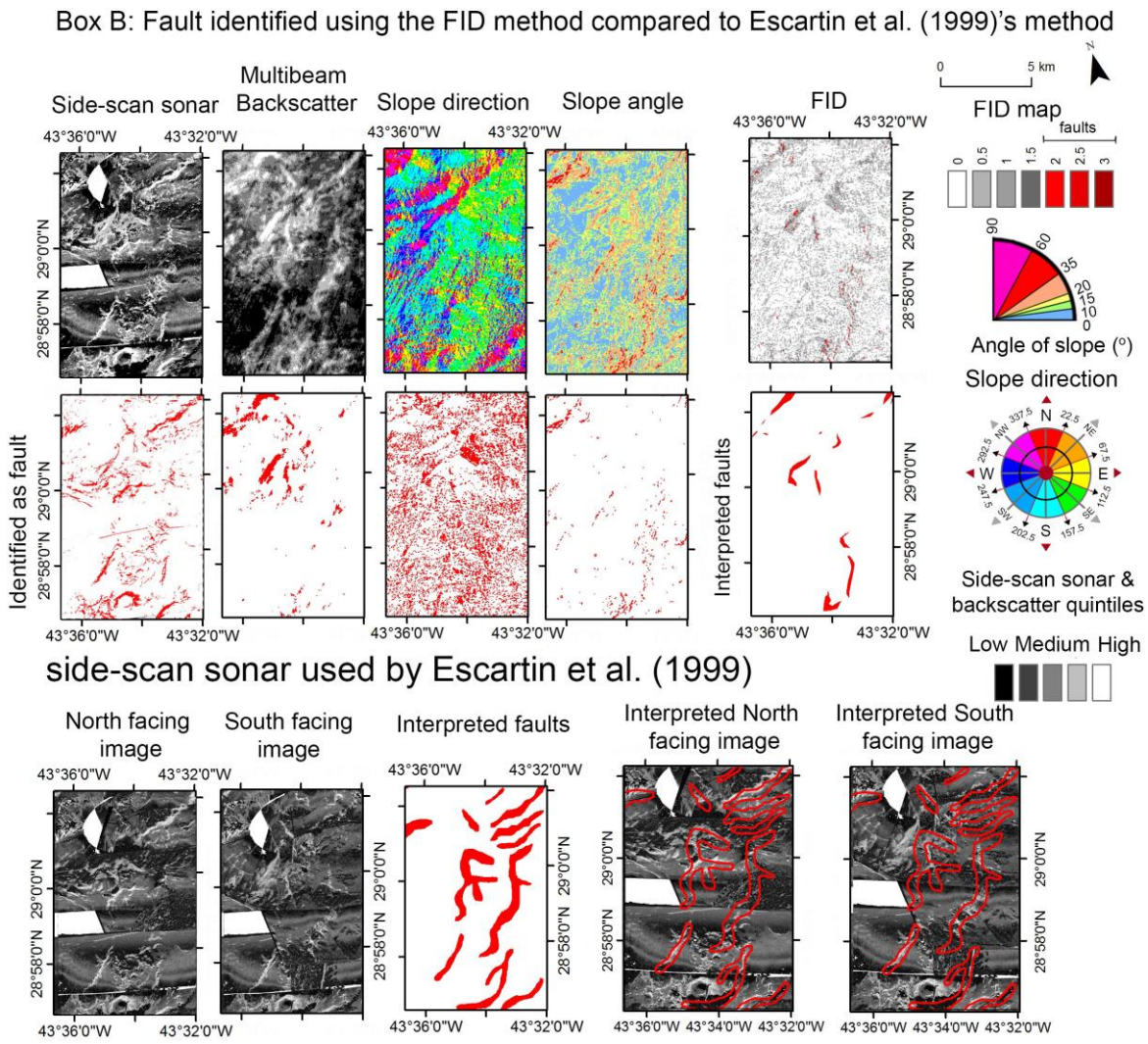

[GH8]

***Figure 3.22**: How fault identification differs within Box B of Figure 3.20. Top two rows of panels are the parameters used in the FID method to identify faults. Bottom five panels are the north and south looking side-scan sonar images without any statistical grouping applied with Escartin et al's (1999) fault interpretation overlaid.*

At 43˚33' W; 28˚57' N (box B in Figure 3.20) the FID method identified 4 km^2 of fault surface (Figure 3.22), while Escartin's method identified 25 km^2. The slope parameter of the FID method did not identify many potential faults indicating the seafloor is smooth in this region. The FID faults that were identified relied on acoustic reflectivity and slope direction. Escartin's north and south looking side-scan sonar's strong

reflectors do not cover the same extent as the fault polygons, especially for a 6.6 km long and 500 m wide fault located at 43°33'3" W; 28°58'56" N.

The upper most quantile of side-scan sonar used in the FID (Figure 3.22) creates a different fault pattern to that identified by Escartin. For example, there are regions in the side-scan sonar's FID that appears to be a 4 km long and 600 m wide fault at 43°35'3" W; 29°0'7" N, that was not identified by Escartin.

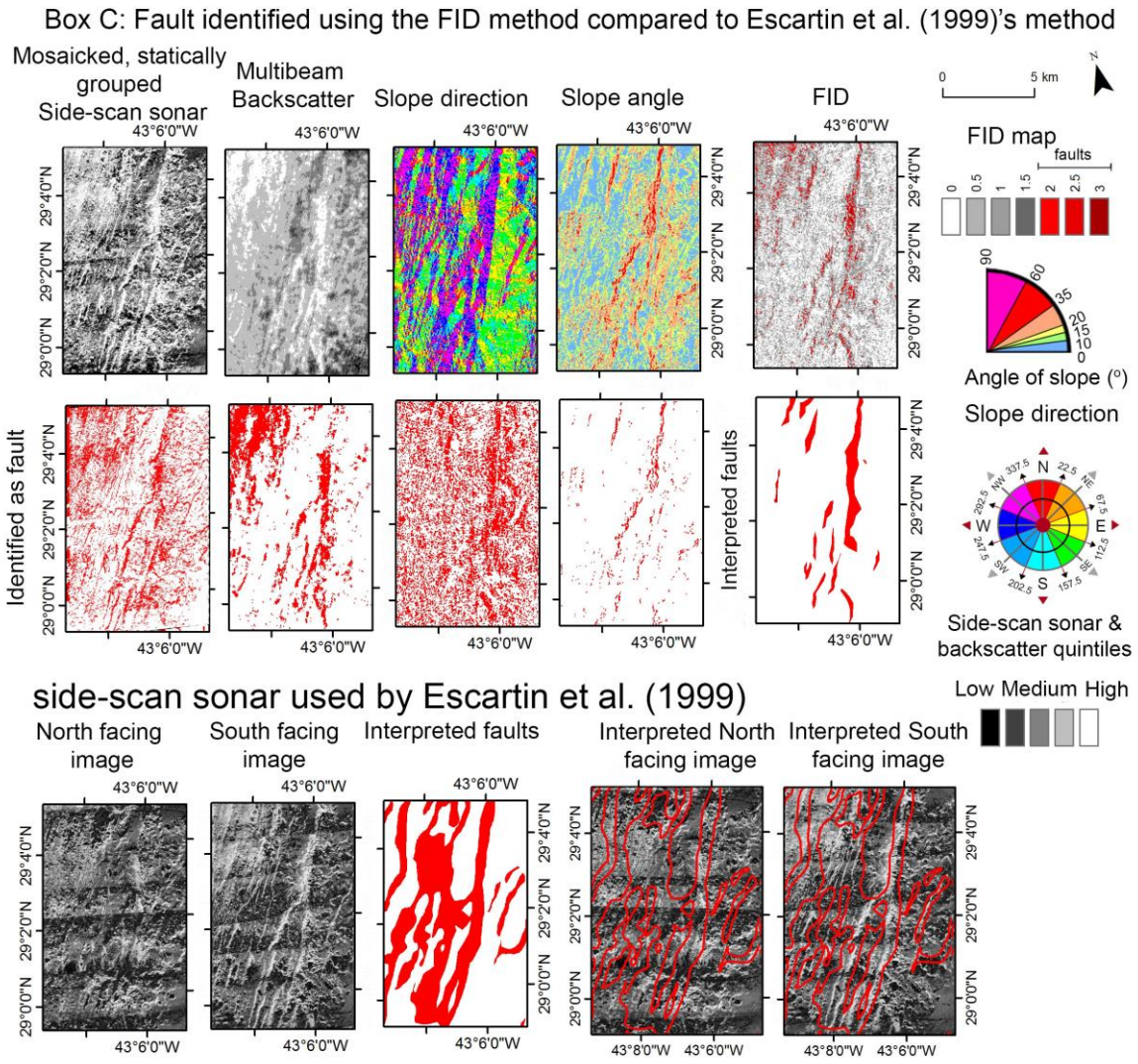

[GH9]

Figure 3.23: *How fault identification differs within Box C of Figure 3.20. Top two rows of panels are the parameters used in the FID method to identify faults. Bottom five panels are the north and south looking side-scan sonar images without any statistical grouping applied with Escartin et al's (1999) fault interpretation overlaid.*

Near 43°7' W; 29°2' N (Box C Figure 3.20) Escartin has identified 47 km^2 of faults while the FID has identified 10 km^2 (Figure 3.23). This region is less than 10 km from the spreading axis so the acoustic reflectivity is very high and not useful for identifying faults. Here, the FID method identifies faults primarily using slope. The north and south looking side-scan sonar images used by Escartin identify multiple thin lineations, >10 km long and 400 m wide. However, Escartin's fault polygons are 200 m wider than the extent of the strong reflectors indicating the fault extent is subjective.

The second part of a comparison between Escartin's fault method and mine is to determine the difference in measured tectonic extension. Escartin's fault map (Figure 3.20A) was used to calculate T% (Figure 3.24A) allowing for the distribution and magnitude of tectonic extension between the two methods to be compared. The T% method calculated using Escartin et al. (1999)'s faults, found that the spreading centre west region had a mean T% of 21±2.4% (range: 1 – 44%). The spreading centre east region had a mean T% of 19±2.2% (range: 3 – 37%). The inside corner region had a mean T% of 16±1.8% (range: 1 – 45%). Finally, the outside corner region had a mean T% of 13±1.5% (range: 0 – 46%). These mean regional T% values using Escartin's faults produced a much higher T% than those using the (Table 3.2). As determined from the fault method comparison, this T% difference results from their fault polygons being drawn wider than those of the FID method (Figures 3.21, 3.22, and 3.23) because of a subjective definition of what constitutes a fault in side-scan sonar and poorly constrained interpretation polygons. The higher T% also results from Escartin identifying more faults off-axis (Figure 3.20) using acoustic reflectivity that were not found using the FID method (Figure 3.22).

Escartin's faults produced a much higher T% for the same location as T% calculated using the FID method (Figure 3.29C). A cross-plot of the two T% maps reveals no correlation ($R^2 = 0.3$) (Figure 3.29C).

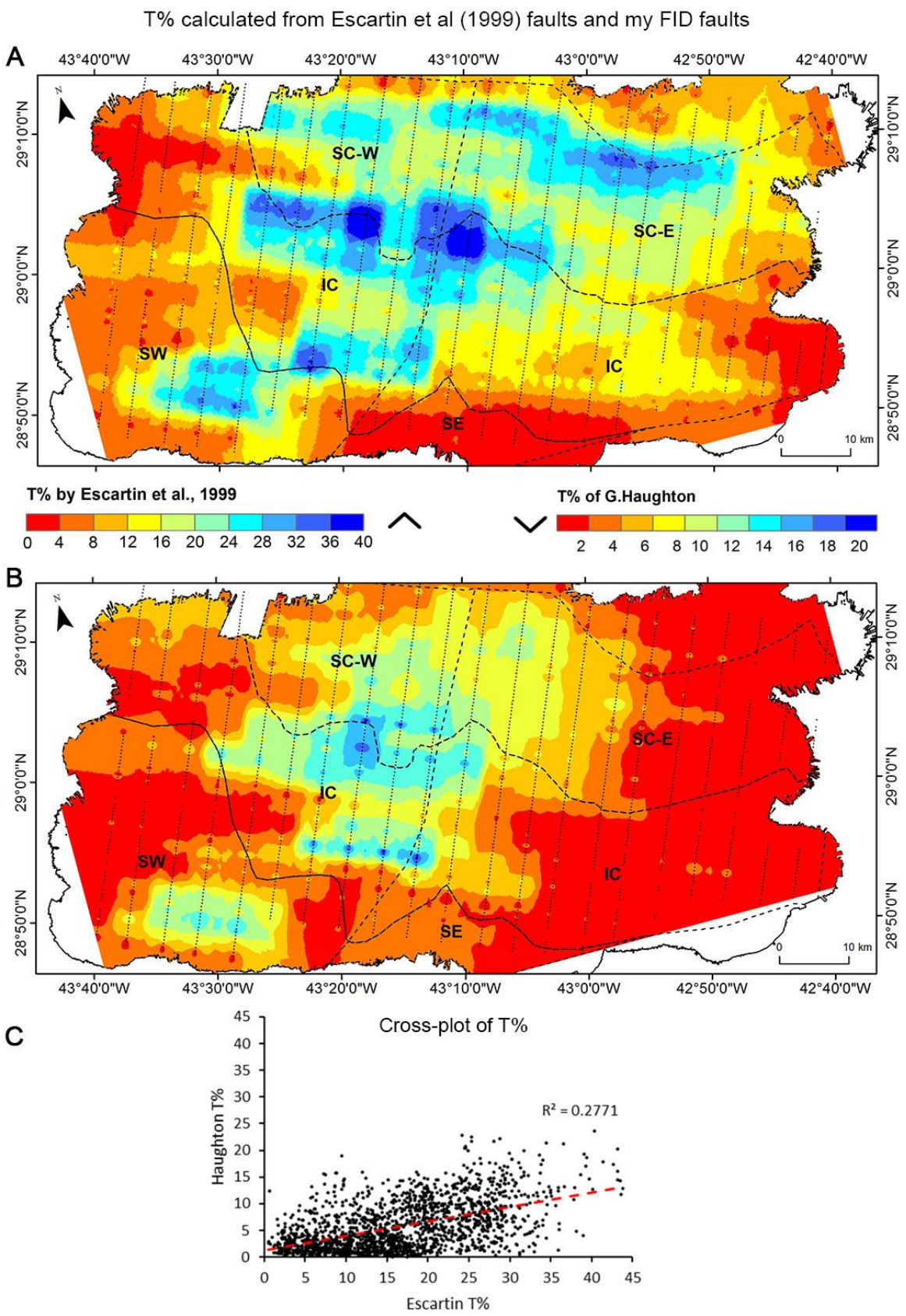

***Figure 3.24**: Comparing T% maps generated from different fault identification methods (Figure 3.20). **A**: Using Escartin et al., (1999)'s faults. **B**: Using the FID method's faults (Figure 3.15). **C**: Cross-plot of FID T% vs Escartin's faults T%.*

To more precisely illustrate the difference in measured tectonic extension, the two T% maps (Figure 3.24) were used to calculate two difference maps (Figure 3.25). The first difference map was calculated by subtracting the FID T% map from Escartin's faults' T% map (Figure 3.25A). The second map identifies the relative T% differences. This was done by through weighting the maps by calculating the T% as a percentage of the maximum measured T% value. The weighted FID T% was then subtracted from the weighted Escartin's T% map (Figure 3.25B). In the difference maps, cooler colours have a higher T% using Escartin's faults, while warmer colours represent higher T% using the FID method's faults.

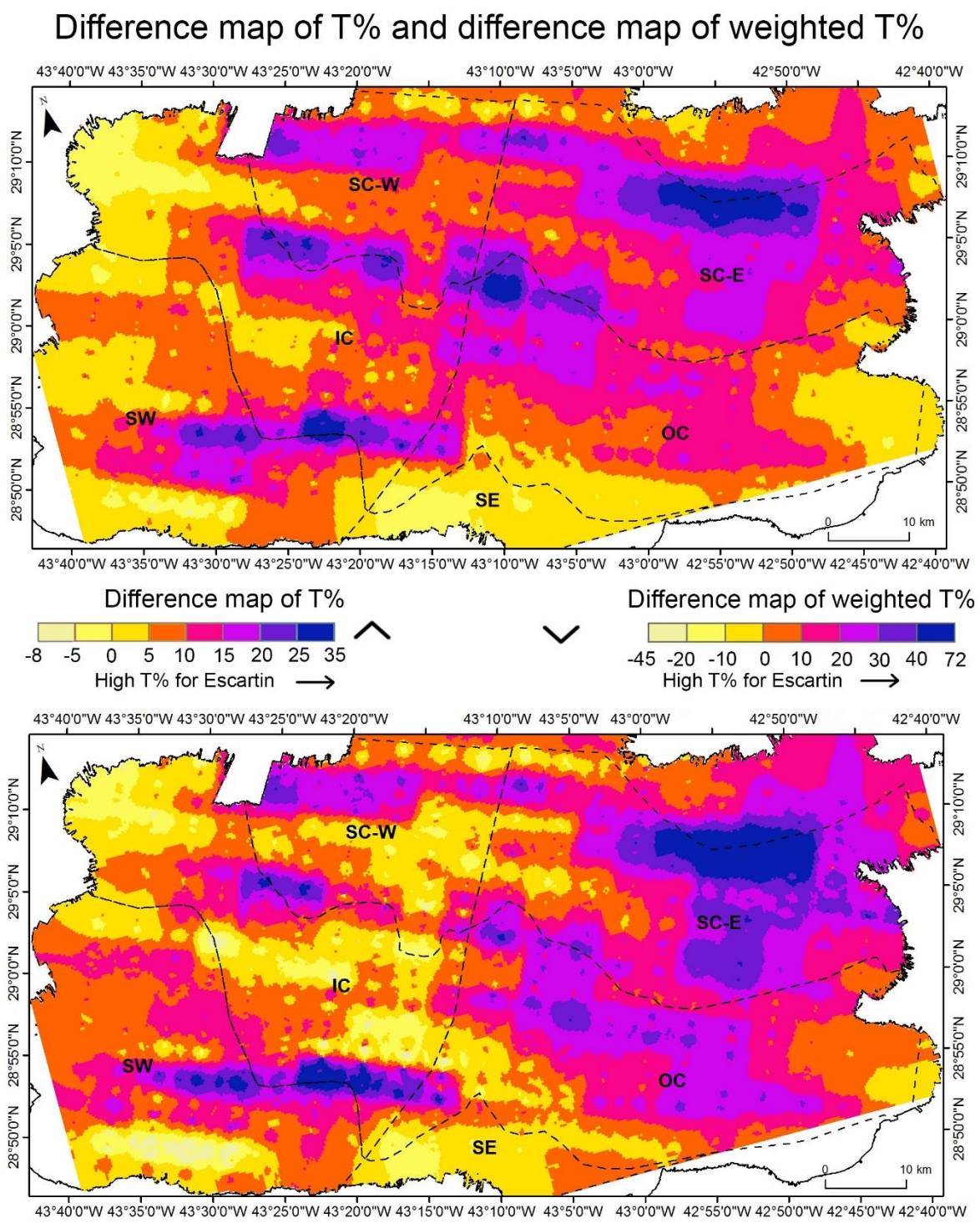

***Figure 3.25**: T% difference maps between using FID faults or Escartin's faults. **A**: A difference map created by subtracting the FID T% map from Escartin's faults' T% map. **B**: A weighted T% map created by calculating the T% value as a percentage of the maximum value, then subtracting the weighted FID T% map from the weighted Escartin's faults' T% map.*

Escartin et al. identified faults that created a higher T% over most of the segment (Figure 3.25A). The weighting difference map indicated that,

on average across the study area, the difference was within 10 – 20% (Figure 3.25B). The spreading centre west region has a mean weighted T% of 7% higher using Escartin's faults. The spreading centre east region has a mean weighted T% of 21% higher using Escartin's faults, the largest mean difference of all the regions. The outside corner has a mean weighted T% difference of 13% higher using Escartins' faults. The inside corner region has a mean weighted T% difference of 3% higher using Escartin's faults. The southwest region has a mean weighted T% difference of 7% higher using Escartin's faults, and the southeast region has a mean increase of 4% using the FID faults. This indicates that on the regional scale, there can be up to 21% difference in the total amount of T% measured between the two fault identification methods.

The main differences in T% distribution occurs at 42°53' W; 29°6' N, in the spreading centre east region and 43°22' W; 28°53' N along the boundary of the southwest region and the inside corner region. At these two locations, the weighted T% difference can be 60% higher using Escartin's faults. Another difference is that Escartin's faults have 30% higher weighted T% over the oceanic core complex. In the south of the southwest region the FID method generated 20% weighted T% more when using Escartin's faults.

3.2.7 Residual topography anomaly and T%

The residual topography anomaly (RTA) was calculated by removing sediment loading on the basement and the effect of off-axis subsidence from plate cooling (see Chapter 2 for a detailed description of the methodology). The crust was isostatically adjusted for the removal of sediment using the equation for the depth before sediment loading, t_b, (Le Douaran & Parsons, 1982): $t_b = t'_b - t_s \frac{(\rho_a - \rho_s)}{(\rho_a - \rho_w)}$, where, t'_b = depth after sediment loading, t_s = sediment thickness, ρ_a = density of asthenosphere (3.2 g cm^{-3}), ρ_w = density of seawater (1.027 g cm^{-3}), and ρ_s = density of sediment (1.59 g cm^{-3}).

There are no available seismic reflection profiles across the Broken Spur segment to measure sediment thickness. Instead, sediment thickness was calculated using a sedimentation rate of 10 mm Ka^{-1}, determined from acoustic sub-bottom profiler data that imaged sediment thicknesses in a zone out to 30 km from the spreading axis, in crust up to 2 Ma (Mitchell et al., 1998). This was extrapolated across the plate with increasing age (Figure 3.26), determined from the age map from Müller et al., (2008) that also matches the magnetic isochon dates for the area derived by Searle et al., (1998).

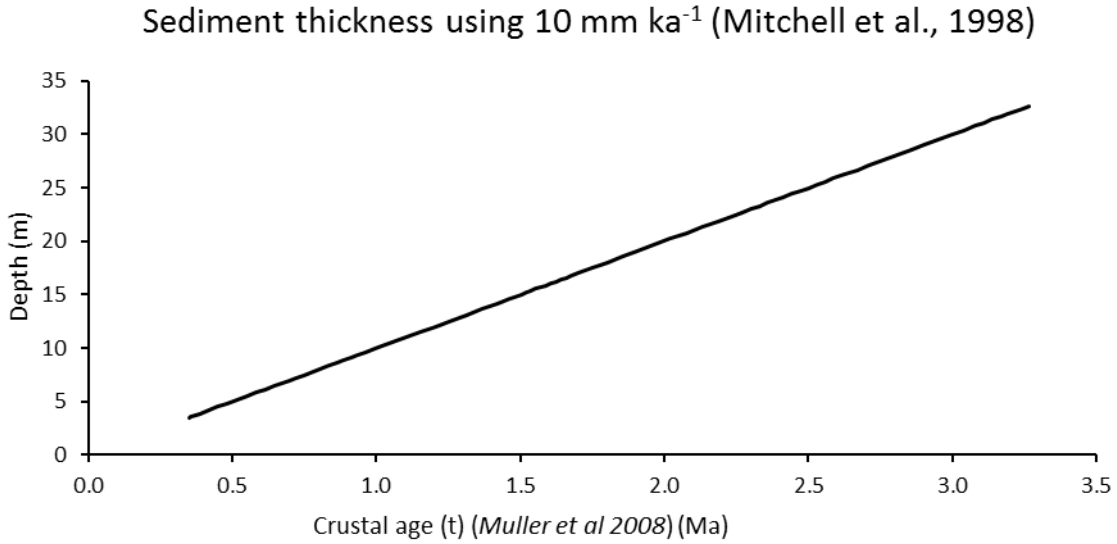

***Figure 3.26**: Sediment thickness plot using the sedimentation rate from Mitchell et al., (1998) and the crustal age from Müller et al., (2008).*

Mitchell et al., (1998) found the thickest sediment was ~15 m on 2.2 Ma crust. As a result of the overall thin mean sediment thickness (<30 m), isostatically unloading the crust did not influence the bathymetry by more than 10 m (Figure 3.28).

On a small scale, sediment thickness is likely to vary from the predicted mean as a result of being remobilised by bottom currents and accumulating in depressions and swept off highs, reducing the amplitude of bathymetric variance on a short (100 m) wavelength. For example, a 30 m thickness of sediment will obscure small fault scarps, creating a smoother bathymetry and reducing acoustic reflectivity, suppressing their detection and reducing their representation on the FID map (Figure 3.10).

The mean sediment unloaded bathymetry along each isochron was then subtracted from the mean plate depth. This mean plate depth was empirically calculated by first measuring the mean sediment unloaded bathymetry depth along age isochrones at 100 Kyr intervals from Müller et al., (2008)'s age map (Figure 3.27B, C). Müller et al., (2008)'s age contours between 0 – 600 Ka were not parallel to the spreading axis. These age isochrons crossed the spreading axis and formed closed circles and so could not be used to calculate mean depth with age. The age isochrons between 0 – 600 Ka were estimated by drawing isochrons parallel to the spreading axis and the 700 Ka isochron at 1.7 km, 100 Ka, intervals (Figure 3.27A).

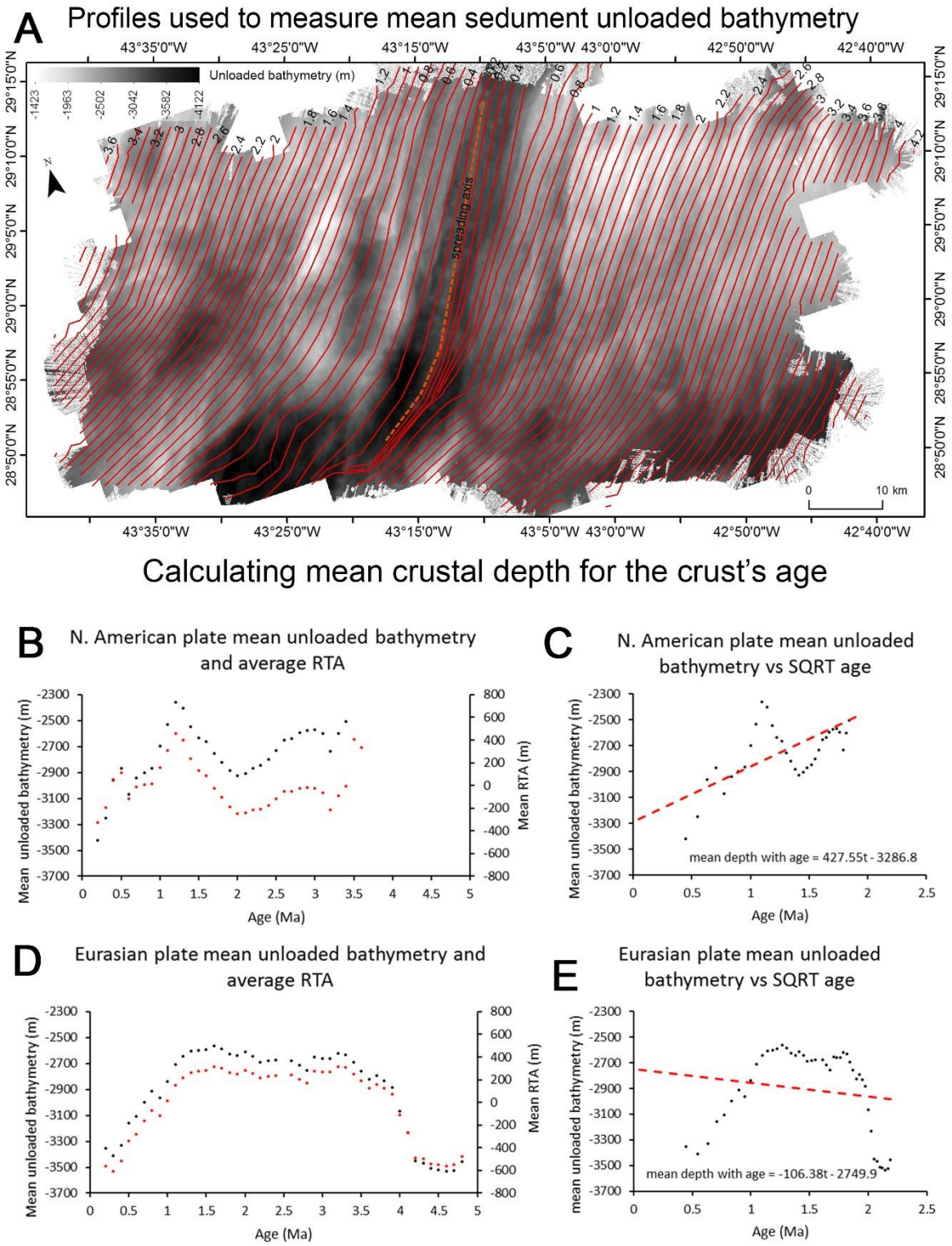

***Figure 3.27**: Calculating RTA from the mean crustal depth at each age isochron. **A**: Age isochron map from Müller et al., (2008) with isochrones between 0 – 600 Ka being manually interpreted. **B**: N. American Plate's mean unloaded bathymetry (black dots) and mean RTA (calculated using panel C) taken along each isochron. **C**: Plotting mean unloaded crustal depth against the square root of age allows for a linear equation (dashed*

red line) to describe the mean crustal depth on the N. American Plate. Subtracting the mean unloaded bathymetry of the N. American Plate (panel B) from the linear equation calculates the mean RTA (red dots in panel B) for the N. American Plate. ***D****: Eurasian Plate's mean unloaded bathymetry (black dots) and mean RTA (calculated using panel E) taken along each isochron.* ***E****: Plotting mean unloaded crustal depth against the square root of age allows for a linear equation (dashed red line) to describe the mean crustal depth on the Eurasian Plate. Subtracting the mean unloaded bathymetry of the Eurasian Plate (panel D) from the linear equation calculates the mean RTA (red dots in panel B) for the Eurasian Plate.*

Calculating a linear fit for the mean unloaded bathymetry along each isochron of each Plate against the square root of age calculated the average plate depth as 427 $t^{1/2}$ when t ≤5 Myrs for the N. American Plate and -106 $t^{1/2}$ when t ≤5 Myrs for the Eurasian Plate (Figure 3.27C, E). The trend of the mean plate depth for both Plates does not extend to old enough crust to measure the off-axis plate subsidence due to cooling. Therefore, the linear fits to the mean unloaded bathymetry should be considered to represent the average plate depth, not the crust subsidence rate which has been calculated by Hasterok, (2013) to be 414.5 $t^{1/2}$ when t ≤17.5 Myrs. Subtracting the unloaded bathymetry map from the linear trend describing the average plate depth calculates RTA (Figure 3.27B, D). RTA quantitatively defines bathymetry that is more shallow (positive) or more deep (negative) than the average plate depth.

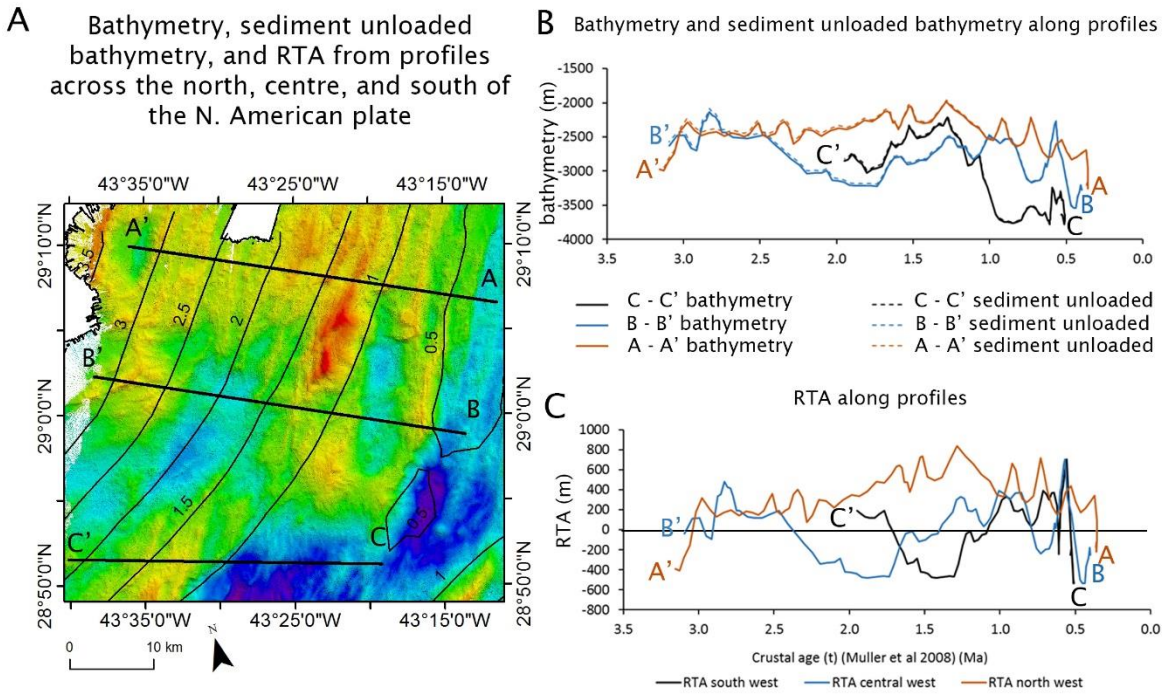

***Figure 3.28**: Examples of calculating RTA along profiles on the N. American Plate. **A**: Bathymetry with original age isochrones from Müller et al., (2008), profile A – A' is over the shallow region and spreading centre west region. Profile B – B' is over basins. Profile C – C' is over the NTD and the south west region. **B**: The profile's bathymetry (solid line) and sediment unloaded bathymetry (dashed line). **C**: Subtracting the unloaded bathymetry profiles from panel A from the linear equation describing average plate depth (Figure 3.27C) calculates the RTA profiles.*

Crust close to the axial valley is not in isostatic equilibrium because of dynamic support provided by hot, upwelling asthenosphere under the spreading axis, and the time lag between continuous tectonic extension of the crust and the viscous response of the mantle. An example of this is the axial valley wall which is formed by a large normal fault that downthrows the hanging wall, generating a deep axial valley. Because of this I avoid any interpretation of RTA within the axial valley. Close to the NTD, shear forces can form regions of compression and extension. This allows for structural support within the upper crust that can form features like shallow Inside Corners or, with extension, deep Outside Corners (Tucholke & Lin, 1994). Bathymetric features supported structurally cannot be explained with Pratt or Airy isostatic models. Near the edge of the bathymetry coverage the

depth sample density reduces. The bathymetry in this low sample region is not as reliable and neither is the RTA calculated from it. For these reason I do not interpret RTA within the NTD, along the spreading axis, or where depth sample density is low.

RTA is not too dissimilar to bathymetry (compare graph B to graph C in Figure 3.28), because sediment thickness is low and the crust is mostly less than 3 Ma. In this young crust, RTA quantitatively identifies shallow and deep bathymetric features. The RTA of these features can be compared to the Pratt and Airy isostasy models (Chapter 2) to provide an explanation for their deviation away from the average, predicted bathymetry. According to the Pratt model, a positive bathymetry anomaly could have been created from low-density crust which is either hot or is formed of low density mafic crust (low-density in comparison to ultra-mafic mantle). Alternatively, Airy isostasy explains topographic differences as being due to differences in crustal thickness. In this model, regardless of crustal thickness, all crust is neutrally buoyant at the same level within a plastically deforming asthenosphere. Therefore, thicker crust produces shallower bathymetry than thinner crust (Lowrie, 2007; Suppe, 1985).

To explore whether the RTA can be explained using the Pratt model, requires RTA to produce a reasonable upper crustal density, ρ_1, using the Pratt equation; $\rho_1 = \rho_c \frac{c}{h_1+c}$, where ρ_1 is the density of the elevated crust, ρ_c is the density of the crust (3 g cm^{-3}), c is the thickness of the crust (6 km) and h_1 is the RTA (km). To explore whether the RTA can be explained using the Airy model, requires RTA to produce a reasonable additional depth below the assumed crustal thickness, b_1, using the Airy equation; $b_1 = \frac{h_1\rho_c}{\rho_m-\rho_c}$, where ρ_m is mantle density (3.3 g cm^{-3}) (Lowrie, 2007; Supper, 1985).

Profiles A – C (Figure 3.28) on the N. American Plate are examples of how RTA is used to estimate crustal thickness and density. Profile A – A' (Figure 3.28) across the shallow bathymetry within the spreading centre west region produces an RTA of 800 m around 1.3 Ma. If the crust here

was in isostatic equilibrium, then the 800 m RTA could be explained using the Pratt model as having a crustal density of 2.6 g cm^{-3}, or using the Airy model the crustal thickness would be 14 km.

Profile B – B' (Figure 3.28) crosses several basins in the inside corner region, north of the NTD. The RTA over the basin between 1.5 and 2.5 Ma reaches a minimum RTA of -400 m. The Pratt model calculates the crust of this basin having a density of 3.2 g cm^{-3}, and the Airy model calculates a crustal thickness of 2 km.

Profile C - C' (Figure 3.28) crosses the NTD and the outside corner high of the next segment in the southwest region. The positive RTA of the outside corner between 0.7 – 1.3 Ma reaches 400 m, while the basin further off-axis between 1.3 – 1.7 Ma reaches -400 m. The Pratt model calculates the crust of this outside corner high as having a density of 2.8 g cm^{-3}, and the crust of the off-axis basin as having a density of 3.2 g cm^{-3}. The Airy model calculates the outside corner high as having a crustal thickness of 10 km, and the off-axis basin as having a crustal thickness of 2 km. Low melt supply and structural support within the NTD's basin means that the inside corner high is unlikely to be a result of thick crust, and is likely a structural feature not explainable using Airy or Pratt isostasy. The basin further off-axis between 1.3 – 1.7 Ma is away from the NTD and its shear forces, so could possibly be explained by isostasy. These examples illustrate how negative RTA suggests thin or high density crust and positive RTA suggests thick or low density crust.

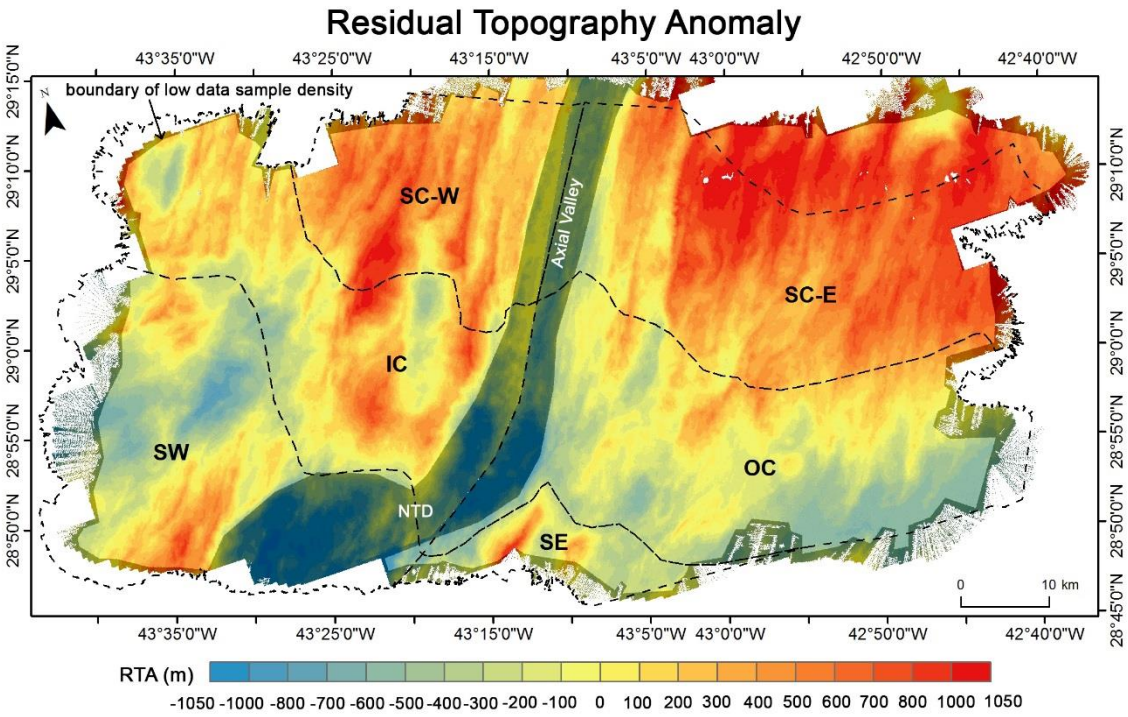

***Figure 3.29**: RTA of the Broken Spur segment quantifies deep and shallow bathymetry in respect to the plate's average depth. The darkened region covering the axial valley, the NTD, and the edge of the bathymetry where data samples are poor are not reliable or included in the statistical calculation of Table 3.5.*

Region	mean RTA	max RTA	min RTA
SC-W	404	1263	-303
SC-E	509	1461	-506
IC	93	1265	-735
OC	-148	680	-895
SW	-144	916	-987
SE	-130	975	-730

***Table 3.5**: The mean, maximum, and minimum RTA within each region in Figure 3.29, in meters.*

The RTA map (Figure 3.29) indicates a split between north and south along 29° N. RTA is high north of 29° N with a mean of 389 m (range: -595 to 1460 m), and low in the south with a mean of -92 m (range: -990 to 975 m). Using the Pratt model, the area north of 29° N would have a mean crustal density of 2.8 g cm^{-3} and south of 29° N would have a mean crustal density of 3 g cm^{-3}. Alternatively, using the Airy model, the area north of

29° N this would have a mean crustal thickness of 9.9 km thick, while south of 29° N would have a mean crustal thickness of 5.1 km thick.

Applying Pratt and Airy isostasy to the RTA values calculated for the study regions (Table 3.5) offers potential explanations for their values. Mean RTA for the spreading centre east region was 509 m, resulting in a mean density of 2.8 g cm^{-3} or a mean crustal thickness of 11.1 km. This was less, but not too dissimilar, than the spreading centre west region's mean RTA of 404 m, resulting in a mean density of 2.8 g cm^{-3} or a mean crustal thickness of 10 km. The inside corner region had a mean RTA of 93 m, resulting in a mean density of 3 g cm^{-3} or mean crustal thickness of 6.9 km. This is higher than the mean RTA of the outside corner region of -148 m, resulting in a mean density of 3.1 g cm^{-3} or a mean crustal thickness of 4.5 km. The mean RTA of the southwest region was -144 m, resulting in a mean density of 3.1 g cm^{-3} or a mean crustal thickness of 4.6 km. The mean RTA of the southeast region was -130 m, however this region is too small for useful comparison to other regions. The RTA values within the axial valley and NTD (blacked region in Figure 3.29) were omitted from the statistical calculations (Table 3.5).

Negative RTA in the inside corner region of -400 m at 43°18' W; 29°2' N and in the SW region of -700 m at 43°32' W; 28°57' N are basins, identified in Figure 3.13. RTA illustrates how the basins are significantly subsided regions below the predicted seafloor depth. The Eurasian Plate has fewer basins, although one measures -300 m at 43°5' W; 28°58' N, and another measures -500 m at 43°5' W; 28°51' N in the outside corner region. These basins could be explained using a crustal density of 3.1 g cm^{-3} for an RTA of -100 m, or 3.2 g cm^{-3} for an RTA of -400 m. The basins <-300 m potentially represents crust 3 km thick, and trace along the off-axis relic of the NTD where crust is expected to be thinner because of a lower melt supply.

The crustal densities calculated by the Pratt isostasy equation between 2.6 g cm^{-3}, lowest density of Layer 2b, and 3 g cm^{-3}, highest density of Layer 3, are within a believable range (Carlson & Herrick, 1990). The crustal thickness predicted by the Airy isostasy model are believable

for non-transform, non-hotspot influenced oceanic crust is they are between 4 - 8 km thick (Chen, 1992; White et al., 1992). This suggests that the very high or very low densities and thickness outside of the acceptable range must be explained by other processes.

The predicted crustal densities and thickness could also be influenced by our assumed crustal thickness (6 km), mantle density (3.3 g cm^{-3}), and crustal density (3 g cm^{-3}). If these assumptions are inaccurate then the calculated densities and thickness will also be. By comparing RTA to a different proxy for crustal thickness and density, I can determine if the Airy or Pratt calculations are reasonable explanations for the RTA. I do this by comparing RTA to Residual Mantle Bouguer Anomaly (RMBA) (Lin et al., 1990).

3.2.8 Residual Mantle Bouguer Anomaly (RMBA)

RMBA identifies regions of higher or lower densities than predicted by a plate model. Lower density can be explained by thicker mafic crust. This produces a lower gravitational anomaly over the region because the overall density is lower than predicted. The opposite is true for regions of high density, where the crustal depth is less than predicted.

RMBA from Lin et al. (1990)

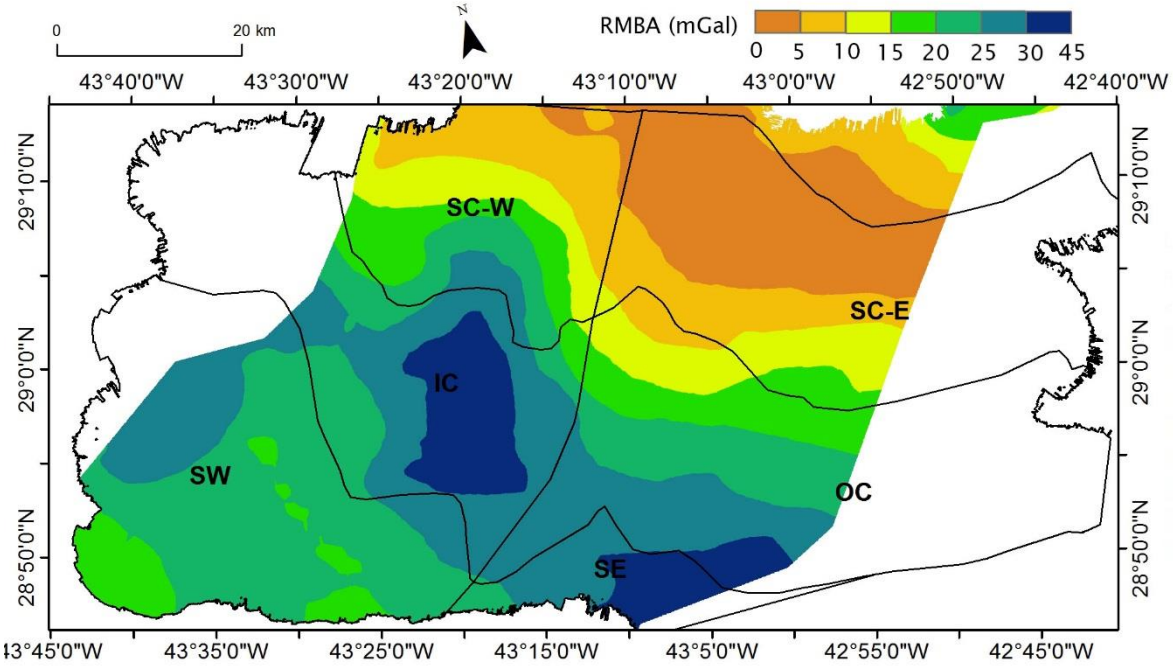

***Figure 3.30**: RMBA from Lin et al., (1990). Higher RMBA is a proxy for thinner crust.*

Across the study area, the broad distribution of RMBA (Figure 3.30) indicated higher values to the south, near the NTD and across the inside corner, outside corner, and southeast regions. Lower values were detected in the north over the spreading centre west and spreading centre east regions. This was interpreted as thick crust (6 km) at the segment centre providing a low RMBA, and thin (4 - 5 km) crust at the discontinuity providing a high RMBA (Lin et al., 1990). These crustal thicknesses were much lower than those proposed by my Airy calculations, which were 10 km thick north of 29° N and 5 km thick south of 29° N.

The mean RMBA across each study region and plate is shown in Table 3.6, higher RMBA is interpreted as thinner crust.

Region	mean RMBA	max RMBA	min RMBA
SC-W	14	28	4
SC-E	6	18	1
IC	27	32	13
OC	22	32	7
SW	22	30	15
SE	29	32	22
N. America	20	32	4
Eurasia	14	32	1

***Table 3.6**: The mean, maximum and minimum RMBA for geological regions in mGal.*

To correlate RMBA and RTA a measurement was taken from each data set in a 1 x 1 km grid (Figure 3.31). Data was only correlated over regions where both the RTA and RMBA datasets have 100% coverage within 1 km^2, this resulted in less comparison close to the edge of the bathymetry's extent and only within the extent of the gravity survey lines (Lin et al., 1990). Data for correlation was not taken within the axialqq valley or NTD because the RTA in these regions were expected to not be in isostatic equilibrium, and so not expected to reflect crustal density or thickness.

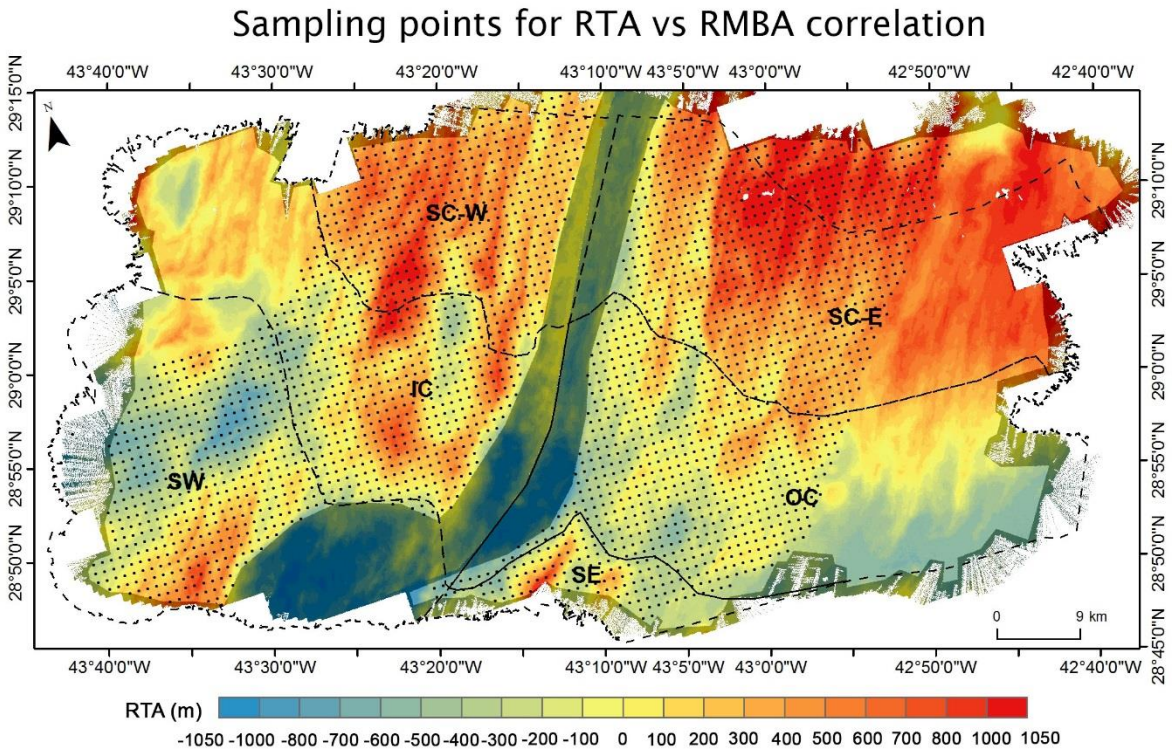

***Figure 3.31**: Location of sample points (black dots) in a 1 x 1 km grid for correlation between RMBA and RTA. Sampling avoids the axial valley and NTD, regions of low data coverage, and where both data sets do not overlap.*

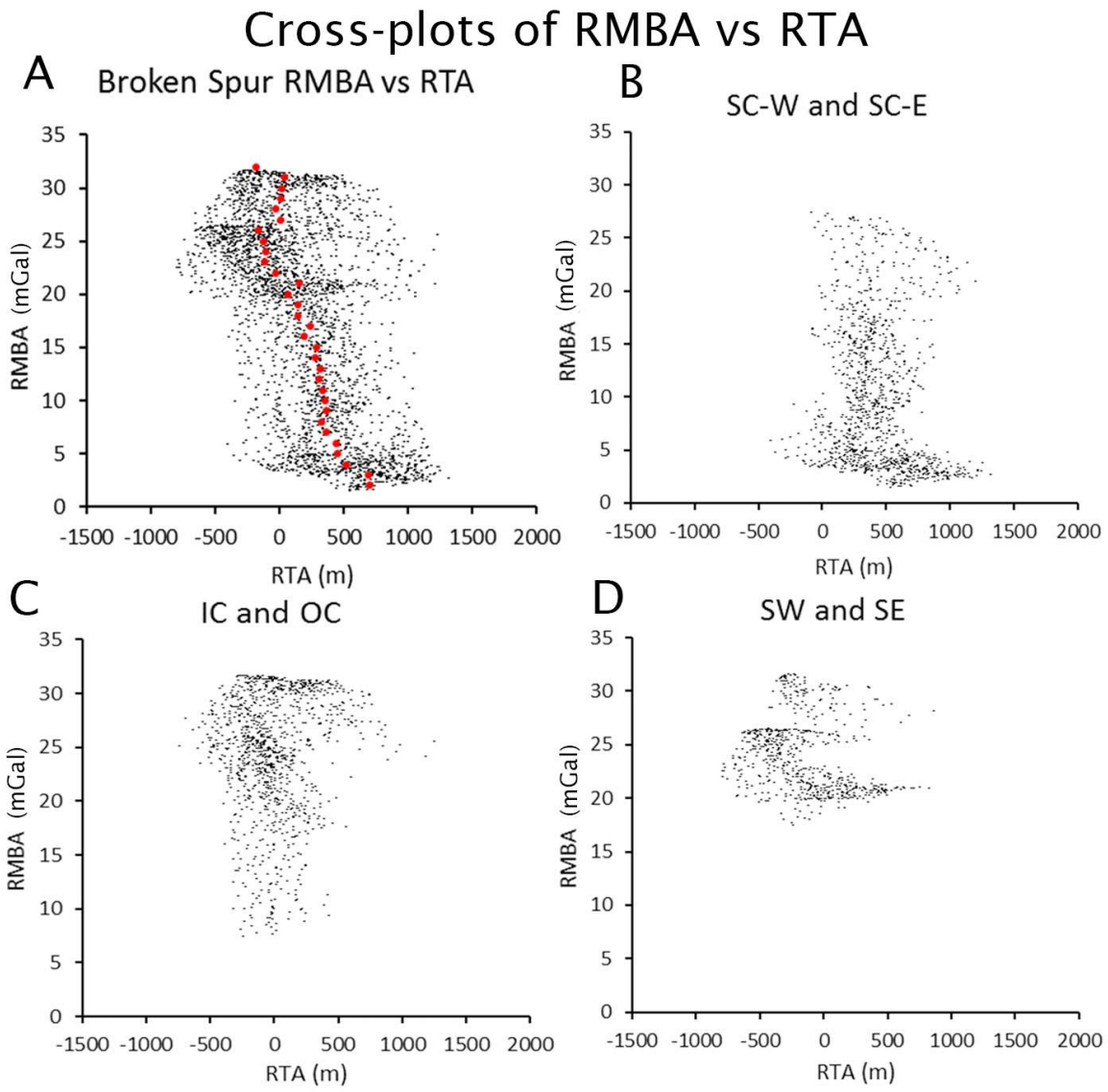

***Figure 3.32**: Cross-plots of RMBA and RTA using points from Figure 3.31. **A**: The entire study area, with red points showing the mean RTA at 1 mGal RMBA intervals; **B**: The spreading centre west and spreading centre east regions; **C**: The inside corner and outside corner regions; **D**: The southwest and southeast regions.*

When RTA and RMBA measured at 1 km intervals across the entire segment are compared there is no statistical strong correlation (R^2 = 0.33) (Figure 3.32A). Along the positive RTA of the spreading centre west region and the spreading centre east region, RMBA is low (mostly between 2 – 20 mGal) and the RTA range is not correlated to the RMBA (R^2 = 0.02) (Figure 3.32B). The positive RTA of the inside corner region and outside corner region has a high RMBA (mostly between 20 – 32 mGal) that is not correlated to RTA values (R^2 = 0) (Figure 3.32C). The southwest region and

the southeast region have high RMBA (between 20 – 32 mGal) (Figure 3.32D) that shows no correlation to RTA (R^2 = 0.06). This indicates that no statistical correlation between RMBA and RTA was found within the study regions (Figure 3.32B, C, and D) when measured at 1 km intervals.

However, a relation starts to emerge at larger scales. The mean of RTA at RMBA intervals of 1 mGal reveals a negative correlation of high RMBA (32 mGal) to low mean RTA (20 m), and low RMBA (2 mGal) to high mean RTA (60 m). A visual relation between the mean RTA (Table 3.4) and mean RMBA (Table 3.5) of each region identifies an inverse relation between high RMBA and low RTA inside and outside corner regions and low RMBA and high RTA in the inside corner regions. This relation is illustrated by mean RTA and mean RMBA of each study region plotted against each other to find a correlation on the 20 – 50 km scale (Figure 3.33). Each study region was also divided centrally into an eastern and western half to identify if a regional relation existed on a 10 – 20 km scale (Figure 3.33).

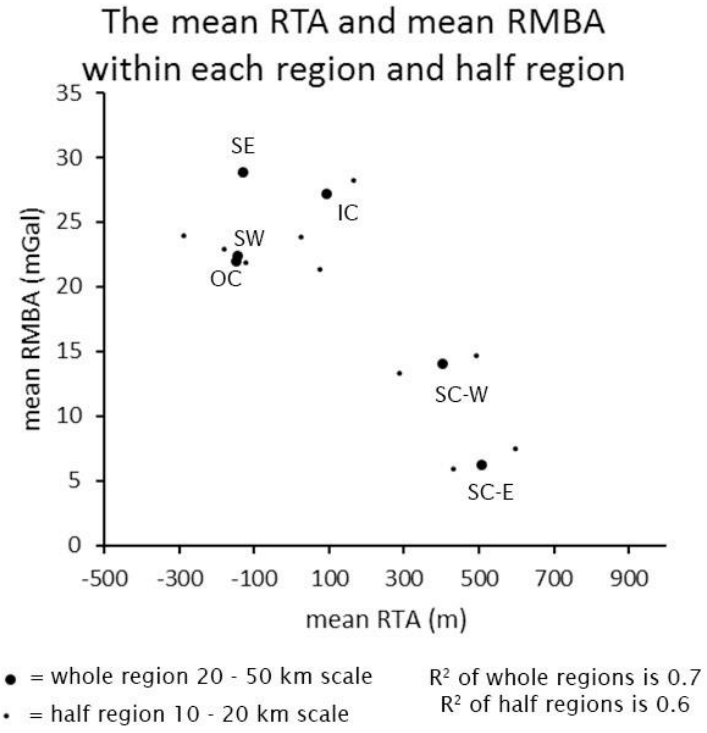

Figure 3.33*: The mean RTA and mean RMBA of each region (big dot) and the half region (small dot). The plot identifies a large scale inverse relation between RTA and RMBA when compared at scales >10 km.*

This analysis has identified an inverse relation between RTA and RMBA on the half regional scale of 10 – 20 km (R^2 = 0.6 in Figure 3.33) and on the regional scale of 20 – 50 km (R^2 = 0.7 in Figure 3.33), while no correlation was found at smaller scales <10 km (Figure 3.32A). The correlation on scales <10 km may be a result of RMBA identifying features with wavelengths of several kilometres while RTA measures deviations from the mean crustal depth, these deviations occur on various scales from 500 m – 10 km. Additionally, a stronger correlation may not exist because the shallow and deep topography identified in RTA are diagnostic of upper crustal properties that may not related to lower or whole crustal variation in thickness and density identified by RMBA. Further comparisons are required to determine if T% is related to the properties being measured by RTA or those being measured by RMBA.

3.2.9 Comparing T% to RTA and RMBA

When comparing the RMBA and RTA at each T% point no statistical correlation is seen between RTA and T% (R^2 = 0) (Figure 3.34A) or between RMBA and T% (R^2 = 0) (Figure 3.34B).

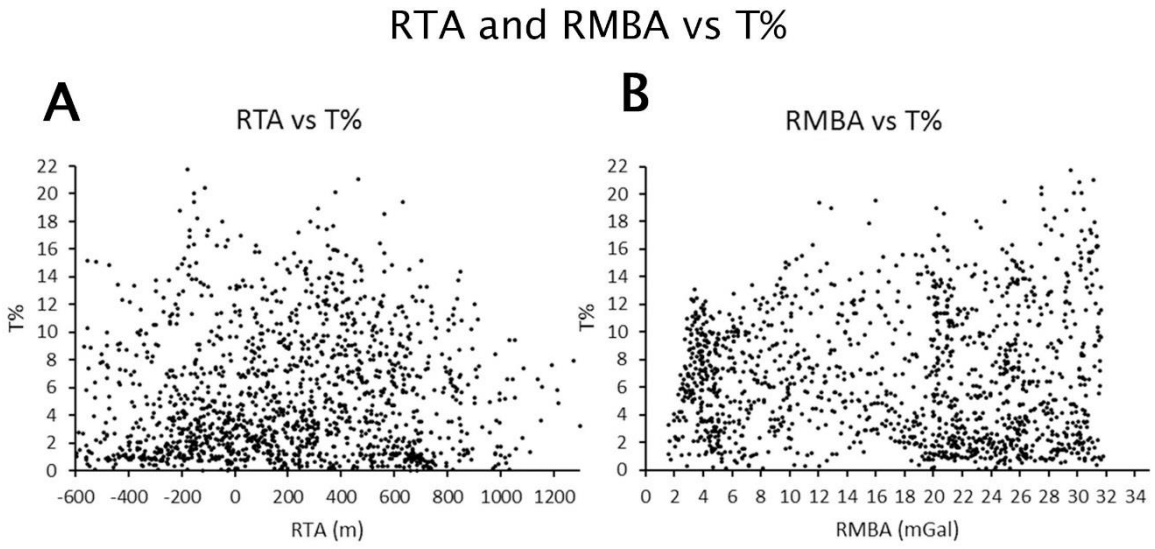

***Figure 3.34**: **A**: Cross-plot of RTA vs T%. **B**: Cross-plot of RMBA vs T%.*

Comparing the mean T% (Table 3.2) to the mean RTA (Table 3.5) and mean RMBA (Table 3.6) for each region (20 – 50 km scale) and half region

(10 – 20 km scale) identified that there is no relation (Figure 3.35) between T% and RTA (R^2 = 0.4 for region and 0.1 for half region) and between T% and RMBA (R^2 = 0.1 for region and 0.0 for half region).

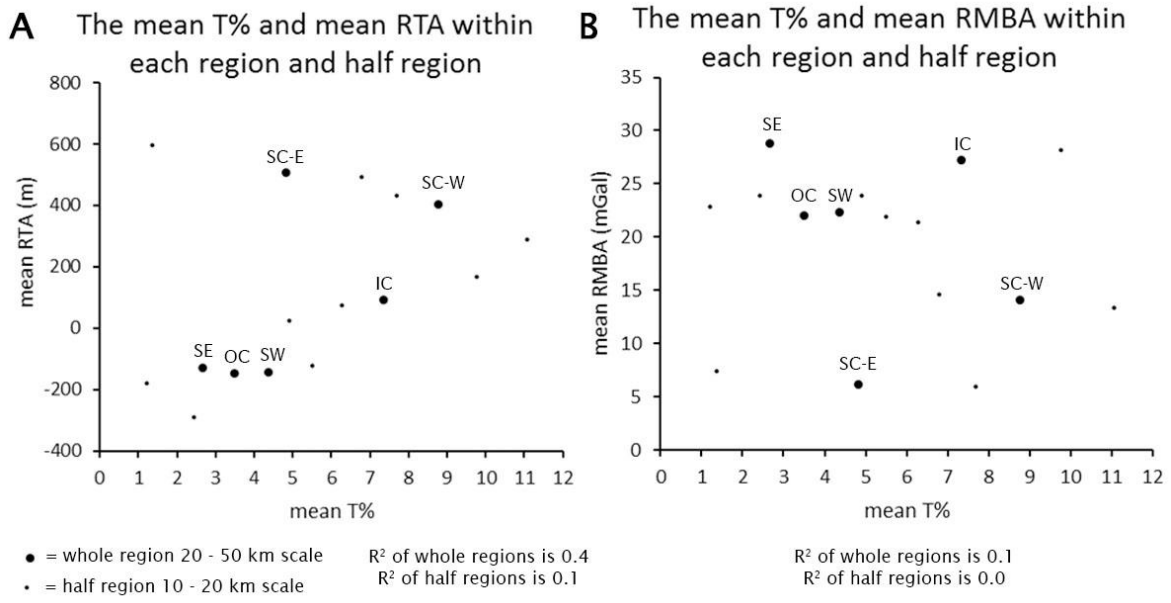

***Figure 3.35**: **A**: Comparing the mean T% to the mean RTA within the regions (big dots) (20 – 50 km scale) and half regions (small dots) (10 – 20 km scale). **B**: Comparing the mean T% to mean RMBA within the regions (big dots) (20 – 50 km scale) and half regions (small dots) (10 – 20 km scale). No correlation is found.*

3.3 Discussion

3.3.1 The reliability of the FID method

Acoustic reflectivity measured by the side-scan sonar and multibeam backscatter was weighted to a value of 0.5 each in the FID map, because they both represent similar seafloor attributes (Figure 3.6). Acoustic reflectivity is not reliable within the axial valley because of low sediment cover making fault traces indistinguishable from the rest of the seafloor. Acoustic reflectivity divided into quintiles is not useful for identifying fault traces far off-axis because of low reflectivity, and because the high reflectivity close to the axis is a major contributor to the upper most quintile. This could potentially be resolved by dividing the side-scan sonar and multibeam backscatter into ~20 km bands parallel to the spreading

axis and dividing each band into quintiles. This way the strong reflectivity on-axis wouldn't account for most the upper quintile, and the low reflectivity off-axis would not fall into the second highest quintile, and therefore could be identified as fault scarps.

Comparing the acoustic reflectivity parameter of the FID method to the north and south looking side-scan sonar images used by Escartin, that are not statistically grouped, showed that the fault polygons were more tightly constrained by the strong reflectors (Figures 3.20 – 3.23). Escartin's fault polygons did not tightly follow the strong reflectors, with some incorporating low reflectors. It appears that the strong reflectors were used to guide the fault traces, however there was more subjective fault interpretation occurring in Escartin et al., (1999). Therefore, I conclude that the acoustic reflectivity component of my FID method increased the objectivity and hence reliability (repeatability) of the fault trace detection compared to the method used by Escartin et al., (1999).

Steep slopes were another parameter of my FID method. Slope was an important contributing factor to identifying faults, this was also true for Escartin's faults. The slope attribute in my FID identified faults within the NTD both close to the spreading axis and far off-axis, unless the change in seafloor relief was <120 m (Figure 3.10) creating a slope <35˚. Slope was important for identifying faults in regions where acoustic reflectivity was low.

Slope direction, both towards and away from the spreading axis, was the final parameter of the FID method (Figure 3.5). Slope direction was important when combined with slope to identify faults in regions where acoustic reflectivity was not effective. Slope direction did not do well at identifying faults within the NTD or along the relic NTD, where shear forces had caused faults to strike away from the trend of the spreading axis (Figure 3.11). However, the T% analysis is used here to measure the extension parallel to plate separation (in this case perpendicular to the spreading axis), hence faults more than 22˚ oblique to the axis were not included.

The fault polygons draw around the FID method were tightly bound to the extent of the FID values 2 – 3 (Figures 3.9 – 3.11). This resulted in more precise fault polygons with smaller heaves than those drawn by Escartin. The combination of multiple fault parameters provides more reliable and less subjective fault polygons than the subjective highlighting faults used in Escartin et al (1999). Comparisons of the faults identified by the FID method to bathymetry profiles highlight that the automatic method capture the tops and bottoms of most faults (Figures 3.9 – 3.11).

The FID method and the Escartin method were unable to identify the shallow dip and low acoustic reflectivity an oceanic core complex (Figure 3.17). The oceanic core complex was identified by its distinctive morphology, suggesting that at future sites any oceanic core complexes would be easily identified in shaded relief bathymetry and can be accounted for, even if it's heave was not measured using the FID method.

The purpose of the FID method is to identify faults that formed at the spreading axis and were pressured off-axis, enabling the T% method to determine regional differences in tectonic extension. Smith et al., (1995) mapped the segment using side-scan sonar and identified young volcanism as hummocky lava flows within the axial valley and, elsewhere, a seamount density of 110 per 10^3 km^2. These volcanic features indicate volcanism is concentrated in the axial valley and there are no significant regions of off-axis volcanism that could over-print the tectonic fabric created on-axis and preserved off-axis. Therefore, the T% and RTA measurements should be representing volcanic and tectonic processes occurring at the spreading axis.

3.3.2 T% results

Analysis provided new insight into the T% method beyond that discussed in Chapter 2. The 20 km profiles spaced at 5 km intervals provided better T% resolution in a north – south direction than in an east – west direction. The 20 km profiles meant that T% could not be precisely linked to any individual feature measuring less than 20 km across, for example; when two clusters of faults occur at each end of a profile, the T%

point was placed at the centre, even if there were no faults at the centre. This could be partially corrected if the T% point's location was weighted towards where heave measurements occur. T% provided 20 km scale extensional measurements comparable in scale to RMBA. Another influence on T% is the detection limit of the FID method unable to identify faults with less than 150 m heave, potentially reducing T% measurements by 11.5%.

My T% method identified areas of high tectonic extension, >10%, related to the regional geology (Figure 3.15). The largest area of high extension was west of the spreading axis and in the southwest region. Close to the spreading axis in the inside corner region, there was an area of high T%, a mean of 13±1.5% in area 'C' in Figure 3.15, which likely joined up to the spreading centre west region of high T%, a mean of 13±1.5% in area A in Figure 3.15. However, they do not join because the FID method failed to identify the southwest facing axial valley wall fault.

The high T% in the southwest region, mean T% of 11±1.3% in area B in Figures 3.15 and 3.18, coincides with the location of the Outside Corner of the segment to the south of the Broken Spur segment. This region, close to the NTD, is expected to have a low melt supply and high tectonic extension. Outside Corners are typically deeper than Inside Corners, have a covering of basaltic rocks, regular normal faulting, and a normal thickness of crust (Tucholke & Line, 1994). However, this Outside Corner has a maximum RTA of 700 m, similar to that of the Inside Corner to the north indicating they have similar topographic heights, and both the Inside and Outside Corners have a high mean T% around 12±1.4%.

Within T% area A (Figure 3.16) a salient of low T% (4±0.5%) can be explained by the FID method failing to identify the oceanic core complex's detachment fault. T% is high to the south (12±1.4%) and east (11±1.3%) of the oceanic core complex (Figure 3.17) however the FID method failed to measure heave over the 2.5 km detachment fault that would have raised the T% of the surrounding area to 22±2.5%.

The largest influence on T% is the distance from the spreading axis, with T% reducing to almost 0% after 34 km off-axis. To determine if a different fault identification method was able to identify more off-axis faulting I calculated a T% map using Escartin et al., (1999)'s fault picks, which are more subjective, especially off-axis. There was no good correlation between the T% map using my FID faults and those using Escartin's faults. The main differences in T% is that Escartin's faults produce, on average across the whole study area, twice the T%. The difference in the distribution of high T% areas occurs in the northeast of the spreading centre east region and the southeast area of the inside corner region, where weighted T% differences were as high as 60%. In these areas Escartin had identified more faults, which generated a higher T%.

Escartin et al., (1999) calculated that the Eurasian Plate had 50% less tectonism than the N. American Plate. Using the T% method I found that within 18 km of the axis, the Eurasian Plate had 20% less tectonic extension than the N. American Plate. Escartin et al., (1999) also found that the eastern flank had 7% extension while the western flank had 15% extension within 10 km of the spreading axis and north of the NTD. I calculated T% of the eastern flank as 8% within 18 km of the axis, similar to what Escartin found. However, I calculated 10% for the western flank, which is 5% lower than that calculated by Escartin. The results of the FID method are more reliable because they cross-correlate multiple fault parameters to objectively identify faults and the fault polygon is tightly constrained to those pixels. Whereas Escartin's method only uses one dataset whose fault identification parameter of high reflectivity is not empirical defined. The fault polygons are then drawn subjectively and does not consistently follow the identifying parameter.

3.3.3 The relation of RTA to RMBA

Two proxies were used for crustal thickness, RTA and RMBA. RTA was hypothesised to relate to crustal thickness because of the Airy isostasy model or density using the Pratt model. The mean RTA at 1 mGal intervals

calculated a negative correlation (R^2 = 0.87) (Figure 3.32). There was a visual relation between relative difference in mean RTA and mean RMBA between regions (Figure 3.30 and Table 3.6). Along the spreading centre west and east regions low mean RMBA (6 – 14 mGal) and high mean RTA (404 – 509 m). Compare these to the inside corner and outside corner regions where RMBA is high (22 – 27 mGal) and RTA is low (93 – -148 m). The southwest and south east regions also have high RMBA (22 – 29 mGal) and low RTA (-130 – -144 m). There was also a regional relation between the two plates, where the N. American Plate had a high mean RMBA (20 mGal) and low RTA (105 m), and the Eurasian Plate had the opposite relation with a high mean RTA (221 m) and low RMBA (14 mGal). Plotting the mean RTA and mean RMBA for each region (20 – 50 km) and half region (10 – 20 km) identified an inverse relation with R^2 of 0.7 and 0.6 respectively (Figure 3.33).

However, no statistical relation between RMBA and RTA could be identified at a 1 km scale (Figure 3.32) and the relation deteriorated at scales smaller than the regions (shown by reducing R^2 values at smaller scale in Figure 3.33). Additionally, the crustal thicknesses calculated from the RTA were not the same as those calculated using the RMBA suggesting that RTA cannot be used for calculating crustal thickness with the Airy isostasy equation.

Rommevaux et al., (1994) compared bathymetry depth to gravity anomalies in the south of the Broken Spur segment (28° N – 29° N). Interestingly, they observed that the shallow bathymetry towards the north of the study area (Figure 3.1) aligned with the spreading centre, was offset by ~10 km from gravity lows that represents the location of focused melt supply towards the spreading axis. On the N. American Plate the offset was to the south, while on the Eurasian Plate the offset was to the north. The offset between crustal thickness and bathymetric depth was explained by Rommevaux et al., (1994) as the bathymetry depth being controlled primarily by tectonic processes in the upper crust that do not affect all the crust. This observation may explain why there is not a better statistical

correlation between RMBA and RTA within the regions at scales less than 20 km.

RTA was not as useful for calculating crustal thickness, however, it is useful for quantifying broad regions (>5 km) of shallow and deep bathymetry that may be diagnostic of melt supply along the spreading axis, and preserved in the crust off-axis. Two relic regions were identified using RTA. Firstly the basins (Figure 3.3) that produced areas of negative RTA (<-500 m) in the southwest region and the outside corner region aligned with the NTD, interpreted as the trace of the relic NTD. The second was regions of shallow seafloor (Figure 3.3) that produced positive RTA (>500 m) in the spreading centre west and spreading centre east regions that identified the off-axis relic of the spreading segment's domed magmatic centre (Figure 3.4). Additionally, the positive RTA in the inside corner region (700 m) located the inside-corner high, while low RTA (<-200 m) on the opposite side of the spreading axis in the outside corner region identified the deep outside corner feature (Tucholke & Lin, 1994.

3.3.4 The relation of RTA and RMBA to T%

When cross-plotting the RTA and RMBA at each T% point against the measured T% no correlation is found, similar to how RTA and RMBA were not correlated on the small scale. When mean T% was compared to mean RTA and mean RMBA at the region (20 – 50 km) and half region (10 – 20 km) scales there was also no correlation found (Figure 3.35). This indicates crustal thickness responsible for RMBA and the unidentified processes responsible for RTA are not related to T%.

The only relation that could be identified was on the whole plate scale. The N. American Plate had a higher and more uneven T% distribution, while the Eurasian Plate had a lower and more evenly distributed T%. This asymmetry is detectable in the RMBA distribution, suggesting that the Eurasian Plate has thicker crust (Lin et al., 1990).

Escartin et al., (1999) found that the tectonic extension measured along axis does not relate to predicted melt supply. They therefore

concluded that fault spacing and heave are primarily controlled by rheology, and secondarily by lithospheric thickness. This conclusion is supported by our findings where T% measuring fault heave over large areas (20 km) was not related to RMBA that measured crustal thickness. Fault extension was also not related to where melt supply was expected to be highest along the relic segment centre identified by the positive RTA, or where melt supply was expected to be lowest along the relic NTD identified by negative RTA.

3.4 Conclusion

The FID method more precisely and reliably identifies faults when compared to the subjective interpretation of a single dataset used in Escartin et al. (1999). The FID method becomes more unreliable after 30 – 40 km off-axis and over oceanic core complexes. The T% method calculates extension over a 20 km distance which is not comparable to individual seafloor features, however this distance is comparable to the RMBA and large wavelength deviations from mean crustal depth in the RTA.

RTA and RMBA are inversely related at scales >10 – 20 km, however no correlation is found at smaller scales. RTA is unable to calculate crustal thickness using Airy isostasy and should be used to quantitatively identify shallow and deep bathymetric features at wavelengths >5 km that are potentially related to relic segment centres and relic discontinuities.

The slow spreading, orthogonal segment of the Broken Spur segment has asymmetric tectonic extension, with the Eurasian Plate having 20% less tectonic extension than the N. American Plate. T% was not correlated at any scale to crustal thickness as determined by RMBA or to relic segment centres or relic NTDs as identified by RTA. This suggests T% is related to upper crustal processes independent of melt supply that influences crustal thickness and the position of second order segment centres and discontinuities. If T% and crustal thickness are unrelated then no correlation should be found at faster spreading ridges (Chapter 4) or where melt supply varies over time (Chapter 5).

Chapter 4: Costa Rica Segment

4.1 Introduction

This chapter focuses on the comparison of T% to the melt supply that occur at a Mid-Ocean Ridge segment centre and ends. The segment being investigated is the Costa Rica segment with an intermediate spreading rate (6.6 cm yr^{-1} full rate) (Lonsdale & Klitgord, 1978). The Costa Rica segment is the most eastern segment of the Cocos - Nazca Ridge that generated the Panama Basin (Figure 4.1). The Cocos - Nazca Ridge was initiated during the breakup of the Farallon plate around 23 Ma, and its current configuration originated around 14.7 Ma (Lonsdale, 2005; Meschede & Barckhausen, 2000). Spreading rates increase towards the eastern end of the Cocos - Nazca Ridge allowing the Cocos Plate to rotate counter-clockwise, with occasional southward ridge jumps to keep the Mid-Ocean Ridge aligned with the Galapagos hotspot (Barckhausen et al., 2001).

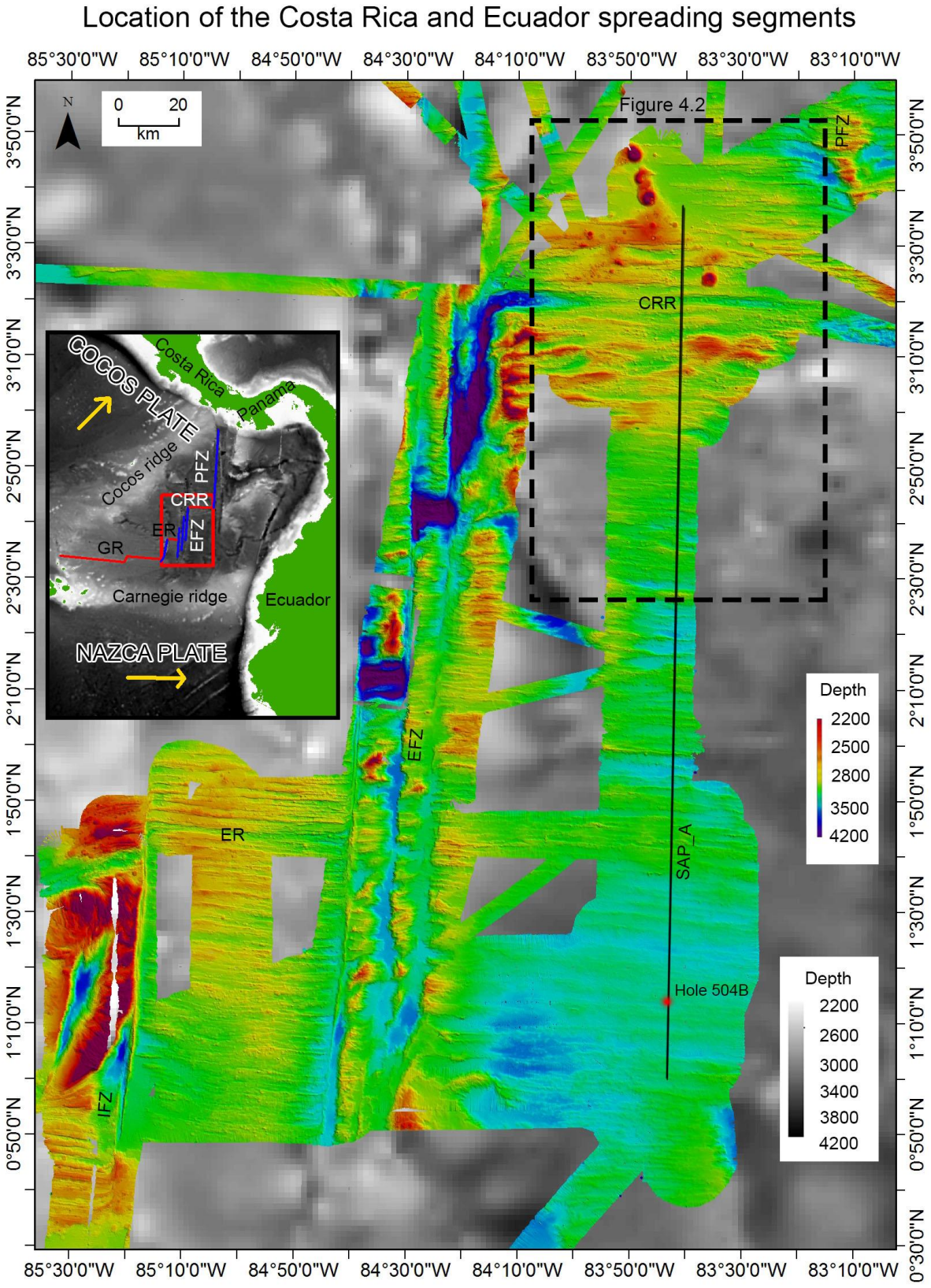

***Figure 4.1**: Location of Panama Basin with JC112, 113, and 114 bathymetry in rainbow colour. CRR = Costa Rica Ridge, ER = Ecuador Ridge, PFZ = Panama Fracture Zone, EFZ = Ecuador Fracture Zone, IFZ = Inca Fracture Zone, SAP_A = Synthetic Aperture Profile A. Grey scale*

background is satellite bathymetry provided by NOAA (Amanta & Eakins, 2009). Dashed black line is the extent of the study area shown in Figure 4.2. In the global location inset the first order segments are marked in red and fracture zones marked in blue.

The OCSAR project (Hobbs & Peirce, 2015) collected multibeam bathymetry and backscatter data as well as three Synthetic Aperture Profiles (SAP). The Costa Rica Ridge and Ecuador Ridge bathymetry and backscatter data sets are derived from multibeam echo sounder data acquired in 2015 for the OSCAR project (Hobbs & Peirce, 2015) (Figures 4.1 and 4.2), collected by the *RRS James Cook* during cruises JC112/113 and JC114. The bathymetry and backscatter was cleaned manually to remove poor data, then gridded at 50 m. The multichannel seismic reflection profiles used two ships to synthesize an 8.5 km long streamer, which was used in this study to measure sediment thickness. The seismic reflection processing was done on-board and interpreted by Dr Wilson at the University of Durham.

4.2 Results

Bathymetry coverage of the Costa Rica segment extends off-axis to 40 km north of the spreading axis, and 277 km south of the spreading axis. As was discussed in Section 2.1.3, increasing sediment thickness reduces the reliability of the FID method beyond 70 km off-axis. My analysis focuses on data within 100 km of the spreading axis, extending as far south as 2˚25’ N and as far north as 3˚52’ N (Figure 4.2). The extra 30 km beyond the reliability range of the FID method is to further test this approach.

4.2.1. Identification of bathymetric features

The bathymetry north of 2˚55’ N has an average depth of 2910 m (range: 3880 – 2170 m) with a large range of 1715 m, a standard deviation of 148 m, and appears rugged (Figure 4.2). South of 2˚55’ N the bathymetry is deeper, having an average depth of 3200 m (range 3980 –

2690 m) with a narrower range of 1287 m, standard deviation of 121 m, and appears smoother.

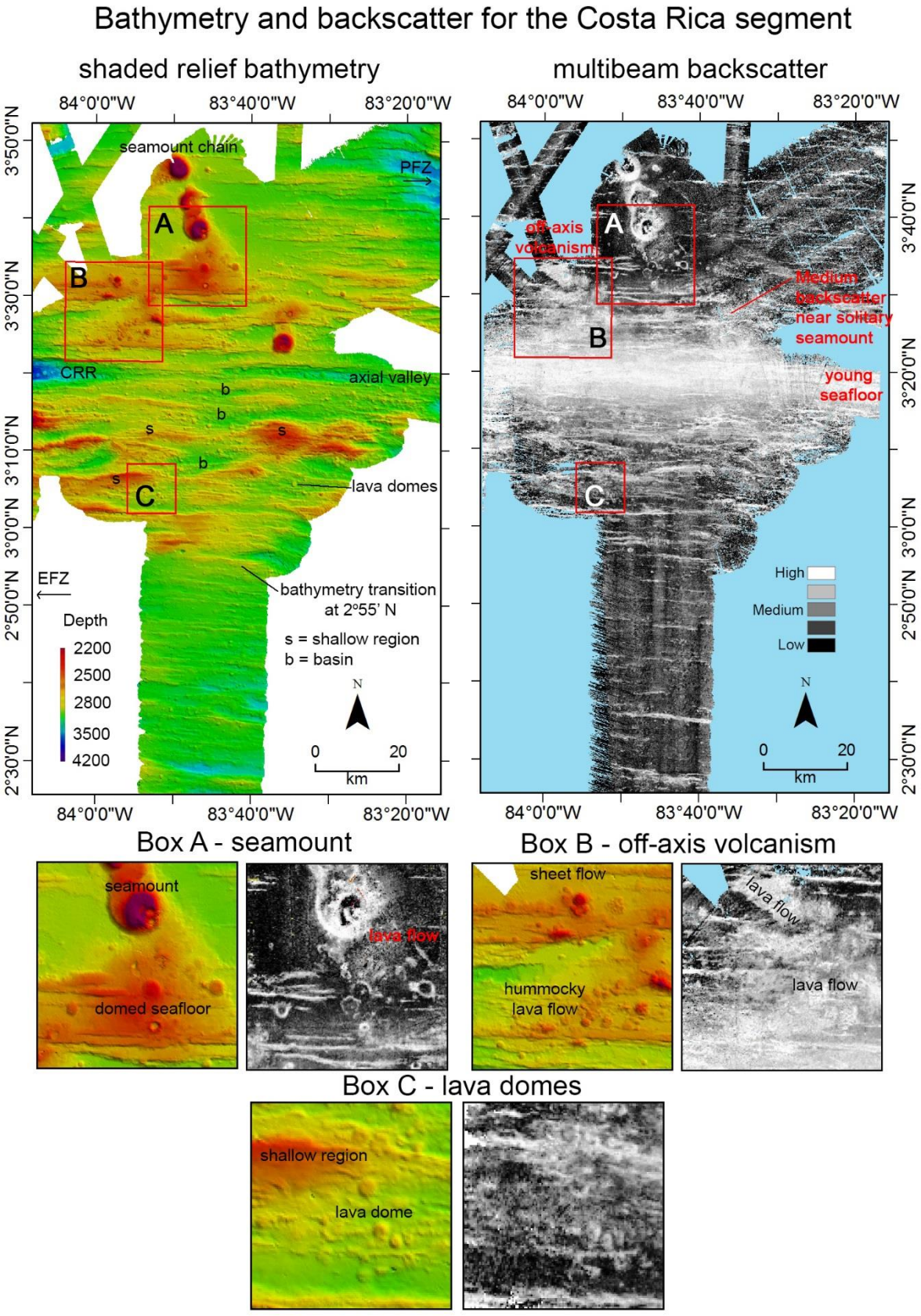

***Figure 4.2**: 50 m resolution shipboard multibeam bathymetry (top left) and multibeam backscatter (top right). Strong E – W backscatter band (top right) indicated youngest seafloor and spreading axis. Box A illustrates seamounts and domed seafloor off-axis. Box B illustrates off-axis volcanism with sheet flows and hummocky lava flows. Box C illustrates lava domes.*

Multibeam backscatter identifies that a region of seafloor with strong reflectivity within the upper quintile occurs between 3˚23' N - 3˚16' N (Figure 4.2 top right) indicating a band of hard seafloor. Young crust does not have a thick sediment cover that is acoustically absorbent indicating that the centre of this high reflectivity band is the location of the spreading axis. Reflectivity within the upper quintile extends for 8 km either side of the spreading axis.

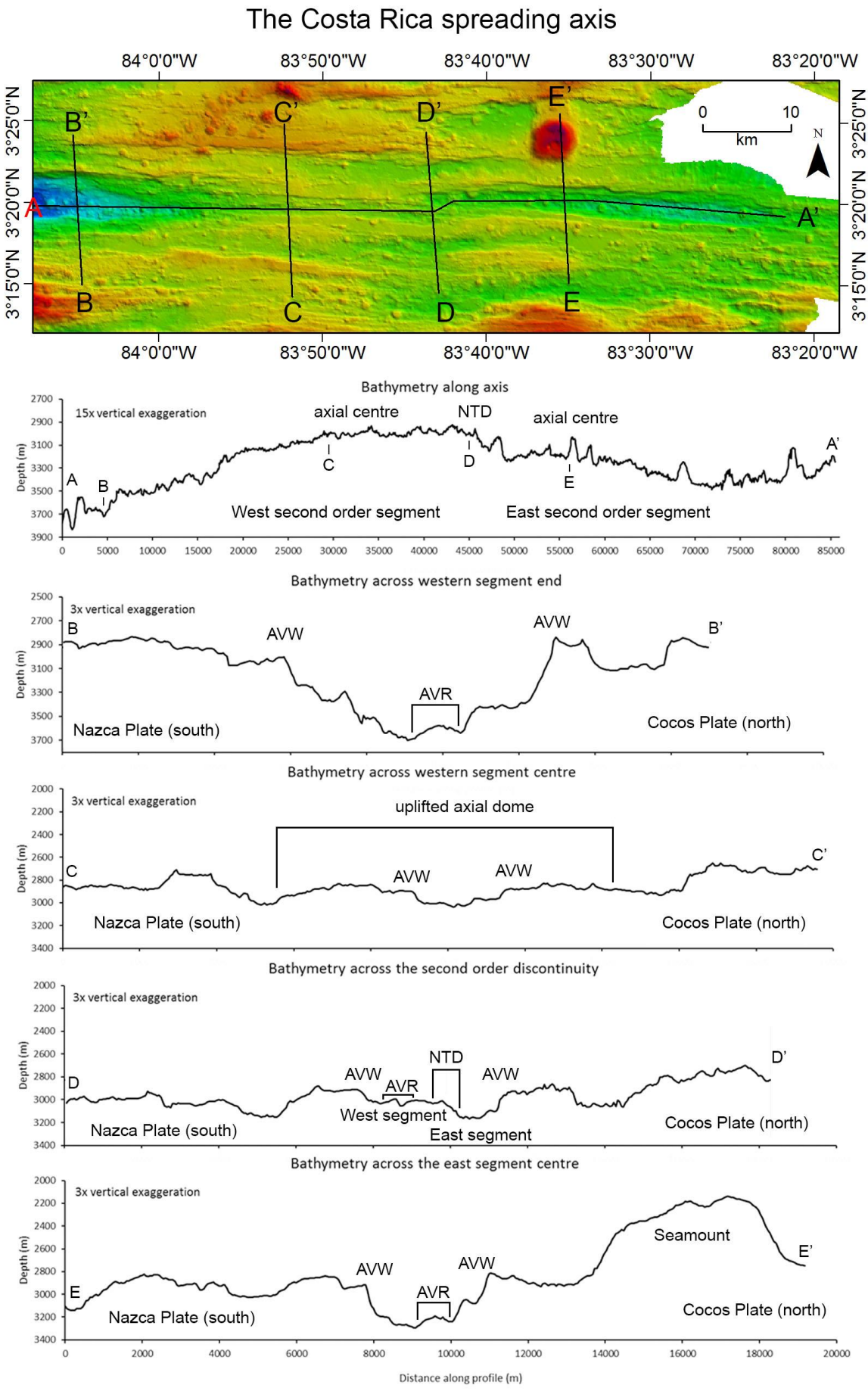
The Costa Rica spreading axis
84°0'0"W
83°50'0"W
83°40'0"W
83°30'0"W
83°20'0"W
3°25'0"N
3°20'0"N
3°15'0"N
A
A'
B
B'
C
C'
D
D'
E
E'
0
10
km
N
Bathymetry along axis
15x vertical exaggeration
axial centre
NTD
axial centre
Depth (m)
West second order segment
East second order segment
Bathymetry across western segment end
3x vertical exaggeration
AVW
AVR
Nazca Plate (south)
Cocos Plate (north)
Bathymetry across western segment centre
uplifted axial dome
Bathymetry across the second order discontinuity
West segment
East segment
Bathymetry across the east segment centre
Seamount
Distance along profile (m)

***Figure 4.3**: Bathymetry of the axial valley and spreading axis of the Costa Rica segment. AVW = Axial Valley Wall, AVR = Axial Volcanic Ridge, and NTD = Non-Transform Discontinuity. Profile A – A' illustrates the two second order segments visible along axis. Profile B – B' illustrates the wide axial valley at the first order segment end. Profile C – C' illustrated the domed centre of the western second order segment. Profile D – D' illustrates the overlapping tips of two second order segments in the NTD. Profile E – E' illustrates the axial valley of the eastern second order segment and an off-axis seamount.*

The Costa Rica Ridge's (CRR's) axial valley was identified from 200 - 600 m fault scarps facing towards each other and bounding a deep valley (Figure 4.3 profiles B – E). The axial valley's width ranges from 6.5 km in the west, to 1.9 km at its thinnest near the segment centre, and 3.7 km in the east. Depth from the top of the axial valley walls to their bases range from 140 m at the segment centre to 650 m at the segment ends. Within the axial valley between 83˚57' W – 83˚37' W, are east - west trending symmetrical ridges that are 2 – 4 km long and 200 m high. These are interpreted as the axial volcanic ridges (AVRs) (Figure 4.3 profiles B and C).

The spreading axis is located by tracing along the centre of axial valley. The spreading axis trends at 091˚, is 148 km long (from 3˚20' N; 84˚11' W to 82˚55' W; 3˚17' N), and bound by sinistral transform fault zones orientated 177˚ S - 357˚ N (Figure 4.1). My study area (Figure 4.2) covers the eastern 94 km of the CRR. Within my study area the average depth along axis is 3300 m, with the greatest depth at 3800 m where the spreading axis intersects the Ecuador fracture zone. The spreading axis is divided into 2 second order segments, with a 1.5 km left-stepping separation across-axis and a 2.4 km overlap along axis between 83˚44' W - 83˚42' W (profile D in Figure 4.3). The 2 second order segments are separated by a non-transform discontinuity (NTD).

The western second order segment is ~200 m shallower than the eastern segment (Profile A in Figure 4.3). The western segment has a shallow axial valley only 100 m deep and low relief in the off-axis

direction. The off-axis crust within 4 km either side of the western spreading axis is uplifted into a dome (Profile C in Figure 4.3). The eastern second order segment has a deep axial valley 300 – 400 m in depth with a prominent AVR along the axis. The seafloor around the eastern segment has an axial dome extending for 2 km in the off-axis direction, either side of the axis (profile E in Figure 4.3).

Off-axis, within the rugged seafloor between the spreading axis and 2˚55' N, there are large regions of shallow bathymetry (labelled 's' in Figure 4.2). They range from 12 - 19 km long and 2 - 8 km wide. On the Nazca Plate, several large and prominent shallow regions reach heights of 700 m when measured from their base to peak, and are elongated in an E – W direction. The annotated shallow features on the Nazca Plate can be traced to align with the current on-axis domed centres for the second order spreading segments, suggesting they are the off-axis relics of the segment centres. However, on the Cocos Plate the regions of shallow bathymetry have a different morphology and do not align with the segment centres. The shallow regions on the Cocos Plate appear as domes with hummocky lava flows and strong backscatter (Boxes A and B in Figure 4.2). The smoothness of the shallow regions on the Cocos Plate suggests they could be volcanic terrains, developed from active off-axis volcanism that has over printed seafloor morphology inherited at the spreading axis.

On the Nazca Plate, between the shallow regions are a series of basins aligned along 83˚44' W (labelled 'b' in Figure 4.2). These basins have a length of 8 - 15 km, width of 2 - 5 km, and depth below the surrounding seafloor of 130 - 330 m. These basins align with the NTD (profile D Figure 4.3), suggesting they may be the off-axis relics of the discontinuity. The basins cannot be traced on the Cocos Plate, however, the presence of multiple seamounts (Profile E in Figure 4.3 and box A in Figure 4.2) and fresh lava fields (Box B in Figure 4.2) suggests that if these are the off-axis relics of the NTD they have subsequently been infilled by off-axis volcanism.

Seafloor volcanic features were identified from bathymetry and high backscatter. The seamounts on the Cocos Plate are circular features, 5 –

7 km in diameter, and 800 - 1000 m high (Box A in Figure 4.2). They have shallow profiles with steep flanks and flat, often cratered, tops resulting in low aspect ratios (Profile E in Figure 4.3). The seamounts are not cut by faults, suggesting that they form off-axis, outside the zone where axial valley walls form. Seamounts are only visible on the Cocos Plate indicating their origin is from off-axis volcanism. Their volumes were calculated using a triangular irregular network (TIN) in ArcGIS™, calculated from the bathymetry data. A TIN keeps the feature's original shape while assuming a flat base at the feature's deepest point. The seamount chain (Figure 4.2) has a volume of 8.4 km^3 and height of 770 m. The southern-end of this seamount chain has a domed region, extending over 13x11 km and centred at 83˚46'31" W; 3˚33'4" N (Box A in Figure 4.2). Although this volcanic feature is located ~50 km from the spreading axis, strong acoustic backscatter indicates recent lava flows suggesting this is a focus for off-axis volcanism. There is a solitary seamount within 5 km of the spreading axis at 83˚35' W; 3˚23' N (Profile E in Figure 4.3) with a volume of 0.8 km^3 and height of 260 m.

Lava flows were identified as having an amorphous outline, having strong multibeam backscatter, and flat topography (Box B in Figure 4.2). Lava flows were identified on the Cocos Plate near 83˚57' W; 3˚32' N over an area of 46 km^2 and at 83˚57' W; 3˚29' N with an area of 34 km^2. These lava flows occur as two morphological types. Sheet flows have a flat morphology and fill basins while hummocky flows form overlapping mounds generating positive relief. Recent lava flows on the Cocos Plate are concentrated to the west of the segment, whereas, towards the east, lava flows near the solitary seamount have a lower backscatter suggesting greater age (backscatter map in Figure 4.2). On the Nazca Plate there are no easily identifiable large areas of fresh lava flows like those identified on the Cocos Plate. This suggests off-axis volcanism is focused on the Cocos Plate, primarily towards the west.

Lava domes were identified as circular features that are distinctive from seamounts because they appear domed or conical in profile. Lava domes have diameters ranging from 100 - 1000's m, and heights of 10 -

100's m (Box C in Figure 4.2). Lava domes are often cut by faults, suggesting formation on-axis and then were transported off-axis through the region of axial valley wall formation within the active tectonic zone either side of the spreading axis. The volumes of the lava domes were calculated using a TIN. Lava domes have an average aspect ratio (width/height) of 8 (range: 1 - 22), mean height of 140 m (range: 30 – 680 m), and mean width of 940 m (range: 350 - 2230 m). Their volumes are wide ranging with a mean of 3.9×10^7 m^3 (range: 3×10^3 m^3 – 2.3×10^8 m^3), an average area of 7.8×10^5 m^2 (range: 9.0×10^4 m^2 – 3.9×10^6 m^2). Lava domes occur at a density of 2 per km^2.

The distribution and attributes of volcanic features and larger bathymetric features such as the relic spreading centres or relic NTD are useful proxies for the focus and magnitude of magmatism. The proxy for tectonic extension I use is the heave of normal faults.

4.2.2 Identifying faults

In Chapter 4, the FID method described in Chapter 2 used the fault criteria of slope angles between 35˚ - 60˚ (Figure 4.4A), slope directions between 336.5˚ – 021.5˚ and 158.5˚ – 203.5˚ (Figure 4.4B), and multibeam backscatter in the upper most quintile (Figure 4.4C). Within the study area 1% of cells met the criteria for slope angles (Figure 4.4D), 32% of the seafloor met the fault criteria for slope direction (Figure 4.4E), and 20% met the criteria for backscatter (Figure 4.4F).

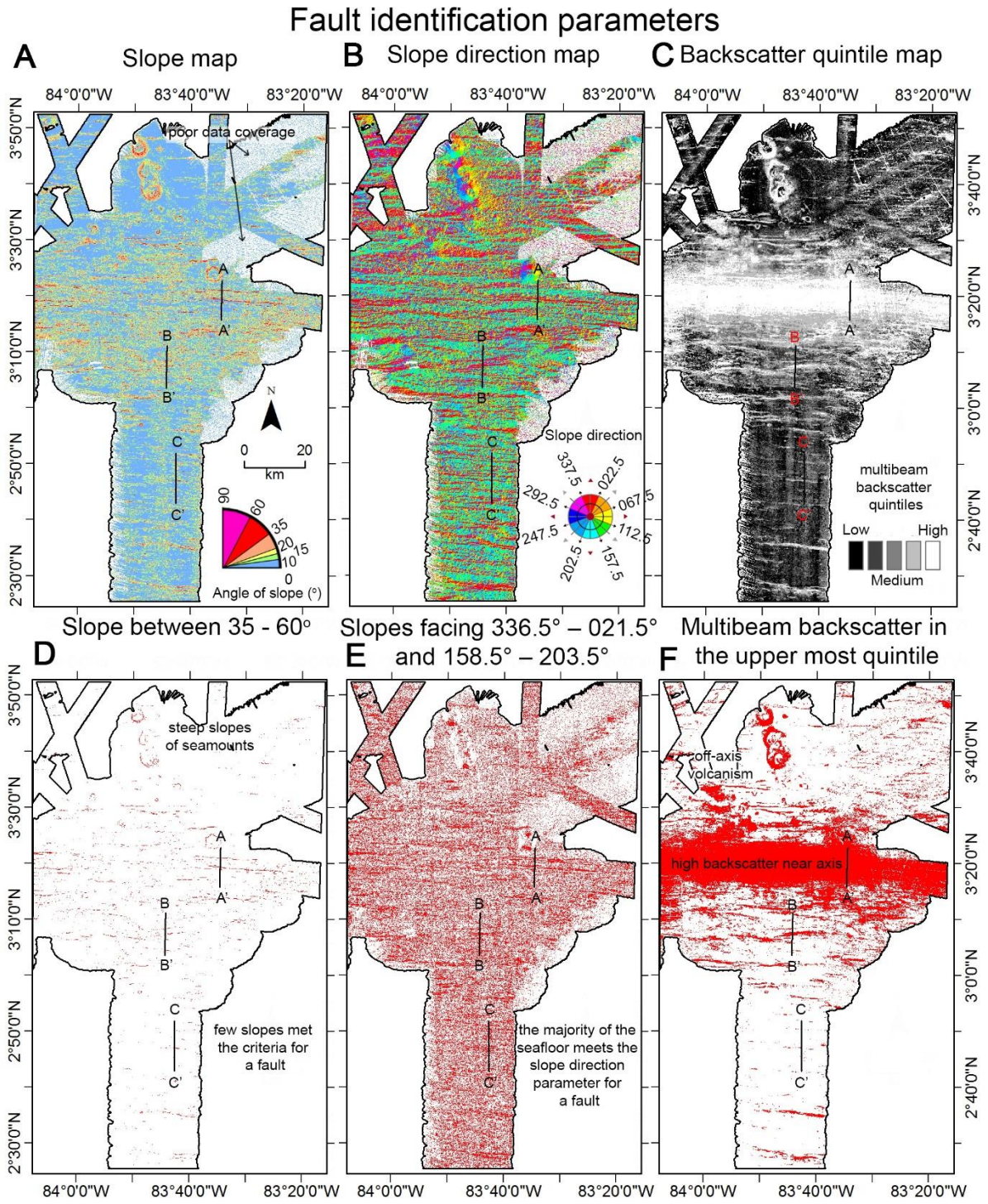

***Figure 4.4**: The parameters used in the FID method to identify normal faults. **A**: Slope angles between 35˚ - 60˚. **B**: Slope direction between 336.5˚ – 021.5˚ and 158.5˚ – 203.5˚. **C**: Backscatter in the upper most quintile. **D**: Pixels that met the slope parameter. **E**: Pixels that met the slope direction parameter. **F**: Pixels that met the backscatter parameters. Profiles A, B, and C are used to illustrate the fault parameters against bathymetry in Figure 4.5. Regions of poor sonar reflection density in panels A, B, and E appear speckled and cannot be used in the analysis. In Figure 4.2 these*

regions have had an interpolation applied. These regions of poor data coverage are removed for the final analysis (Figure 4.15).

The fault polygons circle 6% of pixels that met the slope direction criteria, 1% of pixels that met the slope angle criteria, and 8% of pixels that met the backscatter criteria. This meant that backscatter was the most reliable criteria to indicate faults. The majority of the seafloor was covered by slope direction values, making it a poor indicator by itself of a fault. The low percentage that steep slopes contributed to faults is unexpected because in Chapter 3 it was the highest contributor. The low percentage of backscatter contributing to fault polygons could be because backscatter is mostly concentrated within 8 km of the spreading axis.

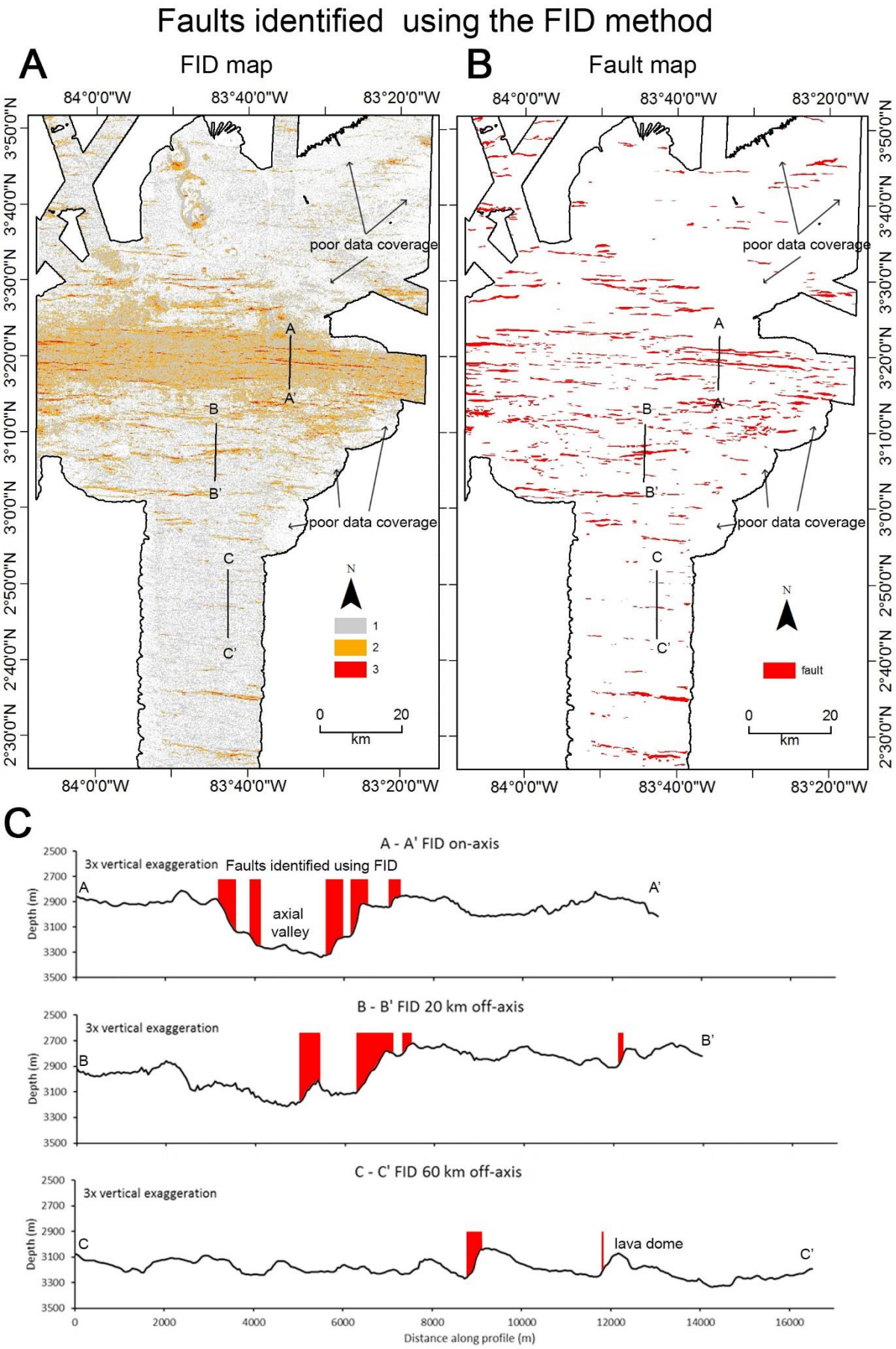
Faults identified using the FID method
A
FID map
B
Fault map
84°0'0"W
83°40'0"W
83°20'0"W
3°50'0"N
3°40'0"N
3°30'0"N
3°20'0"N
3°10'0"N
3°0'0"N
2°50'0"N
2°40'0"N
2°30'0"N
poor data coverage
A
A'
B
B'
C
C'
N
1
2
3
fault
0
20
km
C
A - A' FID on-axis
3x vertical exaggeration
Faults identified using FID
axial valley
B - B' FID 20 km off-axis
C - C' FID 60 km off-axis
lava dome
Depth (m)
2500
2700
2900
3100
3300
3500
0
2000
4000
6000
8000
10000
12000
14000
16000
Distance along profile (m)

***Figure 4.5**: **A**: Fault identification map (FID). **B**: Fault polygons are drawn around FID values of 2 – 3. Regions of poor data coverage (Figure 4.4) create FID values of 0 and so fail to identify faults. **C**: Bathymetry profiles A, B, and C illustrate how the FID method has identified faults when compared to bathymetry. Profile A – A' crosses the axial valley and highlights the axial valley wall faults. Profile B – B' is 20 km south of the spreading axis outside the region of strong backscatter. Profile C – C' is 60 km off-axis approaching the limit of the FID method reliable range.*

Bathymetric profiles perpendicular to fault trace allow for visual identification of fault scarps as asymmetrical half-grabens with their steep slopes facing towards the spreading axis. The FID method is able to identify these fault scarps close to the spreading axis (Figure 4.5 Profiles A and B). Section 2.1.3.1 illustrated that at distances >70 km off-axis thick sediment masks steep half-grabens creating a smooth seafloor (Figure 4.5 Profile C). At distances of >60 km off-axis the FID method identified fewer faults, past 80 km off-axis only the largest fault scarps are identified by the FID method.

To measure the heave of the faults identified using the FID method (Figure 4.5 top right) I used 190 profiles that were 180 km long, stretching from 3˚52' N – 2˚25' N, and were orientated 000˚. The profiles were spaced at 500 m intervals in an E – W direction. This results in each fault being crossed by multiple profiles, ensuring that heave was measured at the fault's thinnest and widest points in order to get a representative measurement (Figure 4.6). This resulted in the frequency of fault heave measurements being much higher than the number of faults identified within the study area, which was 693. Using this method, the mean fault heave was 264 m (range: 50 – 1618 m) (Figure 4.6).

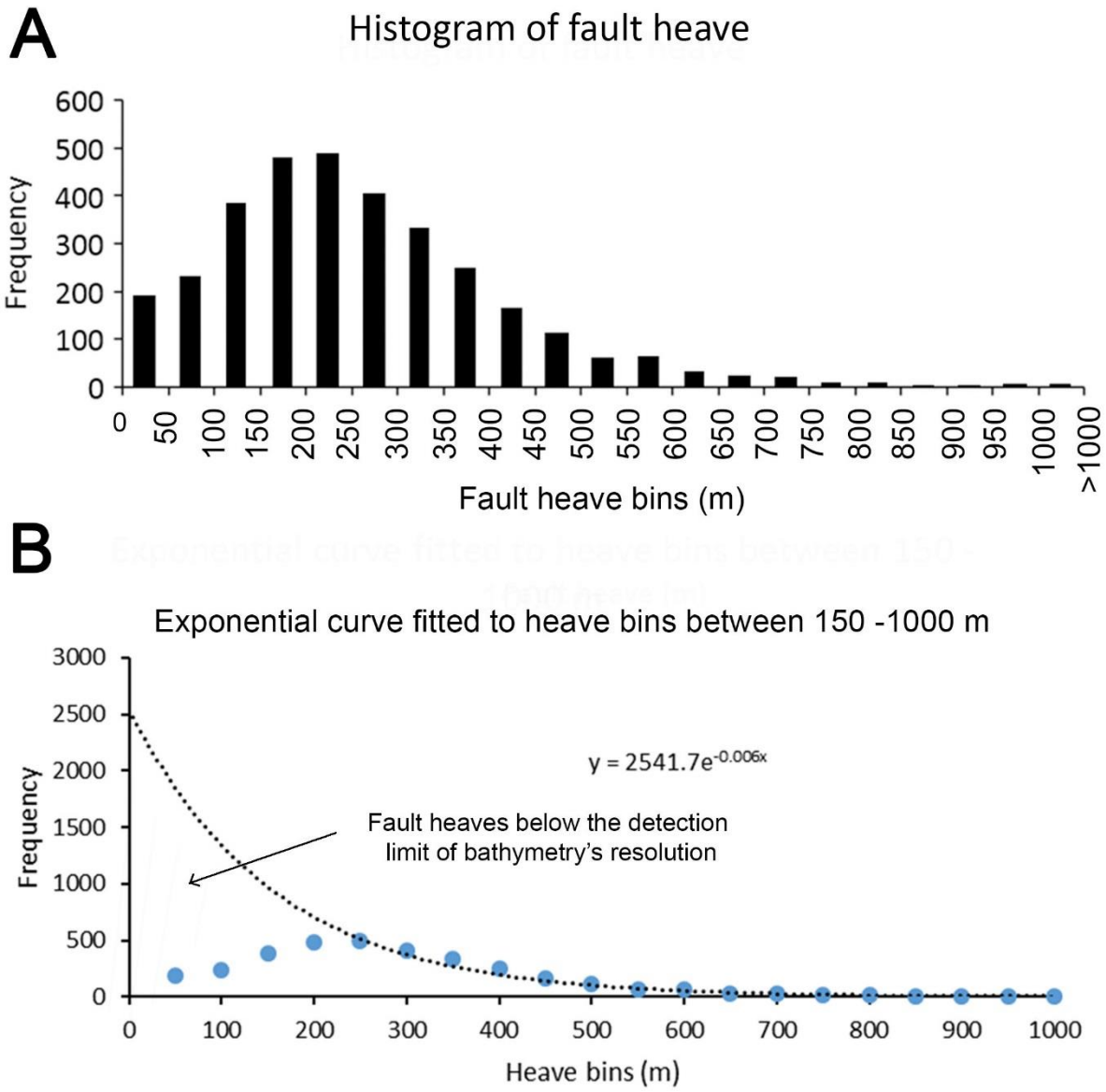

***Figure 4.6**: Fault heave measured at 500 m intervals along each fault to provide a representative distribution. **A**: Histogram of fault heaves. **B**: Measured fault heave for heave bins (blue dots), exponential curve fitted for bins between 150 – 1000 m to predict smaller fault heave that is missing because of the bathymetry's 50 m resolution.*

Small faults would be expected to be more numerous than large ones however faults with heave below 150 m are not detected because of the bathymetry resolution. The missing heave from the faults smaller than the detection limit can be predicted by applying an exponential equation to heaves measured between 150 – 1000 m (Figure 4.6B). The integral of the measured faults is 950 km, while the integral of the exponential curve is 1,380 km. This means I am potentially missing 429 km of heave across

the study area due to the bathymetry resolution. To calculate the potential influence this has on T% I calculated what percentage the missing heave is of the total length of the profiles used to measure heave. The total length of the profiles clipped within the data's extent is 19,076 km. This meant that the measured faults calculated 5% extension, and the predicted missing faults calculated 7.2% extension. T% is calculated slightly differently, however the principle is similar suggesting that the bathymetry resolution is potentially reducing T% by 0.6%. Assuming that this unaccounted for heave is evenly spread across the study area, the T% distribution will underestimate brittle extension by 30% of the total.

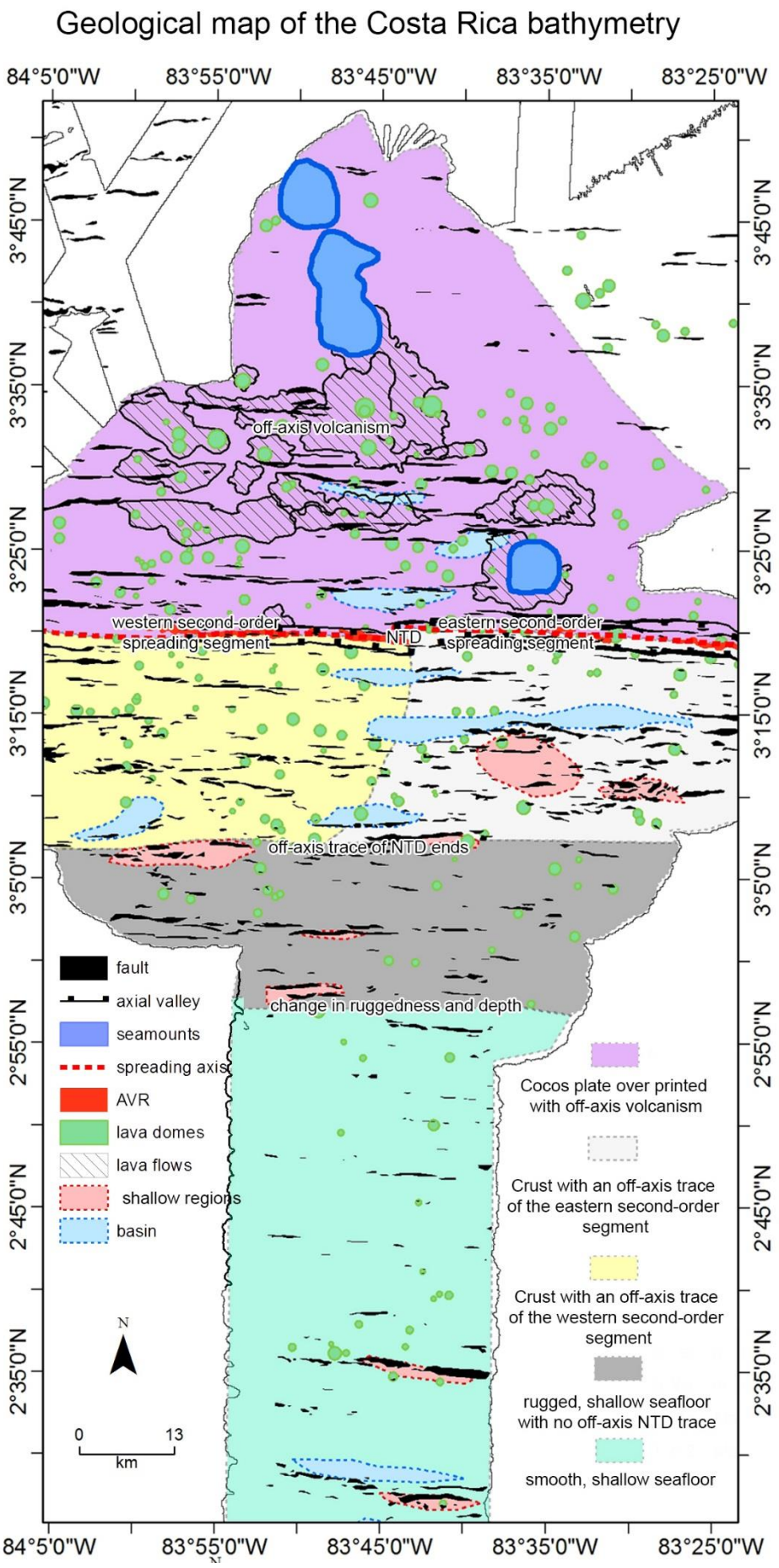
Geological map of the Costa Rica bathymetry
84°5'0"W
83°55'0"W
83°45'0"W
83°35'0"W
83°25'0"W
3°45'0"N
3°35'0"N
3°25'0"N
3°15'0"N
3°5'0"N
2°55'0"N
2°45'0"N
2°35'0"N
off-axis volcanism
western second-order spreading segment
NTD
eastern second-order spreading segment
off-axis trace of NTD ends
change in ruggedness and depth
fault
axial valley
seamounts
spreading axis
AVR
lava domes
lava flows
shallow regions
basin
N
0
13
km
Cocos plate over printed with off-axis volcanism
Crust with an off-axis trace of the eastern second-order segment
Crust with an off-axis trace of the western second-order segment
rugged, shallow seafloor with no off-axis NTD trace
smooth, shallow seafloor

Figure 4.7*: Summary of described geological features and regions. The bathymetry descriptions from Figure 4.2 were used to divide the study area into 5 geological regions. The lava domes, spreading axis, axial valley, shallow regions, AVRs, and the off-axis volcanism of seamounts and lava flows are described in Section 4.2.1. The faults were identified using the FID method in Figure 4.5 and described in Section 4.2.2. The geological regions are revisited in Section 4.2.6 and 4.3, and in Figure 4.15.*

The description of geological features results in the study area being divided into 5 geological regions (Figure 4.7). North of the spreading axis, off-axis volcanism has over printed large areas of the bathymetry. There are off-axis relics of 2 second order spreading segments between the spreading axis and 3˚7' N separated along 83˚44' W. Between 3˚7' N - 2˚55' N there is no evidence of second order segmentation. Between 2˚55' N and the southern end of the study area the bathymetry is smooth and few faults are identified.

4.2.3 Cumulative heave

The FID method underwent various tests in Chapter 3 for its reliability to identify faults using pre-set parameters and through a comparison to the fault map from Escartin et al., (1999). In this Chapter I will test how T% identifies tectonic extension compared with cumulative heave. The rate of cumulative heave that grows faster or slower that the average cumulative heave rate is revealed by calculating a residual of the cumulative heave. This should establish whether the T% method measures extension in a similar way to the commonly used method of cumulative heave (Escartin et al., 1999; Parnell-Turner et al., 2017).

Cumulative heave sums individual fault heave with distance from the spreading axis. A change in the slope of the curve is used to determine how far off-axis faulting is occurring or is measurable; when the rate of cumulative heave reduces this indicates fewer faults are being identified. Cumulative heave is also used to compare extension between plates (Escartin et al., 1999; Parnell-Turner et al., 2017). Cumulative heave is only reliable where the bathymetry has almost total coverage from overlapping

ship track. For this reason I have only calculated cumulative heave where data has full coverage within 40 km north and 80 km south of the spreading axis, this was between 84˚1’ W - 83˚28’ W in the along axis direction and 3˚37’ N - 2˚25’ N in the off-axis direction (red box in Figure 4.8A).

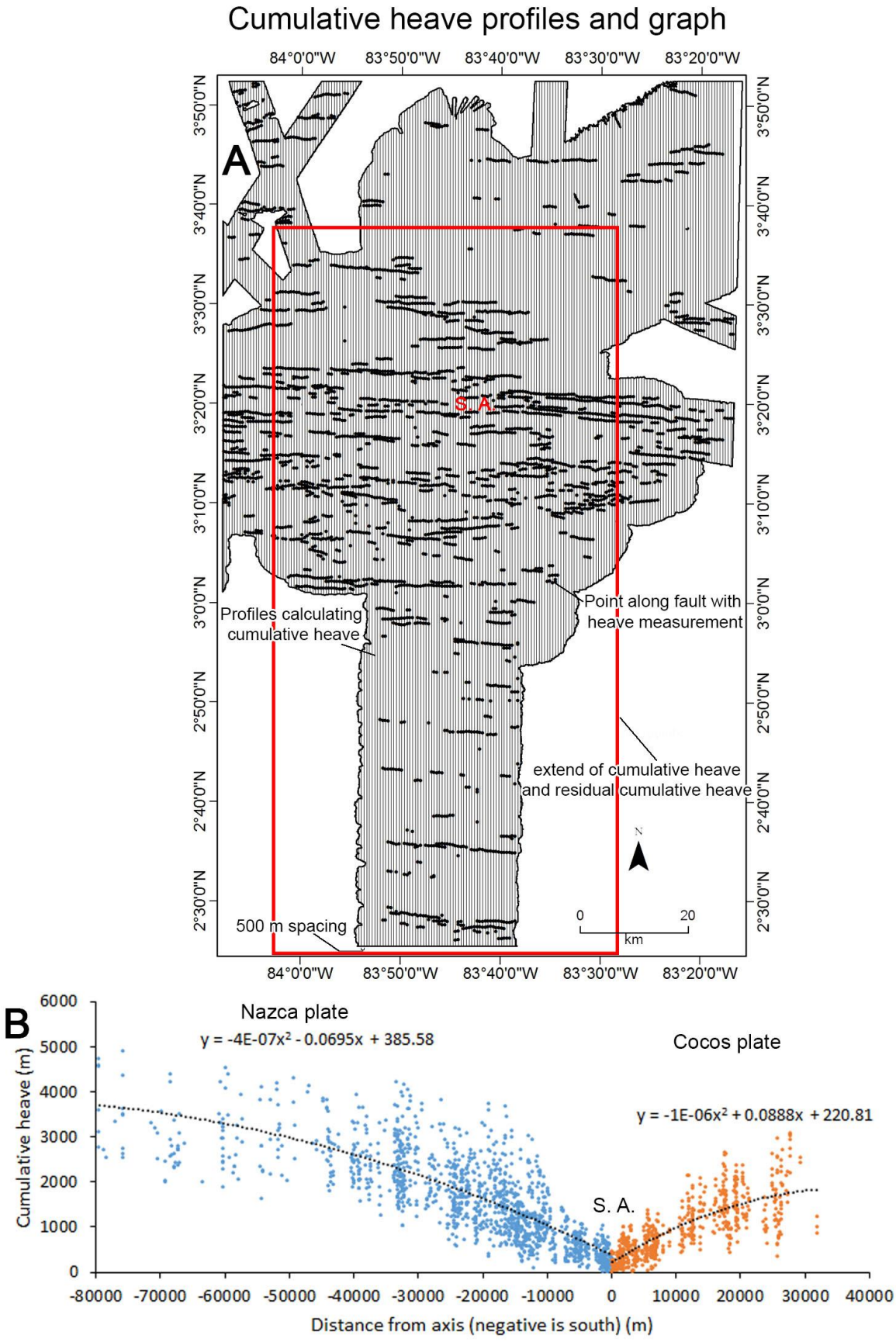

***Figure 4.8**: **A**: profiles used to calculate cumulative heave (black lines) and faults with heave measurements (black dots). Profiles are spaced at 500 m intervals. Red box covers data where there is almost total coverage within*

40 km of the spreading axis. The red box is the extent of the cumulative heave and residual cumulative heave maps. S. A. = Spreading Axis. ***B****: Cumulative heave plot for the Cocos (orange) and Nazca (blue) Plates against distance from axis. Dotted black line is a second order polynomial to describe the mean cumulative heave with distance off-axis for each plate.*

The second order polynomial of the cumulative heave calculates the average cumulative heave with distance (Figure 4.8B). Both the Nazca and Cocos Plates accumulate an average of 1000 m of cumulative heave within 10 km of the axis. At a distance of 20 km off-axis the Cocos Plate has an average cumulative heave of 1600 m while the Nazca Plate has 1800 m. At 30 km off-axis the Cocos Plate has an average cumulative heave of 1800 m while the Nazca Plate has an average of 2200 m. This indicates that there is asymmetry between the Plates in measurable tectonic extension. The density of cumulative heave measurements on the Nazca Plate reduces after 40 km off-axis indicating fewer faults were identified. This coincides with a reduction in slope of cumulative heave. The asymmetry between the Plates with greater distance off-axis and the variation in along axis cumulative heave can better be visualised as a map (Figure 4.8A).

Cumulative heave is most useful for visualising off-axis change in tectonism (Figure 4.9A), however in the along axis direction heave can vary as much as 1000 m over a few kilometres. To visualise the along axis variability I to calculated a residual cumulative heave map (Figure 4.9B). This residual map illustrates the relative variation in heave along axis by calculating how much the cumulative heave deviates from average at a given distance from the spreading axis.

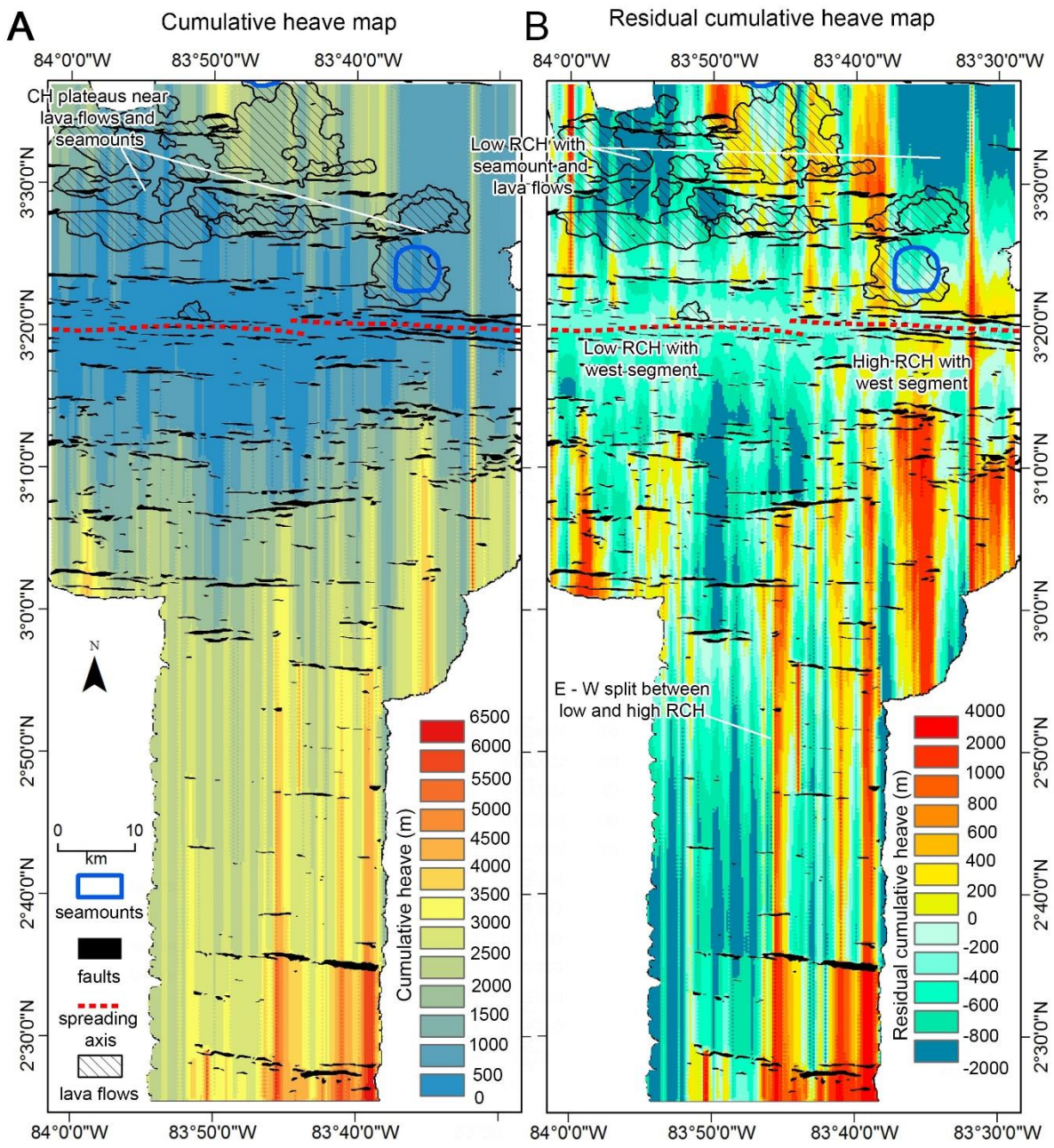

***Figure 4.9**: **A**: Cumulative heave map. **B**: Residual cumulative heave map. Key trends are annotated; CH = cumulative heave, RCH = residual cumulative heave.*

The cumulative heave plot asymmetry between Plates can be explained using the cumulative map (Figure 4.9A). Cumulative heave is symmetrical across the spreading axis up to 10 km off-axis on either plate. On the Cocos Plate at 83˚35' W; 3˚24' N there is a seamount and at 83˚54' W; 3˚30' N and 83˚35' W; 3˚27' N there are lava flows with few to no faults between. Near these features the cumulative heave plateaus at 600 – 700 m. No identified lava flows or seamounts have been identified on the

Nazca Plate at a similar distance from the spreading axis. This results in the cumulative heave continuing to rise >700 m. These results suggest that, assuming that extension is equally distributed between the plates, the asymmetry in measurable heave between the Plates results from masking by off-axis volcanism.

Residual cumulative heave illustrates the E – W variation in measured extension (Figure 4.9B). Interpretation of the residual cumulative heave relies on its relation to mapped features. On the Cocos Plate there are low levels (< -500 m) of residual cumulative heave over 211 km^2 between 83˚59' W - 83˚50' W and over 328 km^2 between 83˚37' W - 83˚29' W. These regions are where lava flows and seamounts were mapped (Figure 4.9B). There is high residual cumulative heave >200 m over 280 km^2 between 83˚49' W - 83˚37' W. This occurs where several faults are identified between the lava flows.

On the Nazca Plate between the spreading axis and 3˚11' N and between 84˚1' W - 83˚43' W there is low residual cumulative heave < -300 m. This occurs over the off-axis trace of the relic western second order segment. Within the same distance off-axis but between 83˚43' W - 83˚29' W residual cumulative heave is high >100 m. This occurs over the off-axis trace of the relic eastern second order segment. These results suggests that extension was higher when crust was created at the eastern second order segment. Further off-axis on the Nazca Plate between 3˚11' N - 2˚57' N, residual cumulative heave is high (>100 m) from E – W except for a low band of < -1000 m along 83˚49' W. This low band persists further off-axis between 2˚57' N - 2˚25' N, while east of 83˚45' W residual cumulative heave is high >100 m. There are no distinguishable changes in bathymetry or volcanic features that could explain this E – W divide.

Comparing the results of cumulative heave to my T% method will determine if they are identifying similar trends, or whether the T% method brings new analytical insight.

4.2.4 The percentage of tectonic extension

T% is described in Chapter 2 and applied in Chapter 3. Here, Figure 4.10 illustrates how T% is calculated using profiles arranged in windows. The profiles were orientated towards 001˚ so as to be perpendicular to the spreading axis trend of 091˚. Near the spreading axis between 84˚1' W – 83˚28' W each window consists of 123 profiles. Further off-axis on the Nazca Plate where the bathymetry extent is only between 83˚54' W – 83˚38' W, each window consists of 60 profiles. The T% map is shown in Figure 4.11.

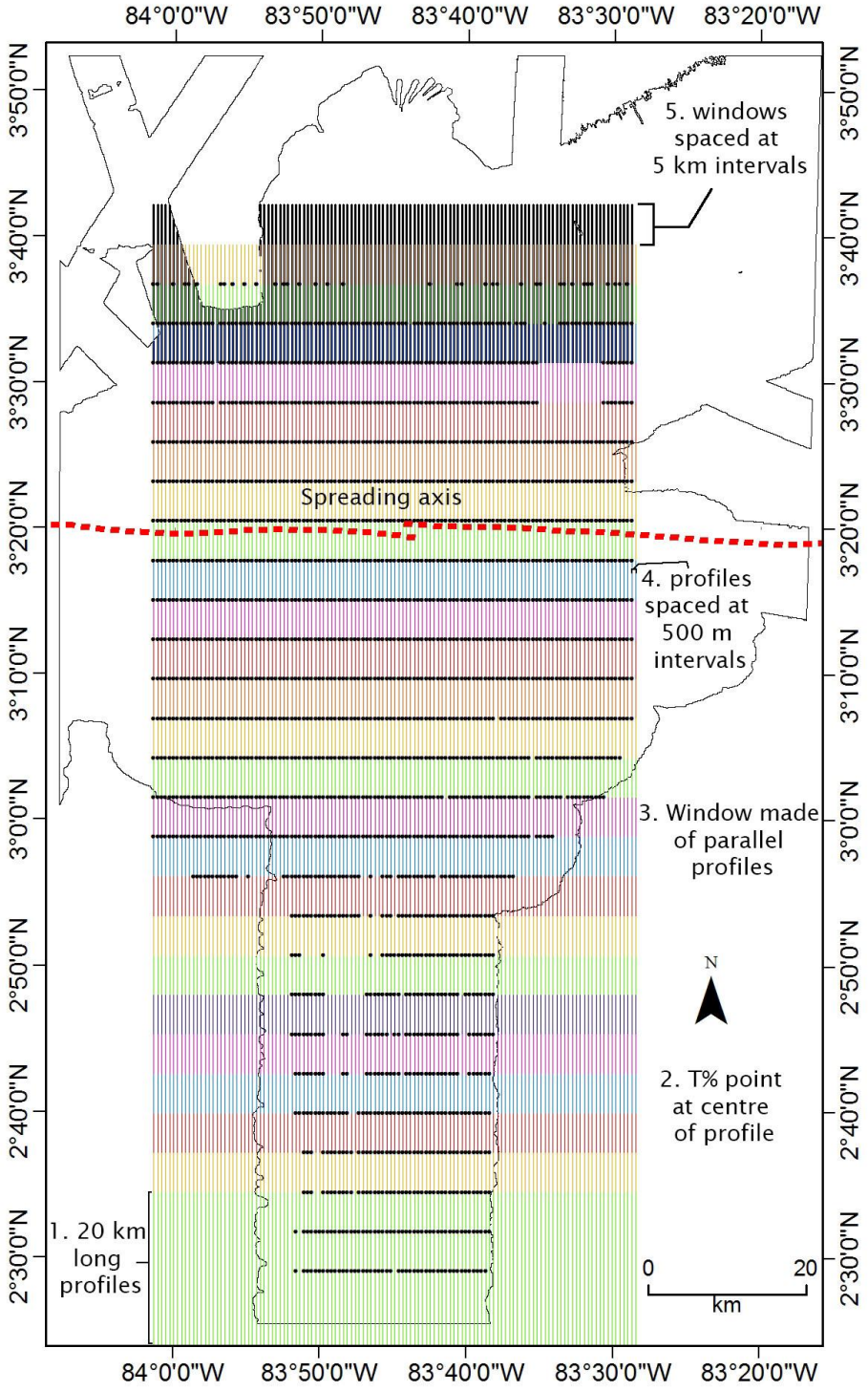

***Figure 4.10**: The T% windows and profiles. T% windows consist of the parallel profiles of the same colours. Each windows consists of T% profiles that are 20 km long, orientated 001˚, and placed parallel with a spacing of 500 m. The windows step in an N – S direction at 5 km intervals. T% points (black dots) are placed at the centre of each profile that intercepted a fault. These points are joined by linear interpolation to create a T% map (Figure 4.11).*

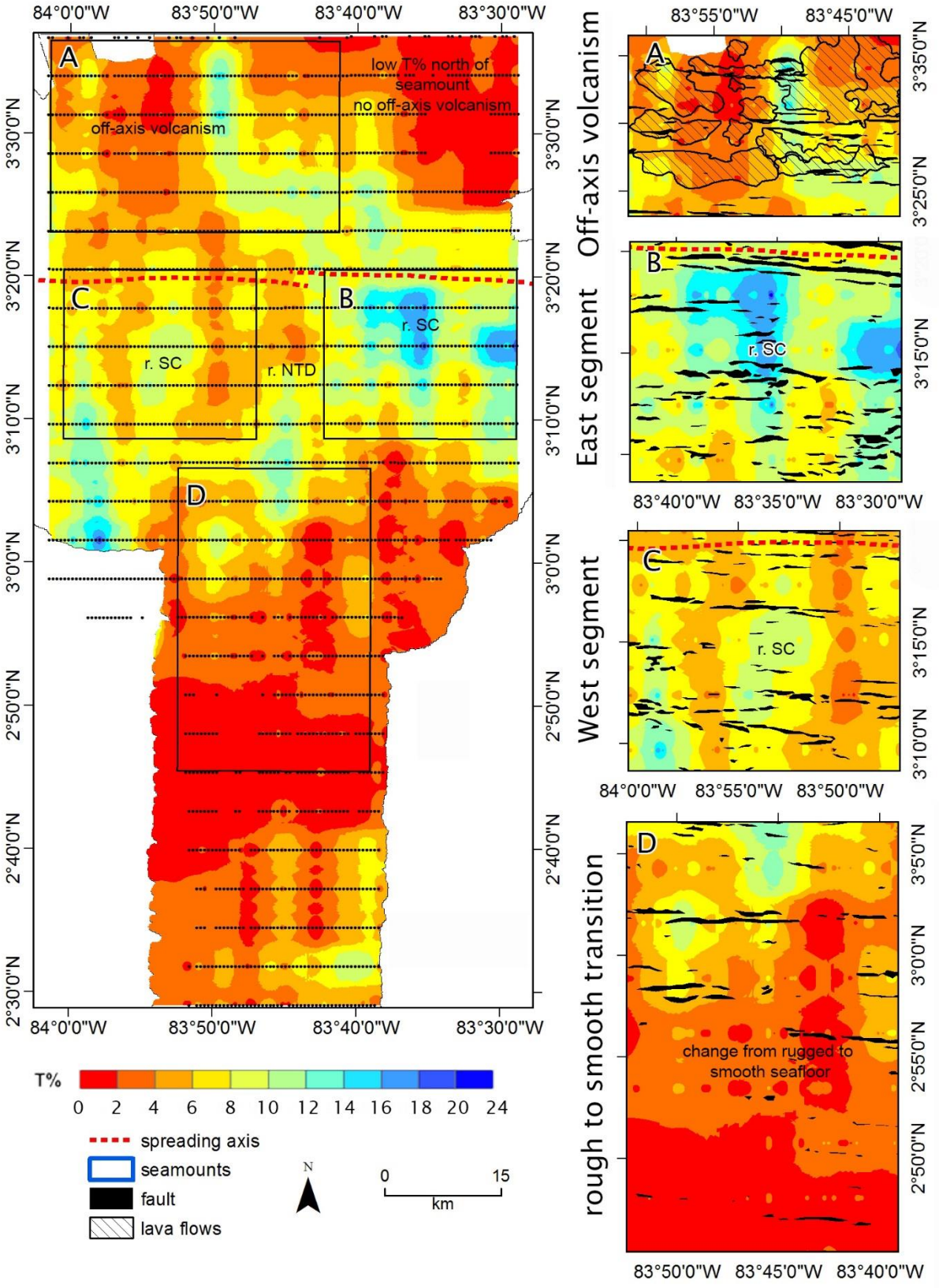

***Figure 4.11**: T% map. Black dots are sites of T% calculations joined by linear interpolation. Study windows A – D are based on geological regions in Figure 4.7. Annotated regions: r. NTD = relic NTD, r. SC = relic spreading centre. **A**: Off-axis volcanism on the Cocos Plate. **B**: Off-axis*

trace of the eastern second order segment on the Nazca Plate. ***C****: Off-axis trace of the western second order segment on the Nazca Plate.* ***D****: Transition from rugged to smooth seafloor around 2˚55' N.*

The Costa Rica segment's T% can broadly being divided into two regions, high T% (>5%) within 40 km of the spreading axis, and low (<5%) T% more than 40 km off-axis (Figure 4.11), similar to the broad division based on seafloor morphology (Figure 4.7). The region of high T% (>4%) between 3˚36' N – 3˚7' N has a mean value of 6.1±1.8%. This region covers the Cocos Plate's off-axis volcanism and the Nazca Plate's off-axis trace of the relic second order segment centres and relic NTD. The region of low T% (<5%) between 3˚7' N – 2˚29' N has a mean value of 3.5±1%. This region of low T% contains the rugged seafloor on the Nazca Plate that has no trace of the relic second order segments, and the region further south with smooth seafloor (Figure 4.7).

The two broad regions of T% can be further subdivided (Figure 4.11). Box A is the Cocos Plate between 3˚36' N – 3˚7' N. Between 3˚36' N - 3˚20' N the average T% of 4.9±1.5%. Within this region are two areas of low T%, 1.5±0.5% at 83˚53' W; 3˚32' N, and 1.2±0.4% at 83˚33' W; 3˚31' N. The first of these occurs over lava flows from off-axis volcanism (box A Figure 4.11). There is a region of high T% (10%) where faults are found between the lava flows. The second region of low T% to the east occurs north of the solitary seamount near the spreading axis.

The Nazca Plate between the spreading axis and 3˚7' N is divided into the off-axis traces of the second order segments. Box B is the Nazca Plate's eastern relic second order segment (Figure 4.11), and has a mean T% of 8.9±2.7%. Box C is the Nazca Plate's western relic second order segment, and has a mean T% of 6.4±1.9%. The Nazca Plate's T% within 24 km of the spreading axis has a higher level of tectonic extension than the Cocos Plate. On the Nazca Plate, the eastern segment has produced more tectonically extended crust than the western segment. These regional trends were also identified in the residual cumulative heave map (Figure 4.10B). The higher T% for the eastern segment results from larger axial valley wall faults (Figure 4.3) and large faults off-axis (Figure 4.9 &

4.11B). The western segment has a less pronounced axial valley (Figure 4.3 & 4.9) and fewer large off axis faults (Figure 4.12C).

Box D between 3˚7' N – 2˚57' N, covers an area where T% gradually decreases from ~10% to ~2% with a mean over the region of 5.1±1.5%. This region is where there is no longer any trace of relic second order segment centres and the relic NTD. Around 2˚55' N there is a change in bathymetry from rugged in the north to smooth in the south (Figure 4.8). T% continues to drop across this boundary from 2% to 0% at 2˚48' N where no faults were identified (Figure 4.12D). South of 2˚42' N T% starts to rise, reaching a peak of 8±2.4% near the study area's southern edge. This higher T% is a result of a few large faults that are able to appear above the thick sediment, however because of the thick sediment is this area the T% here is expected to be underestimating the true T%.

4.2.5 Calculating a Residual Topographic Anomaly (RTA)

T% has identified differences in extension which need to be compared to crustal features that are diagnostic of relative difference in melt supply. In Chapter 3, the relative topographic anomaly (RTA) correlated with the residual mantle Bouguer anomaly on the 20 – 50 km scale to indicate relative changes in crustal thickness along the length of a segment. In this chapter I will use the RTA to quantitatively identify bathymetry that is shallower or deeper than the crustal average for the crust's age. Comparison of volcanic and structural features to these shallow and deep crustal regions will be used to interpret their relative differences in melt supply during formation.

To construct the average bathymetry curve used to calculate RTA I used bathymetry from the Nazca Plate because it had 24 km of east – west coverage up to 270 km off-axis and has no off-axis volcanism, therefore is more representative of bathymetry formed at the spreading axis. Average depth was calculated along profiles orientated 091˚ (Figure 4.12A). 540 of these profiles were used and they spaced at 500 m intervals in an N – S direction. The E – W profiles start at the plate boundary and extend as far

south as 2˚25' N. This produced a plot of average bathymetry with distance from the spreading axis (Figure 4.12B).

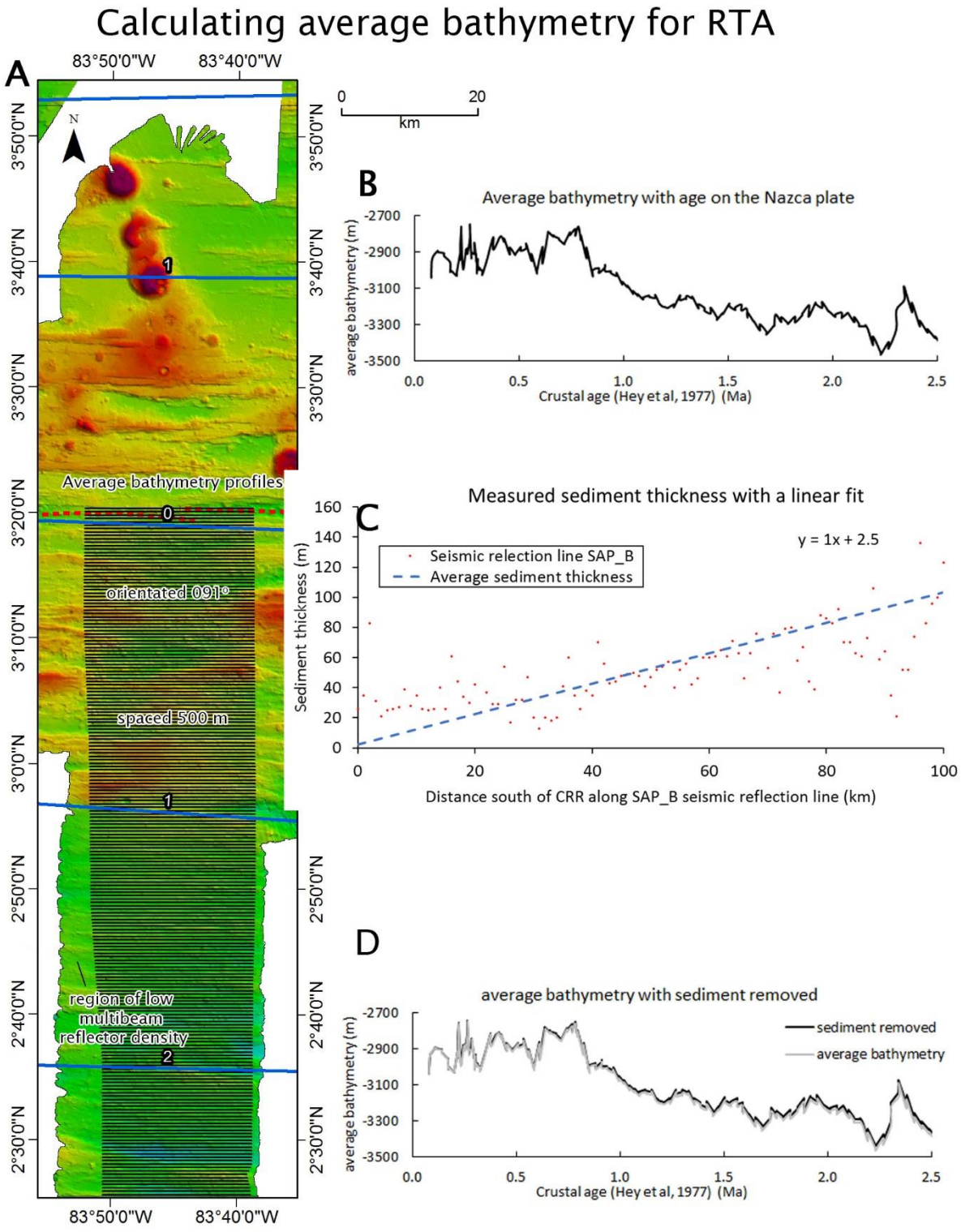

***Figure 4.12**: **A**: Map of the profiles used to calculate average depth with distance off-axis. Blue lines are crustal ages from Hey (1977). **B**: Plot of*

average bathymetry off-axis. ***C****: Sediment depth south of the axis along SAP_A.* ***D****: Average bathymetry off-axis adjusted for removal of sediment.*

To calculate the average bathymetry depth with age I used the magnetic isochrons of Hey (1977) (blue lines in Figure 4.12A). This map was tested against Borehole ODP 504B, which is dated to 6.9 Ma (Wilson et al., 2003). The age for the crust containing ODP 504B was calculated as 6.2 Ma according to the Hey (1977) isochron map, giving an error of 700 kyrs at this distance. His 0 Ma isochron is ~60 kyrs (1 - 2 km) out from the geographic location of the spreading axis. Despite these errors, it provides a useful age map for analysis of large scale bathymetry (10 km) that covers ~300 kyrs of crustal age (Figure 4.12B).

First, the bathymetry is corrected for the loading of water and sediment. This is done using the equation for the depth before sediment loading, $t_b : t_b = t'_b + t_s \frac{(\rho_a - \rho_s)}{(\rho_a - \rho_w)}$, Where, t'_b = depth after sediment loading, t_s = sediment thickness, ρ_a = density of asthenosphere (3.2 g cm^{-3}), ρ_w = density of seawater (1.027 g cm^{-3}) and ρ_s = density of sediment (1.59 g cm^{-3}) (Le Douaran & Parsons, 1982). The sediment thickness was calculated by Dr. Wilson from the University of Durham from the depth converted seismic reflection profile SAP_A (Figure 4.12C). A linear fit to the sediment thickness provided an average sediment thickness with distance off axis. This calculated the bathymetry without sediment loading (Figure 4.12C), which only slightly reduced bathymetry depth by ~10 m at 1 Ma, and ~20 m at 2 Ma because of the thin sediment thickness.

Next, the influence of off axis subsidence on bathymetry is calculated. The unloaded bathymetry is plotted against the square root of age and a linear trend line is obtained (Figure 4.13), this calculated a time-dependent subsidence curve for the Nazca Plate of 231 $t^{1/2}$ when t ≤4 Myrs. This subsidence trend is then subtracted from the sediment unloaded bathymetry and the differences extracted as RTA (Figure 4.14).

The method does not account for changes in mantle density or other non-isostatic changes in depth caused, for example, by far-field stresses. It is also subject to errors near the plate boundary because the crustal age

model may not precisely match the location of the spreading axis. Additionally, the seafloor covered by bathymetry with a poor sample density (Figure 4.5) are less reliable. For this reason the RTA calculated within the axial valley and in areas of poor bathymetry sample density will be ignored. Nevertheless, the RTA is an effective method to identify bathymetry that is shallower or deeper than the average plate bathymetry for the crust's age.

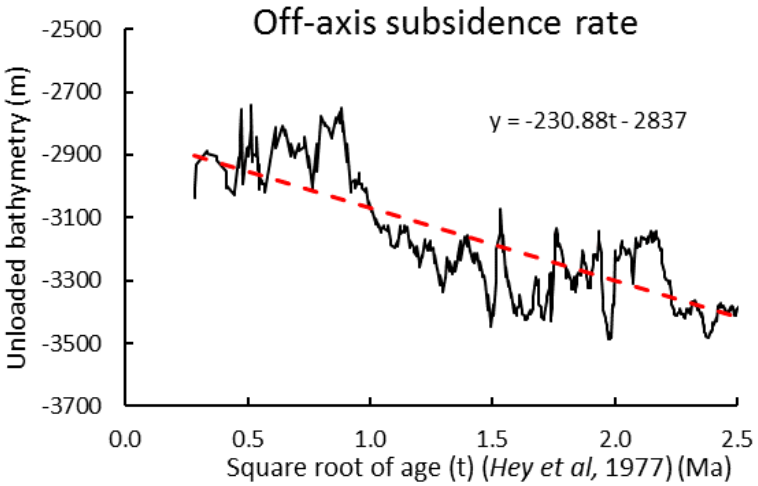

***Figure 4.13**: The unloaded bathymetry plotted against the square root of age to calculate off axis subsidence of the Nazca Plate. A linear fit to the plot describes the off axis subsidence trend. Subtracting this linear fit from the unloaded bathymetry calculates RTA, positive and negative deviations away from the predicted depth for the age of the crust.*

The subsidence rate of 231 $t^{1/2}$ when t ≤4 Myrs seems low when compared to the global subsidence rates found by Stein & Stein, (1992) of 365 $t^{1/2}$, and revised by Hasterok, (2013) to 414.5 $t^{1/2}$ when t ≤17.5 Myrs. However, these subsidence rates are primarily based on data from the North Pacific and North Atlantic Plates. The Nazca Plate has a much lower subsidence rate, measured to be 206 $t^{1/2}$ when t ≤100 Myrs by Marty & Cazenave, (1989). Therefore, my calculated subsidence rate seems appropriate to crust created at the CRR, which are similar to the North Nazca Plate, or the proximal section of the Pacific Plate that has a subsidence rate of 262 ±12 m $t^{1/2}$ (Marty & Cazenave, 1989).

In Chapter 3, the crustal depths calculated from RTA using the Airy isostasy was found to not precisely match those calculated using residual mantle Bouguer anomalies, suggesting that it does not directly reflect changes in crustal thickness. In this Chapter I will use RTA to identify areas of bathymetry that are shallower or deeper than the average for the crust's age. Regions of anomalously shallow and deep bathymetry are then interpreted in respect to other seafloor features in order to gain an understanding of melt supply along axis, and through time.

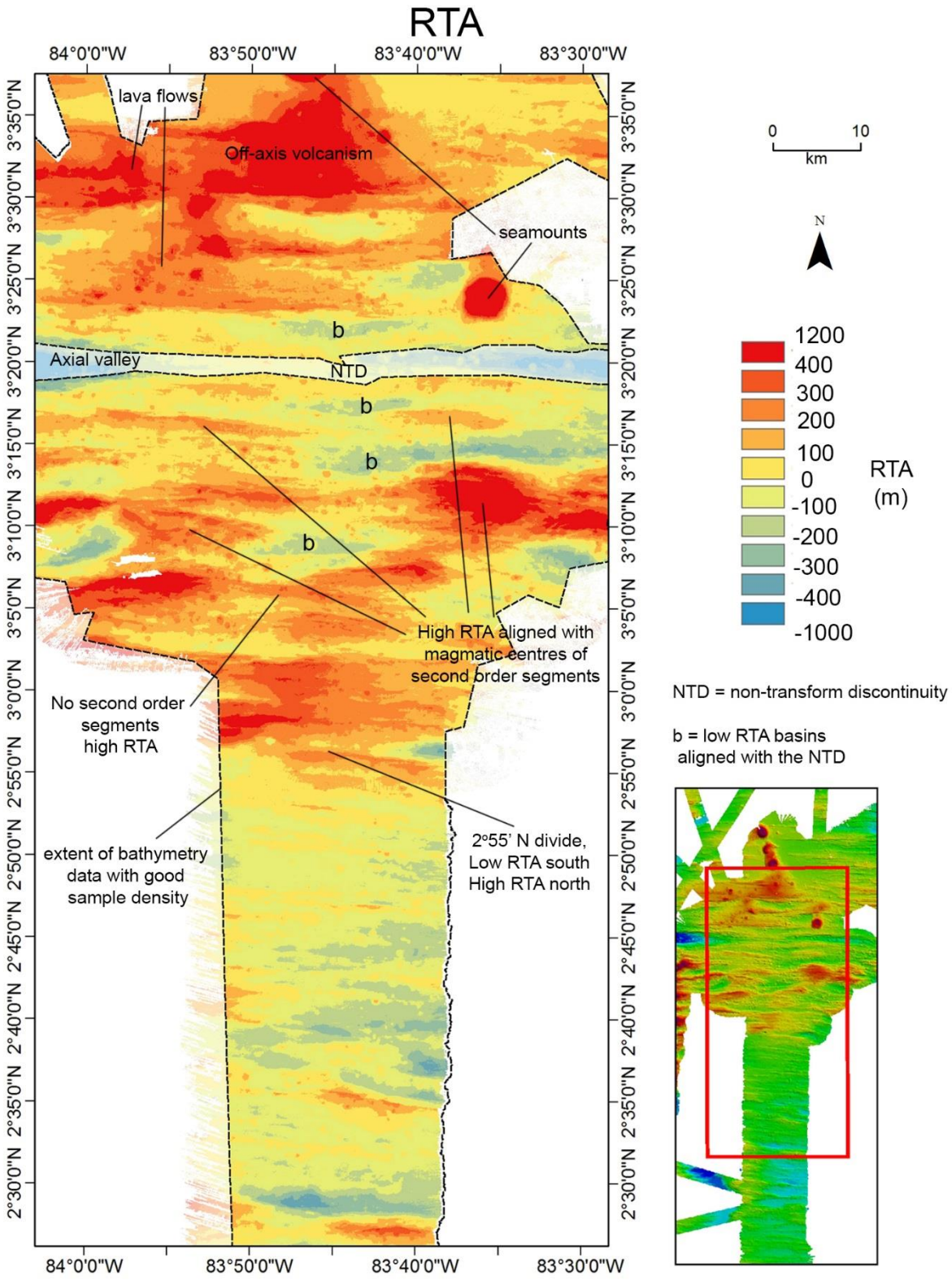

***Figure 4.14**: Residual topography anomaly map. Dashed outline is the extent of RTA analysis that is reliable because it is not within the axial valley and was calculated using bathymetry with a high sample density. Negative RTA basins aligning with the NTD are highlighted as 'b'. Main trends in RTA are annotated.*

4.2.6 Main features of the RTA

The RTA map (Figure 4.14) can be divided into two main regions at 2˚55' N. North of 2˚55' N the RTA is high with a mean of 136 m and a broad range of -610 m – 1380 m. South of 2˚55' N, RTA is low with a mean of -27 m and a narrow range between -730 m – 435 m. This division is the same as that made using bathymetry (Figure 4.7).

The RTA region north of 2˚55' N is further divided into the Cocos and Nazca Plates. The Cocos Plate between the spreading axis and 3˚48' N has an average RTA of 177 m (range: -884 m – 892 m). The Nazca Plate between the spreading axis and 2˚55' N has an average RTA of 105 m (range: -560 m – 833 m), making it on average deeper than the Cocos Plate.

Within the Cocos Plate, the areas of highest RTA (>300 m) occur near the seamount at 83˚35' W; 3˚23' N, the domed seafloor at 83˚46' W; 3˚32' N, and lava flows at 83˚54' W; 3˚25' N and 83˚57' W; 3˚31' N (Figure 4.14). The high RTA regions on the Cocos Plate appears to be associated with off-axis volcanism indicating the RTA here is not a signal representative of the crust formed at the spreading axis.

The RTA of the Nazca Plate between the spreading axis and 2˚55' N can be subdivided into three regions. The first division occurs along the string of negative RTA basins (labelled 'b' in Figure 4.14). These basins have an arcuate alignment along ~83˚44' W, and have a mean length of 11.3 km (±3 km) and mean width of 3.1 km (±2 km). These negative RTA basins meet the NTD suggesting the basins are the off-axis relics of the NTD separating the two second order segments as far as 3˚7' N. The alignment of the basin centres indicates that the NTD migrated east over 0.4 Ma. NTDs have lower magmatic accretion than the segment centres (Macdonald et al., 1988) suggesting the low RTA of these basins is due to crust created with a low melt supply.

Either side of the relic NTD basins have high RTA (>200 m) centred along 83˚52' W and 83˚37' W reaching as far south as 3˚7' N. These regions of high RTA include the shallow regions (Figure 4.7) and aligned

with the domed centres of the second order spreading axis (Figure 4.3) where melt supply is thought to be highest (Macdonald et al., 1988). These positive RTA features are interpreted as the off axis relics of the magmatic centres of the two second order segments. The western second order segment's relic centre is between 83˚58' W – 83˚46' W, and the eastern second order segment's relic centre is between 83˚42' W - 83˚32' W. These features are expected to be symmetrical between Plates, however, off axis volcanism on the Cocos Plate has over printed these relic features. The Nazca Plate between the spreading axis and 3˚7' N and west of the relic NTD has an average RTA of 111 m (range: -852 m – 873 m). The Nazca Plate between the spreading axis and 3˚7' N and east of the relic NTD has a mean RTA of 83 m (range: -472 m – 729 m). This identifies that the crust created from the eastern segment is deeper. The association of positive RTA along the centre of the spreading segments where magma supply is highest indicates that broad regions (>5 km) of positive RTA between the spreading axis and 3˚7' N on the Nazca Plate corresponds with high melt supply.

On the Nazca Plate, between 3˚7' N – 2˚55' N RTA has a mean of 187 m (range: -562 m – 646 m). This region has a continuous high RTA region from E – W where no negative RTA associated with the relic NTD is observed. This high RTA region from E – W could indicate a period of no second order segments. Segmentation reduces with higher melt supply (Abelson & Agnon, 1997) suggesting this continuous high RTA region could indicate high melt supply.

4.3 Discussion

4.3.1 Reliability of extensional measurements

A comparison between RTA and T% depends on how reliable these methods are and what crustal processes they are representing. The reliability of T% primarily depends on the identification of faults using my FID method. Three fault parameters were used to identify faults; slope angle, slope direction, and acoustic backscatter (Figure 4.4). Each parameter had its inaccuracies, with the main ones being that; slope angles between 35˚ - 60˚ also selected the side of seamounts and only covered 1% of the study area; slope directions between 336.5˚ – 021.5˚ and 158.5˚ – 203.5˚ identified undulating terrain with an E – W fabric as 32% of the study area; and the upper quintile of backscatter highlighted 8 km either side of the spreading axis and 20% of the study area (Figure 4.4). I combined the three parameters into the FID map to minimise the chance of each parameter miss-identifying a fault. Comparing the FID faults to bathymetric profiles (Figure 4.5) illustrated that it was able to locate the axial valley wall faults and performed well at identifying the steep scarps of asymmetric half-grabens facing towards the spreading axis. Beyond 60 km off-axis, sediment thickness is >60 m, creating a smooth bathymetry (Figure 4.5C) making it more difficult to identify faults based on slope angle and slope direction. By 80 km off-axis the 80 m thick sediment obscured all but the largest faults, as was examined in Section 2.1.3.1.

An estimated 30% of T% could have been missed across the entire study area because of the bathymetry resolution preventing the FID method from identifying faults with heave <150 m (Figure 4.6). Normal faults initiate from small fractures that rotate and coalesce, then grow with increasing extension (Behn & Ito, 2008; Buck, 1988; Thatcher & Hill, 1995). Faults with small heaves are being missed by the FID method. However if the size of the faults are proportional to the amount of extension, then the clusters of large faults, identified using T%, represent areas of higher extension.

To examine what the T% method measures I have compared it to cumulative heave, this is a method used in other tectonic studies (Escartin et al., 1999; Parnell-Turner et al., 2017). Cumulative heave continually increases with distance off axis (Figure 4.9) making it best suited for identifying differences in heave in the off axis direction. To identify variation in heave in the along axis direction I calculated a residual of the cumulative heave (Figure 4.9).

At 30 km off axis the Cocos Plate has an average cumulative heave of 400 m lower than that on the Nazca Plate. This indicates that there is asymmetry between the plates in measurable tectonic extension. This could be a result of off axis volcanism on the Cocos Plate covering fault scarps. This relation was also identified using the T% method, with the Cocos Plate having 2.7±0.8% less extension than the Nazca Plate. Residual cumulative heave is more sensitive to changes in tectonic extension parallel to the spreading axis. The residual cumulative heave identified that the Nazca Plate's crust formed from the eastern segment has around ~400 m more extension than crust from the western segment. This relation was also identified using the T%, with the eastern segment producing crust with 2.5±0.8% less extension than the western segment. This suggests that at the large scale of geological regions ranging from 20 – 50 km both methods identify the same relative changes in crustal extension.

4.3.2 Comparing extension to melt supply

To compare T% to melt supply I need to be able to identify crustal features that record the relative changes in the melt supply at the spreading axis when the crust was created. In Chapter 3 I used crustal thickness as determined from gravity anomalies. However, in this study area no residual mantle Bouguer anomalies are available to determine crustal thickness. Another method to calculate crustal thickness is Airy isostasy using the RTA measurements. According to the Airy isostasy model, regardless of crustal thickness, all crust is neutrally buoyant at the same level within a plastically deforming asthenosphere. Therefore, thicker

crust produces shallower bathymetry than thinner crust (Lowrie, 2007; Suppe, 1985). I determined in Chapter 3 that, at least at the Mid-Atlantic Ridge, the relative differences in crustal thickness identified by RTA and residual mantle Bouguer anomalies agreed, however the specific calculated thicknesses slightly differed.

I have no second proxy for crustal thickness to check if the RTA in this chapter is reliably calculating relative differences in crustal thickness. Therefore, in this chapters, instead of using RTA as a proxy for crustal thickness I use RTA to quantify shallow and deep bathymetry relative to the mean depth for the crustal age. The shallow and deep regions identified in RTA are then compared to structural and volcanic features that have known relations to melt supply. North of 3˚7' N, positive RTA was associated with high melt supply features such as off axis volcanism and the relic centres of spreading segments (Figure 4.14). South of 3˚7' N there were no obvious structural or volcanic features to explain the RTA.

Visual comparison of the T% map to the RTA and geological features is done by breaking the study area into five geological regions (Figure 4.15). The most striking divide in the data sets occurs along 2˚55' N. North of this average RTA is high (136 m), the seafloor is rugged, and average T% is high (6.1±1.8%). South of this divide average RTA is low (-27 m), seafloor is smooth, and average T% is low (3.5±1%) (Figure 4.16G). The smooth and deep bathymetry with low amounts of measured extension south of 2˚55' N could be a result of the growth of thick sediment drapes. Alternatively, the smooth crust could be typical smooth seafloor created at fast spreading ridges with a high melt supply (Macdonald, 1982), while the rugged seafloor north of 2˚55' N could be typical rugged seafloor with high abyssal hills that forms at intermediate spreading ridges where melt supply is lower (Macdonald, 1982). Without measurements of crustal thickness I cannot confidently determine if the morphological change across the 2˚55' N divide is a result of changes in relative melt supply.

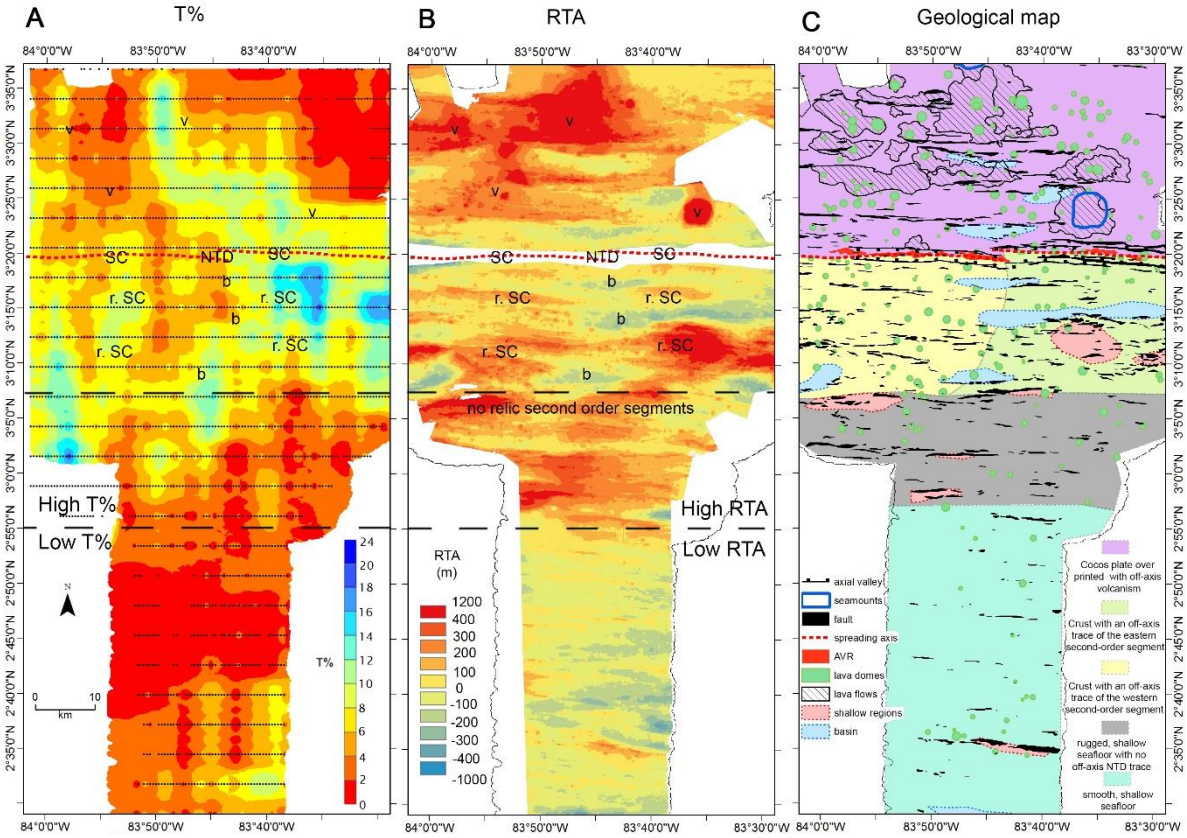

***Figure 4.15**: Visual comparison between T%, RTA, and geological features. Abbreviated annotations are interpretations of RTA features; v = off axis volcanism, NTD = non-transform discontinuity, b = basins along the relic NTD, SC = magmatic centres of segments, r. SC = relic segment centres. Dashed E – W lines mark major changes in RTA and T%. **A**: T% map. **B**: RTA map. RTA has had unreliable data cut out where multibeam sonar ping density was low and within the axial valley. **C**: Geology map with coloured regions based on common trends in bathymetry, RTA, and T%.*

The study area north of 2˚55' N is divided into the Nazca and Cocos Plates. At the 40 km scale the Cocos Plate has a high average RTA (177 m), low average T% (4.9±1.5%) (Figure 4.16G), and off axis volcanism. The off axis volcanism has covered the seafloor topography created at the spreading axis preventing the measured T% and RTA being representative of the processes at the plate margin. This prevents the plates being directly compared to each other. The regions of off axis volcanism have low T% because the faults have been buried by lava flows and seamounts. There is no statistical correlation between T% and RTA within the Cocos Plate geological region (R^2 = 0.08 in Figure 4.16B) at the 1 km scale.

The Nazca Plate has low average RTA (105 m), high average T% (7±2.1%) (Figure 4.16G). The Nazca Plate has not been influenced by off axis volcanism so provides a better region to determine if extension and melt supply at the spreading axis are related. The Nazca Plate preserves the off axis relics of the domed centres of the segments (labelled r. SC in Figure 4.15). The NTD is a 1.8 km overlap between the spreading centre segments (between 83˚43'26" W and 83˚44'40" W). The off axis trace of the discontinuity is seen in the form of a series of basins on the Nazca Plate that are centred on an arcuate line that curves to the west as it moves away from the spreading axis (labelled 'b' in Figure 4.15) extending as far south as 3˚7' N. This relic NTD feature is not visible on the Cocos Plate because off axis volcanism has infilling the basins.

First, I will compare melt supply and extension at the local scales of <10 km along the geological regions labelled the western and eastern segments. These regions have high RTA (>200 m) and N – S bands of high T% (>8%) along 83˚53' W and 83˚36' W, and low T% bands (<6%) along 83˚49' W, providing no consistent relation at scales of <10 km. Low RTA (<-100 m) along the relic NTD coincides with low T% (<6%) between 3˚19' N - 3˚13' N and a high T% (>8%) between 3˚13' N – 3˚3' N, providing no consistent relation at scales of <10 km. RTA and T% are not statistically correlated within the eastern (R^2 = 0.02) or western (R^2 = 0.02) segment regions (Figure 4.16C & D) at scales of 1 km.

At the large regional scale of 20 – 40 km, the western and eastern off axis segment regions (Figure 4.15) are geologically different. The average RTA is slightly higher on the western segment region (111 m) than the eastern (83 m) (Figure 4.16G). This suggests that the past melt supply was higher at the western segment. The domed spreading axis is ~200 m shallower and extends 2 km further off-axis (Figure 4.3) at the western segment than at the eastern segment. An axial melt lens under the western CRR was imaged during a 2D multichannel seismic reflection survey in 1994 (Floyd et al., 2002). This suggests that on axis melt supply is currently higher along the western segment than the eastern segment, supporting the finding that past melt supply had a similar distribution.

This difference in melt supply at the regional scale is reflected by a difference in T%, with the mean T% across the width of the western segment having 2.5±0.8% lower average T% than that measured across the width of the eastern segment (Figure 4.16G). These results suggest an inverse relation where relative changes in melt supply are reflected by relative changes in extension on the regional scale.

Between 3˚7' N - 2˚55' N, there are no off-axis traces of the relic segment centres and the relic NTD (Figure 4.15) suggesting there was no second order segmentation at this time. This region has a continuous E - W trending zone of high average RTA (187 m) and a southwards reducing T% from ~10 – ~2%. The seafloor morphology is similar to that of the relic segment centres to the north, suggesting a similar melt supply but along the entire spreading axis. There is no statistical correlation between the RTA and T% in this region (R^2 = 0.00 in Figure 4.16E) at the 1 km scale. At the regional scale, the values are similar to those of the Cocos Plate (Figure 4.16G), with low average T% (5±1.5%) and high average RTA, suggesting an inverse relation.

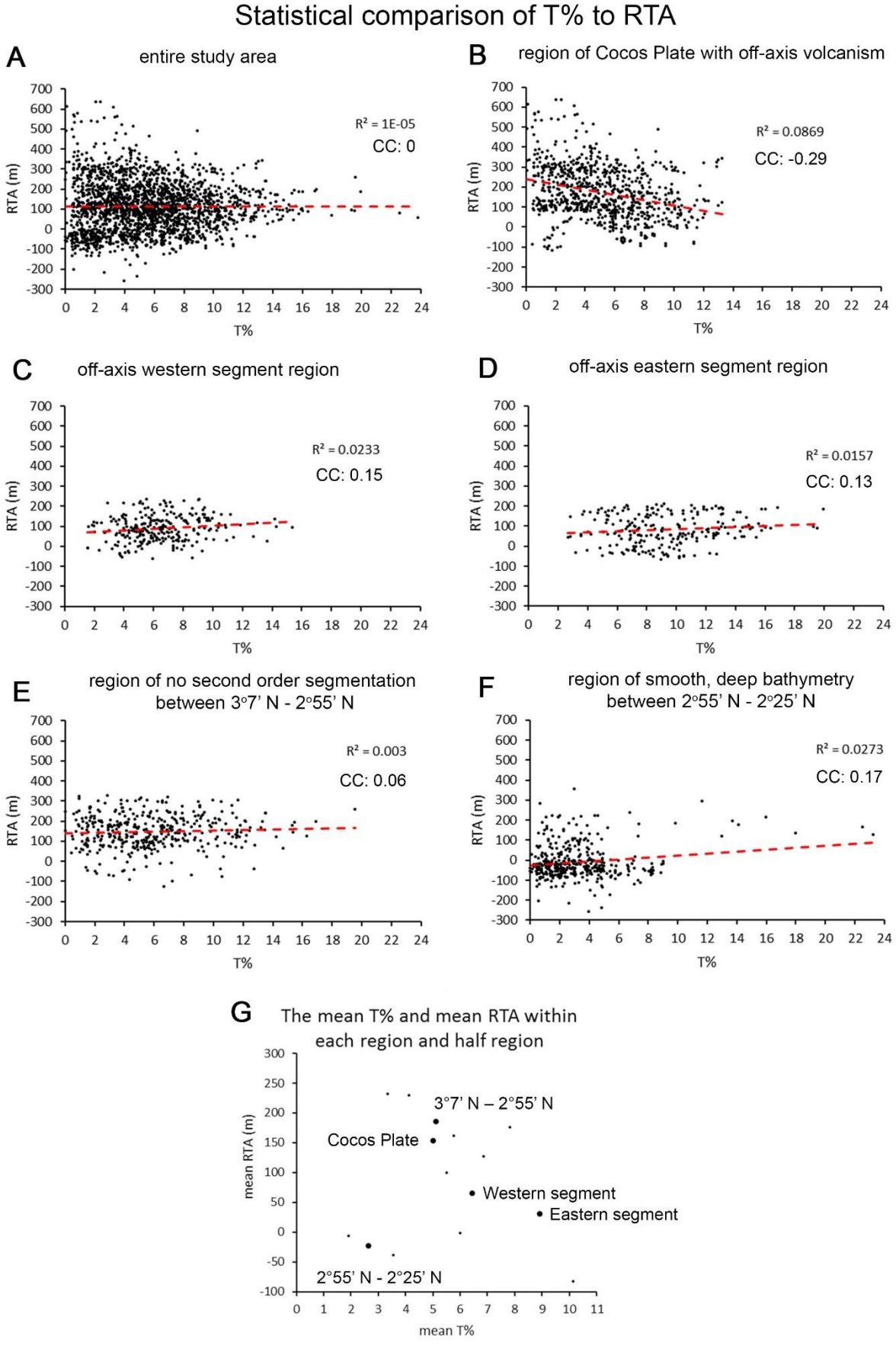

***Figure 4.16**: **A** – **F**: Cross-plots of T% vs RTA for the whole study area and each geological region identified in Figure 4.15. CC = correlation*

coefficient. The cross-plots and the correlation coefficient indicate there are no statistical correlations using these methods. ***G****: The mean RTA and T% within each geological region (big dots) and half region (small dots). If the regions of smooth seafloor between 2˚55' N - 2˚25' N is ignored for potentially being fast spreading ridge crust, there is a weak inverse relation between RTA and T% at scales of >20 km.*

To determine if there was a consistent relation between T% and RTA at the regional scales (~40 km) I plotted the mean RTA and mean T% within each region. The regions are also divided in half from E – W to determine if there is a relation on the 20 km scale. There is no consistent relation between all the half regions and regions. However, the smooth seafloor between 2˚55' N - 2˚25' N possibly formed during fast spreading and has a very different morphology to the rest of the study area. Ignoring the region between 2˚55' N - 2˚25' N, there is a weak inverse relation between T% and RTA for regions and half regions for crust north of 2˚25' N. Suggesting that melt supply and extension at the Costa Rica Ridge are not related at scales <20 km, and only start to show an inverse relation at the larger scale >20 km.

A study by Howell et al. (2016) of fault geometry related to along axis magmatism at the intermediate spreading Chile Ridge identified that as magmatism increased from segment end to segment centre, fault throw reduced and fault spacing did not change. Although the measured seafloor geometry was slightly different, my T% at the intermediate spreading Costa Rica ridge does not show a similar relation of high extension at the segment end compare to the segment centre.

4.4 Conclusions

Through analysis of crust created at the Costa Rica spreading ridge using RTA and mapping volcanic and axial features I identified traceable off axis relics of the domed centres of the second order segments and the subsided non-transform discontinuity between the spreading axis and 3˚7' N. The western of the second order spreading segments had a higher RTA and a larger axial dome suggesting it has a higher melt supply than

the eastern segment. The crust north of the spreading axis was over printed with off axis volcanism preventing it being useful for analysing axial processes. The crust south of 3˚7’ N did not have a clear mode of formation or had thick sediment obscuring faults. The relic structures between the spreading axis and 3˚7’ N provided proxies for high and low melt supply at the time of crustal formation that was tested for a relation between the amount of tectonic extension and magmatism.

At scales less than 20 km parallel to the spreading axis, the regions with relic segment structures had bands of high and low T% along the relic segment centres. T% appears high and low over the relic non-transform discontinuity. This meant that no statistical or consistent visual relation could be determined between melt supply and extension at scales <20 km, suggesting there is not a simple linear relation between melt supply and tectonic extension. The mean T% over scales of 20 – 50 km suggested that the western segment, that had a higher melt supply, had a lower amount of tectonic extension than the eastern segment. This suggests at scales >20 km a relation between extension and melt supply is possible.

Chapter 5: Reykjanes Ridge

5.1 Introduction

The Reykjanes Ridge is located between Iceland and the Bight Transform zone at 57˚ N; 33˚ W along the Mid-Atlantic Ridge (Figure 5.1B). The Reykjanes Ridge is 900 km long, trends between 030˚ - 040˚, and has a full spreading rate of 25 mm yr^{-1} in the oblique direction of 110˚ - 120˚ (Dauteuil & Brun, 1993; Keeton et al., 1996; Talwani et al., 1971). It is crossed obliquely at several locations by positive Free Air Gravity Anomaly (FAA) ridges (Figure 5.1A). These oblique structures form V-Shaped Ridges (VSRs) in plan view that are almost symmetrical between the N. American and Eurasian Plates. By measuring the distances from the axis to conjugate pairs of VSRs, asymmetry was measured to be small, ranging from 5 – 20 km (Hey et al., 2010; Parnell-Turner et al., 2014).

Crustal thickness variations and geochemical parameters indicate these V-shaped ridges are the result of an increase in mantle melting that is due to pulses of hotter mantle migrating southwards away from the Iceland plume (Jones et al., 2002; 2014; Parnell-Turner et al., 2017; White et al., 1995). As a result, increased volcanism and thicker oceanic crust is produced above the hot pulses. This phenomenon allows the opportunity, here, to explore the effects of variations in melt supply or melt flux on the brittle extension expressed as upper-crustal faulting.

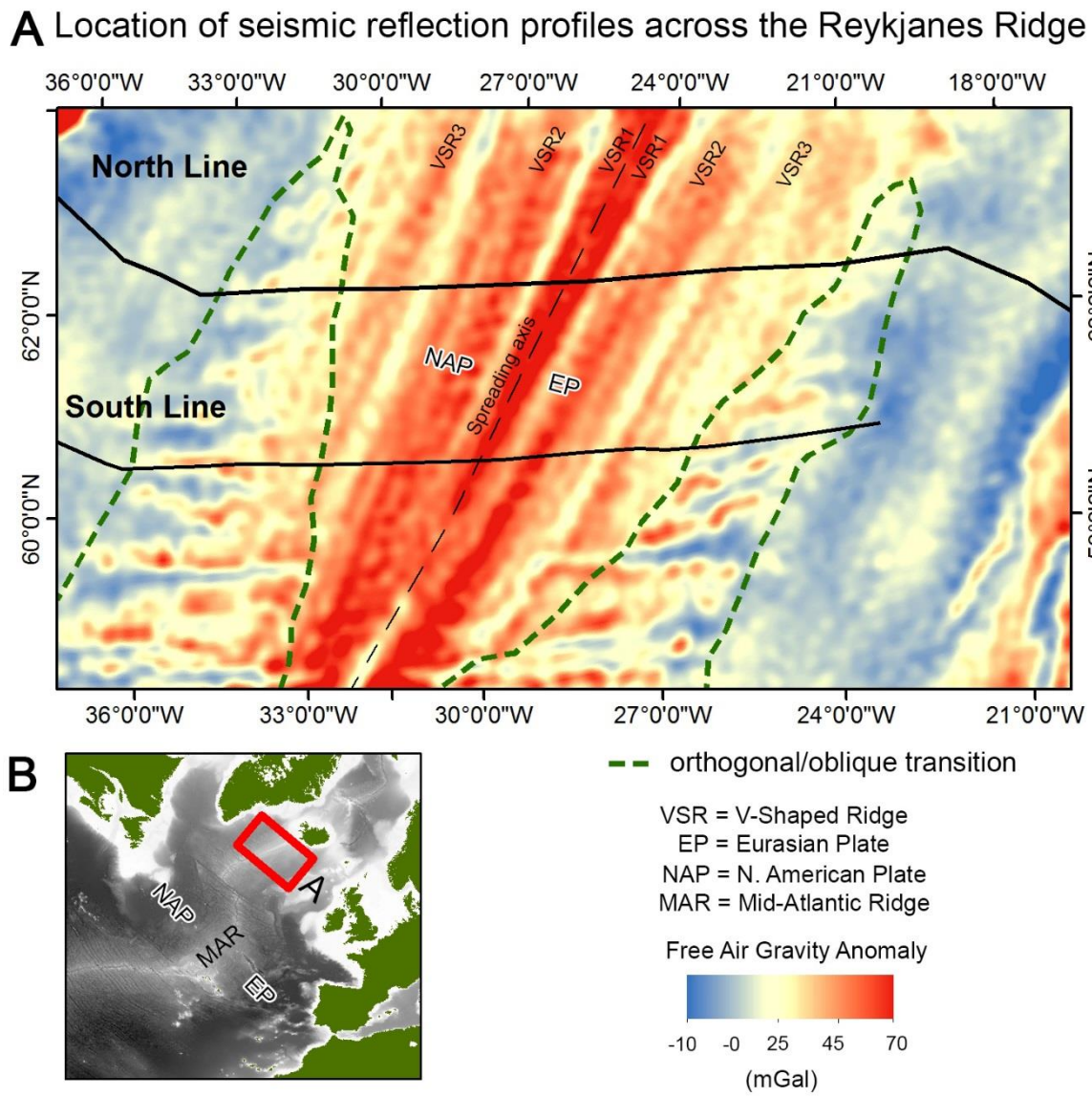

***Figure 5.1**: **A**: Free Air Gravity Anomaly (FAA) map (Bonvalot et al., 2012). Black lines are seismic reflection profiles North Line and South Line. Dashed green line is the transition between crust with fracture zones (E – W FAA fabric) and crust without fracture zones (VSRs and smooth crust near to continents) (White, 1997). This transition marks the oblique/orthogonal transition (White, 1997) discussed below. **B**: Bathymetry map showing location of Reykjanes Ridge in the North Atlantic.*

5.1.1 Geology of the Reykjanes Ridge

The Reykjanes Ridge separates the North American and Eurasian Plates. Over time it has changed its configuration (Parkin & White, 2008). The spreading boundary's origin was determined by analysis of seismic

velocities and crustal thickness over the Hatton Bank and Faroes-Shetland Basin. This indicated that the Iceland plume started 62 Ma, with seafloor spreading around 55 Ma. At 55 Ma mantle temperatures were 100 - 150˚C above the normal mantle temperature of ~1300˚C, they then cooled by 75˚C over the next 10 - 12 Myrs (Parkin & White, 2008). From 55 - 37 Ma the Reykjanes Ridge formed a right stepping series of orthogonal spreading segments, separated by transform zones (White, 1997). The crust created from these orthogonal segments produces an E – W FAA (Figure 5.1A).

Around 37 Ma, there was a reconfiguration of the Reykjanes Ridge from orthogonal spreading to oblique spreading (the orthogonal/oblique transition in Figure 5.1A). This is thought to coincide with either an increase in melt supply, likely because of hotter asthenosphere from the Iceland plume started to move southwards along the ridge axis (White, 1997), or due to the Reykjanes Ridge migrating towards Iceland and hence being increasingly influenced by hot mantle from the Iceland plume (Jones, 2003; Smallwood & White, 2002).

Along its length, the Reykjanes Ridge has changes in crustal thickness related to its proximity to the Iceland hotspot. Searle et al., (1998) observed that along axis, between 58˚ N – 62˚ N, the mantle Bouguer anomaly decreased by 50 mGals over 550 km towards the north, which was interpreted as an increase in crustal thickness of 3 km.

Geochemical analyses have identified that the thicker crust on and around Iceland originated from increased melt supply from elevated temperatures in an upwelling mantle plume (Hilton et al., 1999; Schilling, 1973). On the axis of the Reykjanes Ridge, dredging of fresh volcanic rocks reveal a high $^{3}He/^{4}He$ anomaly detectable up to 2400 km away from Iceland (Poreda et al., 1986) this ratio increases towards Iceland indicating an increase in the sourcing of melt from the lower mantle. Also found, were isotopes of Pb and isotopic ratios of $^{87}Sr/^{86}Sr$ and $^{143}Nd/^{144}Nd$ that were indicative of an enriched mantle plume influence, within 1200 km of Iceland (Taylor et al., 1997; Murton et al., 2002). Isotope analysis from 61˚ N to 63˚ N found that $^{87}Sr/^{86}Sr$ increased from 0.7027 to 0.7031 due to

a higher input of radioactive ^{87}Rb indicating the presence of enriched mantle in the melting region (Murton et al., 2002). Conversely from 61˚ N to 63˚ N $^{143}Nd/^{144}Nd$ decreased from 0.51316 to 0.51305 due to decreasing ^{147}Sm, indicating a reduced depleted mantle component (Murton et al., 2002).

Geochemical studies have also indicated that the Iceland plume produces thicker crust along the Reykjanes Ridge. Changes in incompatible element ratios such as Na and Ti indicate an increase in melting with proximity to Iceland, while decreasing MgO concentrations from 8.6 wt% at 57˚ N to 7.5 wt% at 62˚ N indicate increasing fractional crystallisation as a result of thicker crust (Murton et al., 2002). Si and Fe concentrations, normalised to MgO of 8 wt.% (i.e. denoted using the suffix [8]) to account for crystal fractionation, were used as proxies for the solidus depth (Klein & Langmuir, 1987). $Si^{[8]}$ has a 0.8% average decrease northwards, and $Fe^{[8]}$ has a 1% average increase northwards (Murton et al., 2002) indicating a deepening of the solidus towards Iceland and hence hotter mantle temperatures.

Crustal thickness was also determined by seismically measuring the depth of the Moho. A compilation of 12 seismic profiles across the Reykjanes Ridge near Iceland, but not directly above the plume, measured depth anomalies of 0.9 – 2.4 km thicker than average (White et al., 1992). This revealed that south of the Bight Fracture Zone around 55˚ N the crust has an average thickness of 5 km (White et al., 1992). While at 62˚ N, nearer Iceland, the crust has a thickness of 10 km. It was also noted that above the thicker crust at 62˚ N, the bathymetry was 2.5 km shallower than expected for the Reykjanes Ridge (White et al., 1995). Of this, one kilometre can be accounted for by the thicker crust, while the other 1.5 km requires support from a 100˚C hotter than average mantle (White et al., 1995).

The Reykjanes Ridge's VSRs are important features utilised for our analysis. Jones et al., (2002) used 30 mGal anomalies, ½ to ¼ the amplitude of fracture zone anomalies, to identify 7 VSRs. Parnell-Turner et al., (2014) used shallow bathymetry and high FAA to identify 6 VSRs which

had formed at intervals of 3 - 8 Myrs since 35 Ma. In crust older than 35 Ma, a further 3, albeit weak, linear anomalies were interpreted as potential VSRs under the sediment of the Irminger Basin (Parnell-Turner et al., 2014; White, 1997). Of these, only one weak linear anomaly has been identified at the corresponding locations on the opposite, European Plate where the sediment is thicker. The FAAs are thought to represent basement topography beneath the sediment layer, indicating the VSRs are 15 – 70 km wide and up to 750 m high (Parnell-Turner et al., 2017). At the point where the present-day spreading axis and the most recent VSR (#1) intersects, between 59˚30' N and 61˚30' N, the bathymetry shows faults at the seafloor have lower-amplitudes and shorter spacing than in between the VSRs (the troughs). The change in fault geometry indicates that the crust's elastic thickness is shallower at the VSRs. VSR 1 has a high density of seamounts, ~150 per 1000 km^2, compared to ~100 per 1000 km^2 in the troughs (Searle et al., 1998). These volcanic features indicate that volcanism is higher at the VSRs, suggesting that the crust here is hotter than in the troughs.

Crustal thickness determined from residual depth analysis of seismic reflection profiles suggests that the crustal thickness at VSRs is 2 km greater than the average for the Reykjanes Ridge of 7 km (Parnell-Turner et al., 2017); if we explain this only by temperature variations they require a mantle temperature increase of 30˚C (White et al., 1995). However, the VSRs may not only result from temperature increases. Periodic volume fluctuations of 6.5 ± 4.9 x 10^6 km^3 Myr^{-1} every 8 Myrs was modelled by expanding the plumes width. This simulated pluses in the melt supply to the Reykjanes Ridge by bringing more of the plume's centre into contact with the spreading axis, without changing the plume's average temperature. The model indicated the VSR's 35 mGal variation over 600 km could be generated by melt volume increase. This volume increase produced a similar signal to a 35 – 56˚C increase in temperature (Ito, 2001). Alternatively, Benediktsdottir et al., (2012) and Hey et al., (2010) observe that the VSRs are asymmetric and not continuous, and suggested they may have resulted from southwards propagating rifts. Neither of

these latter two explanations explain the geochemical evidence for greater degrees of mantle melting (Murton et al., 2002).

In this chapter, I use the VSRs as proxies for periods of high melt supply and compare them to the amount of tectonic extension expressed as brittle faulting of the upper crust and seafloor.

Although the previous two chapters have used bathymetry to analyse fault heave, I have already shown that this method is limited to areas where sediment thickness does not obscure the basement faults (see Chapter 2 and 4). This means fault heave calculated from bathymetry alone cannot be used when measuring fault heave at distances greater than about 40 km off-axis (depending on sedimentation rate). Therefore, I cannot use bathymetry to compare fault heave at the VSRs and instead, in this Chapter, I use seismic reflection profiles to identify faults beneath the sediment at distances >40 km off-axis.

5.1.2 Data sets

Two seismic reflection profiles across the Reykjanes Ridge were used to identify faults. The North Line is 1340 km long and the South Line is 1050 km long (Figure 5.2). These were collected during the JC050 cruise and follow parallel to the spreading flow lines (White, 2011). The North Line starts at 36˚53’ W; 63˚2’ N, crosses the spreading axis at 26˚52’ W; 61˚45’ N and ends at 15˚33’ W; 58˚46’ N. The South Line starts at 39˚27’ W; 61˚44’ N, crosses the spreading axis at 29˚9’ W; 60˚16’ N and ends at 22˚5’ W; 59˚46’ N (Figure 5.1). Two 355 cubic inch capacity GI guns firing at 14s intervals (approximately 40 m distance) were used to create the seismic signal, these where recorded along a 1650 m long streamer with 132 channels at a 12.5 m spacing (White, 2011).

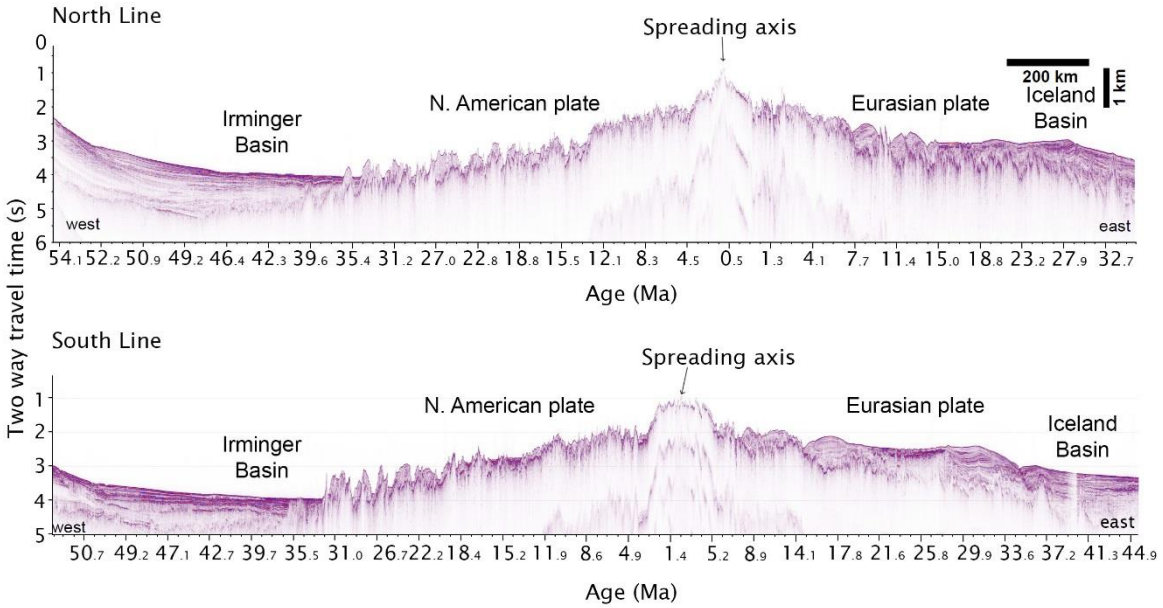

***Figure 5.2**: Seismic reflections profiles illustrated in the cruise report for JC050 (White, 2011).*

5.2 Results

5.2.1 Identifying faults

The seismic reflection profiles are divided along two horizons (Figure 5.3). The shallowest horizon is the first strong, continuous, and mostly horizontal reflector indicating the water/sediment boundary (Figure 5.3). Below the water/sediment boundary, reflectors are mostly continuous and horizontal, indicative of stratified sediment. This I label the sediment layer, often described as seismic Layer 1. The sediment layer is thickest further off axis and cannot be found as a continuous layer within 15 km of the spreading axis. The next interpretive horizon occurs where continuous reflections meet chaotic reflectors, usually along an irregular boundary (Figure 5.3). This boundary can sometimes appear as a strong reflector, with horizontal reflectors above chaotic reflectors, in other locations there is no strong reflector at the boundary. This boundary is interpreted as the sediment/crust boundary. Below the sediment/crust boundary, reflectors are weak, chaotic, and irregular indicating no stratification within the upper oceanic crust.

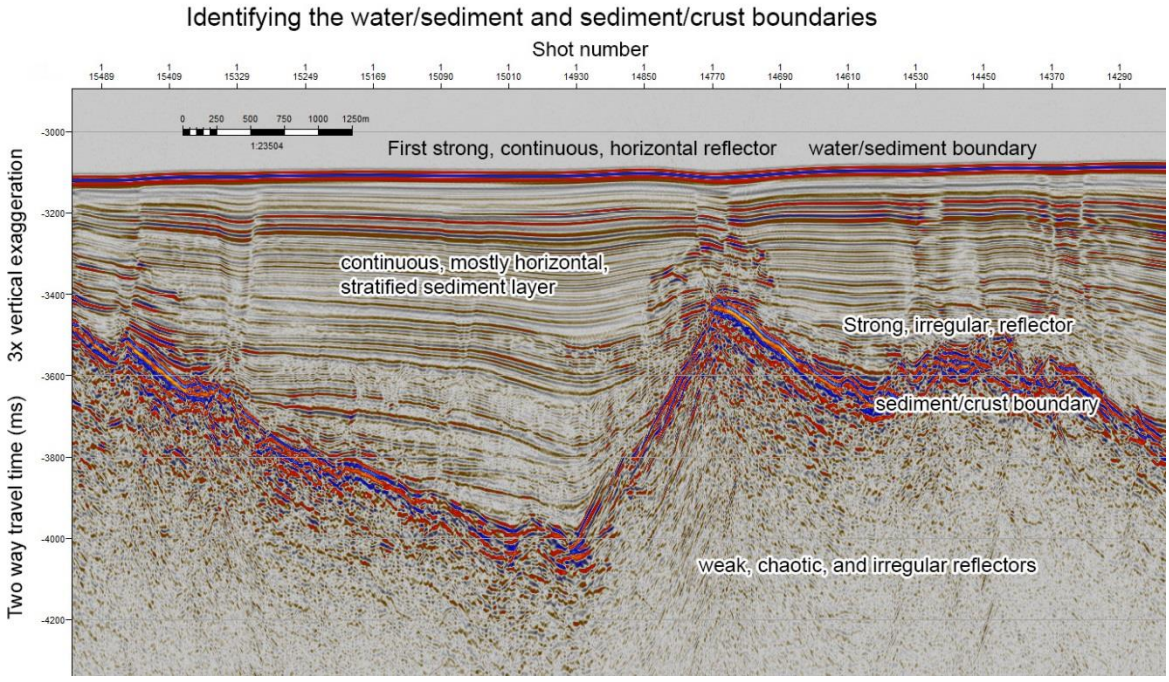

***Figure 5.3**: A typical section along the seismic reflection profiles illustrating the two main boundaries observed, the water/sediment boundary and the sediment/crust boundary.*

After the seismic boundaries were identified the profiles were depth converted using a constant velocity of 1500 m s^{-1} above the water/sediment boundary and a constant velocity of 2200 m s^{-1} between the water/sediment boundary and the sediment/crust boundary (Figure 5.4). As I am only interested here in the depth for the sediment/crust boundary so a velocity for the profile beneath the sediment/crust boundary was not necessary.

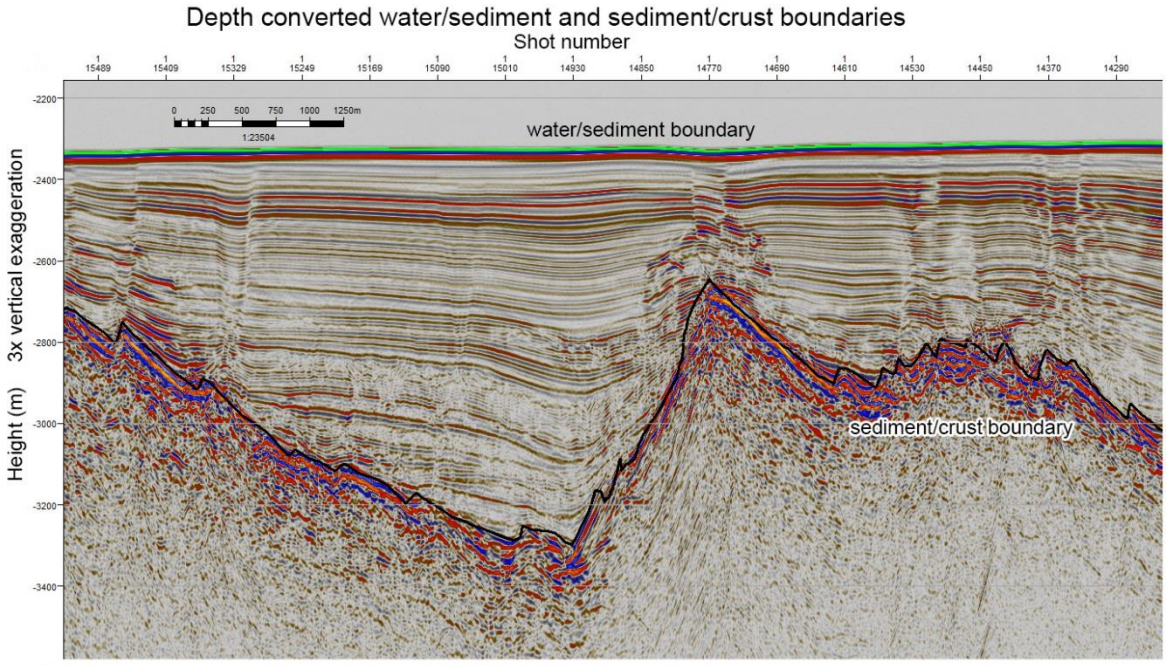

***Figure 5.4**: Illustration of a depth converted seismic reflection profile using the two seismic boundaries illustrated in Figure 5.3. Depth converting the boundaries allows for sediment thickness to be calculated.*

The sediment layer starts appearing between 15 – 20 km off axis as depositional ponds between peaks in the sediment/crust boundary (Figure 5.5A). Once the sediment thickness has reached ~400 m it starts to form a continuous sediment layer above the sediment/crust boundary (Figure 5.5B). A fully continues sediment layer is established at distances over 200 - 300 km off axis. When the sediment layer reaches ~1 km thick after ~400 km off axis, the sediment/crust boundary is no longer visible (Figure 5.5C).

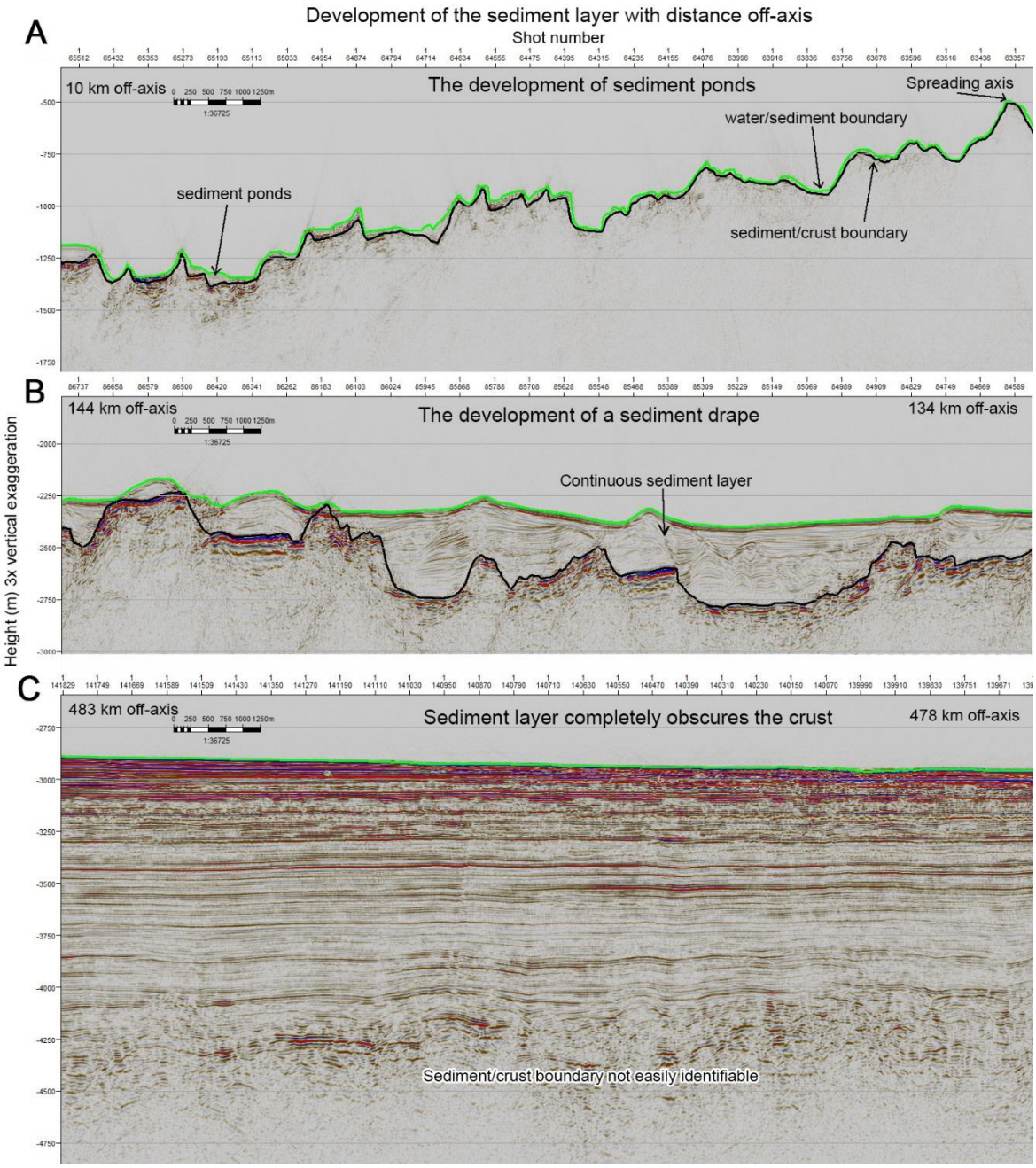

***Figure 5.5**: Changes in sediment thickness along the seismic reflection profiles with distance off axis. Green line is the water/sediment boundary and black line is the sediment/crust boundary. **A**: Between the spreading axis and the 10 km off axis there is very little sediment coverage apart from where sediment ponds start to form in deep regions. **B**: Between 134 – 144 km off axis illustrates where, off axis, the sediment layer is thick enough to form a continuous sediment drape over the crust. **C**: Between 478 – 483 km off axis, the sediment layer is thick enough to obscure the sediment/crust boundary.*

I identify faults under the sediment layer along the sediment/crust boundary using multiple methods. Primarily, I identified asymmetrical sections of the sediment/crust boundary as half-grabens between 200 – 2000 m across and 50 – 800 m high (Figure 5.6). The steeper slope of these half-grabens typically faces towards the spreading axis and are identified as fault planes. Fault heave is measured as the horizontal distance between the top of the half-graben and bottom of the half-graben.

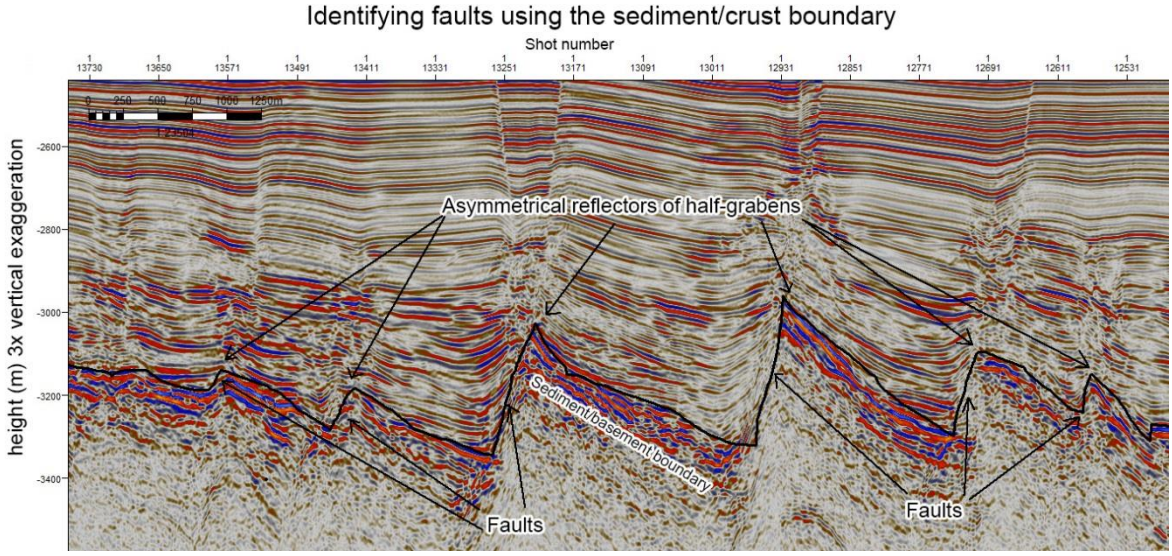

Figure 5.6*: Asymmetric half-grabens along the sediment/crust boundary have their steep faces interpreted as fault scarps. On the Eurasian Plate the steep slopes typically face west while on the North American Plate they face east.*

Another method used at distances >15 km off-axis, where sediment ponds are more common, is to use deformation within the sediment layer that abuts against a vertical sediment/crust boundary. This deformation is represented by parallel reflectors in the sediment layer changing dip direction, folding, or breaks the stratigraphy near the sediment/crust boundary (Figure 5.7A). The change in the strata's dip direction can be attributed to increasing accommodation space as the hanging wall subsides, and shear stress near an active fault plane. Faults can also be identified when sudden breaks and off sets within the continuous reflectors of the sediment layer are traced down through the strata and contacts the sediment/crust boundary (Figure 5.7B). Only if the offsets

reach the crust then I can interpret that there must be a fault within the crust and not just the sediment layer.

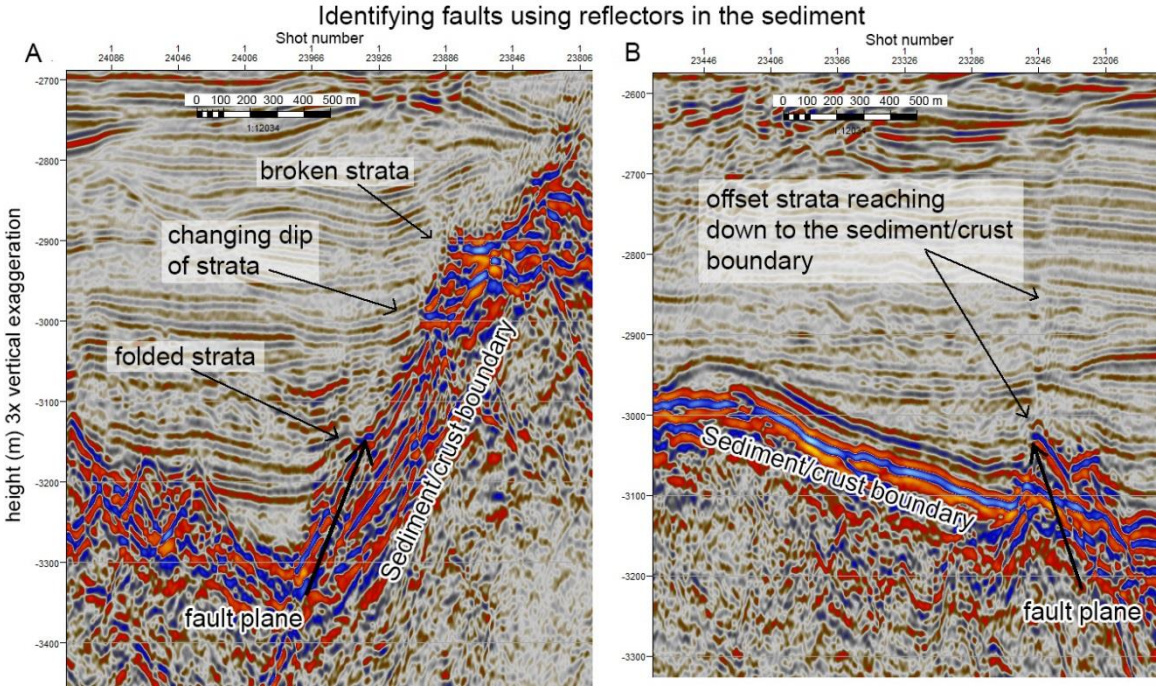

***Figure 5.7**: Identifying faults using the sediment layer. **A**: A fault can be identified from a change in strata dip, break in strata, or folding of the strata near an almost vertical sediment/crust boundary. **B**: A fault can also be identified where offset strata within the sediment layer reaches down to the sediment/crust boundary.*

Interpretation of faults and seismic boundaries can be difficult where very thick sediment prevents the sediment/crust boundary being identified (Figure 5.5C). It is also difficult to identify faults in the sediment/crust boundary when the sediment/crust boundary is highly irregular and has no strong reflectors separating the sediment and crust layers (Figure 5.8C). The lack of a strong reflector at this boundary possibly arises because of excessive acoustic scattering when the sediment/crust interface is very rugged. In some regions, there is a diffuse boundary between the sediment and crust along the steep edge of a half-graben. This makes the precise location of a fault plane difficult. In some regions there are very strong horizontal reflectors in the sediment layer that acoustically shade the deeper layers (Figure 5.8B). These are potential gas pockets that make it difficult to interpret the sediment/crust boundary

beneath. Occasionally, within the sediment layer, the stratigraphy is broken and irregular at depth (Figure 5.8C), this potentially results from fluid or gas escape deforming and de-stratifying the sediment layer, also making the sediment/crust boundary difficult to identify. Despite these difficulties, great care has been taken to accurately pick the sediment/crust boundary and the fault scarps, with repeated, blind iterations to test whether the same interface is chosen.

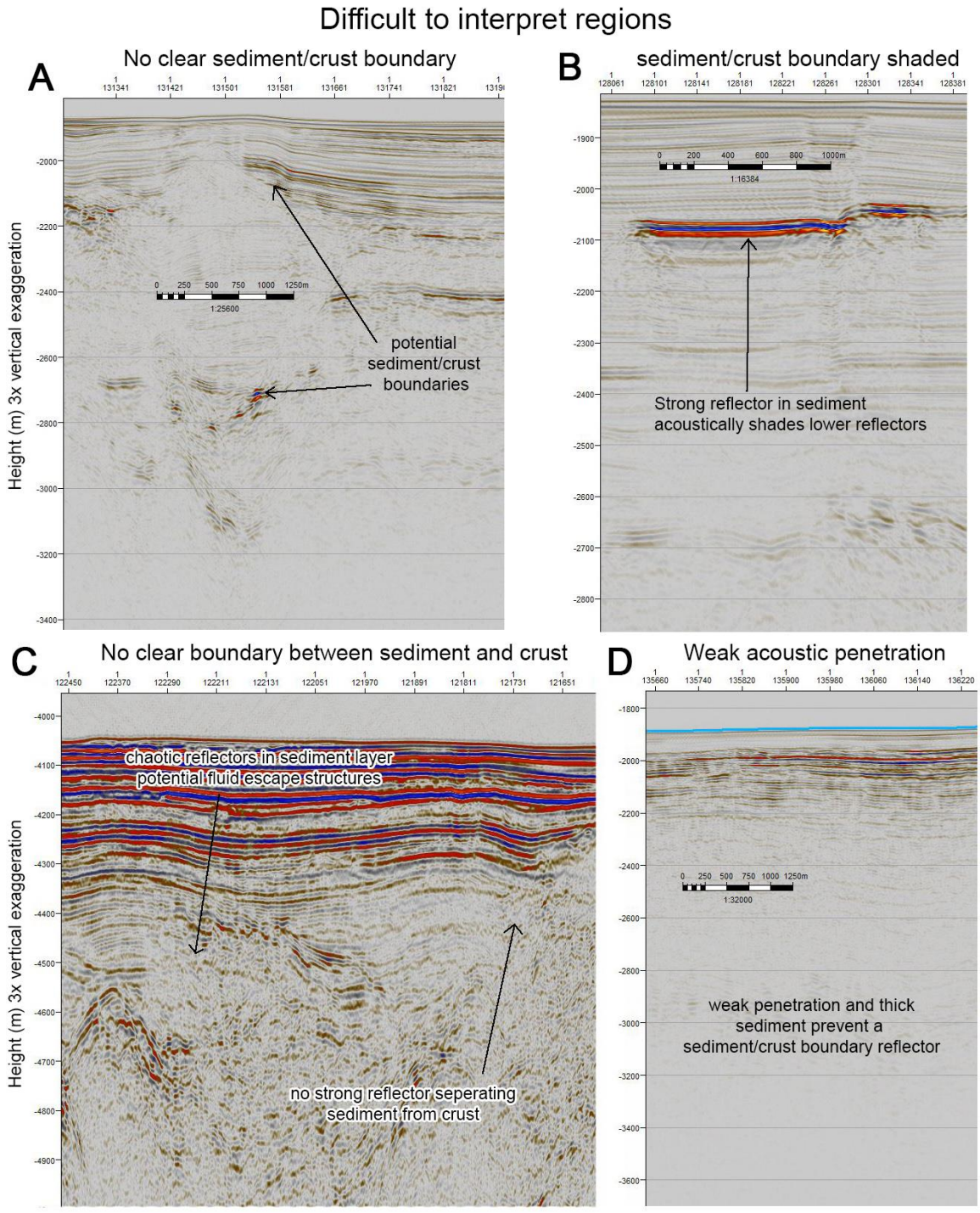

***Figure 5.8**: Examples along the seismic reflection profiles where interpreting boundaries and faults are difficult. **A**: No clear sediment/crust boundary because of weak reflectors or multiple strong reflectors. **B**: Strong acoustic reflector within the sediment layer shadows deeper signals. **C**: There is not a strong reflector to separate the chaotic crustal reflectors from the stratified sediment reflectors. **D**: Weak penetration that does not image the sediment/crust boundary.*

Once the faults were identified in Petrel™ they were exported as an XYZ point file into ArcGIS™ at 6 m intervals along the profiles (Figure 5.9A). The points within 6 m of each other were grouped together into a single fault polygon (Figure 5.9D). The heave of the fault was calculated as the length along the profile line occupied by a fault polygon (Figure 5.9D).

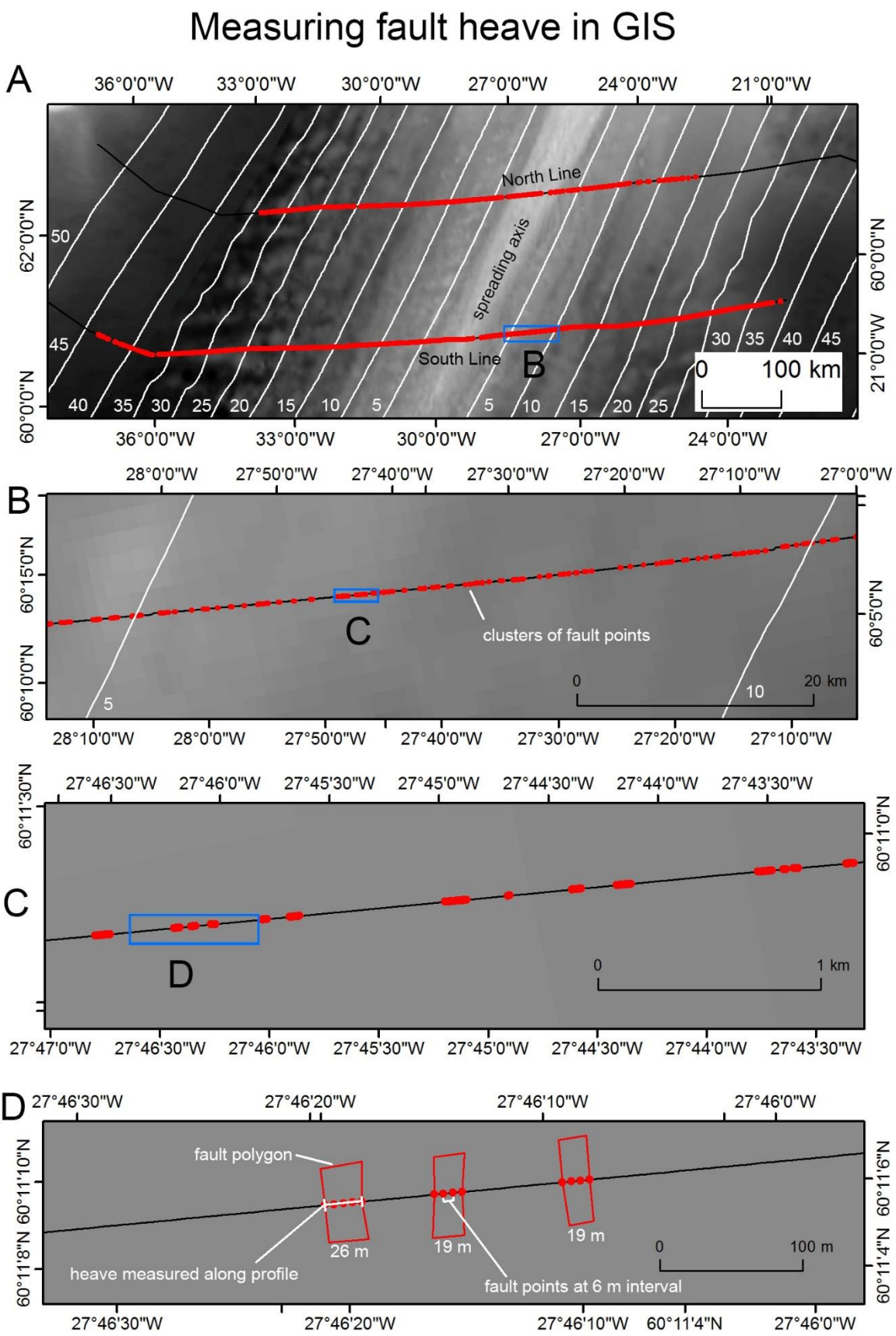

***Figure 5.9**: Illustrating the process of measuring fault heave in ArcGIS™ once the faults have been identified from the seismic reflection profiles in Petrel™. **A**: Black lines are the North and South Lines, and red dots are the*

identified faults. White lines are age contours in millions of years (Müller et al., 2008). Blue box is the extent of panel B. ***B****: Zoom in along the South Line illustrating the faults in red. Blue box is the extent of panel C.* ***C****: Zoom in on a cluster of faults illustrating that they are clusters of points. Blue box is extent of panel D.* ***D****: Zoom in on clusters of faults to illustrate they are points spaced at 6 m intervals. Points within 6 m of other points are grouped into one fault polygon, red box. The heave of this fault is measured as the distance along profile, black line, across the fault polygon.*

5.2.2 Calculating T%

T%, as explained in Chapters 2, 3, and 4, is calculated along each seismic reflection profile (Figure 5.10C). Along the Reykjanes Ridge seismic reflection profiles, T% is calculated in 2D.

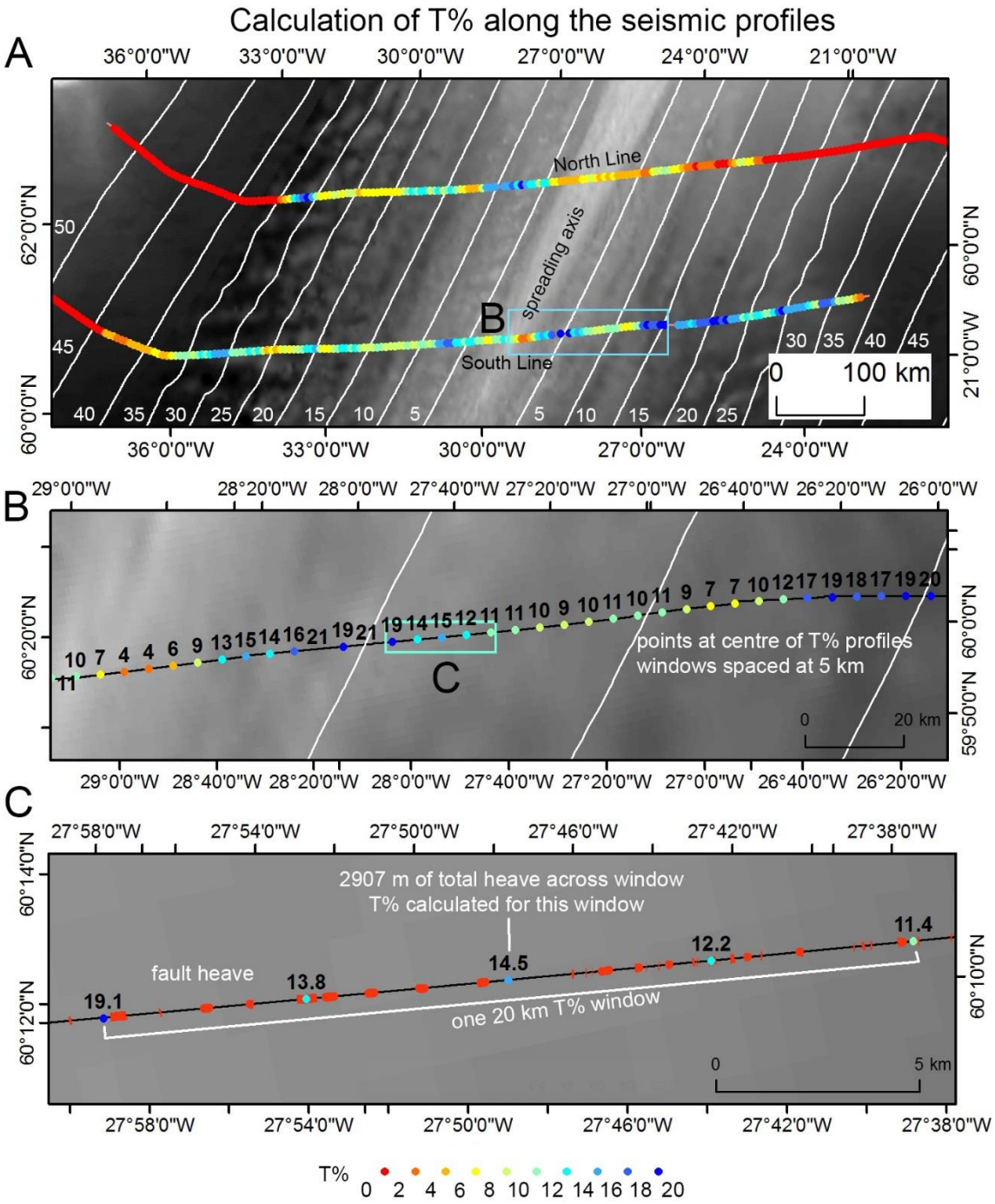

***Figure 5.10**: Calculating T% from the measured fault heave. **A**: The T% of the North and South Line, warmer colours are lower T%. White lines are age contours in millions of years (Müller et al., 2008). The blue box is the extent of panel B. **B**: Illustration of the individual T% points spaced at 5 km intervals along the South Line. The number above the T% point is the calculated T%. Blue box is the extent of panel C. **C**: Red boxes are the fault polygons (Figure 5.9D) illustrating fault heave along the South Line.*

Analysis of the T% profiles relies on changes in T% from the plate's mean value (Figure 5.11A and B). Additionally, T% from both plates are plotted on the same time axis to determine if the centres of T% peaks' periods are in-phase between plates (Figure 5.11C and D).

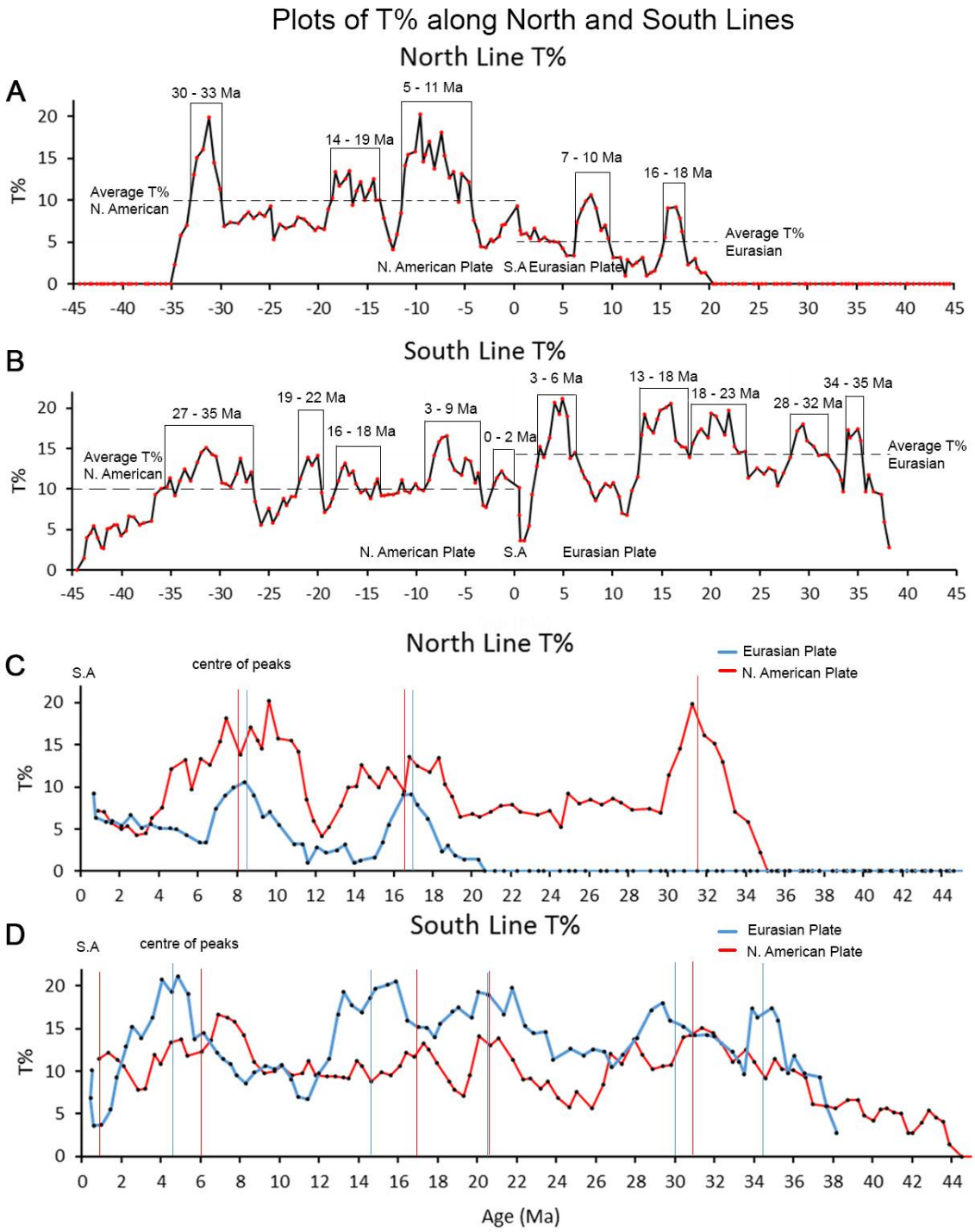

***Figure 5.11**: T% plots along North and South Lines, S.A is Spreading Axis. **A**: North Line where negative age is the North American Plate and positive age is the Eurasian Plate. Horizontal dashed line is the average T% for*

each plate. Black boxes illustrate the T% peaks identified as T% being higher than the plate average. ***B****: South Line with highlighted T% peaks.* ***C****: North Line plotted against the same age axis to identify in-phase signals between the plates. Blue is the Eurasian Plate, red is the North American Plate. Vertical coloured lines are the centres of T% peaks.* ***D****: South Line plotted against the same age axis.*

T% along the North Line was measured out to 35 Ma on the North American Plate and 20 Ma on the Eurasian Plate. The average T% for the North American Plate between 0 – 35 Ma was 10%, and the average T% for the Eurasian Plate between 0 – 20 Ma was 5% (Figure 5.11A). Periods of high T% are defined as being above the average for the plate and are listed in Table 5.1. A visual comparison of the centres of the peaks in T% for each plate suggests the two youngest peaks, centred around ~8 Ma and ~17 Ma, are symmetrical and hence in phase (Figure 5.11C). However, the magnitude and period of the peaks are not symmetrical.

T% along the South line was measured to 44 Ma on the North American Plate and 38 Ma on the Eurasian Plate. The average T% for the North American Plate between 0 – 44 Ma was 10%, and the average T% for the Eurasian Plate between 0 – 38 Ma was 14% (Figure 5.11B). Periods of high T% are listed in Table 5.1. A visual comparison of the centres of the T% peaks of each plate reveals the peaks centred at 20.5 Ma and ~30.5 Ma are in phase, all other peaks are out of phase (Figure 5.11D).

North Line			
North American Plate		Eurasian Plate	
Age (Ma)	Maximum T%	Age (Ma)	Maximum T%
5 - 11	21	7 - 10	11
14 - 19	14	16 - 18	9
30 - 33	20		
South Line			
0 - 2	13	3 - 6	22
3 - 9	17	13 -18	21
16 - 18	13	18 - 23	20
19 - 22	14	28 - 32	18
27 - 35	16	34 - 35	17

Table 5.1*: The age period and maximum T% for the periods of high T% along the North and South Lines in Figure 5.11.*

The T% profiles (Figure 5.11) and periods of high T% (Table 5.1) display irregular variability along profiles and between plates. This suggests the controlling variable for T% changes through time and influences conjugate plates differently. To determine if the amount of tectonic extension indicated by T% is related to melt supply I compare them to VSRs identified from FAA.

5.2.3 Identifying V-shaped ridges from Free Air Gravity Anomalies

VSRs are easily identified in FAA as laterally extensive ridges of 45 - 70 mGal (Hey et al., 2010; Jones et al., 2002; Martinez & Hey, 2017; Parnell-Turner et al 2014; Vogt, 1971; White et al., 1995). The FAA map used here is a 1' x 1' (~1.8 x 0.8 km at 62°N) world gravity map by the Bureau Gravimetrique International (WGM2012) derived from the EGM2008 Geopotential model and the ETOPO1 Global Relief model (Bonvalot et al., 2012).

Using the WGM2012 FAA map (Figure 5.12A), VSRs were identified as: positive FAA anomalies that trace NE – SW on the Eurasian Plate, and NW – SE on the North American Plate; are at an acute angle to the spreading axis; are between 100 - 800 km long; and have an anomaly on the opposite plate that is temporarily symmetrical within 1 Ma. Several positive FAA ridges can appear superimposed on large FAA highs, when this occurs the larger ridge is labelled with a number while the smaller,

sub-ridges are labelled with a letter (Figure 5.12B). There are also positive FAA ridges that do not have a temporally symmetrical conjugate on the opposite plate, these are highlighted but not given a label. These unlabelled FAA ridges are not included in the analysis.

There is a second prominent signal displayed in the FAA that are not VSRs. The FAA map displays E – W orientated bands of positive and negative FAA ranging from 20 – 60 km wide (Figure 5.12A). These bands are 30 km long in the north around 61˚ N and get longer towards the south, reaching 300 km long around 57˚ N. The E – W banding has very little overlap with the VSRs. The low FAA, E – W bands are interpreted to represent deep crustal anomalies and are possibly the off axis traces of first order segment discontinuities created when the Reykjanes Ridge was spreading orthogonally. I traced where the smooth FAA near the continents and the VSRs meet this E – W FAA fabric as the oldest oblique/orthogonal transition, and where the E – W FAA fabric meets the VSRs as the youngest oblique-orthogonal boundary (Figure 5.12B).

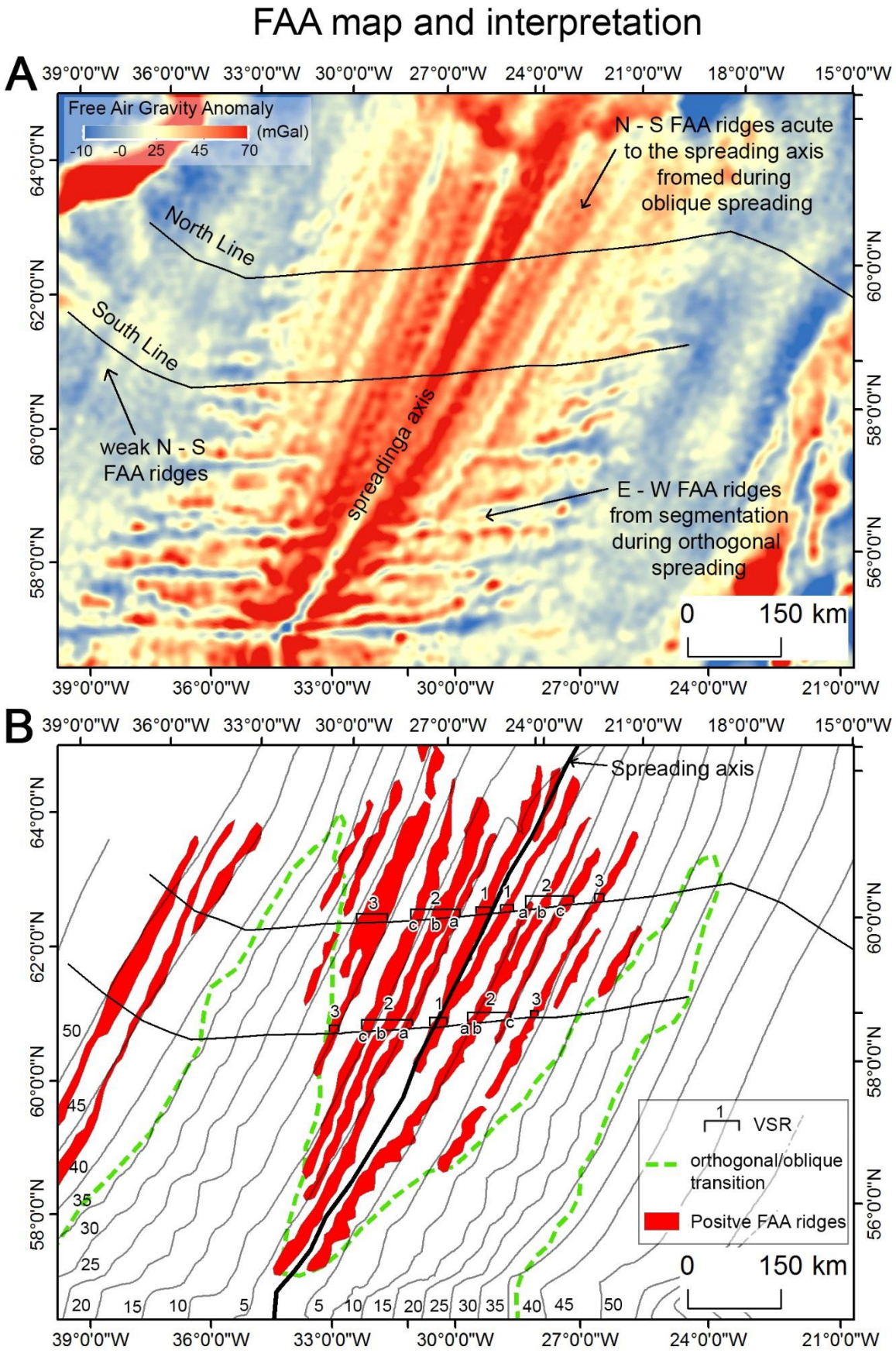

***Figure 5.12**: FAA map WGM2012 (Bonvalot et al., 2012) used to identify VSRs. **A**: FAA map for the North Atlantic with warmer colours indicating*

higher gravitational attraction. Two types of FAA terrains are identifiable, the N – S fabric and the E – W fabric. ***B****: Interpreted FAA map, black contours are age in Ma. Red bands are positive FAA ridges. The positive FAA ridges that meet the VSR criteria are labelled 1, 2, and 3. Dashed green line is the boundary between orthogonal and oblique spreading.*

The orthogonal/oblique transition separating the smooth seafloor near the continents from the rugged orthogonal seafloor occurs between 35 - 40 Ma on the North American and Eurasian Plates (Figure 5.12B and 5.13). The orthogonal/oblique transition separating the E – W fabric of the orthogonal crust from the smoother oblique crust with the VSRs occurs at around 30 Ma in the far north near 63˚35' N then crosses the age isochrones into younger crust towards the south, reaching the spreading axis at the Bight Fracture Zone at 56˚50' N (Figure 5.12B and 5.13). Orthogonal crust intersects the North Line on the North American Plate between 22 – 37 Ma (Figure 5.13A). Orthogonal crust intersects the South Line on the North American Plate between 16 – 36 Ma (Figure 5.13B). Orthogonal crust intersects the North Line on the Eurasian Plate between 30 – 35 Ma (Figure 5.13A). Orthogonal crust intersects the South Line on the Eurasian Plate between 20 – 39 Ma (Figure 5.13B).

In the FAA map, I identified three VSRs labelled 1, 2, and 3 (Figure 5.12B). I also identified possible FAA ridges between the North American continent and the orthogonal/oblique transition at 40 – 50 Ma (Figure 5.12B). However, these ridges are not acute to the spreading axis and do not have a symmetrical ridge on the Eurasian Plate, and so are not identified as VSRs. My analysis will focus on the labelled ridges.

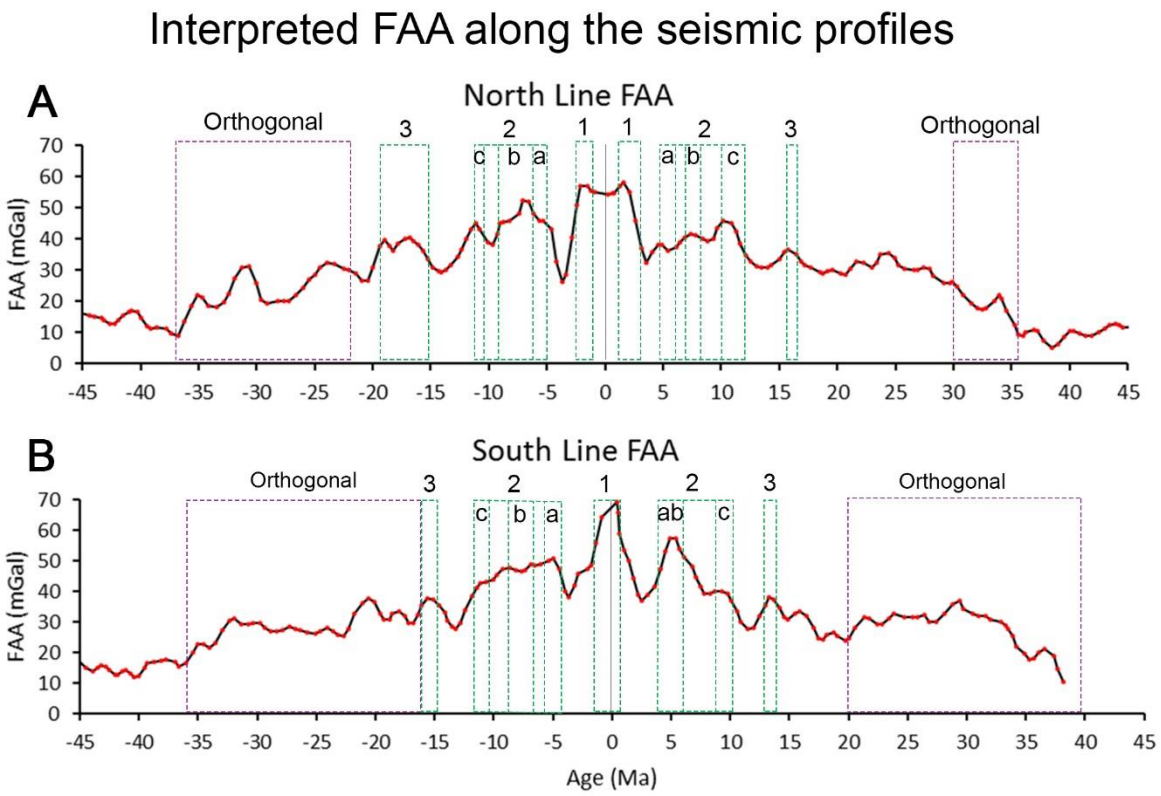

***Figure 5.13**: Profiles across the FAA map (Bonvalot et al., 2012) along the two seismic reflection profiles. Red dots are locations of T% points where the FAA was measured allowing for direct spatial comparison, while the black line is a linear interpolation between points. Dashed purple boxes are the region of orthogonal spreading (Figure 5.12B). Dashed green boxes are the locations of VSRs (Figure 5.12B). **A**: North Line. **B**: South Line.*

VSR1 on the North American Plate is 530 km long and 20 km wide, and on the Eurasian Plate VSR1 is 540 km long and 20 km wide. VSR2 on the North American Plate is 680 – 790 km long, 78 km wide and can be subdivided into three smaller sub-ridges labelled as VSR2a, VSR2b, and VSR2c. On the Eurasian Plate VSR2 is between 350 - 860 km long, 60 km wide and can be subdivided into three smaller sub-ridges labelled as VSR2a, VSR2b, and VSR2c. VSR3 on the North American Plate is 420 – 550 km long and 43 km wide. VSR3 on the Eurasian Plate is 630 km long and 10 km wide (Figure 5.12B). The VSRs' periods and range are displayed in Table 5.2.

FAA of VSRs				
North Line				
N. American plate			Eurasian plate	
VSR label	Period (Ma)	FAA range (mGal)	Period (Ma)	FAA range (mGal)
1	1 - 2.5	50 - 57	1 - 3	50 - 68
2a	5 - 6.3	43 - 48	4.6 - 6	36 - 38
2b	6.3 - 9.4	45 - 53	6.8 - 8	40 - 42
2c	10.4 - 12.2	41 - 45	10 - 12	35 - 45
3	15.2 - 19.5	33 - 40	15.6 - 16.6	35 - 37
South Line				
N. American plate			Eurasian plate	
1	0 - 1.3	50 - 68	0 - 1	58 - 70
2a	4.3 - 5.7	45 - 49	4 - 6.2	46 - 58
2b	6.8 - 8.8	46 - 49		
2c	10.3 - 11.6	40 - 44	9 - 10.4	36 - 40
3	14.7 - 15.9	36 - 38	13 - 14	35 - 39

***Table 5.2**: Table of identified VSRs using the FAA map in Figure 5.12 and plotted in Figure 5.13. Table displays the VSRs' label, period, and FAA range for both the North and South Lines and the North American and Eurasian Plates.*

The VSR are hypothesised to represent periods of high melt supply resulting in thicker oceanic crust (Vogt, 1971; White et al., 1995; Ito, 2001; Parnell-Turner et al., 2017). Thicker oceanic crust should produce shallower bathymetry according to the Airy isostasy model. To test this, I use my Residual Topographic Anomaly (RTA) method to identify regions of shallow crust and compare the results to the identified VSRs.

5.2.4 Calculating Residual Topographic Anomaly

RTA was calculated by first converting the depth converted point file of the water/sediment and sediment/crust boundaries into raster files and re-gridding them from 6 m to 550 m using the mean value of overlapping cells. This re-gridding allowed the raster's resolution to be comparable to the ~1.8 x 1 km resolution of the FAA map (Bonvalot et al., 2012) and the age map (Müller et al., 2008). Sediment thickness was then calculated by subtracting the sediment/crust boundary from the water/sediment boundary. Re-gridding the boundaries smooths them with a 550 m filter, removing the high relief signal of many faults, however this does not affect the RTA being compared to the VSR features that are >20 km wide.

The smoothed raster for the sediment/crust boundary was then isostatically corrected for the removal of sediment loading using the equation for the depth before sediment loading, t_b, (Le Douaran & Parsons, 1982): $t_b = t'_b - t_s \frac{(\rho_a - \rho_s)}{(\rho_a - \rho_w)}$, where, t'_b = depth after sediment loading, t_s = sediment thickness, ρ_a = density of asthenosphere (3200 kg m^{-3}), ρ_w = density of seawater (1027 kg m^{-3}) and ρ_s = density of sediment (1590 kg m^{-3}) (Figures 5.14A and 5.15A).

The unloaded crust was then plotted against the square root of age and a linear regression was fitted to determine the off axis subsidence trend that resulted from plate cooling and subsidence away from the spreading axis (Figures 5.14B and 5.15B). This subsidence trend obscures the smaller RTA fluctuations on 1 – 2 Myr periodicity that could relate to the VSRs. The linear regression describing the subsidence is used to subtract the cooling curve from the unloaded crust to produce a profile for the crust that is deeper (negative) or shallower (positive) from the average off axis crustal depth. This I call the RTA plot (Figures 5.14C and 5.15C).

The RTA plot has a very high frequency signal despite the 550 m filter applied to the seismic boundaries during re-gridding. This high frequency signal obscures signals at a 1 - 2 million year periodicity that may relate to VSRs. To filter the signal to focus on the periodicity of VSRs I applied a 2 Myr moving average to the RTA (Figures 5.14C and 5.15C).

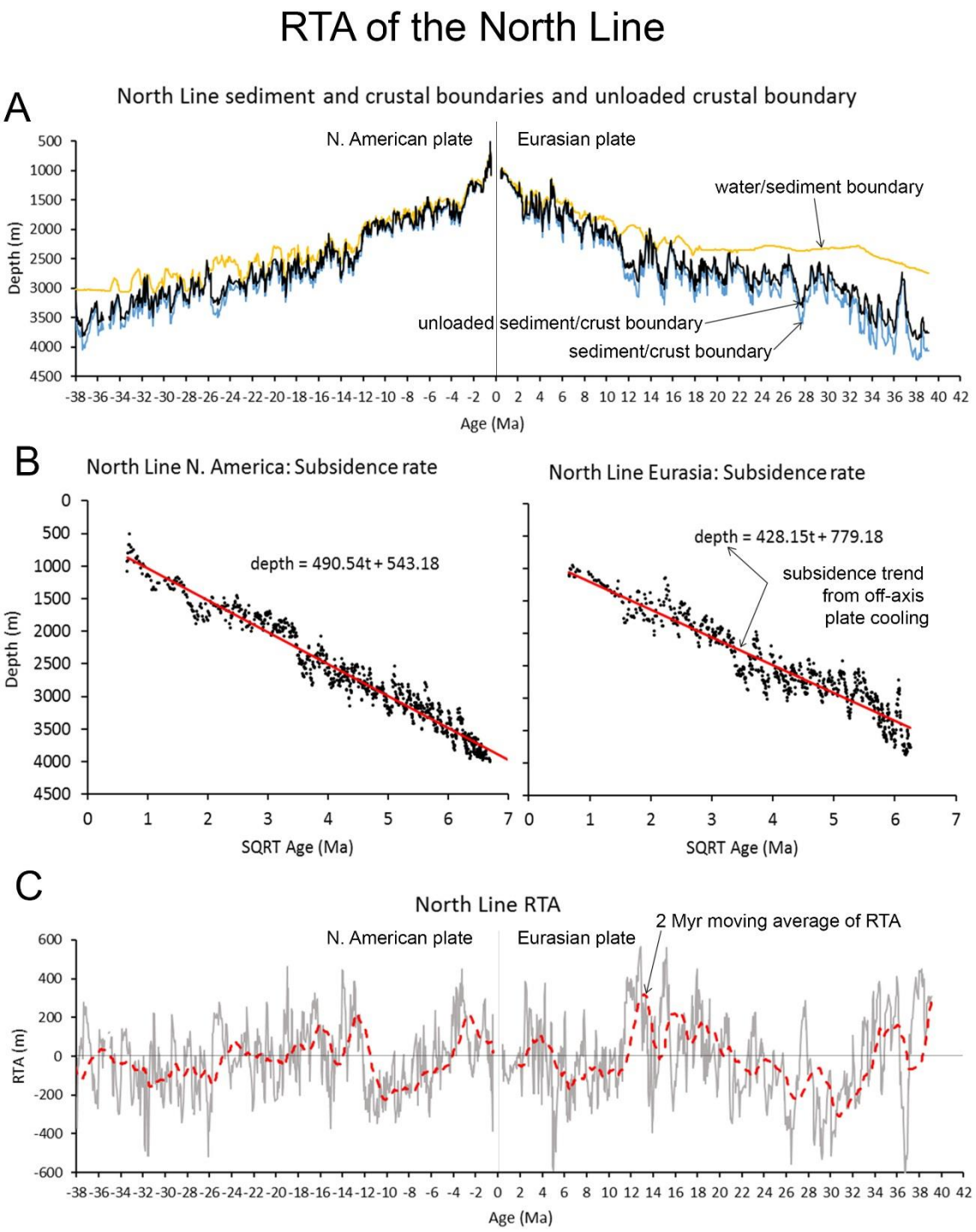

***Figure 5.14**: Calculation of RTA along the North Line. **A**: The water/sediment boundary (yellow line) is subtracted from the sediment/crust boundary (blue line) to calculate sediment thickness. The sediment/crust boundary is then isostatically compensated for the removal of sediment to produce the unloaded sediment/crust boundary (black line). **B**: The unloaded sediment/crust boundary is plotted against the square root of age for the North American Plate (left) and the Eurasian Plate (right). A linear regression describes the trend of increasing depth with*

distance off axis that results from off axis plate cooling and subsidence. ***C****: The linear regressions describing off axis subsidence in panels B are subtracted from the unloaded sediment/crust boundary to produce the RTA (grey line), indicating crust shallower or deeper than predicted. A 2 Myr moving average (dashed red line) is fitted to the RTA to reveal signals on a comparable periodicity to the VSRs.*

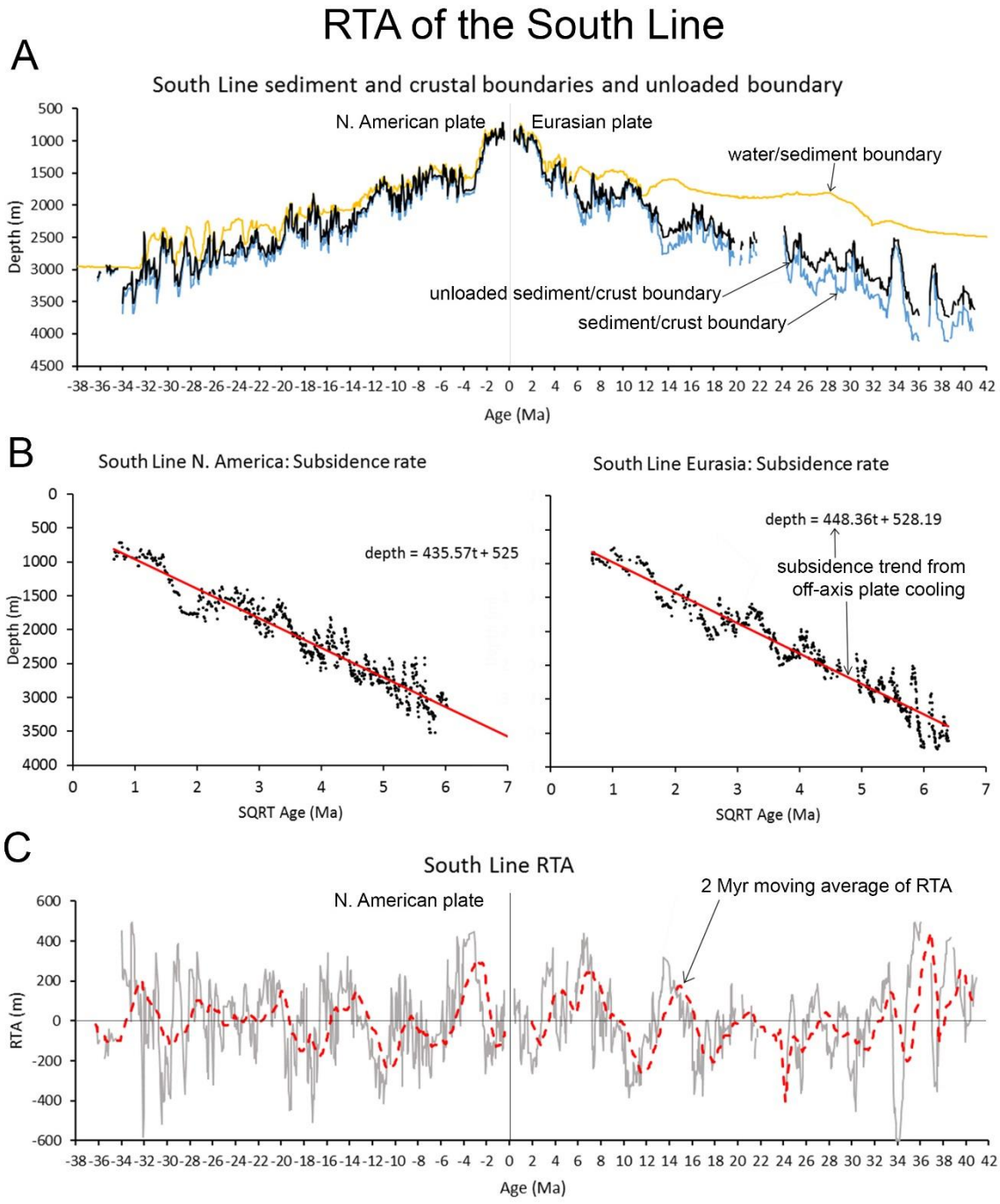

Figure 5.15*: Calculation of RTA along the South Line.* ***A****: The water/sediment boundary (yellow line) is subtracted from the*

*sediment/crust boundary (blue line) to calculate sediment thickness. The sediment/crust boundary is then isostatically compensated for the removal of sediment to produce the unloaded sediment/crust boundary (black line). **B**: The unloaded sediment/crust boundary is plotted against the square root of age for the North American Plate (left) and the Eurasian Plate (right). A linear regression describes the trend of increasing depth with distance off axis that results from off axis plate cooling and subsidence. **C**: The linear regressions describing off axis subsidence in panels B are subtracted from the unloaded sediment/crust boundary to produce the RTA (grey line), indicting crust shallower or deeper than predicted. A 2 Myr moving average (dashed red line) is fitted to the RTA to reveal signals on a comparable periodicity to the VSRs.*

Along the North and South Lines, I identify periods of positive RTA using the 2 Ma moving average (Table 5.2) so they can be compared to the VSR identified from the FAA. I then use the maximum value of the 2 Ma moving average within the periods of positive RTA to calculate a predicted crustal thickness. The predicted crustal thickness is calculated using the Airy isostasy equation; $c + b_1 = \frac{h_1 \rho_c}{\rho_m - \rho_c}$, where c is the thickness of the crust (6 km), b_1 is the additional crust, ρ_c is the density of the crust (3 g cm^{-3}), h_1 is the positive RTA, and ρ_m is mantle density (3.3 g cm^{-3}) (Lowrie, 2007; Suppe, 1985). This assumes a constant crustal density of 3 g cm^{-3} and plate thickness of 6 km and that the variation in RTA is resulting from crustal thickness rather than crustal density as described by the Pratt model (Table 5.2).

RTA and predicted crustal thickness					
North Line					
N. American plate			Eurasian plate		
Period (Ma)	Maximum RTA (m)	Airy crustal thickness (km)	Period (Ma)	Maximum RTA (m)	Airy crustal thickness (km)
0.5 - 4.1	210	8.1	2.8 - 5.2	100	7
11.8 - 14	230	8.3	12.2 - 14.6	320	9.2
14.8 - 18.8	160	7.6	15 - 21.3	220	8.2
22.2 - 24.8	80	6.8	34 - 37	180	7.8
34.9 - 36.5	40	6.4			
South Line					
N. American plate			Eurasian plate		
1.6 - 4.8	300	9	3.5 - 9.6	250	8.5
8.4 - 9	20	6.2	13.3 - 16.3	180	7.8
12.2 - 15.6	150	7.5	20.4 - 21.5	40	6.4
19.4 - 21.5	150	7.5	27.3 - 28.4	40	6.4
22.4 - 23.1	20	6.2	32.4 - 33.8	150	7.5
23.8 - 24.4	20	6.2	35.5 - 37.5	440	10.4
25.2 - 28	100	7	38.1 - 41	260	8.6
30.7 - 33.8	200	8			

***Table 5.3**: Periods of positive RTA (Figures 5.14C and 5.15C) for the North and South Lines' North American and Eurasian Plates. Displayed are the maximum RTA for each period and the predicted crustal thickness using the maximum RTA in the Airy isostasy equation.*

The RTA peaks along the North and South Lines display irregular variability and the peaks are out of phase between the plates (Table 5.3). If Airy isostasy can be applied to calculate crustal thickness from the RTA (Table 5.3) then the RTA should correlate to the FAA. Additionally, if the positive RTA peaks identified represent periods of thick crust, then they should correlate with the identified VSRs.

5.2.5 Comparing RTA to FAA and VSR

To directly compare the FAA to the RTA I had to de-trend the FAA for the gradual increase in plate density off axis as the crust cools. To do this I plotted the FAA of each plate against the square root of age, then calculated a linear regression. This linear regression was then subtracted from the FAA. This was the same method used to de-trend the unloaded sediment/crust boundary when calculating RTA.

North Line detrended FAA vs RTA

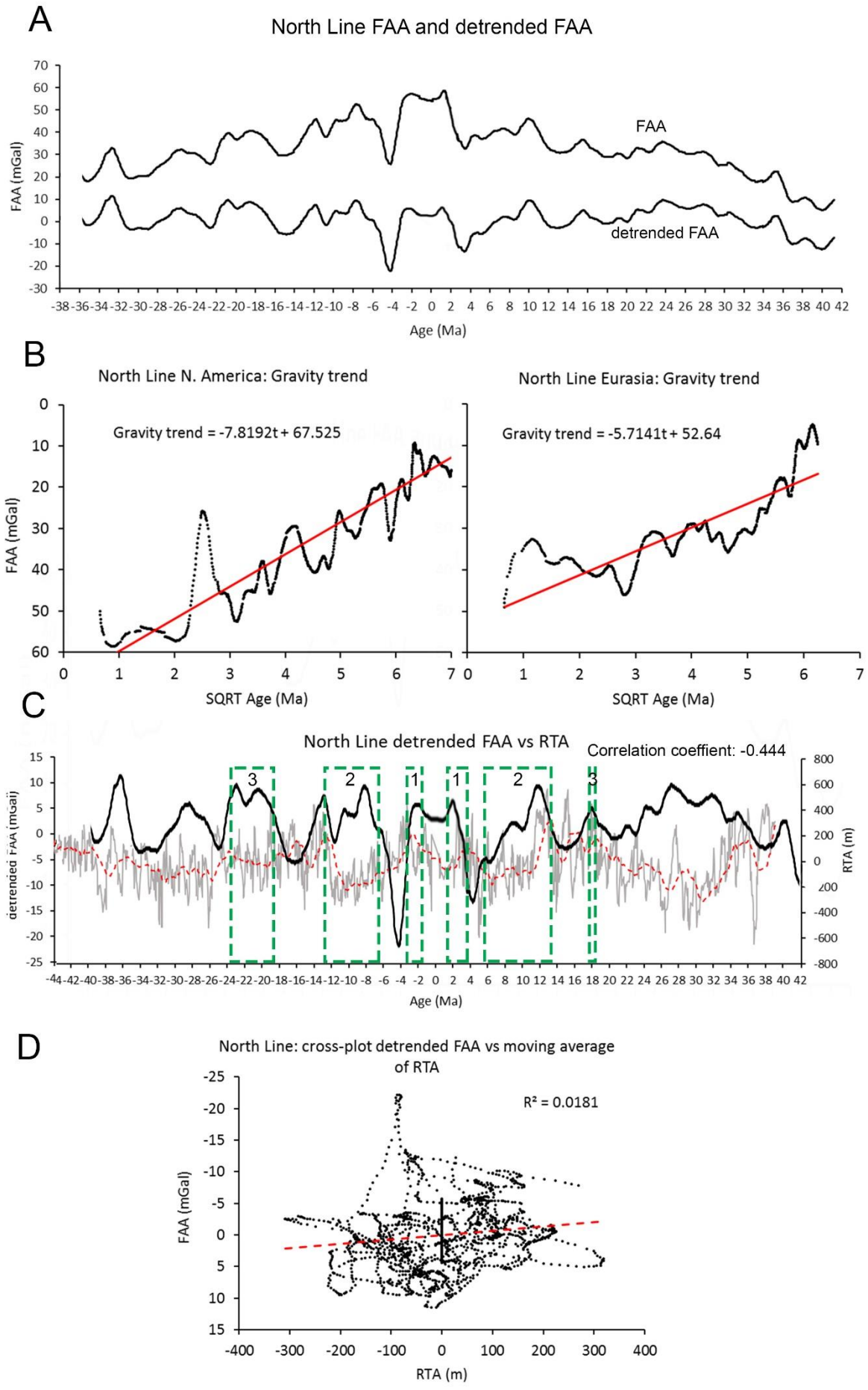

Figure 5.16*: North Line comparison of the RTA to the FAA and VSRs.* ***A****: FAA along the North Line decreases with distance off axis because of plate cooling and subsiding (top line). The FAA is de-trended using the linear regressions calculated in panels B (bottom line).* ***B****: Off axis subsidence is calculated by plotting the FAA for each plate against the square root of age, North American Plate is left and Eurasian Plate is right. A linear regression for these plots is subtracted from the FAA to calculate the de-trended FAA in panel A, C, and D.* ***C****: Visual comparison of de-trended FAA (black line) to RTA (grey line) and 2 Myr smoothed RTA (dashed red line). VSRs are highlighted in dashed green boxes. The correlation coefficient of the RTA and the de-trended FAA is -0.44.* ***D****: Cross-plot of 2 Myr moving average of RTA vs de-trended FAA. Linear fit (red dashed line) calculates the* R^2 *value as 0.02, meaning no correlation.*

Along the North Line a cross-plot of the de-trended FAA against the moving average of the RTA reveals no correlation with an R^2 value of 0.02 (Figure 5.16D). The correlation coefficient of de-trended FAA and moving average of the RTA is -0.04 indicating no correlation (Figure 5.16C). A visual comparison of the moving average of the RTA against the VSRs indicates no obvious relation (Figure 5.16C). From this I conclude that RTA and FAA are not correlated and that RTA and VSRs are also not correlated along the North Line.

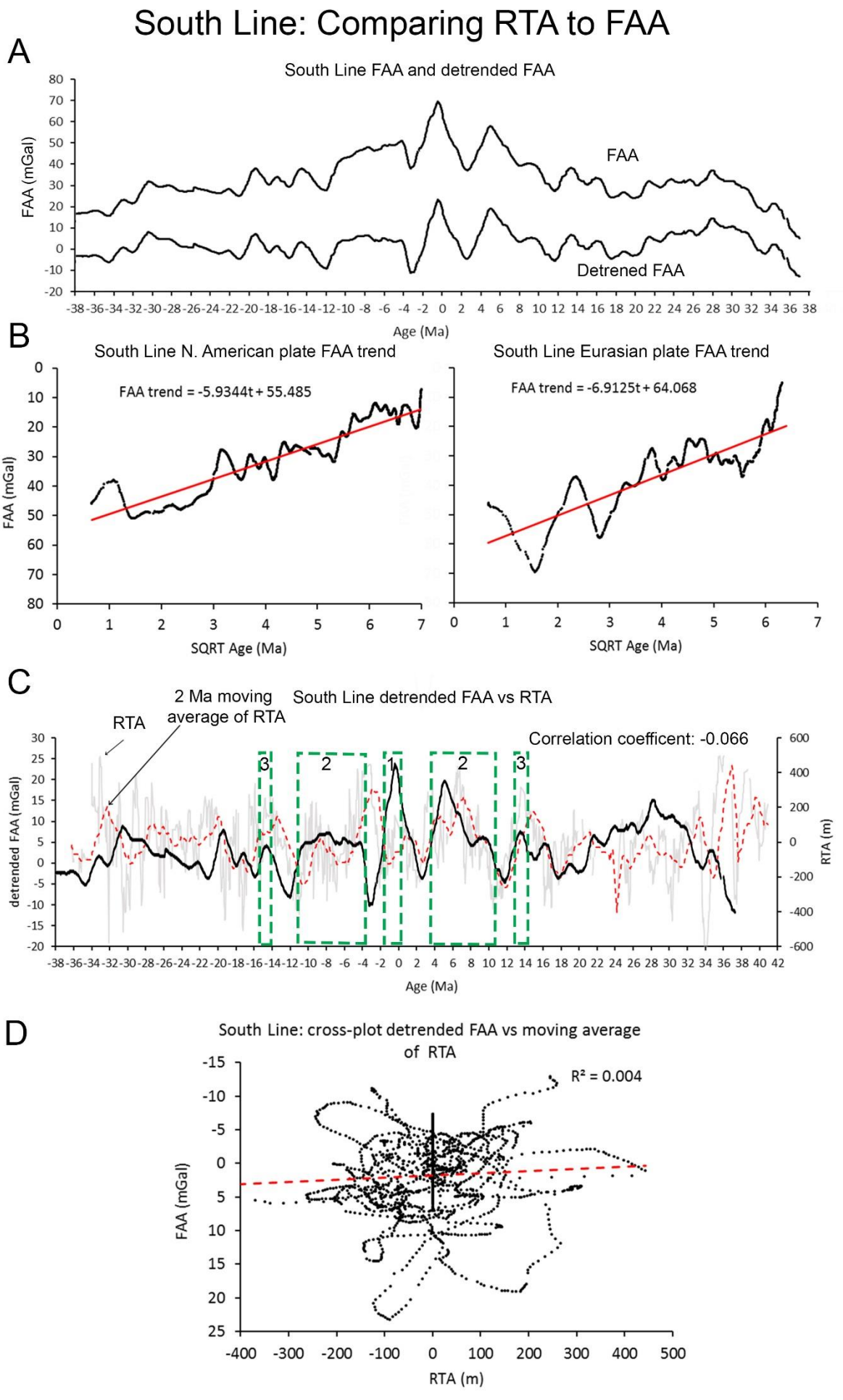
South Line: Comparing RTA to FAA
A
South Line FAA and detrended FAA
FAA (mGal)
FAA
Detrened FAA
Age (Ma)
B
South Line N. American plate FAA trend
FAA trend = -5.9344t + 55.485
South Line Eurasian plate FAA trend
FAA trend = -6.9125t + 64.068
FAA (mGal)
SQRT Age (Ma)
SQRT Age (Ma)
C
2 Ma moving average of RTA
RTA
South Line detrended FAA vs RTA
Correlation coefficent: -0.066
3
2
1
2
3
detrended FAA (mGal)
RTA (m)
Age (Ma)
D
South Line: cross-plot detrended FAA vs moving average of RTA
R² = 0.004
FAA (mGal)
RTA (m)

Figure 5.17*: South Line comparison of the RTA to the FAA and VSRs.* ***A****: FAA (top line) along the North Line decreases with distance off axis because of plate cooling and subsiding. This FAA is de-trended (bottom line) using the linear regressions calculated in panels B.* ***B****: Off axis subsidence is calculated by plotting the FAA for each plate against the square root of age, North American Plate is left and Eurasian Plate is right. A linear regression for these plots is subtracted from the FAA to calculate the de-trended FAA in panel A, C, and D.* ***C****: Visual comparison of de-trended FAA (black line) to RTA (grey line) and 2 Myr smoothed RTA (dashed red line). VSRs are highlighted in dashed green boxes. The correlation coefficient of the RTA and the de-trended FAA is -0.07.* ***D****: Cross-plot of 2 Myr moving average of RTA vs de-trended FAA. Linear fit (red dashed line) calculates the* R^2 *value as 0.004.*

Along the South Line the R^2 value for the de-trended FAA against the moving average of the RTA is 0.004 indicating no correlation (Figure 5.17D). The correlation coefficient for the de-trended FAA and moving average of the RTA is -0.07 indicating no correlation (Figure 5.17C). A visual comparison of the VSRs identified from the FAA and the moving average of the RTA indicates no obvious correlation (Figure 5.17C).

RTA does not correlate with FAA or VSRs along either Line indicating RTA is not a good proxy for crustal thickness or melt supply. Therefore, to determine if there is a relation between tectonic extension and melt supply I will compare T% to VSRs as determined from FAA.

5.2.6 T% vs FAA and VSR

Along the North Line, FAA and T% have an R^2 value of 0.01 (Figure 5.18C) and a correlation coefficient of 0.11 (Figure 5.18A) indicating no correlation. A visual comparison of the periods of VSRs and T% indicates that VSRs 2 and 3 on the North American Plate and VSRs 2b and 3 on the Eurasian Plate coincide with high periods of T% (Figure 5.18A). VSR1 on both plates and VSR2a and 2b on the Eurasian Plate coincide with T% lows

(Figure 5.18A). This suggests there is no reliable correlation between high T% and VSRs.

Along the South Line, FAA and T% have an R^2 value of 0.1 (Figure 5.18C) and a correlation coefficient of 0.32 (Figure 5.18B) indicating no correlation. A visual comparison of the periods of VSRs and T% reveals that on the North American Plate VSR1, VSR2b, VSR2a and on the Eurasian Plate VSRab and VSR3 coincided with positive periods of T% (Figure 5.18B). While VSR3, VSR2a on the North American Plate, and VSR1 and VSR2c on the Eurasian Plate coincide with low periods of T% (Figure 5.18A). This suggests that there is no strong relation between T% peaks and VSRs.

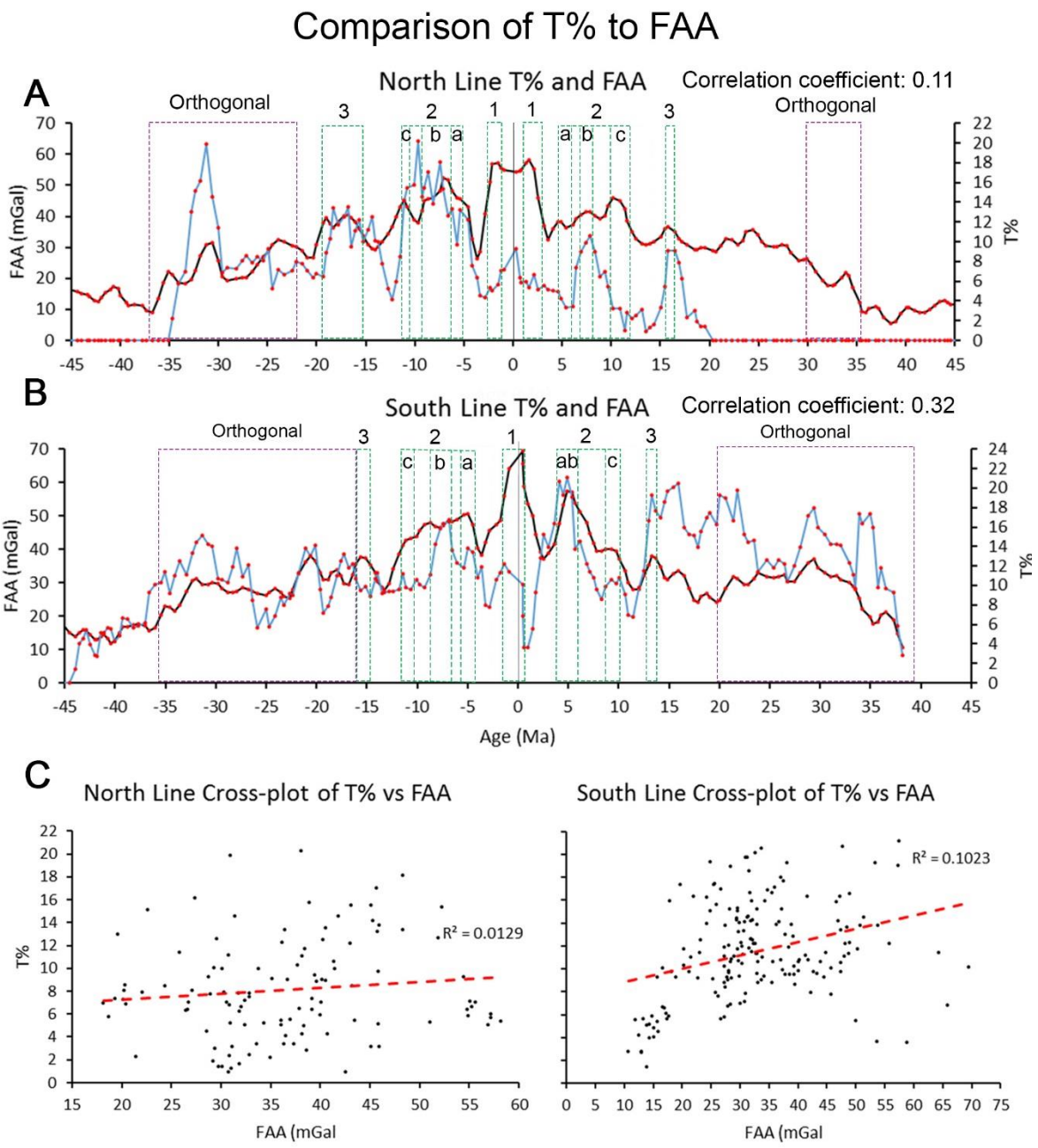

***Figure 5.18**: Comparing T% to VSRs and FAA. **A**: North Line with FAA (black line) and T% (blue line). Red dots are the positions of T% points and FAA measurements. Dashed green boxes are the periods of VSRs. Dashed purple boxes are the periods of orthogonal spreading. **B**: South Line with T% compared to FAA and VSRs. **C**: Cross-plots of T% and FAA, left is the North Line and right is the South Line.*

5.3 Discussion

To determine if melt supply was related to tectonic extension I measured proxies for both. Tectonic extension was determined using my T% method, which relies on the measurement of fault heave as measured along two seismic reflection profiles. Two methods were tested for indicators of melt supply; RTA and the identification of VSRs from FAA.

The good quality of the seismic profiles enabled faults to be easily identified along the sediment/crust boundary using a consistent criteria for their identification (Figures 5.2, 5.3, 5.6, and 5.7). Some regions, further off axis, were difficult to interpret but these effected a minority of the seismic profiles' length (Figure 5.8). From this I am confident in the reliability of the position and size of the fault heave polygons (Figure 5.9). The T% method has been tested in previous chapters and its reliability mostly depended on the identification of faults. Because the faults here have been easily identified I am confident in the T% calculations (Figures 5.10 and 5.11).

T% displayed irregular variability within a pate and between plates (Figure 5.11A and B). Each T% peak differs in period, magnitude and the shape of its signal indicating the process that controls T% must be highly variable through time. Although the T% signal is asymmetric in period and magnitude between the plates, the age of the centres of the T% peaks are in phase along the North Line and occasionally in phase along the South Line (Figure 5.11C and D). This suggests that the controlling variable for the percentage of tectonic extension is primarily focused along the spreading axis, allowing the signal to be divided between the plates and recorded in similarly aged crust. However, because the signal is not always in phase, some tectonic extension must also occur away from the spreading axis allowing some differentiation in the extent of extension that occurs to each plate. These identified attributes of the T% signal fit the description of the active fault zone (Macdonald, 1982) where faults complete most of their strain within 15 - 35 km off axis (Buck et al., 2005; Escartin et al., 1999; Solomon et al., 1988; Wolfe et al., 1995). The active

fault zone is close enough to the spreading axis that the signal can be divided between the plates but extents far enough off axis to enable some differentiation of the plate from its conjugate.

Fault heave was measured along the North and South Lines in Parnell-Turner et al., (2017) and used to calculate cumulative heave. The steepest gradients of their cumulative heave plots occurred along the North Line's North American Plate around 15 ±2 Ma and 35 ±2 Ma off axis, and on the Eurasian Plate around 10 ±2 Ma and 45 ±2 Ma off axis. My T% analysis identified high periods of extension that coincide with their increase in cumulative heave gradient around 15 ±2 Ma and 35 ±2 Ma on the North American Plate, and 10 ±2 Ma on the Eurasian Plate. The sediment thickness prevented me identifying faults as far as 45 Ma on the North Line's Eurasian Plate.

Along the South Line the highest increase in the gradient of cumulative heave along the North American Plate occurred around 24 ±2 Ma off axis and on the Eurasian Plate around 20 ±2 Ma. My T% method also identified high regions of extension 24 ±2 Ma on the North American Plate and 20 ±2 Ma on the Eurasian Plate. Parnell-Turner et al., (2017) and I have identified similar regions of high extension despite identifying faults separately and using different methods to analysis the fault heave. My T% analysis has identified other regions of high extension not identified in Parnell-Turner et al., (2017) when looking for increases in the gradient of cumulative heave. The reasons they may differ is because in Parnell-Turner et al., (2017) faults were also identified within the sediment layer and they used a slightly different criteria for fault identification then was used here.

To determine if RTA could be used as a reliable proxy for melt supply it was compared to FAA and VSRs. The VSRs identifiable from FAA (Parnell-Turner et al., 2017) are hypothesised to represent periods of high melt supply creating thick crust as discussed in the introduction. However, it is shown that the RTA does not correlate with FAA (Figure 5.16 and 5.17), questioning the assumption that the VSRs are underlain by thicker crust (Parnell-Turner et al., 2014; 2017), but may instead represent periods of

denser crust that do not have a topographical expression. Alternatively, this means the hypothesis that the positive RTA peaks represent thicker crust (Table 5.3), calculated using the Airy isostasy, is wrong. Therefore, RTA must represent changes in crustal depth that are related to other changes, such as crustal density. This is similar to the findings by Rommevaux et al., (1994) who compared crustal thickness to bathymetry at the Broken Spur segment of the MAR (Chapter 3). Rommevaux et al., (1994) found that shallow bathymetry was offset from the thickest crust by 10 km, suggested that the tectonic processes in the upper crust are the primary controller of seafloor morphology, while the effect of crustal thickness is secondary.

To explore this further, my T% result was compared to FAA and the locations of VSRs to determine their relation. There is no visible or statistical correlation between the T% and VSRs (Figure 5.18) suggesting that changes in melt supply caused by fluctuations in the underlying mantle such as hot pulses radiating away from the Iceland plume did not influence the percentage of tectonic extension. This finding suggests that though there may be a relation between seafloor volcanic features and the VSRs (Searle et al., 1998), there may not be a similar relation between fault geometry and the VSRs. From this finding I suggest that T% is not controlled by sub-crustal process that probably control the VSRs. Instead, T% may be controlled by processes within the upper crust above the ductile-brittle transition. Melt trapped within the lower crust accretes mostly as gabbro plutons (Chen, 1992), while melt that migrates above the ductile-brittle transition intrudes as blade like dykes (Behn et al., 2006; Buck & Poliakov, 1998) which rely on brittle extension to provide accommodation space. This may explain why changes in melt supply identified by the VSRs change crustal thickness by creating a thicker lower crust, however, the upper brittle crust does not change thickness because extension rate is not affected.

5.4 Conclusions

The comparison of the Residual Topographic Anomaly (RTA) to V-shaped ridges (VSRs) identified using Free Air Gravity Anomaly (FAA) has determined that either: (i) RTA does not provide a proxy for crustal thickness, or (ii) the V-shaped ridges identified from FAA represent crust with a high density that has no topographic extension. RTA quantitatively identifies regions of shallow crust, but these shallow regions should not be assumed to be the result of thick crust.

The comparison of areas of high T% to the locations of VSRs identified that there is no correlation between high melt supply, determined as the cause of VSRs, and the percentage of tectonic extension in the crust. This suggests that the controls of fault heave over tens of kilometres are located above the ductile-brittle transition, and are unrelated to changes in melt supply created by the Iceland hotspot.

Chapter 6 Discussion

Theoretical considerations and numerical modelling have suggested there should be a relationship between brittle tectonic extension and melt supply. Here, I set out to test this hypothesis by making observational measurements of proxies for melt supply and tectonic extension at several Mid-Ocean Ridges with varying spreading rates and spreading obliquities.

The validity of my results are primarily determined by the reliability of my methods, which are explored though a discussion, informed by the various studies, of their strengths and weaknesses inherent in the method. This in turn examines the basis of the theoretical relationship between brittle extension and magmatism and highlights some inconsistencies that relate to the underlying processes.

6.1 My Fault Identification method (FID)

Extension of the oceanic lithosphere mostly occurs through ductile deformation. However, the upper crust, above the brittle-ductile boundary, should extent entirely through brittle extension. Measuring the surface expression of this deformation should provide a measure of a plate's entire extension, assuming that all extension of the ductile section of the lithosphere will be translated into surface brittle extension. Brittle deformation manifests as fractures that rotate and coalesce into faults (Behn & Ito, 2008; Buck, 1988; Thatcher & Hill, 1995). In this thesis, I have developed a methodical and repeatable method (the Fault Identification (FID) method) that cross-correlates a range of seafloor attributes diagnostic of Mid-Ocean Ridge normal faults. This allows me to measure fault heave as a proxy of extension.

6.1.1 Strengths of the FID method

A major strength of the FID method is in how it integrates different seafloor parameters indicating faults by statistically selecting and then numerically cross-correlating those fault indicators. This method

objectively identifies objects (e.g. raster characteristics) in a range of data sets that have the highest probability of indicating fault structures. The combination of these multiple fault parameters increases confidence in the identified fault structures. For example, when the majority of FID values identifying a potential fault structure are greater than 2 out of 3 (i.e having a probability greater than 0.5; Section 2.1.1), a polygon is drawn around the spatial cluster of FID values and the fault structure is thus identified. An analysis of all my data sets reveals that the FID method identifies fault populations that are based on FID values of >2 (i.e. identifying fault structures with a confidence probability greater than 0.66).

Another benefit to the FID method is that analysis becomes more reliable when more data sets are added. For example, this was shown at the Broken Spur segment, where four different fault parameters were used to identify faults, while at the Costa Rica segment three different parameters were used. The data sets of the fault parameters were mainly bathymetry and backscatter. These are widely available because they are commonly acquired, wide-spread and continuous. This makes the FID method repeatable at many different Mid-Ocean Ridges.

Once the FID method has identified the pixels that are most probably fault structures, they are enclosed by a polygon that tightly bounds elongated clusters of FID values 2 – 3. At this stage, human intervention is required, which also ensures that the FID method is screened for false positives such as the sides of lava domes and seamounts or even artefacts in the data sets.

The objectivity of the FID method produced a repeatable, but often very different, fault distribution when compared to the subjective (human) interpretation of a single dataset in previous published studies (see Section 3.2.6). The differences usually originate from highly reflective regions of side-scan sonar imagery around potential fault structures being much wider than the fault extent from FID. Regions of high reflectivity could have very low slope angles and dip directions that are not normal to the spreading axis, suggesting high reflectivity does not simply reflect

spreading normal faults. These regions of high reflectivity could be reflecting talus from eroded fault scarps, debris flows, or lava flows. Some of the features subjectively chosen did not cover high reflectivity regions indicating that a purely human interpretation of faults does not systematically follow the identification criteria.

6.1.2 Weaknesses of the FID method

There are some weaknesses to the FID method that restrict its range of reliability to within tens of kilometres of the spreading axis. This is largely due to the increasing effect of sediment cover obscuring the surface expression of faults. For example, for the study of the intermediate spreading ridge example, comparison of the heave, measured along seismic reflection profiles, to heave measured from bathymetry identified the greatest disparity after 70 km off axis. At this distance sediment thickness of ~70 m obscure fault scarps to generate a smooth, undulating, seafloor where the fault parameters of backscatter and slope are not met (see Section 4.2.2). In crust <70 km off-axis, there is 3% difference in measured extension (Section 2.1.3.1). At the slow spreading ridge example, a sediment thickness of 30 m after 30 km off axis generates a smooth seafloor where fault scarps are not well identified (see Section 3.2.3). This reduces T% to almost 0% after only 32 km off-axis at the slow spreading ridge example, and 70 km off-axis at the intermediate spreading ridge. The differences are due to sedimentation rate and the age of the crust at given distances, given the differences in spreading rate.

Other areas where the FID method does not work well is where faults have been overprinted by lava flows; e.g. very close to the spreading axis or in areas of extensive off axis volcanism (see Section 4.2.4). Furthermore, the FID method has its parameters chosen to identify Mid-Ocean Ridge normal faults. These are faults perpendicular (±22.5°) to the spreading direction. This results in the FID method not identifying fault heave in regions where the faults show significant obliquity, or where they are not extended by simple normal faults, such as Oceanic Core

Complexes (Section 3.2.5), where the extension occurs over large areas exposing low-angle fault surfaces.

The resolution of the data used also influences the reliability of the measured fault heave. Ship-derived bathymetry, with a 50 m resolution, identified on average 45% more heave than 2 m resolution bathymetry. This is due to the lower resolution bathymetry over-extending the fault scarps – i.e. by effectively applying a low-pass filter to the actual seafloor shape. Furthermore, at the slow spreading ridge example it was estimated that the inability to identify faults with heave <150 m resulted in an underestimate of total extension across the study area by 11.5% (Section 3.2.4). At the intermediate spreading ridge example, the lower resolution bathymetry may have underestimated total extension across the study area by as much as 30% (see Chapter 4.2.2).

Some alterations to the FID method will reduce the impact of these weaknesses. Firstly, the slope angle parameter is calculated over a 3x3 cell grid making it reliant on the presence of large faults with a continuous slope. This, however, prevents the FID method from fully recording a fault when the scarp does not produce a constant and steep slope. A fault scarp with an irregular slope may result from the fault being composed of multiple interlinked smaller faults (Section 3.2.3) or the fault scarp has been partially eroded. The 3x3 matrix size also missed faults further off axis where fault scarps are expressed as undulating, elongated hills. The slope parameter could be improved by calculating slope angle over a grid size larger than 3x3, allowing for undulating surfaces and non-continuous fault scarps to be identified. Secondly, the backscatter parameter of the FID method relies on dividing the raster data into quintiles of backscatter intensity. This resulted in most of the highest quintile comprising of the region of high reflectivity found within 8 - 18 km of the spreading axis (i.e. where the recent lava flows are not covered by sediment). This statistical grouping results in fault scarps close to the axis being indistinguishable from young volcanic seafloor, and reflective linear features further off axis falling into the second quintile and not being identified. This could be improved by calculating backscatter quintiles within windows moving off

axis so that the high and low values are relative to their distance off axis. This, of course, involves more subjective interaction with the data, requiring a move away from the value of the FID method which is its objectivity and repeatability.

6.2 The T% method

Faults identified using the FID method were analysed using the T% method to measure tectonic extension on a scale comparable to second order melt supply features. The reasoning behind this is to test changes in brittle extension on scales (both spatial and temporal) that are associated with changes in melt delivery from the mantle including pooling of melt within the crust prior to eruption. We know from the chemistry of MORB that it is not in equilibrium with the mantle, hence there is a process of crystal fractionation through melt storage and migration. Previous studies suggest this takes thousands of years, and the response to melt supply is hence of a similar magnitude (Niu, 1997).

6.2.1 Strengths of the T% method

A useful attribute of the T% method is that it produces a map of tectonic extension that can be easily visually correlated to bathymetric features. A map of extension is easier to interpret than extensional graphs, such as cumulative heave. Another benefit is that the T% method works using data sets other than those derived from the FID method alone, such as using seismic reflection profiles shot parallel to the spreading direction (see Chapter 5.2.2). This also includes re-analysing historical fault maps (Chapter 3.2.6), making T% repeatable at multiple study sites with a variety of datasets.

The moving window allows my T% method to be more systematic in its calculation by always normalising fault heave over a constant and proportional distance. This allows for direct comparison between multiple regions in and between study areas. This is an improvement upon subjective methods (e.g. as used in Escartin et al., 1999). In their investigation, they chose three locations to calculate the percentage of

extension. The positon and extent over which the calculation was made was subjectively chosen in relation to the feature being investigated, making it less repeatable.

6.2.2 Weaknesses of the T% method

The T% method works best where there is total data coverage along axis and off axis so that all faults can be identified. The study areas used here have been chosen to encompass the seafloor that has almost total coverage. The T% resolution has been chosen to measure extension on the scale of second order melt supply features. This results in the T% having a higher resolution along strike than across-strike, in the extension direction. The effect this has is that temporal changes in the amount of extension that occur over time periods that are shorter than that which it takes to accrete 20 km of crust are not identified by the T%. Spatial changes in the amount of extension along axis will be measured by the T% at a 500 m resolution, which is the stepping distance between profiles. The off-axis resolution could be improved by increasing the stepping interval of the normalising windows.

6.3 Proxy for melt supply

My primary indictors of melt supply were bathymetric features and gravity anomalies. Domed seafloor at the centre of many MOR segments is a bathymetric features that is diagnostic of high melt supply at second-order segments (Carbotte et al., 2016; Sempéré et al., 1993; Murton & Rona, 2015). In these cases, the segment centre presents as a narrow axial valley, with small axial valley wall faults, and an axial valley ridge. Such shallow segment centres generate an off-axis trace of shallow bathymetry. At the segment ends, the axial valley is deep and wide, and the axial valley wall faults are large. These are bathymetric features diagnostic of low melt supply at the segment ends. The segment ends generate an off-axis trace of deep bathymetry (Sempéré et al., 1990; 1993).

In this study, bathymetric features were used to identify the magmatic focus at the segment centre along the Costa Rica and Broken Spur

segments. At the Costa Rica Ridge, the centres of the two second order segments presented as domes that were 2 – 4 km in radius and rising 200 m above the neighbouring seafloor. The axial valley walls at the segment centres are 1.9 km apart and 190 m high. At the Broken Spur segment, axial valley walls at the segment centre are 6 km apart and 200 m deep. Bathymetric features also identified the segment ends. The axial valley walls at the segment ends of the Costa Rica Ridge are 6.5 km apart and 650 m deep. At the Broken Spur segment the axial valley walls at the segment ends are 10 km apart and 600 m deep.

Two types of gravity anomalies were used; a residual mantle Bouguer anomaly (RMBA) was used at the Broken Spur segment and a free air gravity anomaly (FAA) was used at the Reykjanes Ridge. Traditionally, high RMBA is interpreted as thin crust generated from low melt supply, and low RMBA is interpreted as thick crust generated from high melt supply (Lin et al., 1990; Rommevaux et al., 1994). At the Reykjanes Ridge, ridges of high FAA was used to identify V-Shaped ridges that are hypothesised to be generated as a result of high melt supply (White, 1997; Jones et al., 2002; Parnell-Turner et al., 2014; 2017).

RTA is used to develop a proxy for melt supply by referring to two theoretical models for crustal isostasy. Firstly, I could use Pratt isostasy, which theorises that differences in topographic relief in isostatically stable crust, without structural support, are due to differences in density (Suppe, 1985; Lowrie, 2007). According to the Pratt model, a positive bathymetry anomaly could be generated by low density crust which is either; hot, or is composed of low density mafic material with a low Fe Mg content (e.g. basaltic), or it has undergone extensive hydrothermally alteration to clays and has high permeability. Alternatively, Airy isostasy explains topographic differences as being due to differences in crustal thickness. In this model, regardless of crustal thickness, all crust is neutrally buoyant at the same level within a plastically deforming asthenosphere. Therefore, thicker crust produces shallower bathymetry than thinner crust (Suppe, 1985; Lowrie, 2007).

The Residual Topography Anomaly (RTA) calculated shallow and deep bathymetry anomalies relative to the crust's average depth, ignoring local or short wavelength features that are effectively unsupported. The RTA could then be compared to gravity anomalies or bathymetric features diagnostic of melt supply to determine if the two proxies correlate to indicate a high or low melt supply at the point of crustal accretion.

6.3.1 Positive results between RTA and melt supply proxies

The correlation between RTA and the other proxies in several locations supports an origin from changes in melt supply. For example, at the Broken Spur segment, on the scale of 10 – 50 km, positive RTA (404 to 509 m) can be traced off axis and correlate with a low RMBA (6 to 14 mGal) where they are aligned along a spreading direction 'flow-line' with the axial dome defining the segment centre. Together, these all indicate crust generated with a high melt supply. At the Costa Rica Ridge, on the Nazca Plate, two regions of positive RTA (>200 m) aligned with the on axis domes at the centre of two second order segments, all indicating crust generated with high melt supply.

RTA also agreed with the established proxies for low melt supply in several locations. At the Broken Spur segment on the scale of 10 – 50 km, negative RTA (93 to -148 m) traced off axis followed a high RMBA (22 to 27 mGal) and aligned with the axial depth of the non-transform discontinuity, all indicating crust generated with a low melt supply. At the Costa Rica segment, on the scale of 10 km, a series of negative RTA (> -100 m) basins aligned along a spreading flow-line with the position of the on-axis non-transform discontinuity, all indicate crust generated with a low melt supply. The smooth seafloor south of 2°55' N did not align with on-axis features, indicative of melt supply, however the smooth seafloor is typical of fast spreading ridge morphology where melt supply is high. This could suggest that the low RTA would reflect high density crust with high Fe and Mg concentrations resulting from high amounts of mantle partial melting (Niu, 1997). Along the seismic reflection profiles across the Reykjanes Ridge, however, low RTA occurs with the troughs between the V-

shaped ridges in only two out of nine times, but positive RTA occurs with the V-shaped ridges in eight out of eleven times. This may indicate changes in crustal composition between V-shaped ridges and troughs.

At some locations, RTA and other proxies for melt supply were able to identify the same relative differences in melt supply between regions. At the Broken Spur segment, asymmetry between the plates is observed in both the RTA and RMBA. For example, the North American Plate has a high mean RMBA (20 mGal) and low mean RTA (+105 m) suggesting it has had a lower melt supply than the Eurasian Plate, with a low mean RMBA (14 mGal) and a high mean RTA (+221 m). At the Costa Rica segment, the western axial dome is shallower than the eastern suggesting a higher melt supply, and this is reflected in the positive RTA of their relic features with the western RTA having an average of +111 m and the eastern having an average of +83 m. This indicates the RTA and axial features agreed in relative magnitude of melt supply between regions of high melt supply.

Features diagnostic of melt supply and RTA have a better correlation at the orthogonal-spreading ridges of the Costa Rica and Broken Spur segments, than the oblique-spreading Reykjanes Ridge. This suggests that increased obliquity could reduce the influence of changes in crustal thickness effects on seafloor morphology.

6.3.2 Negative results between RTA and melt supply proxies

In some locations, the RTA did not correlate well with established proxies for melt supply. At the Broken Spur segment, RTA and RMBA did not correlate over distances of 1 km. This is probably because of the relative scales these proxies work at: RTA at the 1 km scale reflects the presence of abyssal hills which are unsupported features (i.e. not in isostatic equilibrium), whereas RMBA reflects crustal thickness and/or density changes over tens of kilometres. RTA and RMBA also failed to correlate over some geological features measuring 5 – 10 km in size: e.g. the positive RTA over shallow inside corner features and an oceanic core complex. Elsewhere, where seafloor morphology inherited from the spreading axis is overprinted by off-axis volcanism, the resulting RTA

could not be used to indicate axial melt supply. These examples illustrate that positive RTA does not always correlate with other, more established proxies for high melt supply. This disparity may be explained if the assumed mantle and crustal densities, and crustal thickness, used in the Airy isostasy equation were inaccurate. Other explanations may be that structural support from strong lithosphere or uplift from mantle serpentinisation form features with positive bathymetric anomalies such as the inside corners and oceanic core complexes.

The work reported here finds no consistent correlation between high or low RTA and high FAA lineaments diagnostic of the V-shaped ridges found south of Iceland and to each side of the Reykjanes Ridge. Indeed, one V-shaped ridge is located between an RTA low and high, three V-shaped ridges have only low RTA, and seven V-shaped ridges have high RTA (although these are restricted to observations along the southern seismic line). A potential explanation for the V-shaped ridges not appearing in the RTA is that the strong FAA signals are a result of changes in crustal density that do not cause Pratt isostatic readjustment, which would generate a bathymetric signal. For crustal density changes large enough to be detectable in FAA, but not cause an isostatic response, the crust would have to be extra thick to support larger surface features, or supported by thick rigid lithosphere that was unable to undergo ductile deformation. This may be possible at the Reykjanes Ridge where the oceanic crustal thickness is already 3 km thicker than average (White et al., 1992). In addition to a thick crust, the lithospheric mantle can grow to be 70 km thick as the plate ages off-axis. Perhaps an extra thick layer of depleted lithospheric mantle was generated by the higher amounts of partial melting and mantle dehydration at the hot spot-influenced Reykjanes Ridge (Ito et al., 1999).

6.3.3 Conclusions of melt supply proxy

At the orthogonal ridge examples, RTA and proxies for melt supply correlate at distanced of 20 – 50 km, indicating large-scale bathymetric trends can be used to determined relative changes in melt supply. At the

oblique ridge examples, there is not a large scale relationship between these proxies. At distances <20 km, the lack of a good correlation between RTA and gravity signals could result from irregular variation in the crusts density and thickness. The crustal variability results in some areas being best explained using the Airy model, while others using the Pratt model, preventing a simple positive or negative relation between RTA and gravity across the entire study area. At resolutions lower than 10 km, RTA could also reflect upper-crustal features that cannot be explained by isostasy models alone.

6.4 Testing the hypothesis of melt-vs-brittle deformation

The proxies for melt supply have been compared to T% to determine if there is a relationship between melt supply and the surface expression of brittle extension at various scales.

6.4.1 Areas where melt and extension are related

At the Broken Spur segment, the North American Plate had a low melt supply indicated by a high mean RMBA of 20 mGal and low mean RTA of +105 m, while the Eurasian Plate had a high melt supply indicated by a low mean RMBA of 14 mGal and high mean RTA of +221 m. This asymmetry was reflected in the relative amount of tectonic extension, with the North American Plate having 20% higher T% than the Eurasian Plate. Melt supply and tectonism were also related over the inside corner feature, which have a high mean T% of 13±1.5% and low melt supply.

A correlation was also found over the Costa Rica segment, between the seafloor north of 2˚55’ N having high mean RTA (+136 m) and high mean T% (6.1±1.8%), and seafloor south of 2˚55’ N having low mean RTA (-27 m) and low T% (3.5±1%). However, this apparent correlation may not be the result of variations in melt supply alone, but instead could result from increased sediment thickness reducing T% south of 2˚55’ N. Alternatively, the smooth seafloor south of 2˚55’ N may have smaller abyssal hills that have less measureable heave than those from the rugged, high relief seafloor north of 2˚55’N. These smaller abyssal hills are more

susceptible to being covered by sediment, masking the smaller-throw faults. If smooth seafloor formed during fast spreading periods, and the rugged seafloor formed during intermediate spreading, then this would provide an apparent relation between high melt supply at faster spreading rates and lower degrees of extension.

At the Costa Rica segment, an inverse relation was also found for length-scales of 20 – 40 km between all the geological regions north of 2˚55' N, where high mean RTA of the interpreted geological regions (20 - 40 km) and half regions (10 - 20 km) correlated to low mean T%. The regions of 2˚55' N - 3˚7' N and Cocos Plate have high mean RTA of +187 m and +177 m respectively, and low mean T% of 5.1±1.5% and 4.9±1.5% respectively. The regions of the western and eastern segments have a low mean RTA of +111 m and +83 m respectively, and a high mean T% of 6.4±1.9% and 8.9±2.7% respectively.

6.4.2 Negative results, areas that are not related

Far more regions were found to lack any significant correlation between extension and melt supply. No correlation was found between RMBA/RTA signals, diagnostic of melt supply, and T% at the Broken Spur segment on scales of 1 km or 20 – 50 km. Along the seismic reflection profiles crossing the Reykjanes Ridge, no consistent relationship was found between the V-shaped ridges, thought to result from high melt supply, and T%; with five V-shaped ridges and sub-ridges correlating with high T%, and five V-shaped ridges and sub-ridges correlating with low T%.

At the Costa Rica segment, no relation was found at the 1 km scale. The defined geological regions that contain the off axis traces of the second order segment are thought to be the most reliable measure of melt supply. In these regions, high T% (>8%) occurs in bands along the middle of the two relict segment centres (RTA >200 m), and along part of the segment ends (RTA <100 m). Other parts of the segments-ends have low T% (<6%). This provides no consistent relationship between T% and melt supply at scales of <10 km.

Comparing the study sites to each other, no consistent relationship is found between the distribution of melt supply and tectonism, between slow and fast spreading ridges, or oblique and orthogonal ridges.

Several studies have modelled and observed a relation between fault attributes and melt supply. A relationship between the length and strength of a phase of magmatic accretion on axis and the height of abyssal hills has been modelled (Ito & Behn, 2008). Indicating that when magma supply is low, stretching is accommodated by increased heave (Behn & Ito, 2008). Shaw, (1992) found that faults have wider spacing and higher throws at segment ends, were Bouguer anomalies are high, indicating a thinner crust (i.e. where melt supply is lowest). Conversely, fault frequency is higher and throw is lower at the segment centre. Escartin et al., (1999) measured fault heave from side-scan sonar at the Broken Spur segment and found that the amount of extension was the same between the outside corner and segment centre, and that the inside corner had the largest amount of extension. My findings disagree with these studies, and fault heave measured using my T% method does not show any relation to the along axis distribution of melt supply at scales of 1 km or <10 km. If there was a relationship, then I would expect to have identified changes in fault heave at the scale of the abyssal hills. At the Broken Spur segment, my comparison to Escartin's fault analysis identified a high amount of subjectivity in the identification and demarcation of faults and their extent. The uncertainty between real seafloor features and what their fault polygons are actually representing makes Escartin et al.'s results difficult to reproduce and hence are likely unreliable.

There are multiple studies that suggest tectonic extension does not need to be related to changes in melt supply on the scale of second order segments. It has been identified that signals in side-scan sonar that suggest the first appearance of mid-ocean ridge faults nucleate 1 - 4 km off axis (Escartin et al., 1999), and within the zone of crustal fissuring (Macdonal, 1982). These faults then accommodate most of their strain within 15 - 35 km off-axis (Buck et al., 2005; Escartin et al., 1999; Solomon et al., 1988; Wolfe et al., 1995) in the 'active faulting zone' (Macdonald,

1982). This means that, the majority of a faults growth occurs at some distance away from the spreading axis where melt lenses and magma chambers are present and feeding dyking and lava flows. The broad area of fault growth encompassing a significant distance away from the spreading axis results in a large proportion of the brittle extension being uninfluenced by magma supply at the ridge axis, and this may explain why there should not necessarily be a correlation.

6.5 Explanations for why melt supply and tectonic extension are not related

The proxies for melt supply have been compared to T% to determine if there is a relationship between melt supply and the surface expression of brittle extension at various scales. I found several locations where melt supply and extension did have an inverse relation.

At the Broken Spur segment, the North American Plate had a low melt supply indicated by a high mean RMBA of 20 mGal and low mean RTA of +105 m, while the Eurasian Plate had a high melt supply indicated by a low mean RMBA of 14 mGal and high mean RTA of +221 m. This asymmetry was reflected in the relative amount of tectonic extension, with the North American Plate having 20% higher T% than the Eurasian Plate. Melt supply and tectonism were also related over the inside corner feature, which have a high mean T% of 13±1.5% and low melt supply.

At the Costa Rica segment, an inverse relation was also found for length-scales of 20 – 40 km between all the geological regions north of 2˚55’ N, where high mean RTA of the interpreted geological regions (20 – 40 km) and half regions (10 - 20 km) correlated to low mean T%. The regions of 2˚55’ N - 3˚7’ N and Cocos Plate have high mean RTA of +187 m and +177 m respectively, and low mean T% of 5.1±1.5% and 4.9±1.5% respectively. The regions of the western and eastern segments have a low mean RTA of +111 m and +83 m respectively, and a high mean T% of 6.4±1.9% and 8.9±2.7% respectively.

A correlation was also found over the Costa Rica segment, between the seafloor north of 2˚55' N having high mean RTA (+136 m) and high mean T% (6.1±1.8%), and seafloor south of 2˚55' N having low mean RTA (-27 m) and low T% (3.5±1%). However, this apparent correlation may not be the result of variations in melt supply alone, but could result from increased sediment thickness reducing T% south of 2˚55' N. Alternatively, the smooth seafloor south of 2˚55' N may have smaller abyssal hills that have less measureable heave than those from the rugged, high relief seafloor north of 2˚55'N. These smaller abyssal hills are more susceptible to being covered by sediment, masking the smaller-throw faults. If smooth seafloor formed during fast spreading periods, and the rugged seafloor formed during intermediate spreading, then this would provide an apparent relation between high melt supply at faster spreading rates and lower degrees of extension.

These results agree with several studies that modelled and observed a relation between fault attributes and melt supply. A relationship between the length and strength of a phase of magmatic accretion on axis and the height of abyssal hills has been modelled (Ito & Behn, 2008). Indicating that when magma supply is low, stretching is accommodated by increased heave (Behn & Ito, 2008). Shaw, (1992) found that faults have wider spacing and higher throws at segment ends, were Bouguer anomalies are high, indicating a thinner crust (i.e. where melt supply is lowest). Conversely, fault frequency is higher and throw is lower at the segment centre. Escartin et al., (1999) measured fault heave from side-scan sonar at the Broken Spur segment and found that the amount of extension was the same between the outside corner and segment centre, and that the inside corner had the largest amount of extension.

However, I have multiple other findings that disagree with the studies linked extension to melt supply. Fault heave measured using my T% method does not show any relation to the along axis distribution of melt supply at scales of 1 km or <10 km, the scale of abyssal hills. At the Broken Spur segment, my comparison to Escartin's fault analysis identified a high amount of subjectivity in the identification and demarcation of

faults and their extent. The uncertainty between real seafloor features and what their fault polygons are actually representing makes Escartin et al.'s results difficult to reproduce and hence are likely unreliable.

This ties to the possibility that environmental processes modify the fault expression (Figure 6.1) making accurate extension measurements difficult with any observational method. For example, fault scarps become eroded, reducing the top of the scarp and burying the bottom of the scarp in talus; reducing the apparent heave. Additionally, small 'diffuse' faulting is quickly obscured by sediment or is not observable because of the resolution of the bathymetry data as explored in Section 2.1.3.3. Frequently spaced faults with small throws may become buried and eroded into obscurity quicker than large faults as was shown in Section 2.1.3.1. Furthermore, faults can be buried by lava flows, lava domes, and seamounts as was observed on the Cocos Plate in Section 4.2.1. This could result in the FID fault picks, representing apparent heave, and underestimating the actual brittle extension that is the true heave that may be closer to that measured from theoretical models. These alterations of faults on the seafloor may mean that we cannot get an accurate measure of true plate extension by measuring fault scarps alone (Figure 6.1). Without an accurate measure of true extension from observation data, it is not possible to directly compare the results to the predicted fault distribution in numerical models.

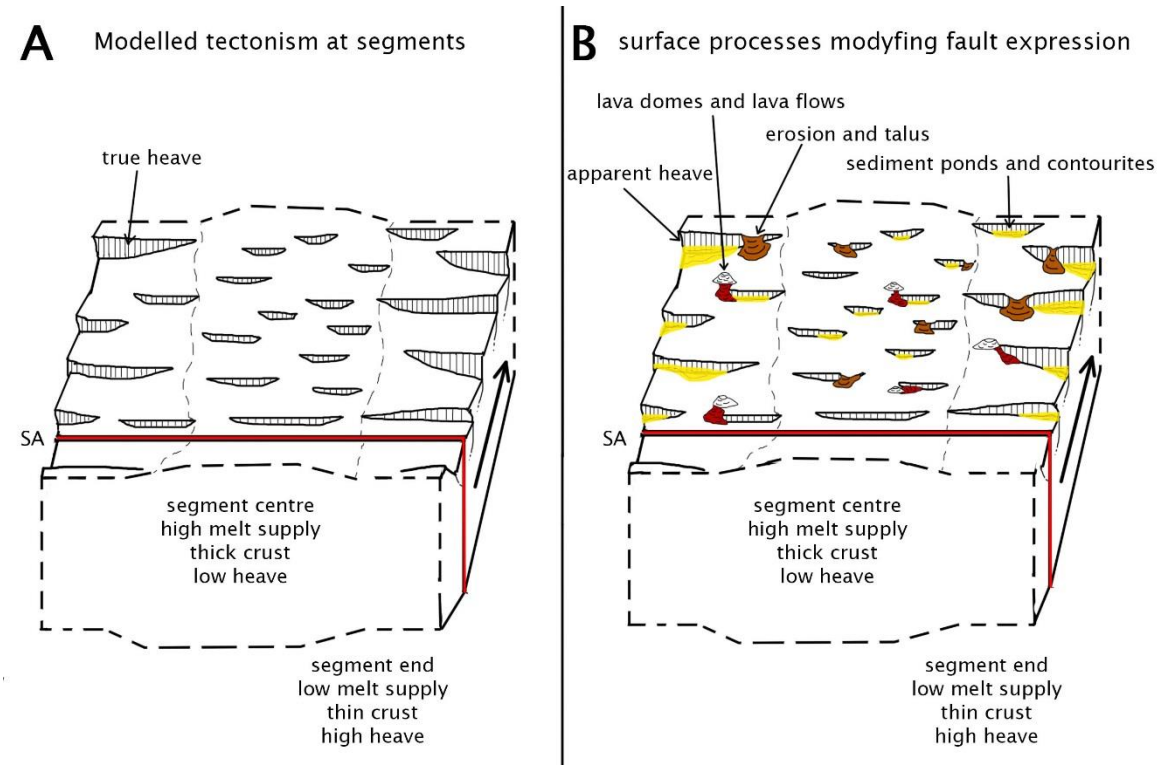

***Figure 6.1**: Illustration of seafloor processes preventing the true heave in 'A' matching apparent heave in 'B'. **A**: Illustration of the modelled relation between fault attributes (dashed features) and second order melt supply, with faults having larger throws and larger spacing at the segment ends than the segment centre. **B**: The faults have been modified by sediment ponds and contourites[HT10][GH11] (yellow), erosion and talus (brown), and lava domes and lava flows (red). This modification results in the apparent heave measured in panel B not resembling the true heave modelled in panel A.*

Despite this uncertainty, my results show many more examples of regions that lack any significant correlation between extension and melt supply. No correlation was found between RMBA/RTA signals, diagnostic of melt supply, and T% at the Broken Spur segment on scales of 1 km or 20 – 50 km. Along the seismic reflection profiles crossing the Reykjanes Ridge, no consistent relationship was found between the V-shaped ridges, thought to result from high melt supply, and T%; with five V-shaped ridges and sub-ridges correlating with high T%, and five V-shaped ridges and sub-ridges correlating with low T%.

A possible explanation is that changes in melt supply, without changes in spreading rate, would change plate thickness but not change the thickness of the brittle upper-crust where extension occurs (Figure 6.2). The thickness of this brittle crust is determined by the plate cooling rate which is largely controlled by hydrothermal cooling. If tectonic plates are all cooling at a similar rate (Hasterok, 2013) because they are reliant on processes of conductive and convective cooling to lose heat at the seafloor, then the depth of the ductile-brittle boundary may not vary greatly between plates (Figure 6.1). Melt in the form of dykes can only reach the surface to build the upper-crust if a magma chamber of sufficient volume is positioned correctly to exploit pathways provided by extension. If melt is not available then extension is accommodated by faulting. Therefore, if no change in spreading rate occurs then an increase in melt supply will result in an increase in the amount of magma accreted to the lower crust and no change to surface brittle extension (Figure 6.2).

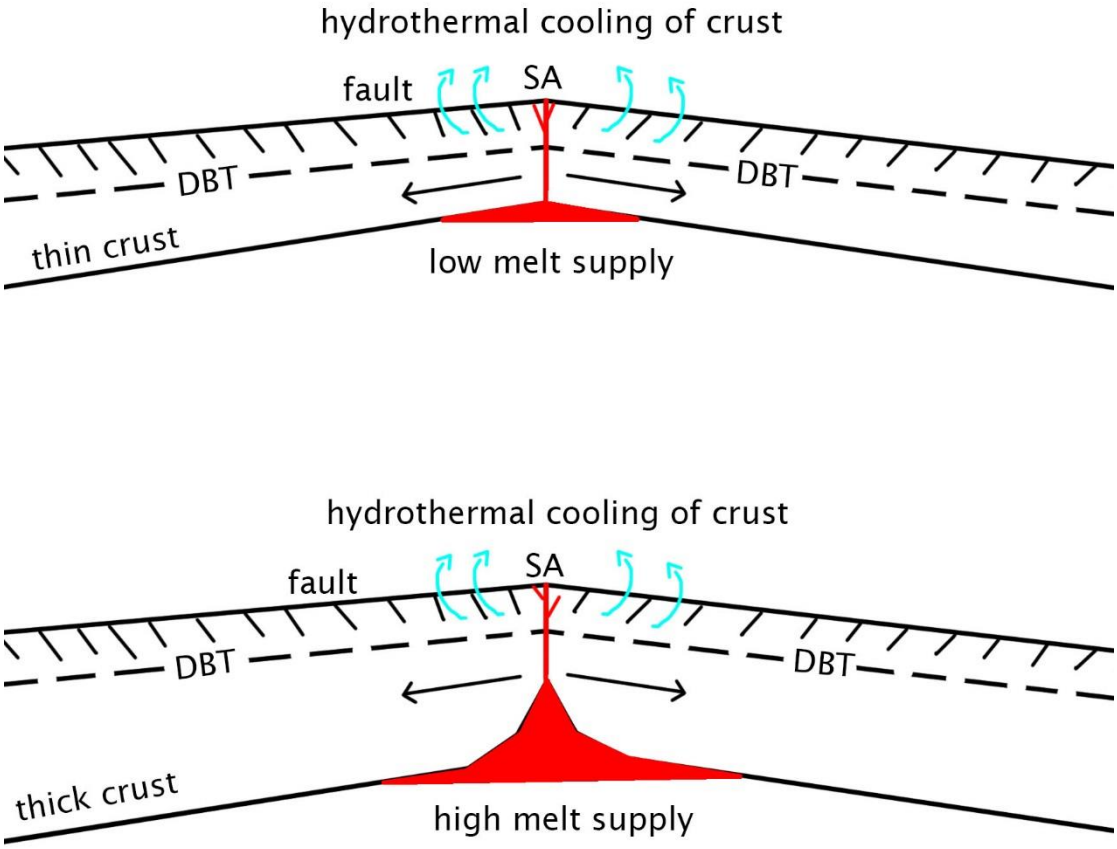

***Figure 6.2**: Without a change in spreading rate a change in melt supply will result in an overall thicker crust shown by the difference between the*

top (low melt supply) and bottom (high melt supply) schematics. Importantly, there has been no change in the depth of the brittle crust, illustrated by the dashed DBT = ductile-brittle transition. The DBT is reliant on conductive and convection (hydrothermal) cooling illustrated by the blue arrows. The rate of cooling at the seafloor may not dramatically change between mid-ocean ridges resulting in a similar DBT depth. Magma below the plate (red) can only reach the surface where extension has provided space, below the DBT space is filled by ductile intrusion of gabbro plutons easily able to deform and fill all spaces. Above the DBT space can only be filled by dykes where magma was available and in enough quantity to allow fluid pressure to overpower the confinement pressure, making it less able to exploit spaces provided by extension. The different behaviour of melt above the BDT results in some extension being accommodated by faults (sub-vertical black lines) where melt for dykes was not available. The majority of melt will remain in the lower crust as plutons, increasing the thickness of the lower crust. Therefore, increasing melt supply may build a thicker crust but may not influence DBT that controls faulting.

At the Costa Rica segment, no relation was found at the 1 km scale. The defined geological regions that contain the off-axis traces of the second order segment are thought to be the most reliable measure of melt supply. In these regions, high T% (>8%) occurs in bands along the middle of the two relic segment centres (RTA >200 m), and along part of the segment ends (RTA <100 m). Other parts of the segments-ends have low T% (<6%). This provides no consistent relationship between T% and melt supply at scales of <10 km.

Assuming that my measurement of seafloor faulting is an accurate representation of brittle plate extension, then the lack of correlation between extension and proxies for melt supply may be a result of extension along axis being determined by local processes, such as the placement and life span of magma chambers (Figure 6.3). Dyking will always occur preferentially to faulting if melt is available, so the distribution of faulting may simply represent upper crustal melt supply along axis. This has been described as the cause of third and fourth order

melt segmentation (Sempéré et al., 1993). The placement of melt lenses at this high order may not be representative of the lower order melt supply (Figure 6.3).

If faulting is only related to fourth order melt supply, occurring on the kilometre scale, then the premise that fault patterns are comparable to second order segments, measured over 20 km, was false. A way to test this in the future would be to measure T% over a 1 km window and compare it to third and fourth order magmatic features, such as clusters of lava domes and volcanic ridges.

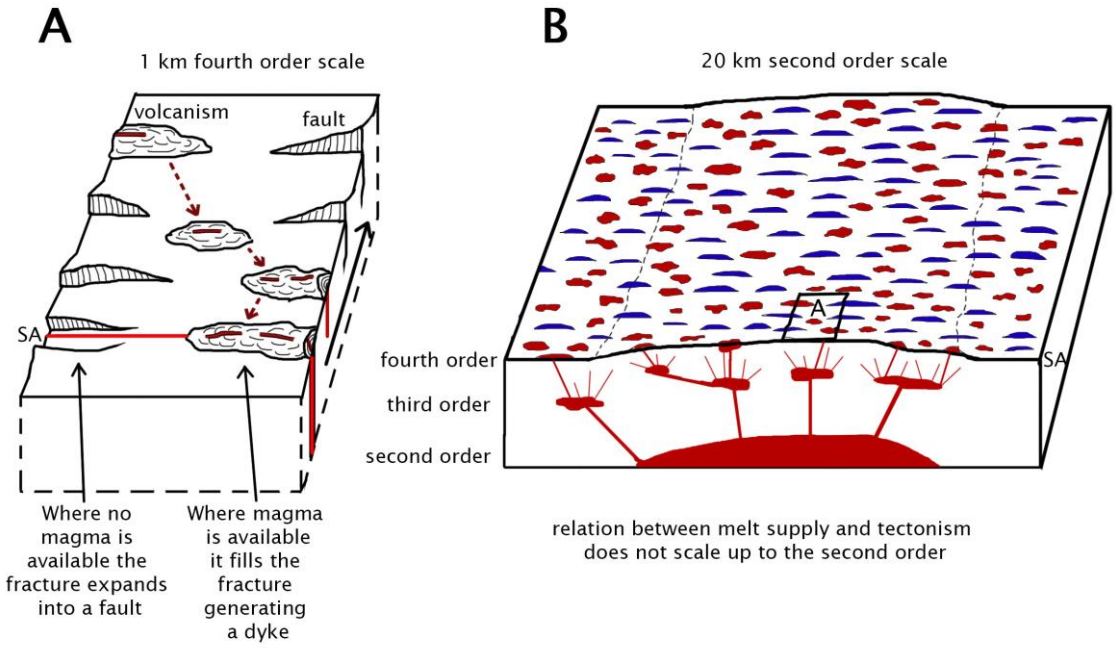

***Figure 6.3**: Cartoon explaining how fault placement may be controlled by segmentation on the fourth order (A) and not the second order (B). **A**: At the fourth order, extension within the upper crust will result in a fault (dashed feature) if there is no magma available. If magma is available then the fracture creates a dyke (red hummocky feature). **B**: Second order segmentation over tens of kilometres has melt focused in the upper mantle towards the segment centre. This large wavelength melt distribution below the crust may not translate into a simple linear relation to the placement of magma chambers at the third order, around the lower crust, and positions of dykes at the fourth order, in the upper crust. If this is true*

then the inverse relation between volcanism (red) and faulting (blue) may not directly translate into a reflection of second order melt supply.

Comparing the study sites to each other, no consistent relationship is found between the distribution of melt supply and tectonism, between slow and fast spreading ridges, or oblique and orthogonal ridges. The lack of correlation of brittle extension to any single process may be a result of extension being controlled by the complex interaction of large-scale processes, such as spreading rate, melt supply, and obliquity, with an over-printing by local processes such as hydrothermal alteration, crustal structure, composition, and local stress fields. These processes may interact in such a way that it is not possible from the observational data explored here to attribute fault patterns to any one process.

There are multiple studies that suggest tectonic extension does not need to be related to changes in melt supply on the scale of second order segments. It has been identified that signals in side-scan sonar that suggest the first appearance of mid-ocean ridge faults nucleate 1 - 4 km off-axis (Escartin et al., 1999), and within the zone of crustal fissuring (Macdonal, 1982). These faults then accommodate most of their strain within 15 - 35 km off-axis (Buck et al., 2005; Escartin et al., 1999; Solomon et al., 1988; Wolfe et al., 1995) in the 'active faulting zone' (Macdonald, 1982). This means that the majority of a fault's growth occurs at some distance away from the spreading axis, and so away from where melt lenses and magma chambers are present and feeding dyking and lava flows. The broad area of fault growth encompassing a significant distance away from the spreading axis results in a large proportion of the brittle extension being uninfluenced by magma supply at the ridge axis, and this may explain why there should not necessarily be a correlation.

My investigation has revealed that, although T% displays irregular variability, it is not a random signal. The largest difference between T% occurs across axis rather than along axis, indicating asymmetrical extension in all of the regions studied here, with 20% in Chapter 3, 55% in Chapter 4, and 40% to 100% in Chapter 5 depending on the seismic

reflection profile. Ten out of five T% peaks at the Reykjanes Ridge were found to be symmetrical across the ridge-axis and hence of similar age in origin, which suggests that T% is controlled near the spreading axis. However, though the uneven amplitude of T% between the North American and Eurasian Plates suggests tectonism, the processes controlling brittle extension, are not evenly or symmetrically partitioned between the plates. This, importantly suggests that the exact control of brittle extension on axis is more complicated than a simple inverse relationship to melt supply. Previous studies have looked for a large scale relation at the second order segment scale between melt supply and tectonism, however, my study has found no consistent relationship for any of the large-scale processes that control brittle extension across any of the study areas. This important observation allows us to hypothesis local scale controls for brittle extension.

6.6 Conclusions

The findings from my study are summarised in the following list of points that outline the results with reference to the aims established at the start of this thesis. This work, described in this thesis has:

- Developed and tested a method for objectively mapping faults 20 – 35 km either side of a mid-ocean spreading ridge. Comparing three seafloor attributes producing fault picks with a high confidence.
- Developed and tested a method for calculating dispersed extension across 20 km as a percentage of crust created at Mid-ocean ridges. This method works using bathymetry and seismic reflection profiles.
- Found that at the Mid-ocean ridges, which are not influenced by hotspots, bathymetry shallower than the seafloor's average depth correlated with indicators of high magmatic flux. At the hotspot-influenced spreading ridge example, V-Shaped ridges identified from gravity anomalies provided a proxy for high melt supply.
- Found no consistent relation was found between extension and melt supply across varying spreading rates, spreading directions, and melt supplies. Potential explanations for this include:

1) Magmatism occurs close to the spreading axis within 2 km while extension occurs away from the spreading axis within 30 – 40 km.
2) The distribution of magmatism and tectonism within the upper crust occurs on a fourth order scale (hundreds of meters to kilometres) that is not reflective of the second order scale (tens of kilometres) I was measuring at.
3) Tectonism is controlled by the thickness of the brittle crust which is influenced by cooling rates off-axis, not by fluctuations in melt supply on-axis.
4) An accurate measurement of extension cannot be measured using observation data because of seafloor processes modifying morphology.

In summary, an analysis of the seafloor morphology, its structure and depth reveals a complex interplay between melt supply, volcanism and brittle extension. The hypothesis that seafloor spreading is accommodated either by brittle extension or magmatic accretion does not hold true, despite different spreading rates and obliquity of spreading. Instead, the expression of extension is manifest as both faulting and volcanism, as well as changes in crustal thickness and internal structure. The study concludes that there is a paradox in so far as seafloor structure is as much a function of short wavelength processes including localised cooling and melt focusing as it of long-wavelength processes such as mantle partial melting. Future studies to resolve this paradox require greater emphasis on the three dimensionality of crustal structure with a better insight into processes occurring at depth within the oceanic crust including the thickness variation of the extrusive and intrusive layers, the role of convective and conductive cooling and the processes controlling melt focusing and brittle failure of the crust over short wavelengths. It is likely that these localised

processes play the dominant role in shaping the seafloor rather than the large-scale processes that give rise to seafloor spreading.

Definitions and Abbreviations

FAA = Free Air Gravity Anomaly

FID = Fault Identification

MAR = Mid-Atlantic Ridge

MOR = Mid-Ocean Ridge

RMBA = Residual Mantle Bouguer Anomaly

RTA = Residual Topography Anomaly

SAP = Seismic Aperture Profile

TOBI = Tower Ocean Bottom Instrument

T% = Percentage of measurable brittle extension

VSR = V-Shaped Ridges

Appendices

Appendix A [HT12]

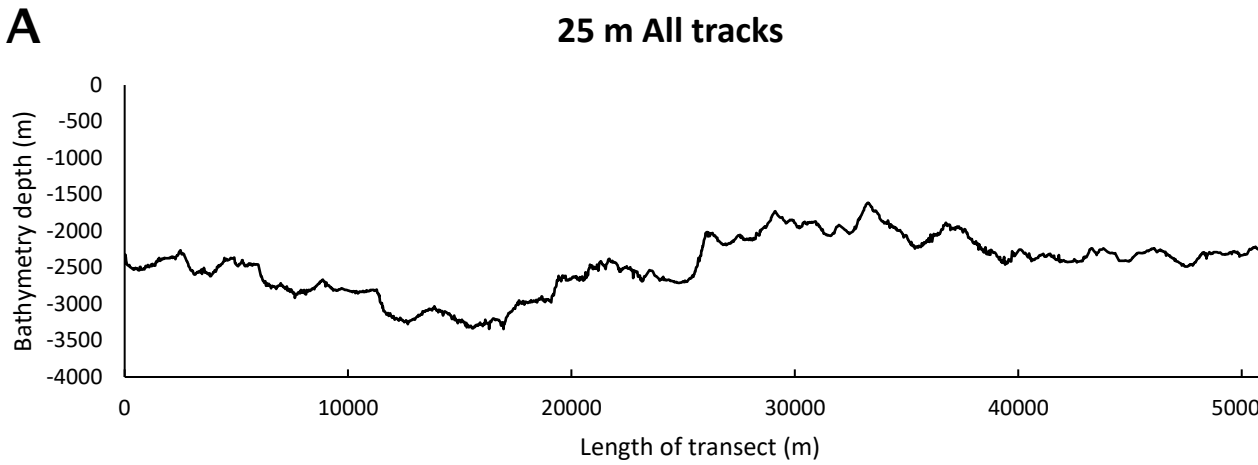

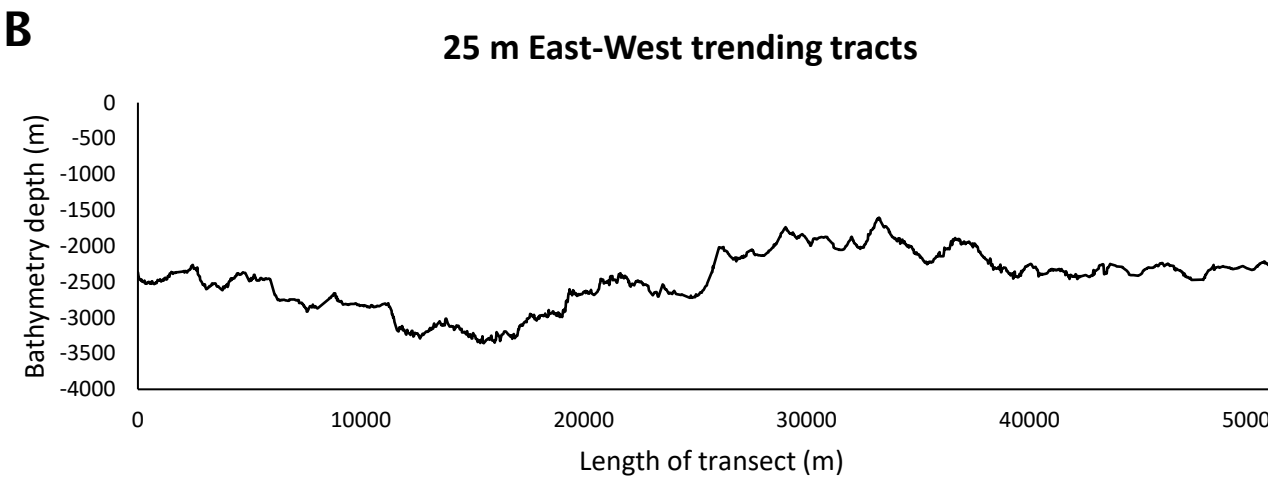

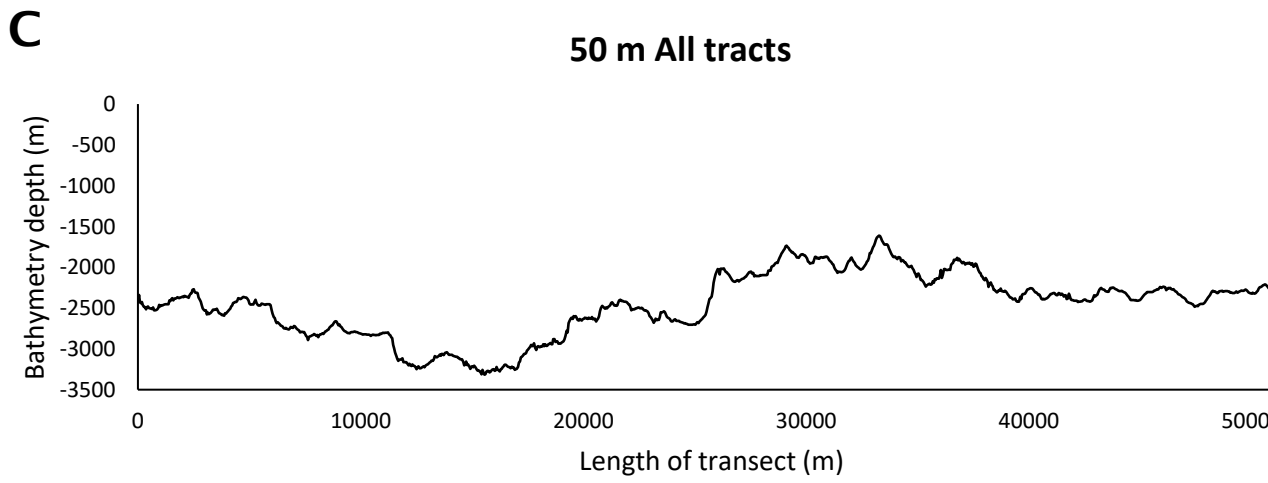

50 m East-West trending tracts

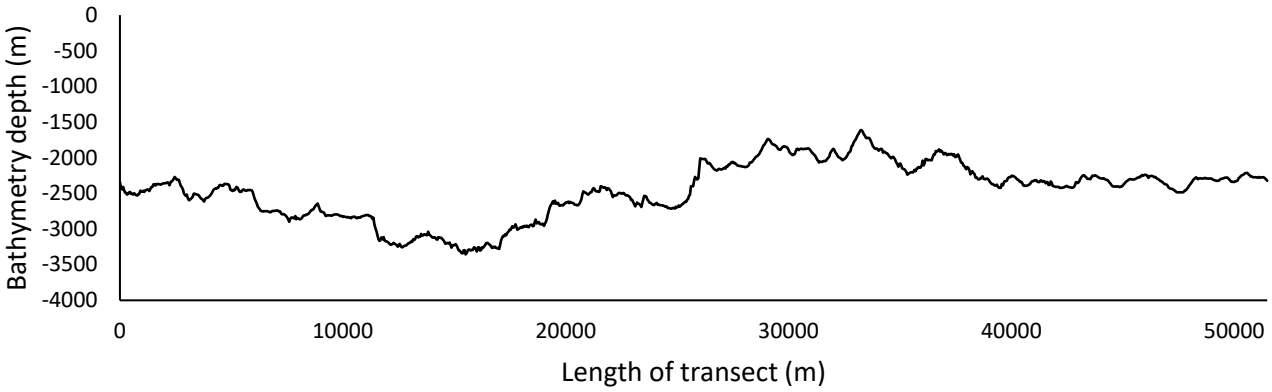

25 m All tracts, 10 km section

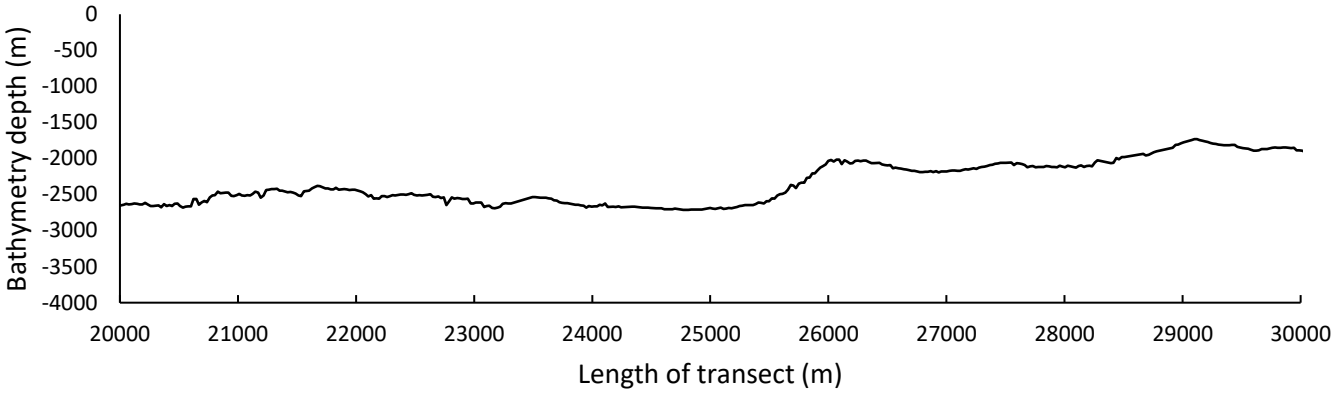

25 m East-West trending tracts, 10 km section

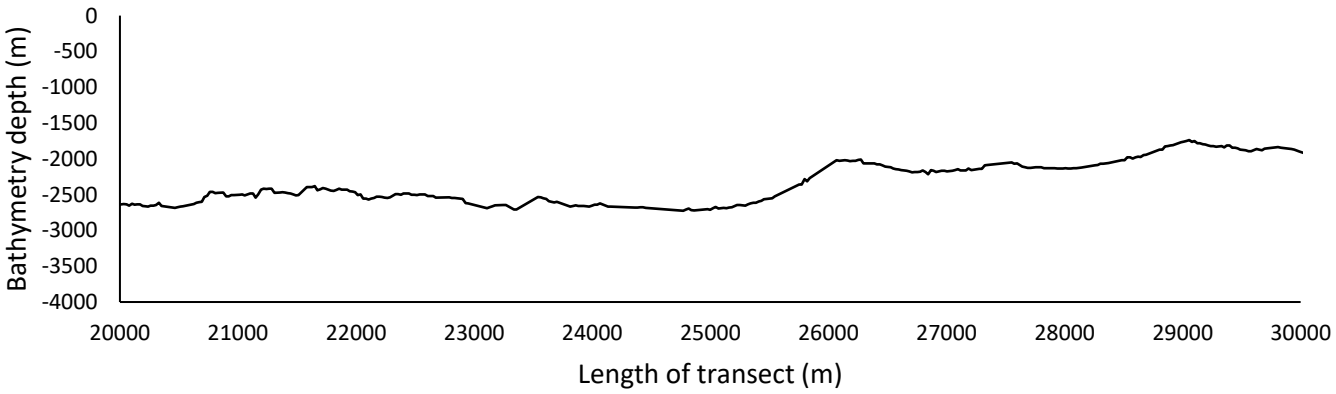

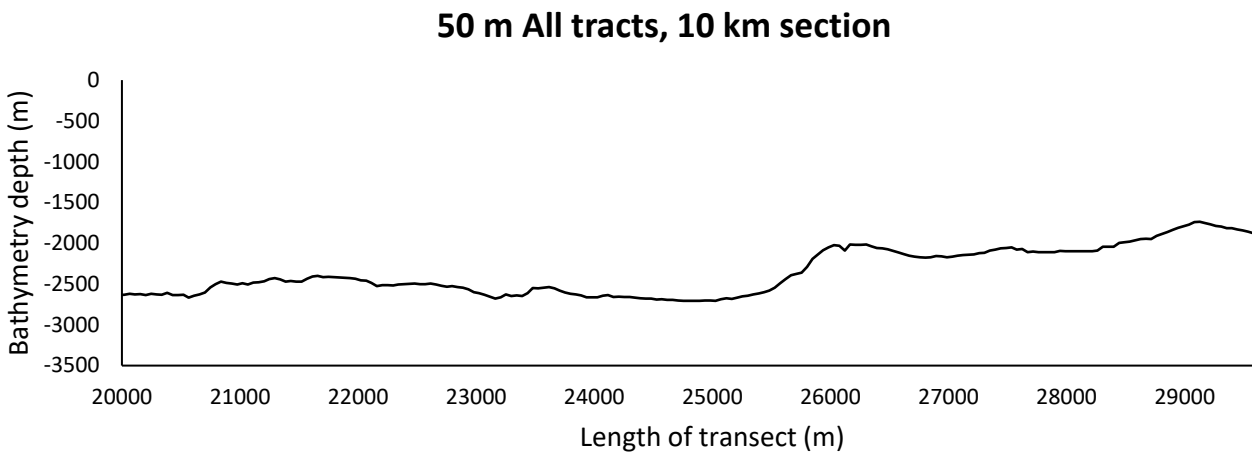
50 m All tracts, 10 km section
Bathymetry depth (m)
0
-500
-1000
-1500
-2000
-2500
-3000
-3500
20000
21000
22000
23000
24000
25000
26000
27000
28000
29000
Length of transect (m)

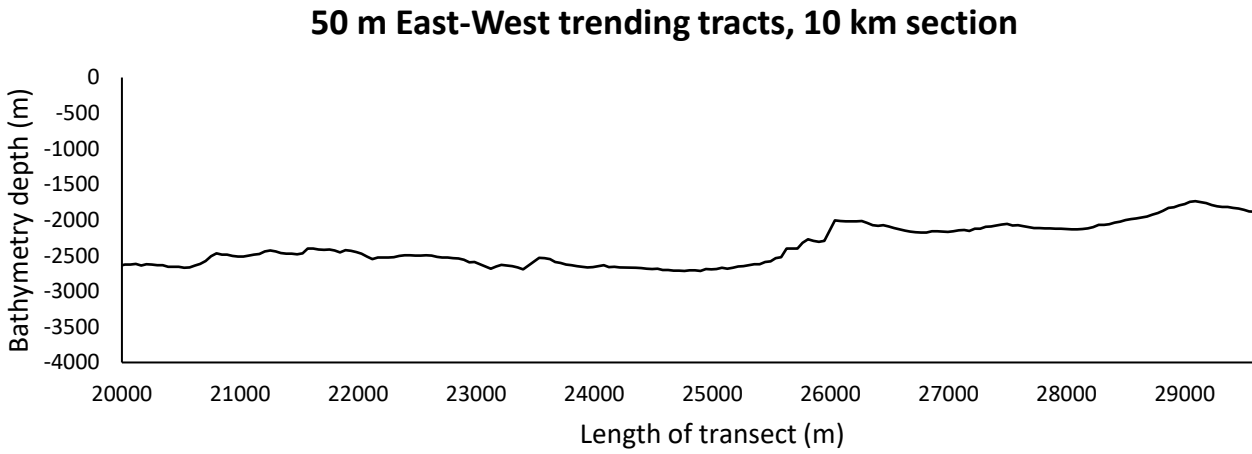
50 m East-West trending tracts, 10 km section
Bathymetry depth (m)
0
-500
-1000
-1500
-2000
-2500
-3000
-3500
-4000
20000
21000
22000
23000
24000
25000
26000
27000
28000
29000
Length of transect (m)

Appendix B

29˚N MAR

Fourier transform MatLab™ code

This MatLab code to perform a Discrete Fourier Transform was written by Dr. Age Vellienga at the University of Southampton.

Contents

Frequency analysis via FFT

```
clear all
close all

load('meandeltad.mat');                    %lead data
urW1=(detrend(data));                      % detrend (tilt)

fs = 68.11787;                             %fs = sample frequency
tlr=time;                                  %tlr = time

plot(tlr,urW1,'k')
hold on
```

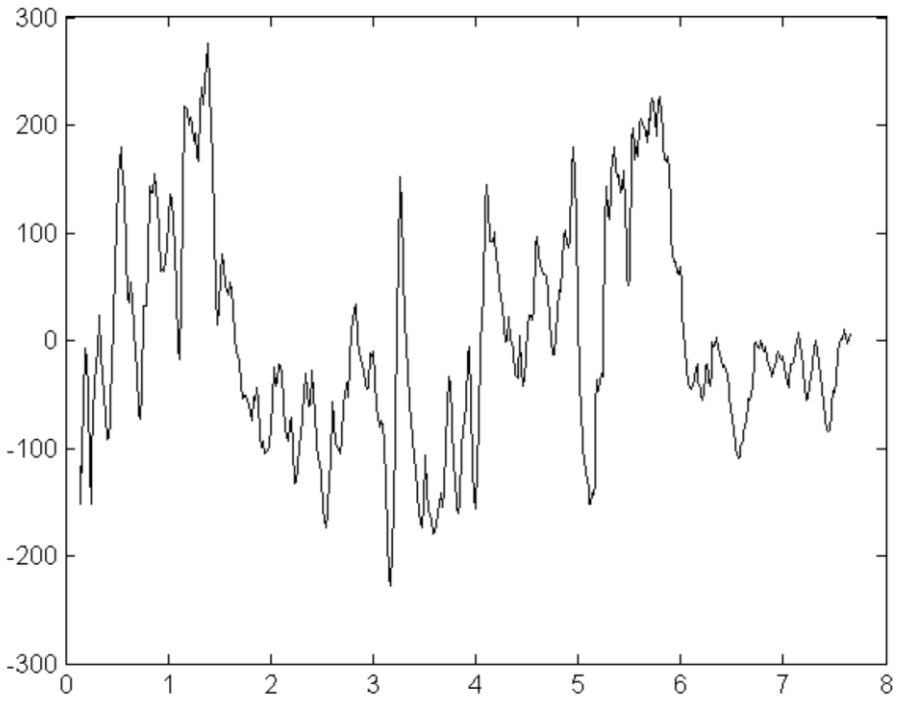

spline data

```
t1=0;                                       %t-start samples
t2=max(tlr);                                      %t-end samples
dt=(t2-t1)/length(tlr);                             %dt


t=t1:dt:t2;                                     %change with sample fequency
fs=1/dt;                                        %sample frequencty

urW=spline(tlr,urW1,t);

figure
subplot(3,1,1)
plot(t,urW);
hold on

plot(tlr,urW1,'*')
```

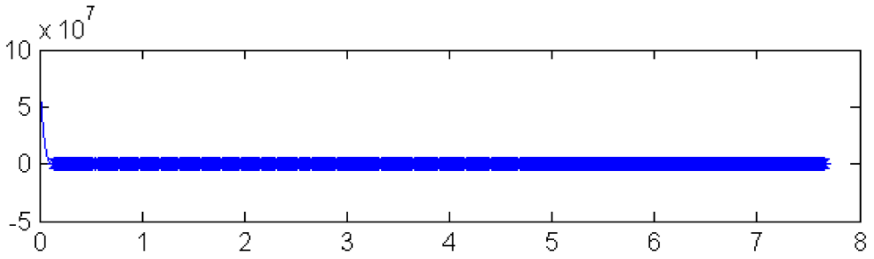

statistics

```
M=2;                                            %number of windows
N=2*floor(0.5*length(urW)/(M*(M+1)))*(M*(M+1)); %length of time series used
N2=N/M;                                         %segment length no overlap
N3=2*N/(M+1);                                   %segment length with 50% overlap

% cosine tapir to prevent step and very high range of sines
```

```
 for i=1:((N3)/2+1)
        fwo(i)=i*(fs/2)/((N3)/2)-(fs/2)/((N3)/2);
 end

for i = 1:(N3)
    z=(2*pi*(i-1))/(N3);
    whco(i)= (1-cos(z))/2;
    if i<=N3/2
        wtco(i)=i*1/(N3/2);
    else
        wtco(i)=(N3-i)/(N3/2);
    end
end

for i=1:M

    eval(['uW' num2str(i) 'o=urW((0.5*i*N3-0.5*N3+1):(0.5*i*N3-0.5*N3+N3)).*whco;'])

    eval(['tDc' num2str(i) 'o=t((0.5*i*N3-0.5*N3+1):(0.5*i*N3-0.5*N3+N3));'])
end
```

Fourier transform

```
st='Fourier Transforms'

for i=1:M

    eval(['FuhWo' num2str(i) '=abs(fft(uW' num2str(i) 'o.*sqrt(8/3),N3));'])

end
```

```
st =

Fourier Transforms
```

Calculate parameters

```
st='Normalization'
fresh=fs/N;
freshw=fs/N2;
freshwo=fs/(N2*2);

S1hwo=sum(whco);
S2hwo=sum(whco.^2);

for j=1:(N3/2+1);
    for i=1:M

        eval(['PShwWo(i,j)=2*FuhWo' num2str(i) '(j).^2;'])
    end
end

PShwWot=sum(PShwWo)./M;
```

```
st =
```

calculate confidence interval

for Bartlett window

```
st='Confidence Intervals'
v=2*2.6666*M;

load('ChiDistr.txt')

%clear vX*
[v1 v2]=min(abs(ChiDistr(:,1)-v));
P95=5;
P90=6;
P10=7;
P5=8;
vX95=v/ChiDistr(v2,P95);
vX5=v/ChiDistr(v2,P5);
    fwoAD=fwo;
    PShwWotAD=PShwWot;
    vXuAD=vX95;
    vXlAD=vX5;
```

```
st =

Confidence Intervals
```

figure no variance preserving

```
figure

set(gca,'fontsize',14)
hold on
semilogx(fwoAD,PShwWotAD,'b');
semilogx(fwoAD,vXuAD.*PShwWotAD,'-.b');
semilogx(fwoAD,vXlAD.*PShwWotAD,'-.b');

xlabel('frequency [Hz]', 'fontsize', 14)
ylabel('Normalized amplitude spectrum', 'fontsize', 14)
```

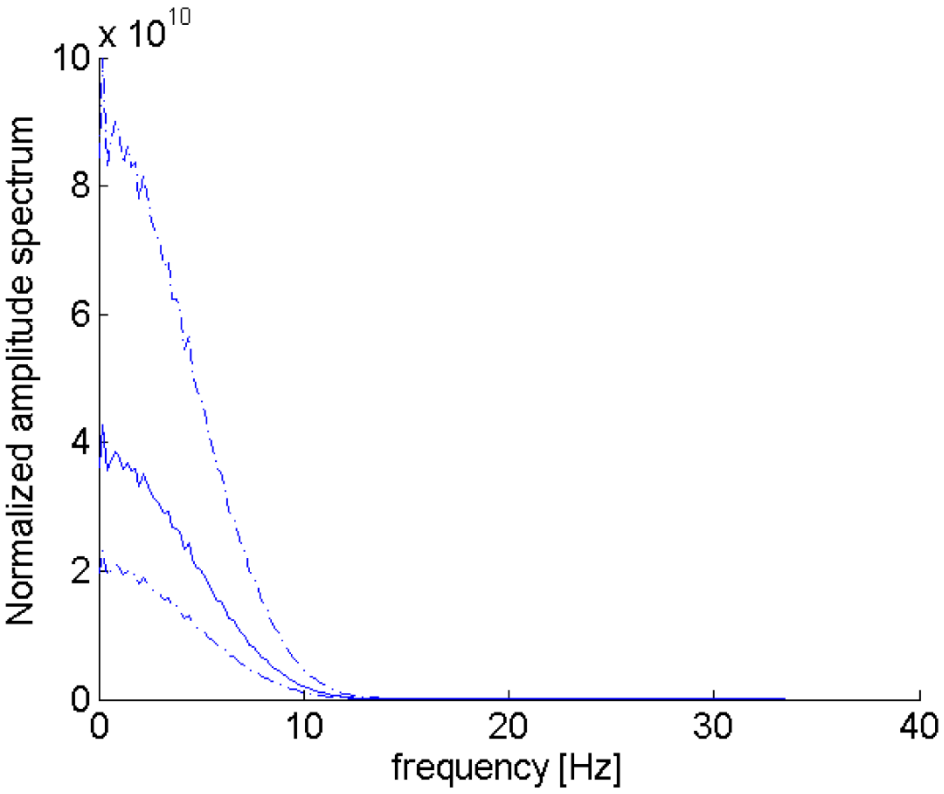

Bibliography

Abelson, M., Agnon, A. (1997). Mechanics of oblique spreading and ridge segmentation. Earth and Planetary Science Letters, 148(3–4), 405–421. https://doi.org/10.1016/S0012-821X(97)00054-X

Agnon, A., Eidelman, A. (1991). Lithospheric breakup in three dimensions: necking of a work-hardening plastic plate. Journal of Geophysical Research, 96(B12), 189-194. http://dx.doi.org/10.1029/91JB01888; doi:10.1029/9

Amanta, C., Eakins, B. (2009). ETOPO1 1 arc-minute global relied model: procedures, data sources and analysis. NOAA Technical Memorandum NESDIS NEDC-24.

Barckhausen, U., Ranero, C., Huene, R., Cande, S., Roeser, H. (2001). Revised tectonic boundaries in the Cocos Plate off Costa Rica: Implications for the segmentation of the convergent margin and for plate tectonic models. Journal of Geophysical Research, 106(B9), 207-220.

Behn, M., Ito, G. (2008). Magmatic and tectonic extension at mid-ocean ridges: 1. Controls on fault characteristics. Geochemistry, Geophysics, Geosystems, 9(8), 1–22. https://doi.org/10.1029/2008GC001965

Behn, M., Buck, W., Sacks, I. (2006). Topographic controls on dike injection in volcanic rift zones. Earth and Planetary Science Letters, 246(3–4), 188–196. https://doi.org/10.1016/j.epsl.2006.04.005

Benediktsdottir, A., Hey, R., Martinez, F., Höskuldsson, A. (2012). Detailed tectonic evolution of the Reykjanes Ridge during the past 15 Ma. Geochemistry, Geophysics, Geosystems, 13(2), 1-27.

Blackman, D., Orcutt, J., Forsyth, D., & Kendall, J. (1993). Seismic anisotropy in the mantle beneath an oceanic spreading centre. Nature, 366, 675–677.

Bonvalot, S., Briais, A., Kukn, M., Peyrefitte, A., Vales, N., Biancale, R., Sarrailh, M. (2012). World Gravity Map. Commission for the Geological Map of the World.

Bott, M. (1991). Ridge push and associated plate interior stress in normal and hot spot regions. Tectonophysics, 200(1-3), 17-32.

Bown, J., White, R. (1994). Variation with spreading rate of oceanic crustal thickness and geochemistry. Earth and Planetary Science Letters, 121(3–4), 435–449. https://doi.org/10.1016/0012-821X(94)90082-5

Brandl, P., Regelous, M., Beier, C., O'Neill, H., Nebel, O., Haase, K. (2016). The timescales of magma evolution at mid-ocean ridges. Lithos 240-243, 49-68. http://dx.doi.org/10.1016/j.lithos.2015.10.020

Buck, W. (1988). Flexural Rotation of Normal Faults. Tectonics, 7(5), 959–973. https://doi.org/10.1029/TC007i005p00959

Buck, W., Poliakov, A. (1998). Abyssal hills formed by stretching oceanic lithosphere. Nature, 392(March), 272–275.

Buck, W., Lavier, L., Poliakov, A. (2005). Modes of faulting at mid-ocean ridges. Nature, 434(7034), 719–723. https://doi.org/10.1038/nature03358

Carbotte, S., Macdonald, K. (1994). Comparison of seafloor tectonic fabric at intermediate, fast, and super fast spreading ridges: Influence of spreading rate, plate motions, and ridge segmentation on fault patterns. Journal of Geophysical Research: Solid Earth, 99(B7), 13609-13631. http://dx.doi.org/10.1029/93JB02971

Carbotte, S., Smith, D., Cannat, M., Klein, E. (2016). Tectonic and magmatic segmentation of the Global Ocean Ridge System: a synthesis of observations. Geological Society, London, Special Publications, 420(1), 249-295. http://sp.lyellcollection.org/lookup/doi/10.1144/SP420.5

Cann, J., Smith, D., Escartín, J., Schouten, H. (2015). Tectonic evolution of 200 km of Mid-Atlantic Ridge over 10 million years: Interplay of volcanism and faulting. Geochemistry, Geophysics, Geosystems, 16, 2303–2321. https://doi.org/10.1002/2015GC005797.Received

Carlson, R., Herrick, C. (1990). Densities and porosities in the oceanic crust and their variations with depth and age. Journal of Geophysical Research, 95(B6), 9153-9170. http://dx.doi.org/10.1029/JB095iB06p09153; doi:10.

Chen, Y. (1992). Oceanic crustal thickness versus spreading rate. Geophysical Research Letters, 19(8), 753-756. https://doi.org/10.1029/92GL00161

Chen, Y., Lin, J. (1999). Mechanisms for the formation of ridge-axis topography at slow-spreading ridges: a lithospheric-plate flexural model. Geophysical Journal International, 136, 8-18.

Chen, Y., Morgan, W. (1990). Rift valley/no rift valley transition at mid-ocean ridges. Journal of Geophysical Research, 95(B11), 17571-17581. http://doi.wiley.com/10.1029/JB095iB11p17571

Colman, A., Sinton, J., White, S., McClinton, J., Bowles, J., Rubin, K., Behn, B., Cushman, B., Eason, D., Gregg, T., Grönvold, K., Hidalgo, S., Howell, J., Neill, O., Russo, C. (2012). Effects of variable magma supply on mid-ocean ridge eruptions: Constraints from mapped lava flow fields along the Galápagos Spreading Center. Geochemistry, Geophysics, Geosystems, 13(8), 1-28. 10.1029/2012GC004163

Dauteuil, O., Brun, J. (1993). Oblique rifting in a slow-spreading ridge. Nature, 361(6408), 145–148.

Dawers, N., Anders, M., Scholz, C. (1993). Growth of normal faults: displacement-length scaling. Geology, 21(12), 1107-1110.

Dean, S., Murton, B., Minshull, T., Henstock, T., White, R. (2009). An integrated kinematic and geochemical model to determine lithospheric extension and mantle temperature from syn-rift volcanic compositions. Earth and Planetary Science Letters, 278(1-2), 26-39.

Dick, H., Lin, J., Schouten, H. (2003). An ultraslow-spreading class of ocean ridge. Nature, 426(6965), 405-412. http://www.ncbi.nlm.nih.gov/pubmed/14647373

Dick, H., Thompson, G., Bryan, W. (1981). Low-angle faulting and steady-state emplacement of plutonic rocks at ridge-transform intersections. American Geophysical Union, 62, 406.

Le Douaran, S., & Parsons, B. E. (1982). A Note on the Correction of Ocean Floor Depths for Sediment Loading. Journal of Geophysical Research, 87(B6), 4715–4722. https://doi.org/10.1029/JB087iB06p04715

Eason, D., Dunn, R., Canales, J., Sohn, R. (2016). Segment-scale variations in seafloor volcanic and tectonic processes form multibeam sonar imaging, Mid-Atlantic Ridge Rainbow region (35˚45'-36˚35'N). Geochemistry, Geophysics, Geosystems, 17, 3560-3579. DOI: 10.1002/2016GC006433

Escartin, J., Cannat, M., Pouliquen, G., Rabain, A., Lin, J. (2001). Crustal thickness of V-shaped ridges south of the Azores: Interaction of the Mid-Atlantic Ridge (36°-39°N) and the Azores hot spot. Journal of Geophysical Research: Solid Earth. 106(B10), 21719-21735. http://doi.wiley.com/10.1029/2001JB000224

Escartin, J., Cowie, P., Searle, R., Allerton, S., Mitchell, N., MacLeod, C., Slootweg, A. (1999). Quantifying tectonic strain and magmatic accretion at a slow spreading ridge segment, Mid-Atlantic Ridge, 29°N. Journal of Geophysical Research, 104(B5), 10421–10437. https://doi.org/10.1029/1998JB900097

Fournier, M., Petit, C. (2007). Oblique rifting at oceanic ridges: Relationship between spreading and stretching directions from earthquake focal mechanisms. Journal of Structural Geology, 29(2), 201-208.

Forsyth, D., Ehrenbard, R., Chapin, S. (1987). Anomalous upper mantle beneath the Australian-Antarctic discordance. Earth and Planetary Science Letters, 84(4), 471-478. DOI: 10.1016/0012-821X(87)90011-2

Forsyth, D., Uyeda, S. (1975). On the Relative Importance of the Driving Forces of Plate Motion. Geophysical Journal of the Royal Astronomical Society, 43(1), 163-200.

Fox, P., Lowrie, A., Heezen, B. (1969). Oceanographer fracture zone. Deep-sea Research and Oceanographic Abstracts, 16(1), 59-66. DOI: 10.1016/0011-7471(69)90050-3

Floyd, J., Mutter, J., Carbotte, S. (2002). Seismic Reflection Imaging of the Evolution of Oceanic Crustal Structure at the Intermediate Rate Spreading Costa Rica Rift. American Geophysical Union, Fall Meeting.

Garfunkel, Z. (1986). Review of oceanic transform activity and development. Journal of the Geological Society, 143(5), 775–784. https://doi.org/10.1144/gsjgs.143.5.0775

Goff, J., Arbic, B. (2010). Global prediction of abyssal hill roughness statistics for use in ocean models from digital maps of paleo-spreading rate, paleo-ridge orientation, and sediment thickness. Ocean Modelling, 32(1–2), 36–43. https://doi.org/10.1016/j.ocemod.2009.10.001

Hasterok, D. (2013). A heat flow based cooling model for tectonic plates. Earth and Planetary Science Letters, 361, 34–43. https://doi.org/10.1016/j.epsl.2012.10.036

Heiskanen, W., Moritz, H. (1967). Physical Geodesy. W. H. Freeman and Company. 130-133

Hey, R., Johnson, G., Lowrie, A. (1977). Recent plate motions in the Galapagos area. Bulletin of the Geological Society of America, 88(10), 1385–1403. https://doi.org/10.1130/0016-7606(1977)88<1385:RPMITG>2.0.CO;2

Hey, R., Martinez, F., Hoskuldsson, A., Benediktsodottir, A. (2010). Propagating rift model for the V-shaped ridges south of Iceland. Geochemistry, Geophysics, Geosystems, 11(March), 1–24. https://doi.org/10.1029/2009GC002865

Hilton, D., Gronvold, K., Macpherson, C., Castillo, P. (1999). Extreme 3He/4He ratios in northwest Iceland: Constraining the common component in mantle plumes. Earth and Planetary Science Letters, 173(1-2), 53-60. http://dx.doi.org/10.1016/S0012-821X(99)00215-0

Hobbs, R., Peirce, C. (2015). RRS James Cook JC114 Cruise report.

Holden, J., Iorio, D., Butterfield, D., Clague, D. (2008). R/V Atlantis – DSV Alvin AT15 - 36 Endeavour Segment and Axial Volcano Juan de Fuca Ridge, Northeast Pacific Ocean. Atlantis.

Ito, G., Behn, M. (2008). Magmatic and tectonic extension at mid-ocean ridges: 2. Origin of axial morphology. Geochemistry, Geophysical, Geosystems, 9(9), 1-20. http://doi.wiley.com/10.1029/2008GC001970

Ito, G., Shen, Y., Hirth, G., Wolfe, C. (1999). Mantle flow, melting, and dehydration of the Iceland mantle plume. Earth and Planetary Science Letters, 165, 81-96. DOI: 10.1109/EEM.2017.7981990

Ito, G. (2001). Reykjanes V-shaped ridges originating from a pulsing and dehydrating mantle plume. Nature, 411(June), 681-684.

Jagoutz, O., Royden, L., Holt, A., Becker, T. (2015). Anomalously fast convergence of India and Eurasia caused by double subduction. Nature Geoscience, 8(6), 475-478. http://www.nature.com/doifinder/10.1038/ngeo2418

Jones, S., Murton, B., Fitton, J., White, N., Maclennan, J., Walters, R. (2014). A joint geochemical-geophysical record of time-dependent mantle convection south of Iceland. Earth and Planetary Science Letters, 386, 86-97. http://dx.doi.org/10.1016/j.epsl.2013.09.029

Jones, S., White, N., Maclennan, J. (2002). V-shaped ridges around Iceland: Implications for spatial and temporal patterns of mantle convection. Geochemistry, Geophysics, Geosystems, 3(October), 1-23. DOI: 10.1029/2002GC000361

Jones, E. (2004). Velocity of off-shore material. Marine Geophysics, 61-64.

Juliani, C. (2019). Automated discrimination of fault scarps along an Arctic mid-ocean ridge using neural networks. Computers and Geoscience, 124, 27-36.

Karson, J., Dick, H. (1983). Tectonics of ridge-transform intersections at the Kane fracture zone. Marine Geophysical Researches, 6(1), 51–98. https://doi.org/10.1007/BF00300398

Keeton, J., & Searle, R. (1996). Analysis of Simrad EM12 Multibeam Bathymetry and Acoustic Backscatter Data for Seafloor Mapping, Exemplified at the Mid-Atlantic Ridge at 45˚N. Marine Geophysical Researches, 18, 663-688.

Keeton, J., Searle, R., Parsons, B., White, R., Murton, B., Parson, L., Sinha, M. (1996). Bathymetry of the Reykjanes Ridge. Marine Geophysical Researchers, 19, 55-64.Kelly, D., Delaney, J. (1987). Two-phase separation and fracturing in mid-ocean ridge gabbros at temperatures greater than 700˚C. Earth and Planetary Science Letters, 83(1-4), 53-66. DOI: 10.1016/0012-821X(87)90050-1

Klein, E., Langmuir, C. (1987). Global correlations of ocean ridge basalt chemistry with axial depth and crustal thickness. Journal of Geophysical Research, 92(B8), 8089–8115. https://doi.org/10.1029/JB092iB08p08089

Kongsberg. (2005). 12 kHz multibeam echo sounder seabed mapping to full ocean depth, (June). Retrieved from http://www.kongsberg-simrad.de/pdf/faecherlot_em120_eng_broch.pdf

Kim, J., Pak, S., Moon, J., Lee, S., Oh, J., Stuart, F. (2017). Mantle heterogeneity in the source region of mid-ocean ridge basalts along the northern Central Indian Ridge (88S–178S). Geochemistry, Geophysics, Geosystems, 18, 1419-1434. DOI: 10.1002/2016GC006673

Kuo, B., Forsyth, D. (1988). Gravity anomalies of the ridge-transform system in the South Atlantic between 31 and 34.5˚S: Upwelling centers and variations in crustal thickness. Marine Geophysical Researchers, 10(3-4), 205-262. DOI: 10.1007/BF00310065

Langmuir, C., Bender, J. (1984). The geochemistry of oceanic basalts in the vicinity of transform faults: observations and implications. Earth and Planetary Science Letters, 69(1), 107-127. DOI: 10.1016/0012-821X(84)90077-3

Larson, R., Pitman , W., Golovchenko, X., Cande, S., Dewey, J., Haxby, W., LaBrecque, J. (1985). The bedrock geology of the world (map).

Lecours, V., Devillers, R., Simms, Al E., Lucieer, V. L., Brown, C. J. (2017). Towards a framework from terrain attribute selection in environmental studies. Environmental Modelling and Software, 89, 19-30. DOI: 10.1016/j.envsoft.2016.11.027

Lonsdale, P., Kiltgord, K. (1978). Structure and tectonic history of the eastern Panama Basin. Geological Society of America Bulletin, 89(80703), 981-999. DOI: 10.1130/0016-7606(1978)89<981:SATHOT>2.0.CO;2

Lonsdale, P. (2005). Creation of the Cocos and Nazca plates by fission of the Farallon plate. Tectonophysics, 404(3-4), 237-264. DOI: 10.1016/j.tecto.2005.05.011

Lowrie, W. (2007). Isostasy. Fundamentals of Geophysics, 101-103.

Lin, J., Purdy, G., Schouten, H., Sempere, J., & Zervas, C. (1990). Evidence from gravity data for focused magmatic accretion along the Mid-Atlantic Ridge. Nature, 344(6267), 627–632.

Ma, Y., Cochran, J. (1996). Transitions in axial morphology along the Southeast Indian Ridge. Journal of Geophysical Research: Solid Earch, 101(B7), 15849-15866.

Macdonald, K. (1982). Mid-Ocean Ridges: fine scale tectonic, volcanic and hydrothermal processes within the plate boundary zone. Annual Review of Earth and Planetary Sciences, 10(1), 155-190.

Macdonald, K., Fox, P., Perram, L., Eisen, M., Haymon, R., Miller, S., Carbotte, S., Cormier, M., Shor, A. (1988). A new view of the mid-ocean ridge from the behaviour of ridge-axis discontinuities. Nature, 335(September), 217-225.

Macdonald, K., Scheirer, D., Carbotte, S. (1991). Mid-Ocean Ridges: Segments and Discontinuities, Giant Cracks. Science, 253(5023), 986-994.

Mckenzie, D., Bickle, M. (1988). The volume and composition of melt generated by extension of the lithosphere. Journal of Petrology, 29(3), 625-679. DOI: 10.1093/petrology/29.3.625

Martinez, F., Hey, R. (2017). Propagating buoyant mantle upwelling on the Reykjanes Ridge. Earth and Planetary Science Letters, 457, 10–22. https://doi.org/10.1016/j.epsl.2016.09.057

Marty, J., Cazenave, A. (1989). Regional variations in subsidence rate of oceanic plates: a global analysis. Earth and Planetary Science Letters, 94, 301–315.

Mark, H., Behn, M., Olive, J., and Liu, Y. (2018). Controls on Mid-ocean Ridge Normal Fault Seismicity Across Spreading Rates From Rate-and-State Friction Models. Journal of Geophysical Research: Solid Earth, 123, 6719-6733. https://doi.org/ 10.1029/2018JB015545

Meschede, M., Barckhausen, U. (2000). Plate tectonic evolution of the Cocos-Nazca Spreading Center. Proceedings of the Ocean Drilling Program, Scientific Results, 170(January), 10.

Mitchell, N., Allerton, S., Escartin, J. (1998). Sedimentation on young ocean floor at the Mid-Atlantic Ridge, 29 degrees N. Marine Geology, 148(1-2), 1-8.

Morgan, J. (1987). Melt migration beneath mid-ocean spreading centers. Geophysical Research Letters, 14(12), 1238-1241. DOI: 10.1029/GL014i012p01238

Morgan, J., Parmentier, E., Lin, J. (1987). Mechanisms for the origin of mid-ocean ridge axial topography: Implications for the thermal and mechanical structure of accreting plate boundaries. Journal of Geophysical Research, 92(B12), 12823-12836. http://dx.doi.org/10.1029/JB092iB12p12823; doi:10

Montési, L., Behn, M., Hebert, L., Lin, J., Barry, J. (2011). Controls on melt migration and extraction at the ultraslow Southwest Indian Ridge 10°–16°E. Journal of Geophysical Research, 116(B10), B10102. https://doi.org/10.1029/2011JB008259

Muirhead, J., Kattenhorn, S., Le Corvec, N. (2015). Varying styles of magmatic strain accommodation across the East African Rift. Geochemistry, Geophysics, Geosystems, 16, 2775-2795. DOI: 10.1002/2015GC005918

Müller, R. D., Sdrolias, M., Gaina, C., & Roest, W. R. (2008). Age, spreading rates, and spreading asymmetry of the world's ocean crust. Geochemistry, Geophysics, Geosystems, 9(4), 1–19. https://doi.org/10.1029/2007GC001743

Murton, B., Parson, L. (1993). Segmentation, volcanism and deformation of oblique spreading centres: A quantitative study of the Reykjanes Ridge. Tectonophysics, 222(2), 237-257. DOI: 10.1016/0040-1951(93)90051-K

Murton, B., Taylor, R., Thirlwall, M. (2002). Plume – Ridge Interaction: a Geochemical Perspective from the Reykjanes Ridge. Journal of Petrology, 43(11), 1987-2012.

Murton, B., Rona, P. (2015). Carlsberg Ridge and Mid-Atlantic Ridge: Comparison of slow spreading centre analogues. Deep-sea Research Part II: Topical studies in oceanography, 121, 71-84. http://dx.doi.org/10.1016/j.dsr2.2015.04.021

Niu, Y. (1997). Mantle Melting and Melt Extraction Processes beneath Ocean Ridges: Evidence from Abyssal Peridotites. Journal of Petrology, 38(8), 1047-1074.

Niu, Y., Bideau, D., Hékinian, R., Batiza, R. (2001). Mantle compositional control on the extent of mantle melting, crust production, gravity anomaly, ridge morphology, and ridge segmentation: A case study at the Mid-Atlantic Ridge 33-35°N. Earth and Planetary Science Letters, 186(3–4), 383–399.

Office of GEOINT Sciences (2008). Gravity station data format and anomaly computations. 0-6.

Paulatto, M., Canales, J. P., Dunn, R. A., Sohn, R. A. (2015). Heterogeneous and asymmetric crustal accretion: New constraints from multibeam bathymetry and potential field data from the Rainbow area of the Mid-Atlantic Ridge (36°15'N). Geochemistry, Geophysics, Geosystems, 16, 2994-3014. DOI: 10.1002/2015GC005743

Parkin, C., White, R. (2008). Influence of the Iceland mantle plume on oceanic crust generation in the North Atlantic. Geophysical Journal International, 173(1), 168-188. DOI: 10.1111/j.1365-246X.2007.03689.x

Parnell-Turner, R., White, N., Henstock, T., Murton, B., Maclennan, J., Jones, S. (2014). A continuous 55-million-year record of transient mantle plume activity beneath Iceland. Nature Geoscience, 7(12), 914–919. https://doi.org/http://dx.doi.org/10.1038/ngeo2281 10.1038/ngeo2281

Parnell-Turner, R., White, N., Henstock, T., Jones, S., Maclennan, J., Murton, B. (2017). Causes and Consequences of Diachronous V-Shaped Ridges in the North Atlantic Ocean. Journal of Geophysical Research: Solid Earth, 122(11), 8675-8708. DOI: 10.1002/2017JB014225

Parson, L., Murton, B., Searle, R., Booth, D., Evans, J., Field, P., Keeton, J., Laughton, A., McAllister, E., Millard, N., Redbourne, L., Rouse, I., Shor, A., Smith, D., Spencer, S., Summerhayes, C., Walker, C. (1993). En echelon axial volcanic ridges at the Reykjanes Ridge: a life cycle of volcanism and tectonics. Earth and Planetary Science Letters, 117(1-2), 73-87. http://linkinghub.elsevier.com/retrieve/pii/0012821X9390118S

Poreda, R., Schilling, J., Craig, H. (1986). Helium and hydrogen isotopes in ocean-ridge basalts north and south of Iceland. Earth and Planetary Science Letters. 78(1), 1-17. DOI: 10.1016/0012-821X(86)90168-8

Puthe, C., Gerya, T. (2014). Dependence of mid-ocean ridge morphology on spreading rates in the numerical 3D models. Gondwana Research, 25, 270-283.

Putrika, K. (2005). Mantle potential temperatures at Hawaii, Iceland, and the mid-ocean ridge system, as inferred from olivine phenocrysts: Evidence for thermally driven mantle plumes. Geochemistry, Geophysics, Geosystems. 6(5), 1-14. DOI: 10.1029/2005GC000915

Riedesel, M., Orcutt, J., MacDonald, D., McClain, J. (1982). Microearthquakes in the Black Smoker Hydrothermal Field, East Pacific Rise at 21°N. Journal of Geophysical Research. 87(B13), 10613-10623. http://dx.doi.org/10.1029/JB087iB13p10613; doi:10

Rommevaux, C., Deplus, C., Patriat, P., Sempere, J. (1994). Three-dimensional gravity study of the Mid-Atlantic Ridge: evolution of the segmentation between 28° and 29°N during the last 10 m.y. Journal of Geophysical Research, 99(B2), 3015–3029. https://doi.org/10.1029/93JB02361

Sauter, D., Sloan, H., Cannat, M., Goff, J., Patriat, P., Schaming, M., Roest, W. (2011). From slow to ultra-slow: How does spreading rate affect seafloor roughness and crustal thickness?. Geology, 39(10), 911-914. http://geology.gsapubs.org/cgi/doi/10.1130/G32028.1

Schellart, W. (2004). Quantifying the net slab pull force as a driving mechanism for plate tectonics. Geophysical Research Letters, 31(7), 10-14. http://dx.doi.org/10.1029/2004GL019528; doi:10.102

Schilling, J., Zajac, M., Evans, R., Johnston, T., White, W., Devine, J., Kingsley, R. (1983). Petrological and Geochemical Variations along the Mid-Atlantic ridge from 29N to 73N. American Journal of Science, 283(June), 510–586.

Schouten, H., Klitgord, K., Whitehea, A. (1985). Segmentation of mid-ocean ridges. Nature, 317(September), 225-229. DOI: 10.1038/316507a0

Scholz, C. (1988). The brittle-plastic transition and the depth of seismic faulting. Geologische Runschau, 77(1), 319-328. DOI: 10.1007/BF01848693

Searle, R. (1996). CD99 cruise report.

Searle, R. (2013). Mid-Ocean Ridges. Cambridge University Press. 129-131.

Searle, R., Keeton, J., Owens, R., White, R., Mecklenburgh, R., Parsons, B. (1998). The Reykjanes Ridge: structure and tectonics of a hot-spot-influenced, slow-spreading ridge, from multibeam bathymetry, gravity and magnetic investigations, 160, 463–478.

Sempéré, J., Lin, J., Brown, H., Schouten, H., Purdy, G. (1993). Segmentation and morphotectonic variations along a slow-spreading center: The Mid-Atlantic Ridge (24°00' N - 30°40' N). Marine Geophysical Researches, 153–200.

Sempéré, J., Palmer, J., Christie, D., Morgan, J., Shor, A. (1991). Australian-Antarctic discordance. Geology, 19(5), 429-432. DOI: 10.1130/0091-7613(1991)019<0429:AAD>2.3.CO;2

Sempéré, J., Purdy, G., Schouten, H. (1990). Segmentation of the Mid-Atlantic Ridge between 24°N and 30'40°N. Nature, 344(March), 427-431. http://www.nature.com/nature/journal/v344/n6265/abs/344427a0.html

Shaw, P. (1992). Ridge segmentation, faulting and crustal thickness in the Atlantic Ocean. Nature, 358(6386), 490-493. DOI: 10.1038/358490a0

Sleep, N., Warren, J. (2014). Effect of latent heat of freezing on crustal generation at low spreading rates. Geochemistry, Geophysics, Geosystems, 15, 3161-3174. DOI: 10.1002/2014GC005423

Smallwood, J., White, R. (2002). Ridge-plume interaction in the North Atlantic and its influence on continental breakup and seafloor spreading. The Geological Society of London, 197, 15–37.

Smith, D., Cann, J., Dougherty, M., Lin, J., Spencer, S., Macleod, C., Robertson, W. (1995). Mid-Atlantic Ridge volcanism from deep-towed side-scan sonar images, 25-29 N. Journal of Volcanology and Geothermal Research, 67, 233–262.

Solomon, S., Huang, P., Meinke, L. (1988). The seismic moment budget of slowly spreading ridges. Nature, 334, 58–60. https://doi.org/10.1038/334058a0

Spudich, P., Orcutt, J. (1980). A new look at the seismic velocity structure of oceanic crust. Reviews of Geophysics and Space Physics, 18(3), 627-645.

Standish, J., Dick, H., Michael, P., Melson, W., O'Hearn, T. (2008). MORB generation beneath the ultraslow spreading Southwest Indian Ridge (9-25°E): Major element chemistry and the importance of process versus source. Geochemistry, Geophysics, Geosystems, 9(5). https://doi.org/10.1029/2008GC001959

Stein, C., Stein, S. (1992). A model for the global variation in oceanic depth and heat flow with lithospheric age. Nature, 107(September), 259–262.

Suppe, J. (1985). Isostasy, Principles of Structural Geology. Princeton University. 17-19.

Talwani, M., Windisctt, C., Langseth, M. (1971). Reykjanes Ridge Crest: A Detailed Geophysical Study. Journal of Geophysical Research, 76(2), 473–517.

Tan, Y., Tolstoy, M., Waldhauser, F., Wilcock, W., (2016). Dynamics of a seafloor-spreading episode at the East Pacific Rise. Nature Publishing Group, 540(7632), 261-265.

Tassara, A. (2005). Interaction between the Nazca and South American plates and formation of the Altiplano-Puna plateau: Review of a flexural analysis along the Andean margin (15°-34°S). Tectonophysics, 399(1-4), 39-57. DOI: 10.1016/j.tecto.2004.12.014

Taylor, R., Thirlwall, M., Murton, B., Hilton, D., Gee, M. (1997). Isotopic constraints on the influence of the Icelandic plume. Earth and Planetary Science Letters, 148(Febuary), E1–E8. https://doi.org/10.1016/S0012-821X(97)00038-1

Thatcher, W., Hill, D. (1995). A simple model for the fault-generated morphology of slow-spreading mid-oceanic ridges. Journal of Geophysical Research, 100(B1), 561–570. https://doi.org/10.1029/94JB02593

Toomey, D., Solomon, S., Purdy, G. (1988). Microearthquakes beneath median valley of Mid-Atlantic Ridge near 23°N: tomography and tectonics. Journal of Geophysical Research, 83(B8), 9093-9112. DOI: 10.1029/JB093iB08p09093

Tucholke, B., Lin, J. (1994). A geological model for the structure of ridge segments in slow spreading ocean crust. Journal of Geophysical Research, 99(B6), 11937-11958. http://dx.doi.org/10.1029/94JB00338; doi:10.1029/9

Tuckwell, G., Bull, J., Sanderson, D. (1999). Mechanical control of oceanic plate boundary geometry. Tectonophysics, 313(3), 265-270. DOI: 10.1016/S0040-1951(99)00206-1

VanderBeek, B., Toomey, D., Hooft, E., Wilcock, W. (2016). Segmentation of mid-ocean ridges attributed to oblique mantle divergence. Nature Geoscience. 9(8), 656-642. DOI: 10.1038/ngeo2745

Violay, M., Gibert, B., Mainprice, D., Evans, B., Dautria, J., Azais, P., Pezard, P. (2012). Journal of Geophysical Research: Solid Earth, 117(3), 3-23. DOI: 10.1029/2011JB008884

Wang, T., Tucholke, B., Lin, J. (2015). Spatial and temporal variations in crustal production at the Mid-Atlantic Ridge, 25°N-27°30'N and 0-27 Ma. Journal of Geophysical Research: Solid Earth. https://doi.org/10.1002/2014JB011501

Weatherley, S., Katz, R. (2016). Melt transport rates in heterogeneous mantle beneath mid-ocean ridges. Geochimica et Cosmochinica Acta, 172, 39-54. DOI: 10.1016/j.gca.2015.09.029

White, N. (2011). RRS James Cook JC050 Cruise report V-Shaped Ridges Experiment (VRE), (November). https://doi.org/10.1007/s13398-014-0173-7.2

White, R. (1997). Rift-plume interaction in the North Atlantic. Philosophical Transactions of the Royal Society A, 355(1723), 319–339.

White, R., Bown, J., & Smallwood, J. (1995). The temperature of the Iceland plume and origin of outward-propagating V-shaped ridges. Journal of the Geological Society, 152, 1039–1045.

White, R., MacKenzie, D., O'Nions, R. (1992). Oceanic crustal thickness from seismic measurements and rare earth element inversions. Journal of Geophysical Research, 97(B13), 19683-19715

Whitehead, S., Dick, H., Shouten, H. (1984). A mechanism for magmatic accretion under spreading centers. Nature, 312, 146–148.

Williams, S., Flament, N., Müller, R. (2016). Alignment between seafloor spreading directions and absolute plate motions through time. Geophysical Research Letters, 43(4), 1472-1480. DOI: 10.1002/2015GL067155.

Wilson, D., Teagle, D., Acton, G. (2003). Leg 203 Summary. Proceedings of the Ocean Drilling Program, 206, 1-113.

Wolfe, C., Purdy, G., Toomey, D., Solomon, S. (1995). Microearthquake characteristics and crustal velocity structure at 29° N on the Mid-Atlantic Ridge: The architecture of a slow spreading segment. Journal of Geophysical Research, 100(B12), 24449–24472. https://doi.org/10.1029/95JB02399

Woodcock, N. (1986). The role of strike-slip fault systems at plate boundaries. Philosophical Transactions of the Royal Society, 317(1539), 13-29.

Zhang, T., Gordon, R. (2016). Plume Flux, Spreading Rate, and Obliquity of Seafloor Spreading. American Geophysical Union.